2024

Modeling To Evaluate The Contribution Of The Built Environment On Heat Microenvironments And Analysis Of The Efficiency And Efficacy Of Electric Vehicle Purchase Incentives

Parker King
University of Vermont

MODELING TO EVALUATE THE CONTRIBUTION OF THE BUILT ENVIRONMENT ON HEAT MICROENVIRONMENTS AND ANALYSIS OF THE EFFICIENCY AND EFFICACY OF ELECTRIC VEHICLE PURCHASE INCENTIVES

A Dissertation Presented

by

Parker King

to

The Faculty of the Graduate College

of

The University of Vermont

In Partial Fulfillment of the Requirements
for the Degree of Doctor of Philosophy
Specializing in Civil and Environmental Engineering

May, 2024

Defense Date: March 18, 2024
Dissertation Examination Committee:

Gregory Rowangould, Ph.D., Advisor
Elizabeth Doran, Ph.D., Advisor
Kelsey Gleason, Ph.D., Chairperson
Dana Rowangould, Ph.D.
Donna M. Rizzo, Ph.D.
Holger Hoock, DPhil, Dean of the Graduate College

Abstract

This dissertation provides an integrated examination of urban heat mitigation strategies and the effectiveness of electric vehicle (EV) purchase incentives, employing innovative methodologies across its four chapters to address pressing environmental and policy challenges. It leverages a unique dataset obtained through extensive mobile sampling, state-of-the-art machine learning techniques, revealed preference data collected through robust survey design, and detailed sociodemographic analyses to offer insights into the dynamics of urban heat islands, sustainable transportation, and policy efficiency.

The first section details the quantifying of micro-environment heat differences pertaining to the influence of the built environment across 10 cities over 20 days, using mobile sampling conducted via e-bike. Building on the empirical findings of the first chapter, I utilize the developed models to conduct a statewide analysis of the potential for heat mitigation through the strategic replacement of pavement with tree cover. Lastly, we advance the discussion by employing the mobile data collected to evaluate the comparative predictive and mapping capabilities of two distinct machine learning algorithms.

The final section shifts focus to examining the awareness and influence of EV purchase incentives through a survey of recent vehicle purchasers. This chapter quantifies the effectiveness and efficiency of these incentives in driving sustainable transportation choices, providing critical insights into consumer behavior and the policy measures most likely to accelerate the adoption of electric vehicles.

The following work offers a comprehensive and multi-faceted exploration of urban heat mitigation and sustainable transportation policies. By combining field-based mobile sampling, advanced analytical models, and sociodemographic insights, this work contributes significantly to our understanding of effective strategies for creating cooler, more sustainable urban environments and promoting the adoption of electric vehicles.

Acknowledgements

This research in this dissertation was funded, partially, by a grant from the National Center for Sustainable Transportation (NCST), supported by the U.S. Department of Transportation (USDOT) through the University Transportation Centers program. I would like to thank the NCST and the USDOT for their support of university-based research in transportation, and especially for the funding provided in support of this project. Additionally, the research in this dissertation was supported and funded by the NOAA Climate Program Office's Extreme Heat Risk Initiative, Cooperative Agreement NA21OAR44310150.

Table of Contents

ABSTRACT I

ACKNOWLEDGEMENTS II

LIST OF FIGURES IV

LIST OF TABLES VII

INTRODUCTION 1

EXTREME HEAT COMPONENT 4

CHAPTER 1—THE CONTRIBUTION OF PAVEMENT TO MICROENVIRONMENT AIR TEMPERATURE IN SMALL CITIES AND TOWNS 4

Introduction 4

Methods 41

Results 58

Conclusion 62

CHAPTER 2—STATEWIDE POTENTIAL FOR HEAT EXPOSURE MITIGATION THROUGH SCENARIOS OF PAVEMENT REDUCTION 69

Introduction 69

Methods 76

Results 79

Conclusion 86

CHAPTER 3—COMPARISON OF DECISION-TREE BASED MACHINE LEARNING TECHNIQUES IN PREDICTING AND MAPPING MICROENVIRONMENT AIR TEMPERATURE 88

Introduction 88

Methods 92

Results 97

Conclusion 115

EV INCENTIVE POLICY COMPONENT 117

CHAPTER 4—THE EFFICACY AND EFFICIENCY OF ELECTRIC VEHICLE PURCHASE INCENTIVE POLICIES 117

Introduction 117

Methods 120

Results 126

Conclusion 142

DISSERTATION CLOSING REMARKS 143

REFERENCES 145

APPENDIX 167

List of Figures

Figure 1: Three different horizontal scales of the UHI effect, and vertical layers within each (Oke, 1997). 7
Figure 2: Subclassifications of LCZs (Stewart & Oke, 2012). 8
Figure 3: Heat fluxes present in the energy budget and their extended drivers (J. Kong et al., 2021). 13
Figure 4: Heat map generated along evening transect by researchers in Rotterdam (Heusinkveld et al., 2014). 37
Figure 5: Study area. Ten cities within Vermont were used for a mobile sampling campaign during the summer of 2022. 42
Figure 6: Photograph of the E-Bike mobile sensor design: (1) Solar radiation shield and location of the thermocouple and humidity sensor. (2) Humidity sensor unit. (3) Frame bag storing Omega 2400 temperature logger, QStarz Travel Recorder XT GPS logging unit, and repair equipment. (4) Taillight. (5) Head light. (6) Phone mount for GPS route navigation. 45
Figure 7: Distribution of air temperature measurements by transect. 46
Figure 8: DATA PROCESSING. Each observation received a value for the percent pavement within 25m, 50m, and 100m of its location. (A) Data was first plotted, cleaned, and buffered at three different radii, (B) Land cover data for each town (C) was then intersected with each buffered observation. Percent pavement was then calculated based on the area of the intersected polygons and the area of their respective buffer. 47
Figure 9: Scatter plot of Percent Pavement area within 25m, 50m, and 100m buffers versus air temperature for A) morning, B) mid-day, and C) evening. Fit lines denote their regression coefficients in the legends to indicate magnitude and direction of association. 49
Figure 10: Spaghetti plots of time after sunrise (minutes) versus measured air temperature (F) for A) Morning, B) Mid-day, and C) Evening transects. Different colors represent separate transects. 51
Figure 11: Gridded (500 m x 500 m) change in household average mid-day air temperature reduction (°F) based on a mitigation scenario involving a replacement of 50% of household pavement exposure with tree cover. Averages are population-weighted. 80
Figure 12: Distribution of household temperature reductions by RUCA Classification for each mitigation scenario. 81
Figure 13. Distribution of temperature reductions per household in the A) 10% reduction scenario, B) 25% reduction scenario, and C) 50% reduction scenario. Red dotted lines signify the separation in deciles. 82

Figure 14. Population shares within temperature reduction deciles across all three mitigation scenarios for the nonwhite alone population. Data is at the block level. 83
Figure 15. Population shares of vulnerable age groups within temperature reduction deciles across all three mitigation scenarios. Data for both are at the census block group level. 84
Figure 16. Population shares of households below the poverty line within temperature reduction deciles across all three mitigation scenarios. The data is at the census tract level. 85
Figure 17. Predictor versus residuals of validation set. 98
Figure 18. Target versus predicted air temperature values in validation set. 98
Figure 19. Feature importance among features from the optimal RF model. 100
Figure 20. Residuals of validation set for optimal RF model. 101
Figure 21. Distribution of RMSE across XGBoost hyperparameter tuning. 103
Figure 22. Side by side comparison of actual versus predicted plots from training and testing of optimal XGBoost model. 105
Figure 23. Pavement exposure feature values versus residuals from validation set of the optimal XGBoost model. 106
Figure 24. Feature importance plot for features from the optimal XGBoost model. 107
Figure 25. Distribution of residuals from predictions made on the validation data by the optimal XGBoost model. 109
Figure 26. ALE plot of pavement exposure's effect on air temperature for optimal RF model. 110
Figure 27. ALE plot of pavement exposure's effect on air temperature for the optimal XGBoost model. 111
Figure 28. High resolution heat map of Montpelier, VT. Map was generated using RF regression model. 112
Figure 29. High resolution heat map of Montpelier, VT. Map was generated using XGBoost regression model. 113
Figure 30. High resolution map of Burlington, VT. Map was generated using RF regression model. 114
Figure 31. High resolution map of Burlington, VT. Map was generated using XGBoost regression model. 114
Figure 32: Categorization of purchase influences. 122
Figure 33. Network of participating Vermont automobile dealerships in survey recruitment. 124
Figure 34. Spatial distribution of survey participants by zip code. Blue dots signify the location of participating dealerships. 127
Figure 35. Distribution of survey participants by vehicle type. 128
Figure 36. Distribution of gender among survey participants. 133
Figure 37. Distribution of the number of vehicles (including recent purchase) in household. 134

FIGURE 38. DISTRIBUTION OF HOUSEHOLD SIZE AMONG SURVEY PARTICIPANTS. 134
FIGURE 39. DISTRIBUTION OF AGE AMONG SURVEY PARTICIPANTS. 135
FIGURE 40. DISTRIBUTION OF HOUSEHOLD INCOME AMONG SURVEY PARTICIPANTS. 136
FIGURE 41. FEATURE IMPORTANCE OF THE XGBOOST CLASSIFIER MODEL. 139
FIGURE 42. DISTRIBUTION OF SHAPLEY VALUES. NUMBERS IN PARENTHESES NEXT TO FEATURE NAMES REPRESENTS AVERAGE SHAPLEY VALUE FOR FEATURES ACROSS ALL OBSERVATIONS. 140

List of Tables

TABLE 1: DETAILS OF MOBILE SAMPLING CONDITIONS. DESCRIPTION OF CITIES AND TOWNS VISITED, AND WEATHER CONDITIONS ON DAYS SAMPLED. 43
TABLE 2. OLS REGRESSION COEFFICIENTS FROM MODELS REPRESENTING NINE COMBINATIONS OF BUFFER SIZES USED TO CALCULATE LAND COVER EXPOSURE AND DIURNAL PHASE THAT DATA WAS COLLECTED. BOLDED VALUES FOR COEFFICIENT ESTIMATES DENOTE STATISTICAL SIGNIFICANCE (α=0.05). 59
TABLE 3. AVERAGE LAND USE COEFFICIENTS AND THEIR INTERACTION TERMS FROM SEM BOOTSTRAPPING. VALUES IN THE TABLE REPRESENT THE MEAN OF THE COEFFICIENTS GENERATED FROM 100 ITERATIONS, THE STANDARD DEVIATION OF THESE COEFFICIENTS, AND THE AVERAGE LOG-LIKELIHOOD VALUES..... 61
TABLE 4. LIST OF FEATURES USED IN PREDICTIVE MACHINE LEARNING MODELS. 93
TABLE 5. PERFORMANCE OF RF MODEL ACROSS DIFFERENT PARAMETERS. BOLDED VALUES INDICATE PARAMETERS OF THE SELECTED OPTIMAL MODEL. 97
TABLE 6. DISTRIBUTION OF PURCHASE FACTORS AND THEIR IMPORTANCE ACROSS VEHICLE TYPE. 129
TABLE 7. DISTRIBUTION OF PURCHASE FACTORS AND THEIR INFLUENCE ACROSS VEHICLE TYPES..... 130
TABLE 8. CONFUSION MATRICES OF PREDICTIONS ON TRAINING AND TESTING OF OPTIMAL XGBOOST CLASSIFIER..... 138

Introduction

Extreme heat surpasses all other weather-related causes of fatalities over the past thirty years, and is increasingly acknowledged as a significant threat to public health (Weather Related Fatality and Injury Statistics, 2021). Exposure to heat can increase discomfort and fatigue, lead to heat cramps, increase emergency room visits and hospitalizations, as well as exacerbate pre-existing chronic conditions (U.S. National Center for Environmental Health, 2013).

However, health impacts of heat exposure are a component of the much broader and complex concern. The escalation of urban temperatures is closely linked with a deterioration in air quality, evidenced by increased concentrations of noxious pollutants such as NO_2, CO_2, and CO, particularly in conjunction with the intensity of urban heat islands (UHIs) (Fallmann et al., 2016; Lai & Cheng, 2009). In addition, warming trends in developing countries are projected to drive a surge in energy demand for cooling, potentially reaching 75% above current levels (Sherman et al., 2022). This convergence of escalating heat exposure, deteriorating air quality, and increasing energy consumption underscores the intricate and expanding challenges confronting populations in warm climates, which are expected to worsen with the advancing trends of climate change.

Additionally, the adoption of electric vehicles (EVs) is commonly regarded as an essential milestone in the global effort to reduce the effects of climate change. In 2021, the transportation sector in the United States was responsible for 28% of the nation's greenhouse gas emissions. This was marked by a 7% surge in CO_2 emissions from fossil

fuel combustion, reflecting a rebound in activity as society emerged from COVID-19 pandemic restrictions (EPA, 2023b). As innovation of this technology trends upward, governments at various levels have been formulating policies to foster and expedite the adoption of electric vehicles (Y. Zhou et al., 2015). Although these policies are evolving to keep pace with shifting economic dynamics, the level of innovation in the EV sector continues to accelerate. This dynamic landscape necessitates a comprehensive suite of options for consumers and manufacturers alike, promoting the spirited electrification of the global vehicle fleet. Additionally, it highlights the need for strategies tailored to overcome obstacles inherent in specific local economies, infrastructures, and climatic conditions.

This dissertation is presented in two larger components, of which the former includes chapters pertaining to the relationship between the built environment and micro-scale heat, and the latter evaluates the performance of financial incentive policies to promote EV adoption. Analysis from the extreme heat component demonstrates a novel approach to data collection and application in heat research to quantify effects of key components in the microenvironment-level heat signal, a series of scenarios for heat mitigation through pavement reduction and tree cover substitution, and comparison of prominent machine learning approaches to render high resolution heat maps on citywide scales. I utilize methods such as spatial regression to quantify the effect size of individual components known to contribute to or reduce the magnitude and presence of the microenvironment UHI signal. I apply two separate machine learning techniques to map heat signals along transportation infrastructure at high resolution and compare each model's output and performance to the current standard for such practices. Additionally, I

generate a selection of scenarios involving modifications to the current built environment on a statewide scale within Vermont to quantify the potential for heat mitigation through land use policy and identify specifically who would benefit from these modifications. The resultant models, maps, and projections offer a framework to assist transportation planners and designers in creating infrastructure that mitigates mesoscale heat signals, enhancing public health and energy efficiency. This research focuses on small cities and towns with climates far from the equator, a less common area of study for heat research. The final chapter investigates the effectiveness of EV purchase incentives available to Vermont consumers through collaboration with statewide auto dealers to gather and model revealed preference data.

Extreme Heat Component

Chapter 1—The Contribution of Pavement to Microenvironment Air Temperature in Small Cities and Towns

Introduction

This chapter aims to quantify the effect of an individual unit-area of pavement on the corresponding micro-scale air temperature. Data collection and model construction is informed by previous work rooted in designing a localized energy budget for a microenvironment, and the evolving methods of those utilizing a mobile sampling approach. The work of this chapter concludes with a tool designed from an empirical approach for engineers and planners to use in estimating the impacts of adding or reducing pavement exposure.

Historical Context—Heat and the Built Environment

Human adaptation to heat has evolved significantly since the initial migrations out of Africa around 90,000 years ago. These early humans surpassed their inherent biological limits to manage the risks associated with extreme heat and its environmental impacts (Balaresque et al., 2007). The advent of the built environment introduced novel ways for societies to regulate their exposure to heat. Of these, one of the earliest approaches that can still be seen today is rooftop sleeping arrangements (Briggs, 2022). The Sumerians utilized novel architecture approaches such as courtyards, wind catchers, and other passive cooling techniques that remain as hallmarks of sustainable design.

Historically, seeking climate refuge and altering behaviors were the primary adaptations as humans began to understand the body's physiological response to heat before the era of industrialization. However, the priority of urban development often overshadowed public

health concerns. This is exemplified by the 1743 heatwave in northern China, which resulted in over 11,000 deaths (D. Zhang & Gaston, 2004) and echoes in the modern era, such as the 79-day heat event from 2023 in the same region, causing heat stress, droughts, wildfires, and power outages (Jiang et al., 2023; Z. Yin et al., 2023).

The post-industrialization world enabled society to better identify, measure, and intensify extreme heat events. The highest temperature on record reached 134ºF, logged during the 1913 heatwave in Death Valley, California (Roof & Callagan, 2003). The Dust Bowl era of the 1930s in the United States bore witness to prolonged and intense heatwaves, exemplified by Yuma, Arizona's staggering 101 consecutive days of temperatures reaching 100ºF or greater (Hutchison, 2008). The 1976 heatwave in the British Isles, coupled with a severe drought, was found to have caused an excess of 20% in summer mortality rates (Ellis et al., 1980). More contemporary instances include the 2010 northern hemisphere heatwave that resulted in 55,000 fatalities, 25% national crop failure, and a 1% GDP reduction in Russia. In 2018, Japan endured a heatwave shortly after significant flooding, leading to over 34,000 heat-related emergency transportations (Hayashida et al., 2019). Additionally, Canada recorded its all-time highest temperature during the heatwave that swept through British Columbia and the Northwestern United States in 2021. This event was categorized as a millennium-scale anomaly, with climate change increasing its likelihood 150-fold and intensity augmented by 3.6°F (Philip et al., 2022).

Earth’s surface temperature has risen by 0.14°F each decade since 1880, and resembling more rapid growth since 1980 with 0.32°F increases per decade (Lindsey & Dahlman,

2023). The ten warmest years on record for global averages since recording began in 1880 have all been since 2010. One cannot help but acknowledge the correlation of this global trend with the growing inclination of urbanization. The United Nations estimated the proportion of the global population living in cities in 2018 to be greater than half and projected to grow to over 6 billion by 2041 (United Nations, 2019). The built environment's ability to amplify heat exposure was coined as an "urban heat island" effect in the 19th century (Howard, 1833). Published research exploring the relationship between pavement and temperature came about in the 1950s and early modeling of the relationship was published in the 1970s (Barber, 1957; Berg, 1974; Williamson, 1972). Continued analyses with expanded methodologies continued through the rest of the century, and an expansive 2004 study pertaining to the UHI effect was conducted on 93 common pavement materials (Asaeda et al., 1996; Choubane & Tia, 1992; Doulos et al., 2004; Oke, 1982). Efforts such as these has since inspired exploration in the potential of alternative pavement materials with focuses on managing evaporation, absorption, and reflection (Golden & Kaloush, 2006; Scholz & Grabowiecki, 2007; Takebayashi & Moriyama, 2012).

The Urban Heat Island Effect

UHI research within biometeorology has revealed multifaceted impacts, including increased rainfall, and reduced air and water quality (Atkinson, 1969; Hester & Bauman, 2013; L.-Y. Xu et al., 2014; Y. Zhang, Miao, et al., 2017). Inequities in heat exposure have also been documented, with a study of 175 large U.S. urban areas showing higher surface UHI (SUHI) effects in communities of color in all but six areas (Hsu et al., 2021). Similarly, 72% of low-income neighborhoods in a global sample of 25 cities faced higher

heat levels (Chakraborty et al., 2019). Trends suggest that with ongoing urbanization and climate change, extreme heat events will intensify. Forecasts for 2050 predict UHI intensity increases of 0.9-0.1.3°F from urban expansion alone, and up to 5.4°F in certain locales—potentially doubling the anticipated rise in air temperature due to greenhouse gas emissions (K. Huang et al., 2019).

Heat in Four Dimensions

In the horizontal dimension, the UHI is studied at a mesoscale, local scale, and micro scale (**Figure 1**). The local scale ranges from a town down to a neighborhood or adjacent blocks, while the microscale extends from less than one meter to hundreds of meters, ranging from a surface to an alleyway (Oke, 1982).

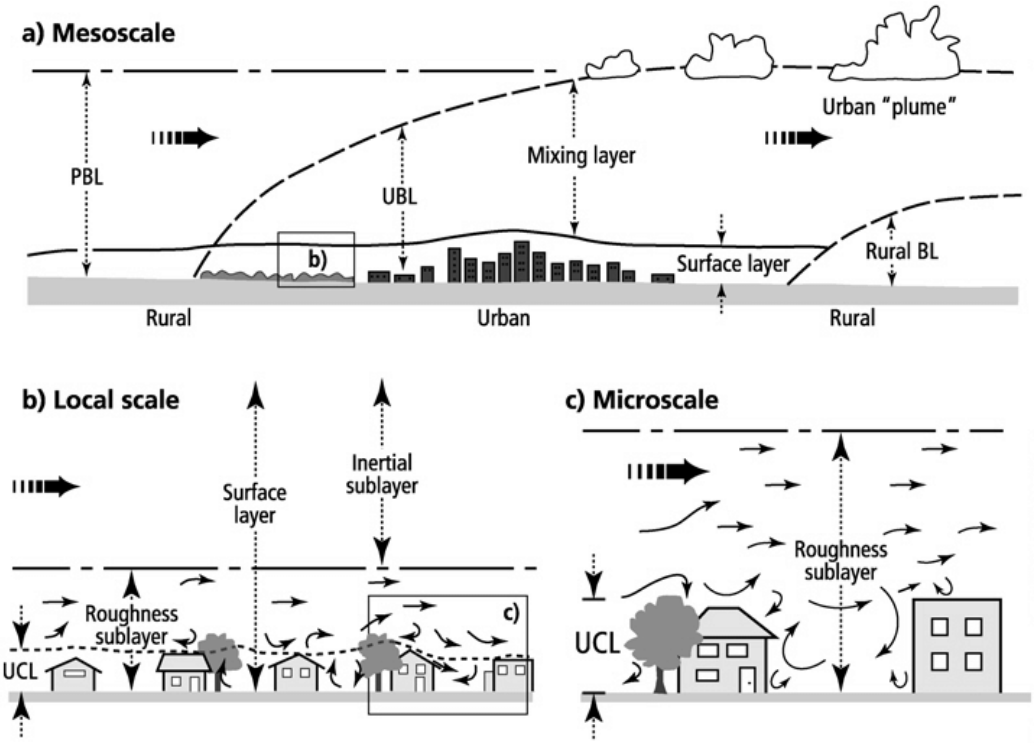

Figure 1: Three different horizontal scales of the UHI effect, and vertical layers within each (Oke, 1997).

The local scale is often the domain of one stationary climate site. It is defined in the urban space as the extent of nearby area sharing a common Local Climate Zone (LCZ) classification (Stewart & Oke, 2012)(**Figure 2**). These classifications are made based on characteristics such as urban fabric and roughness.

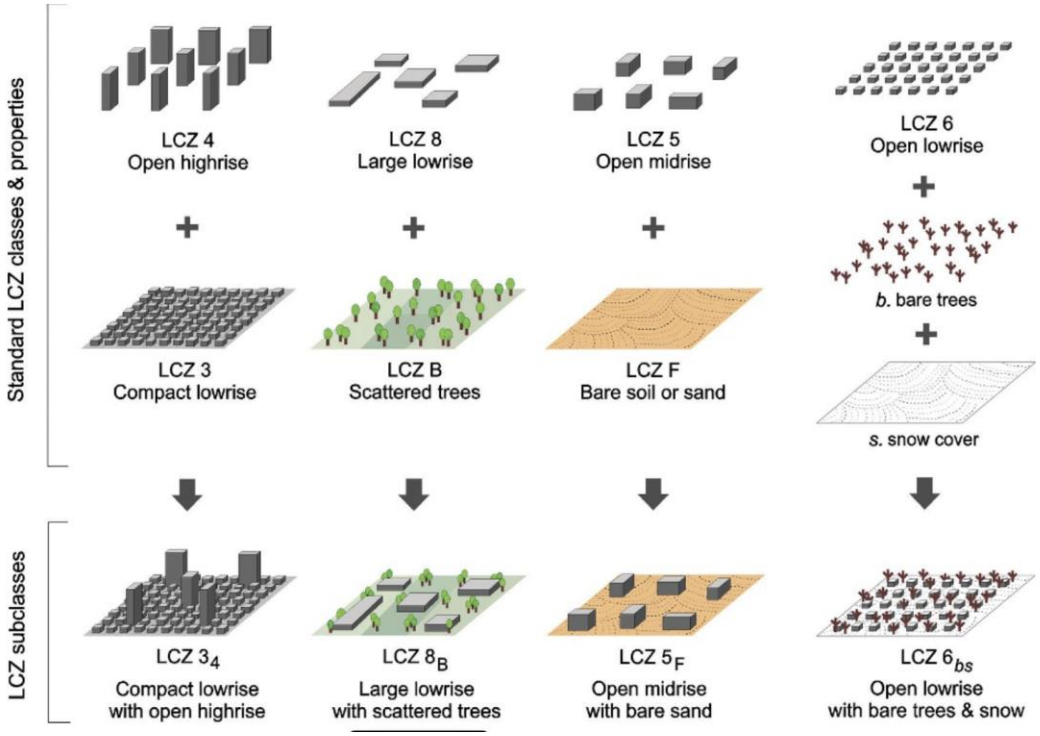

Figure 2: Subclassifications of LCZs (Stewart & Oke, 2012).

In assessing UHI effects on a local scale, data are often gathered from sites deemed most representative of Urban Climate Zones (UCZ) elements with regions spanning one to several kilometers (Oke, 2011). However, selecting such a site can be subjective, risking inaccuracies in characterizing local conditions. An alternative or supplementary approach involves averaging or weighting conditions across multiple spatial and temporal points. A common comparative measure in local scale heat research is the UHI intensity (ΔT),

which is the temperature differential between two spatial points—one within the UCZ and another in a less urbanized area. Although surface UHI measurements are increasingly accessible via satellite infrared data, research with direct implications for public health, air quality, and thermal energy considerations often prioritizes air temperature ΔT metrics (Oke, 2011).

In regions with relatively uniform topography, human activity, and built environment composition, the turbulence and variability of microenvironments typically offer predictable variations in UHI potential without significantly distorting UHI models. Indeed, much of the localized 'noise' can be mitigated by collecting measurements at or above the roughness sublayer (RSL) height—usually twice the average height of the surrounding structures (**Figure 1**). Above the RSL lies the inertial sublayer (ISL), which generally exhibits uniform conditions reflective of the local area. The ISL and RSL constitute what is termed the shared “surface layer” at the local scale. Higher up, the plume of the urban boundary layer (UBL) extends, lagging in shape towards the mesoscale's downwind direction. This broader mixing layer, together with the underlying surface layers, outlines the UBL, which characterizes the air within the mesoscale. The UBL's vertical reach can extend up to 2 km during peak warming and contract to less than 0.5 km at night (Oke, 2011).

At the microscale level, individual surfaces can generate distinct temperature signals. Oke (2011) likens these micro-level climates to a smaller space of warmer air temperature recognizable to a family cat, but also can occupy a thermodynamically homogenous space up to hundreds of meters across. Vertically, they are divided at the

average roof height to what is known below as the urban canopy layer (UCL). In areas with minimal urbanization, the UCL air temperature are assessed at a 1.5m height. Depending on methodology and application, this height or sometimes higher is commonly used for measurements in urban microenvironments as well. Above the UCL exists the remainder of the RSL of which defines the entire vertical bounds of the microenvironment. Mixing occurs between UCL and the RSL to create variability within the local scale.

Mesoscale UHIs manifest through complex dynamics within a city's UBL. Pollutants accumulated in this layer can disrupt the natural radiative warming processes, while heat generated by human activities within the urban canopy layer tends to rise, contributing to an overall upward movement of warm air. As a result, there is a net movement of warmer air descending from the upper reaches of the UBL (Oke, 2011). The intricate vertical and horizontal interactions of various components at different scales present a challenging complexity that researchers address through both empirical and theoretical studies. Research on mesoscale aspects of the UHI effect has identified common urban attributes that contribute to UHI development, including urban layout, geographical setting, and climatic factors (Debbage & Shepherd, 2015). Furthermore, studies find correlation between urban sprawl and an increase in extreme heat events, suggesting that urban expansion may heighten heat-related vulnerabilities (Stone Brian et al., 2010).

The complexity of urban heat dynamics in three spatial dimensions is further compounded by the sun as the original heat source in the system. Solar radiation dictates a diurnal heat cycle across micro, local, and mesoscales. The intensity of heat at each

scale is modulated by the day's varying radiation levels, altering the vertical layers' characteristics. Surface roughness creates shading, reducing direct radiation for parts of the day, while urban canyons add turbulence, affecting the mix of air temperatures. Evapotranspiration, another process demonstrated diurnal patterns, interacts with these warming and cooling cycles. A key distinction between daytime and nocturnal UHI effects lies in the thermal inertia of infrastructure, which retains heat after sunset, leading to a slower decline in surface temperatures compared to air temperatures. This delayed cooling exacerbates UHI effects at night, posing significant public health risks, especially during heatwaves when UHI effects are intensified by successive days of excessive heat (Rogers et al., 2019). The influence of nighttime UHI can also amplify daytime conditions, with data from New York City showing boundary-layer UHI intensities up to twice the decadal average during heatwaves (Ramamurthy et al., 2017).

The relationship between UHIs and heatwaves exhibits inconsistent findings regarding their synergy. A plausible hypothesis is that heatwaves, which blanket entire regions with excessive heat, might intensify the UHI effect in localized environments more than usual. However, an indicator known as heat magnitude—the disparity between UHI intensity during a heatwave and under typical summertime conditions—does not consistently register an increase. Kumar and Mishra (2019) noted an urban cooling effect in majority of the 89 Indian cities studied, attributed to decreased soil moisture and vegetative cover in rural areas during drier periods. Consequently, rural areas may experience more intense heat compared to urban areas, which suffer less from reduced evapotranspiration, thus diminishing UHI intensity during heatwaves. Despite these findings, the majority of

research indicates a synergistic relationship between UHIs and heatwaves (J. Kong et al., 2021).

Thermal Balance

Contribution to the UHI effect is influenced by six distinct heat fluxes. Anthropogenic heat flux is generated by human activities, encompassing vehicular emissions, air conditioning exhaust, construction activities, and human metabolic processes. Advective heat transfer is influenced by heat sinks such as winds or sea breezes that redistribute thermal energy. The primary source of radiative heat flux is solar radiation, which travels from the sun and interacts with various environmental layers and surfaces. Latent heat flux, or evapotranspiration, involves the heat transfer during water's phase changes on the surface. Sensible heat flux describes the energy exchange between the surface and the Urban Boundary Layer (UBL), influenced by temperature disparities, wind, and surface roughness. The storage heat flux refers to the capacity of the environment to absorb radiation and the rate at which it re-emits this stored energy. Kong's diagram (**Figure 3**) illustrates the multifaceted role of materials like pavement in the energy budget, showcasing their involvement through reflective, emissive, and storage drivers of heat flux.

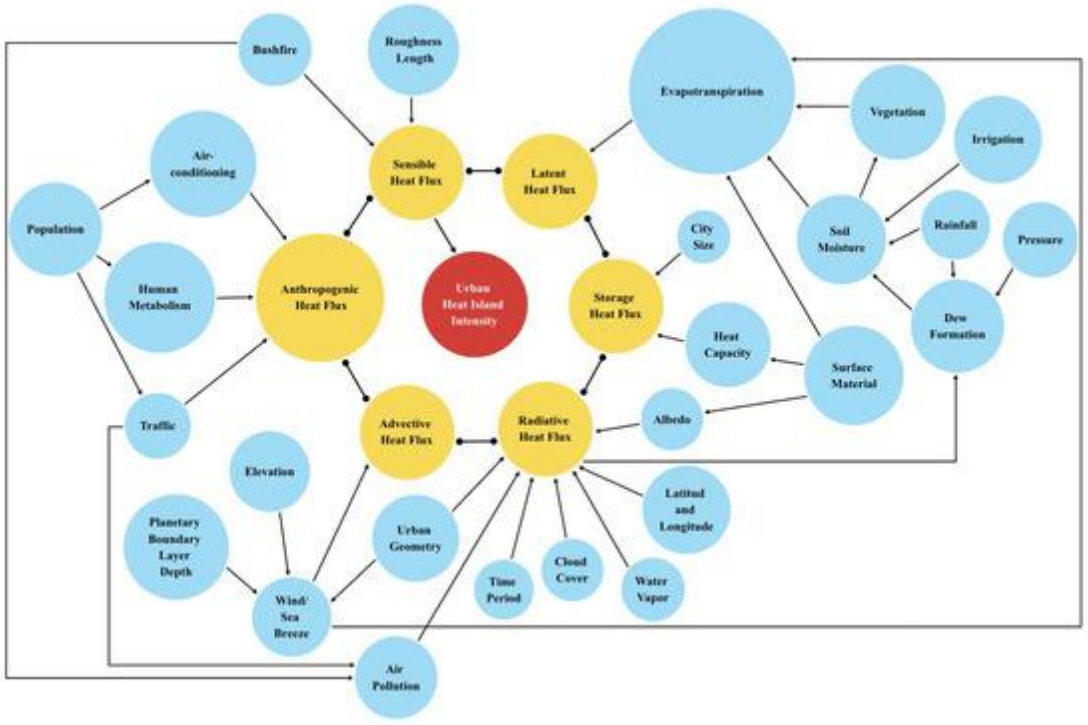

Figure 3: Heat fluxes present in the energy budget and their extended drivers (J. Kong et al., 2021).

These drivers can be further illustrated at the microenvironment level using a thermal balance model (Oke, 1988; Silva et al., 2009) **(*Eq 1*)**:

$$1)\ \frac{mc}{A}\frac{dT}{dt} = (1-\alpha)q_{sol} + q_{anthro} - q_{cond} - q_{evap} - q_{conv} - q_{rad}$$

At its core, a zero-order model is used to determine the time-dependent temperature variation in a system, expressed as $\frac{dT}{dt}$. The term $\frac{mc}{A}$ encapsulates the surface's thermal capacity and conductivity, denoted as the product of its surface density and specific heat capacity. Taking a unit area of transportation infrastructure, such as pavement, we note that it possesses an albedo 'α', which determines the proportion of incoming solar radiation q_{sol} that is absorbed. In addition to solar radiation, the pavement can also

receive heat from anthropogenic sources. The equation further accounts for outgoing heat: q_{cond} signifies heat conducting into the subgrade, q_{evap} denotes heat lost through evapotranspiration, q_{conv} represents convective heat loss to the surrounding air, and q_{rad} corresponds to radiant heat loss to the atmosphere. This thermal balance equation is one among many that have been formed and supported through empirical and numerical studies across various publications (Barber, 1957; Oke, 1988; D. Zhou et al., 2019).

Anthropogenic Contributions

Anthropogenic heat is a significant factor in UHI formation. Human activities contribute to atmospheric pollutants that affect radiative heat loss q_{rad} and modify urban evapotranspiration. Within the thermal balance equation, the term q_{anthro} is exclusively attributed to the heat released through fuel combustion, heat released through human metabolic processes, and the operation of equipment such as air conditioners. In Tomsk, Russia, anthropogenic sources accounted for 40-50% of the excess radiation flux contributing to summer UHI (Dudorova & Belan, 2022). Research in Phoenix revealed that waste heat from air conditioners had a negligible daytime impact but raised nighttime temperatures by more than 1.8°F in some localities (Salamanca et al., 2013). Additionally, heat output from a nearby natural gas facility, estimated to be between 70-230 MW, significantly affected the thermal profile of the locale. This phenomenon explains the pronounced winter UHIs observed in colder regions like Barrow, Alaska, where the magnitude of UHI correlated highly with the consumption of natural gas (Hinkel et al., 2003).

Vehicle traffic is a notable source of anthropogenic heat in urban environments. Studies have explored the impact of transitioning to electric vehicles on urban temperatures. In Singapore, a hypothetical scenario where combustion engine vehicles are entirely replaced by electric ones could result in a near-surface air temperature decrease of up to 1.08ºF. Though this dissertation intends to study topics of heat and EVs separately, we find here a small overlap in the two topics. Similarly, research in Japan indicates that the elimination of heat from vehicles could lead to a temperature reduction of 0.216°F (Mussetti et al., 2022; X. Zhou et al., 2022).). In Brazil, investigations have shown that in summer, anthropogenic heat accounts for about 9% of the total UHI heat flux, with vehicular heat contributing roughly half of this anthropogenic fraction to the UHI effect (Ferreira et al., 2011). Vehicles, stationary heat sources, and human metabolism is the primary breakdown of the anthropogenic contribution **(Eq 2):**

$$2)\ \boldsymbol{q_{anthro} = q_{anthro,vehicle} + q_{anthro,stationary} + q_{anthro,human}}$$

Incident Radiation and Albedo

The solar radiation incident on a surface, denoted as q_{sol}, refers to the sunlight that reaches the surface. The quantity of incoming shortwave radiation is determined by several mesoscale factors including geographical longitude and latitude, the time of day within the diurnal cycle, and the composition of the atmospheric layers, especially concerning water vapor and pollutants. An increase in atmospheric pollutants typically results in a reduction of incident shortwave radiation, a phenomenon that is also observed with denser cloud coverage. At the microscale level, the capacity of a surface to absorb this radiation depends on the material's properties and the type of radiation, with the

albedo of a material—its reflective characteristic—significantly influencing how much shortwave radiation is absorbed. This reflective property of surfaces in the built environment is a key factor in the formation of UHIs.

Initial research into the impact of painting buildings white to enhance cooling efficiency indicated a 19% reduction in electrical energy used for cooling in Sacramento (Taha et al., 1988). In Athens, Greece, increasing the albedo on a large local scale led to ambient air temperature reductions of 3.6°F (Synnefa et al., 2008a). Such measures to diminish heat intensity have advanced with the development of cool and green roofing technologies. The global surface area of roofs was previously estimated to be approximately 10^{11} m^2 (Akbari et al., 2009), signifying a significant mitigation opportunity through the use of reflective materials. Cool roofing, typically involving single-ply or liquid-applied materials, aims to minimize thermal retention and maximize reflection of solar radiation. Simulations have suggested that cool roofing can locally reduce UHI effects by lowering sensible heat transfer to the atmosphere. A hypothetical global shift to white roofs in 2012 was projected to decrease the population-weighted temperature by 0.04°F, but possibly increase the global temperature by 0.126°F (Jacobson & Ten Hoeve, 2012). Green roofing has been shown to similarly influence surrounding air temperatures. However, integrating ecological systems atop buildings introduces complexities in UHI modeling. The height of a building is considered in calculating the area's roughness, while the properties of the rooftop vegetation—such as thickness—play a role in its heat mitigation capacity. The intensity of irrigation for these green roofs is another factor affecting their UHI mitigation potential.

Beyond enhancing building reflectivity, transportation infrastructure has undergone significant advances to reduce UHI contribution. A 2010 study estimated the existence of approximately 2 billion parking spaces in the United States, serving around 250 million registered vehicles. When sidewalks and roadways are included, pavement accounts for 29% of urban areas (Chester et al., 2010; Rose et al., 2003). The emergence of "cool pavements" technology offers an alternative to the traditional impervious surfaces used in transportation, utilizing materials with higher albedo to reflect more sunlight, or incorporating water retention features to facilitate cooling via evaporation. Notable outcomes were observed in Athens, where an urban park's peak air and surface temperatures dropped by 3.42°F and 21.6°F, respectively, after replacing existing materials with cool pavement technologies (Santamouris et al., 2012). Alongside color, surface smoothness has also been recognized to enhance reflectivity and thereby mitigate UHI effects (Doulos et al., 2004). That same study found the maximum temperature differential of 43.56ºF between black granite and white marble surfaces.

Substantial research on the influence of albedo in the thermal balance of UHIs at various scales is informed by infrared imagery from satellites, which assesses near-surface temperatures. A survey of studies comparing surface colors as indicators of reflexivity—or directly measuring a surface’s albedo—consistently confirms that an increase in reflective properties correlates with reduced surface temperatures (Santamouris, 2013).

The albedo of a surface significantly influences the thermal balance equation while the emissivity determines the fraction of energy that contributes to a delayed release of heat after solar radiation has ceased. Through controlled experiments and simulations, research continues to refine our understanding of total incident radiation, which includes both direct solar rays and those reflected from surrounding surfaces. It has been established that reflecting radiation back to the boundary layers is an effective method for mitigating UHI effects. In the thermal balance model, the heat contributions come primarily from two sources: the incident radiation, adjusted for the surface's albedo, and the heat generated from anthropogenic activities.

Thermal Storage

A key element that contributes to heat accumulation in urban environments is the thermal storage capacity of construction materials, as encapsulated by the term $\frac{mc}{A}$, which details a material's conductivity and capacity by incorporating its density and specific heat. The delay in heat absorption and release within a microclimate is evident through these properties. For example, concrete can absorb solar radiation throughout the day and release it during the night. The integration of organic phase changing materials (PCMs) into surface treatments has shown to refine the storage and release patterns of heat, which is instrumental in mitigating UHI effects and is a core feature of advanced cool roof technologies (Chung & Park, 2016; Karlessi et al., 2011). As the ambient air temperature reaches the relatively low melting temperature of PCMs, they start to absorb and store heat, continuing until the temperature falls below their melting point, thus regulating the thermal profile of the surface.

Utilizing materials with high thermal conductivity is an effective alternative to incorporating PCMs for mitigating UHI effects. Materials that conduct heat effectively can utilize the sub-surface Earth as a heat sink, thereby enhancing the value of q_{cond} and restoring the internal temperature of the pavement to more stable levels. Consequently, this results in a lower surface temperature by dissipating heat more efficiently, which also lessens the heat available for convection q_{conv}. Empirical studies have demonstrated that pavements crafted from materials with higher thermal conductivity can achieve a significant reduction in peak surface temperatures (H. Wang et al., 2010).

The potential of harnessing absorbed heat for redistribution has garnered interest. Preliminary findings suggest that utilizing heat from asphalt pavement by incorporating internal piped cold-water systems can lower surface and ambient temperatures and extend the pavement's lifespan. Calculations indicate that a parking area of just over 2000 m² could potentially harvest 1518 kW of energy on a day that receives solar radiation of 5 kW/m² (Mallick et al., 2009). The extracted heat could then be utilized for various applications. This concept of employing "grey infrastructure" is often considered a more viable option than creating green or blue spaces (vegetation or water, respectively), particularly when considering the constraints of urban land use and the scale required for such spaces to effect change (Cao et al., 2010). As urban areas continue to innovate with alternative paving materials, roofing, and building structures, the balance between reducing heat during the day and potentially exacerbating the nocturnal UHI effect remains a critical area of study for informing planners and policymakers.

Evapotranspiration, Greenspace, Trees

The urban landscape often features extensive impervious surfaces that restrict water evaporation and limit green space transpiration, collectively known as evapotranspiration. This design typically results in greater water runoff and less natural cooling. A 2005 study in Phoenix, Arizona, demonstrated that an increase in green space by 1.3% could lead to a decrease in surface temperatures by 1.8-3.6°F, especially pronounced during daylight hours (Y. Zhang, Murray, et al., 2017). The cooling potential of these green spaces is measured in terms of Cooling Effect Intensity (CEI) — the degree of temperature decrease — and Cooling Effect Distance (CED) — the spatial extent of the cooling impact. Park shape and maintenance are found to be significant factors in determining CEI (Z. Yu et al., 2017). A consensus in urban green space research suggests that UHI effects can be mitigated, with temperature reductions of 1.8-3.6°F extending 350 meters beyond the perimeters of parks larger than 100,000 m^2 (Aram et al., 2019). Additionally, it has been quantified that increasing forested areas by 10% correlates with a 1.49°F drop in land surface temperature (LST) (F. Kong et al., 2014).

Evapotranspiration is influenced by several key factors in urban cooling: the prevailing climate, seasonal variations, types of vegetation, irrigation patterns, and soil moisture (Cheung et al., 2022). Soil moisture, in particular, plays a critical role in daily cooling patterns; for instance, a study noted an 32.4°F discrepancy between irrigated and non-irrigated park areas in Vancouver (Spronken-Smith & Oke, 1998). In California, the introduction of drought-resistant plants demonstrated that reduced irrigation altered soil moisture levels, decreasing latent heat flux and increasing sensible heat flux, leading to higher daytime temperatures but an average nighttime cooling of 5.76°F (Vahmani &

Ban-Weiss, 2016). The challenge of designing green spaces for UHI mitigation lies in their varied geometry and composition, as well as the need for tailored irrigation strategies, with the effectiveness of such measures varying significantly from one park to another and across different climate zones.

In urban areas where land use strategies favor the built environment, an effective compromise between built environments and green spaces is the implementation of porous, permeable, and pervious surfaces. Porous surfaces are designed with internal channels that enable water percolation, facilitating evapotranspiration when integrated with vegetation, such as grass, thereby enhancing cooling. Porous pavements allow the underlying moisture to rise to the surface, contributing to additional cooling effects. (Qin, 2015a). Research indicates that such surfaces can exhibit evaporation rates 16% higher than their impervious counterparts, offering a sustainable solution to urban heat challenges without sacrificing infrastructure needs (Starke et al., 2011).

Permeable pavers channel water around such surfaces as opposed to through them. Without the use of vegetation, these surfaces function through the transport of water to where evaporation is more likely. Mixed results have been found from their use as a heat mitigator; some have found that it amplifies daytime UHI and lowers nighttime signals (Asaeda & Ca, 2000) while others found limited potential throughout the diurnal cycle (Andersen et al., 1999).

Pervious surfaces, known for their high porosity, allow water to percolate through, facilitating evaporative cooling. Their thermal performance is nuanced; they trade off some thermal mass for the cooling effect of evapotranspiration (Asaeda & Ca, 2000). Laboratory-controlled studies reveal that these surfaces can achieve evaporation rates greater than 0.02 mm/hour, which decreases as the available water is depleted, offering potential cooling for a duration of 1-2 days post-precipitation (Nemirovsky et al., 2013; Starke et al., 2011; Syrrakou & Pinder, 2014). The integration of pervious surfaces into urban design remains a dynamic field of study, particularly as researchers seek to optimize the balance between their evaporative capacity and other material properties like thermal conductivity, reflectivity, longevity, and cost-effectiveness (Qin, 2015a).

Another component of cooling is the use of trees. Trees play a dual role in urban cooling through both evapotranspiration and shading. The shade provided by trees can significantly reduce temperatures, with studies showing a reduction of up to 34.2°F on shaded concrete surfaces, thereby decreasing the shortwave radiation, denoted by q_{sol} absorbed by these surfaces (Armson et al., 2012). In Melbourne, the presence of trees was shown to create up to 1.8°F difference in air temperature and up to 16.2°F in surface temperature. This effect varied depending on the tree's height and proximity to buildings, indicating the importance of tree placement in urban planning for temperature regulation (Berry et al., 2013).

Research focused on microenvironment tree cover has demonstrated that when relevant factors are controlled for, a solitary street tree typically offers more transpiration than a tree within a vegetated area due to the increased wind movement in urban settings which

boosts the transpiration process. The transpiration rate and consequent cooling effect of a tree are influenced by its species-specific traits. Trees with broader canopies, greater leaf area indices, and higher rates of stomatal conductivity are known to be more effective in cooling, with species differences in these traits being well-documented (Moss et al., 2019; Rahman et al., 2011, 2015). The "CityTree" model, which focuses on the growth processes of trees, estimates that four commonly found Central European tree species can offer a cooling potential ranging from 59 to 75 W/m^2 through transpiration (Rötzer et al., 2019).

Trees have been found to significantly reduce the need for irrigation—by up to 50%—and enhance cooling when integrated with urban green spaces (UGSs) (Shashua-Bar et al., 2009). Meta-analyses have highlighted the complexity of trees as a cooling mechanism, identifying tree canopy density, regional climate, and tree growth in size and surface coverage as the primary determinants of cooling potential (Rahman et al., 2020). Comparing predictive capabilities using both tree surface coverage and tree configuration as indicators of cooling strength showed opposite results across Baltimore and Sacramento, indicating the variability across regions due to the differences in vegetation, climate, and local infrastructure (W. Zhou et al., 2017). The optimal characteristics for a transpiring tree, conducive to cooling, include being in an oceanic climate, underlain by grass, having thin leaves, slight leaf hairiness, tall stature, and a diffuse porous wood structure. Continued research is necessary to better understand and leverage the role of trees in urban energy budgets, particularly for mitigating UHI effects and enhancing local climate conditions.

Convection, Turbulence, Blue Space

Wind and cloud cover are established as significant meteorological variables influencing urban heat island (UHI) intensity, as highlighted in Oke's seminal 1982 study (Oke, 1982). A twenty year analysis on Melbourne UHI conditions associates low wind speed and minimal cloud coverage with the strongest UHI signal (Morris et al., 2001). Similarly, research in Malaysia emphasized the role of wind in UHI mitigation, suggesting a stepped urban canyon design—where building heights decrease with the wind direction—as an effective strategy to reduce heat buildup in urban spaces (Rajagopalan et al., 2014). This concept has led to the exploration of designing wind corridors, often using computational fluid dynamics (CFD) to model airflow at the microenvironment scale. The integration of CFD into least cost path analysis for mapping wind corridors has pinpointed structures within the built environment that could exploit their geometry for localized cooling effects (Hsieh & Huang, 2016). Furthermore, CFD investigations of UHI phenomena in Bozhou City, China, have indicated that increased surface roughness in urban areas impedes ventilation to the core, further exacerbating UHI effects (L. Yang et al., 2016).

The geometry of the built environment plays a crucial role in urban heat island (UHI) phenomena, especially in terms of ventilation. Studies indicate that urban canyons, characterized by their aspect ratios—building height relative to street width—can trap heat and restrict airflow. (Rajagopalan et al., 2014). The largest differences in temperature from simulated aspect ratio comparisons was found during the nocturnal UHI, and daytime UHI's were positively correlated with smaller aspect ratios (Memon et al., 2010). This research also corroborated the inverse relationship between wind speed and air

temperature, with a notable temperature decrease of 2.34ºF when wind speed reduced from 4m/s to 0.5m/s. The interplay between urban geometry and air temperature emerges as a critical factor in understanding the distinct UHI signals when comparing surface and air temperatures. Urban canyons with higher aspect ratios often exhibit lower albedo due to their limited exposure to pavement, culminating in increased heat absorption. Introducing reflective cool pavements in such environments may have the unintended consequence of escalating air temperatures by reflecting solar radiation onto the facades of nearby buildings, thus amplifying their need for cooling (Coseo & Larsen, 2015; Yaghoobian & Kleissl, 2012). Qin (2015b) found that the advantages of reflective pavements are localized and most effective when the aspect ratio is less than or equal to one.

The lesser studied of the reinventing of natural space as a mitigation technique is the use of urban blue space (Völker et al., 2013). Three-dimensional mesoscale models of Chicago reveal that Lake Michigan reduces the city's heat plume by up to 50%, indicating the lake's role as a heat sink (Cosgrove & Berkelhammer, 2018). Weather Research and Forecasting (WRF) models from Wuhan, China, demonstrate the pronounced cooling effect on downtown microenvironments when water bodies are situated upwind of urban areas (Zhu et al., 2022). Unlike adjacent land surfaces, water bodies absorb most incoming radiation, fueling evaporation and subsequently transporting moisture inland, while also undergoing internal convection, conduction, radiation, and advection. Nonetheless, strong surface winds can diminish this cooling effect. Additional WRF studies reveal that the cooling impact is contingent on the blue space's location relative to wind patterns, and factors like the extent of water cover and

the size of the water body are key determinants of its cooling potential. They also noted that during autumn or evening periods when the water temperature is greater than the nearby air temperature, a warming effect can occur (Theeuwes et al., 2013). Although evaporative cooling is effective in temperature reduction, it can also elevate humidity, potentially decreasing thermal comfort. Further, UHI effects can have detrimental ecological impacts by warming watercourses like streams and stormwater runoff, which becomes thermal pollution when it enters ecosystems beyond the urban perimeter (Paul & Meyer, 2001). Meta-analysis quantifies cooling potential of 4.5ºF from blue spaces studied throughout primarily China and Japan (Völker et al., 2013).

Synergistic approaches involving green spaces, blue spaces, and wind flow have demonstrated enhanced cooling effects (Gunawardena et al., 2017). Research in Hong Kong has shown that the daytime cooling benefits of green spaces are doubled when these spaces are aligned with wind corridors and exhibit a high sky view factor (Z. Tan et al., 2016). Additionally, studies using CFD have indicated that positioning blue spaces downwind of urban areas can amplify cooling through enhanced evaporative processes (Tominaga et al., 2015).

Revisiting the thermal energy balance equation, we discern the potential for influencing both the heating and cooling of surfaces and their adjacent air temperatures. Through alternative materials, thoughtful planning of urban geometry, and leverage of existing and future green space and blue space, ongoing research in this field continues to quantify the effects of different components within the urban aesthetic that amplify the mesoscale and macroscale heat signals.

Review of Urban Heat Island + Built Environment Research

My dissertation seeks to advance the quantification of the effect pavement has on thermal energy within a microenvironment. The subsequent section will survey the methodologies utilized in prior research pertinent to this theme.

Data Collection and Sources

Satellite (Remote Sensing)

The utilization of satellites to measure surface temperatures has significantly increased since its inception in 1972, with a notable surge in related academic publications beginning in 2005 (Krishna, 1972; D. Zhou et al., 2019). The Landsat dataset, renowned for its high spatial resolution and data quality, began to influence surface urban heat island (SUHI) research by 1990, and by 2019, its applications in this field had been extensively reviewed (Carnahan & Larson, 1990; D. Zhou et al., 2019). Landsat satellites 5, 7, and 8 have the capability to image Earth's entire surface within a 16-day cycle. The Moderate Resolution Imaging Spectroradiometer (MODIS), offering diurnal satellite imagery at 1km resolution, was first documented for SUHI research in 2004 (X. Zhang et al., 2004). Carried by NASA's Terra and Aqua satellites, MODIS achieves global coverage in less than two days, and it has been widely adopted in SUHI studies for both surface temperature and emissivity data. The accuracy of these satellite measurements is confirmed through various validation techniques, with studies showing high precision in satellite-derived LST data, often reporting less than 5% error (Rigo et al., 2006).

Satellite remote sensing has become an indispensable tool for long-term studies tracking LST changes in relation to shifts in land cover. (Estoque & Murayama, 2017; Meng et al., 2018; S. Wang et al., 2018; L. Zhang, Meng, et al., 2017). However, it's critical to note that the orbital cycle of satellites like Landsat offers only periodic snapshots rather than a nearly continuous stream of data, which leads to a collection of discrete observations over time. For example, in Beijing, researchers harnessed Landsat to filter atmospheric disturbances and delineate land cover, complementing it with MODIS data for LST acquisition from 2003 to 2015 (Meng et al., 2018). Other retrospective SUHI studies using Landsat have uncovered a strong link between SUHI intensity and land cover, a relationship that holds even in complex mountainous regions (Estoque & Murayama, 2017). For comprehensive land cover assessment, Landsat's suite of instruments is often employed to generate indices or indirect measures of urban features, which are then integrated into UHI predictive models. To estimate LST from satellite observations, researchers transform spectral band information from Landsat into radiance and emissivity, applying atmospheric corrections to achieve precise LST figures (J. Peng et al., 2016). In addition to statistical modeling, satellite data have proven useful for high-resolution LST mapping, offering critical data for urban development planning and environmental surveillance (Anniballe et al., 2014; Tran et al., 2006).

In urban heat island research, combining datasets or making inferences from available satellite data is a standard practice. A study in Phoenix integrated Land Surface Temperature (LST) derived from Landsat's Thermal Infrared (TIR) data with high-resolution land cover data from the National Agricultural Imagery Program (NAIP) orthoimagery (X. Li et al., 2016). Their work suggested that the configuration of land had

a more significant effect on Surface Urban Heat Island (SUHI) intensity than the land composition itself, while also recognizing the disparity in data resolution as both a benefit and a constraint. Similarly, research utilizing MODIS instruments in Milan aimed to infer air temperature 2m above ground from the surface brightness temperature. These estimates, applied through statistical methods, achieved high levels of accuracy and precision, up to 5.4°F for 80% of the data. Nevertheless, the consensus remains that the current understanding of the relationship between air and surface temperature is predominantly empirical (Pichierri et al., 2012; Sun et al., 2005; Voogt & Oke, 2003; D. Zhou et al., 2019). This relationship exhibits significant variation over time and space, with Canopy Urban Heat Island (CUHI) intensity typically peaking in the evening due to thermal retention in the built environment, while SUHI tends to reach its maximum during midday due to direct solar radiation.

Satellite remote sensing encounters certain challenges, notably cloud contamination, which introduces noise into LST calculations. Researchers typically counteract this by employing cloud-screening algorithms to eliminate the affected data, although this can result in significant data gaps. Li et al. (2018) have demonstrated the use of ensemble methods to address this issue of data scarcity. The infrequent overpass of satellites like Landsat, coupled with the knowledge that clouds obscure roughly 35% of land scenes globally at any moment, means that data omission can be large and systemic, potentially diminishing the value of what could be a robust dataset (Ju & Roy, 2008). The prevalence of additional data gaps caused by random errors and sensor malfunctions has led to a diversification in the methodologies for managing such missing data. Recent reviews categorize these into four main strategies: spatial, spectral, temporal, and hybrid methods

(Shen et al., 2015). However, these necessary interventions are not without drawbacks; they are resource-intensive and tend to inflate SUHI intensity measurements. This overestimation arises from the common practice of replacing missing data with clear-sky values, which may not consistently represent actual conditions.

The dichotomy between spatial and temporal resolution presents a significant challenge in leveraging satellite data from sources like Landsat and MODIS. Landsat's less frequent data collection, potentially exacerbated by data gaps, is offset by its higher spatial resolution in contrast to MODIS. Consequently, for research into phenomena such as the interplay between Surface Urban Heat Islands (SUHI) and air pollution, which require tracking trends over time, the priority often lies with high temporal resolution. In contrast, high spatial resolution is vital for local-scale studies where a detailed examination of urban landscape elements is necessary (D. Zhou et al., 2019). To address these limitations inherent to both Landsat and MODIS, researchers employ methods such as spatial downscaling to increase spatial detail or temporal upscaling to improve frequency. However, these methods often involve a trade-off, potentially sacrificing data precision for greater resolution or vice versa (Stathopoulou & Cartalis, 2009).

Stationary Sensors

The acquisition of Land Surface Temperature (LST) and air temperature data has traditionally relied on fixed-location sensors and weather stations, a practice that dates back to at least the mid-20th century (Barber, 1957). While a single sensor is limited spatially by its immediate surroundings and local atmospheric effects, it has potential for higher temporal resolution than other sensor designs (Oke, 2004). Additionally, it can observe diurnal UHI behavior and dynamics that are unavailable through satellite data. A single sensor can be used to conduct micro-scale exploration or lab-controlled experiments, and a network of sensors can provide local and mesoscale data. A common approach involves comparing data from an urban sensor with that from a nearby rural sensor to calculate UHI intensity. The accuracy of this method depends heavily on the careful selection of sensor locations to ensure they are representative of their respective environments, mindful of the urban-rural gradient's inherent subjectivity (Stewart & Oke, 2012). Employing weighted averages from multiple sensors categorized by urban or rural settings can provide more comprehensive data, though this can escalate logistical and financial requirements compared to simpler mobile surveys or the use of freely available satellite data. However, to bolster the utility of stationary sensors, researchers can integrate data from widely accessible airport weather stations, which benefit from standardization in both instrumentation and data collection practices (Santamouris et al., 2007; X. Yang et al., 2020).

A systematic review of UHI literature assessed 190 studies that deployed stationary or mobile sensors (88:102, respectively) and evaluated their methodology based on a developed criteria includes a range of supported practices (Stewart, 2011). Studies were

expected to measure air temperature at the approximate shelter height of 1-2m from surface and were broadly defined as either urban or rural stations. They must detail the locations and number of field sites used in quantifying UHI effect, and the data being collected at sites. Further, the measurement precision must be described. The study's metadata must include local or regional scale illustration of the study area, including plan maps, site sketches, and/or aerial photography. In addition, metadata must also include UHI-pertinent metrics of the study area such as sky view factor, roughness, proportions of urban fabric types, etc. In identification of sensors' vision, microenvironment setting of sensors must be representative of the larger horizontal scales. In deciding the number of sensors collecting measurements and the frequency of measurements, a study's sample size is aligned with its objectives. To reduce meteorological noise, the study controls for extraneous weather conditions and measures UHI under the ideal weather conditions. Further, the study accounts for (or avoids) unwanted surface effects such as elevation changes or water bodies. Lastly, temperature is measured synchronously as to avoid the confounding effect of time-induced heat islands. Upon review of this extensive rubric, it was determined that studies utilizing stationary sensors received an average composite score of 8.8 out of a possible 18, which is slightly below the general average score that includes research employing mobile sensors by 0.5 points. The primary shortcomings were identified in the reporting of instrument specifications and the provision of metadata details. The review concluded with the assertion that a limited number of well-controlled, stationary observation sites, which are automated and synchronized to optimize the representativeness at both local and mesoscale levels, may be more advantageous than the use of mobile sensor deployments.

The adoption of crowdsourced amateur weather stations has become an emerging trend in the deployment of stationary sensors (Chapman et al., 2017). This methodology leverages higher spatial coverage due to lower cost and standards of the deployment, at the cost of validity due to the lowered standards of deployment and collection. As instrumentation continues to increase in accessibility, validity, and practicality, a citizen science approach may continue to acquire more share of the literature (Kousis et al., 2021; Shandas et al., 2019).

An example of researchers leveraging the temporal resolution possible through stationary sensors was shown through the collection of 30 years of meteorological records from 11 weather stations within the mesoscale of Shanghai. The study involved regression analyses of daily high temperatures based on urban-rural classifications and UHI effects. In addition, they used mortality data to observe trends in public health compared to temperature fluctuations (J. Tan et al., 2010). In New York City, a network of stationary sensors facilitated a mesoscale analysis that identified diurnal and nocturnal UHI effects and correlated them with various weather conditions and urban form factors (Gedzelman et al., 2003). Such extensive data collections over many years enable research into the connections between UHI phenomena and broader issues such as land use transformations and climate change (Emmanuel & Krüger, 2012; Gedzelman et al., 2003).

Mobile Sensors

Rodriguez et al note the common limitations of mobile sampling (2020):

- Spatial coverage is limited to length of transect, and representation of local and mesoscale is limited to the characteristics of the transect.
- Accuracy of positional equipment and logging speed can provide several sources of noise to models.
- Only one measurement can be recorded at the frequency rate of the equipment as opposed to a network of stationary sensors or remote sensing.
- Subjectivity of transect design can lead to different exposure of heat and environmental factors.

However, they also note the benefits of such techniques. The spatiotemporal resolution is determined by the frequency rate of the equipment and the speed that the route is being traversed. This allows for micro-scale research not available through methods of lower resolution. Mobile surveys can also serve as preliminary assessments to determine optimal locations for permanent sensor networks and may offer logistical and financial advantages over fixed sensors in certain scenarios.

Stewart's systematic review of ground measurement studies identifies 102 publications with mobile data collection having a mean quality score of 9.6 out of 18, only 0.3 above the overall average score when including studies that used stationary sensors (Stewart, 2011). Both mobile and stationary sensor studies often fell short in providing detailed instrument specifications and metadata. Additionally, mobile data collection studies frequently lacked components necessary for replicability, as they required more extensive

transects and repetition under varied conditions to bolster the robustness of the data, crucial for addressing study objectives and accounting for variability in micro-scale conditions.

Walking is a prevalent method for conducting predefined transects, as demonstrated by Vancouver researchers who completed 8-10km routes within 3 hours, creating mobile datasets that complemented stationary sensor and Landsat data (Tsin et al., 2016). The transects were designed to explore possible links between UHI and factors like population density and household income. The equipment used consisted of a shielded sensor housed within a backpack rig. Such methodologies also lend themselves to citizen science initiatives, which can enhance spatiotemporal coverage with multiple participants collecting simultaneously (Pigliautile & Pisello, 2018; Romero Rodríguez et al., 2023). These datasets enable the creation of heat maps and the modeling of temperature or UHI effects in relation to various urban features.

Automobiles offer an alternative mode for mobile data collection, improving spatial coverage quickly and accommodating heavier instruments (Makido et al., 2016; Oke, 1973; Saaroni et al., 2000). This combats the noise introduced to models by the changing mesoscale weather conditions during the span of collection by enhancing the spatial coverage within the same allotted time one would have spent on foot. Dublin researchers constructed vehicle rigs to include thermo-hydro sensors, anemometer, wind-vanes, and rain-gauges to gather a more detailed description of micro-scale weather conditions (Alexander & Mills, 2014). However, air temperatures measured on roadways may not accurately reflect the microenvironments of interest, especially in studies focused on

pedestrian health risks or heat exposure with the potential for heat decay between roadways and sidewalks. Additionally, cars can influence measurements due to engine heat and exhaust emissions.

Bicycles represent a compromise in mobile survey methods, offering greater spatial coverage than walking and a hybrid environmental exposure with access to vehicle and pedestrian infrastructure. In Rotterdam, surveyors utilized cargo bikes equipped with a rig carrying a thermometer, humidity sensor, sonic anemometer, and twelve separate radiation sensors to capture data across diverse land covers (Heusinkveld et al., 2010).

Beyond statistical analyses, mobile data enables heat mapping, as executed in Rotterdam to depict microenvironmental temperature changes (Heusinkveld et al., 2014)(**Figure 4**). Additionally, regression models trained on such data can predict temperatures in unmeasured locales (Ketterer & Matzarakis, 2015).

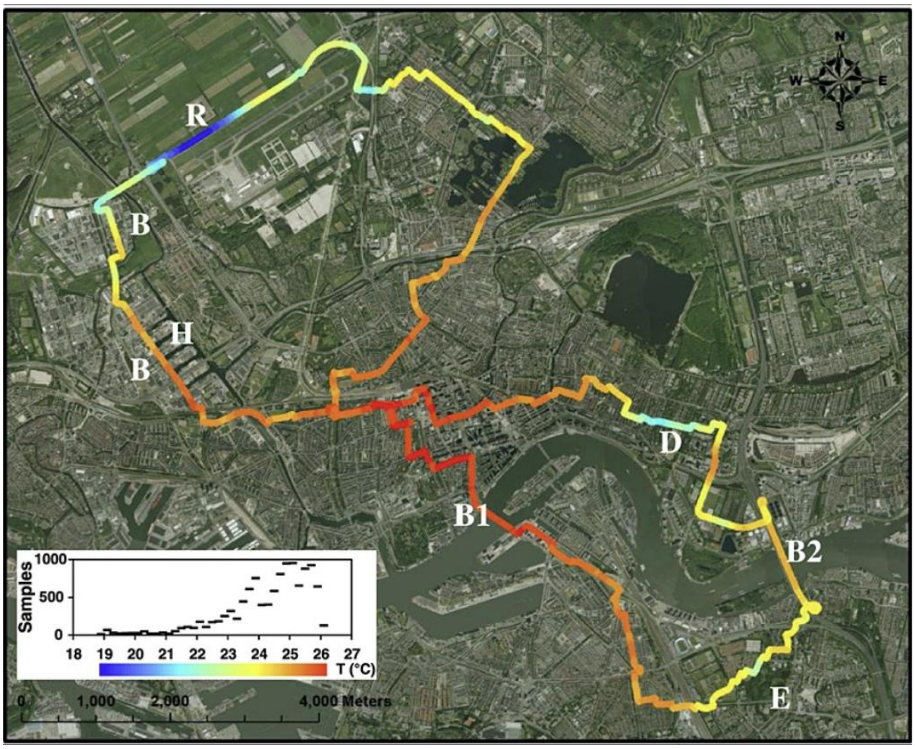

Figure 4: Heat map generated along evening transect by researchers in Rotterdam (Heusinkveld et al., 2014).

The integration of various data collection methods, each with unique strengths, facilitates a comprehensive approach to urban climate research (Shandas et al., 2023; D. Zhou et al., 2019). Research conducted in central Germany gathered aerial imagery from evening flights acquiring LST measurements, while in parallel there were mobile surveyors on the ground measuring near surface air temperature (Schwarz et al., 2012). They combined weather station LST and air temperature measurements from 15 locations for a dataset of all three collection methods. Similarly, in Dublin, a network of weather stations complemented vehicle-based measurements, providing detailed heat maps and identifying local trends (Alexander & Mills, 2014). Use of satellite imagery and weather stations in ensemble have proven to enhance heat mapping capabilities and UHI prediction (Fabrizi et al., 2010).

Statistical Modeling Approaches

Statistical models based in linear regression have been extensively used to understand heat dynamics in association to urban features (H. Li et al., 2018). The metric selected for heat as a dependent variable in these models can vary based on the research objective and available data. Some have used an explicit UHI intensity variable based on an urban-rural calculation or weighted urban-rural difference from a network of simultaneous observations (Heaviside et al., 2016). This can be a problematic approach due to the subjectivity and ranging classifications along the urban-rural continuum, as attempted to remedy by systems such as the Local Climate Zone (LCZ) classification (Stewart & Oke, 2012; D. Zhou et al., 2019). For these reasons, others elect to use LST or canopy air temperature as the dependent variable, especially if data was recorded simultaneously across the spatial coverage. Common environmental predictors in such models include exposure to vegetation, impervious surface area, building density, sky view factor, floor area ratio, distance to urban area, latitude, elevation, and more (Ivajnšič et al., 2014; C. Yin et al., 2018).

Researchers in Slovenia used a semiparametric geographically weighted model with global predictors that influenced temperature with the same effect size throughout the spatial coverage and local predictors based on location and bandwidth value (Ivajnšič et al., 2014). This model demonstrated better model fit, revealed the distortions of an ordinary linear regression (OLS) model, and accounted for spatial autocorrelation. This sort of multilevel modeling continues to make its way into topics of geography and climatology (S. Li et al., 2010). LST data from southern China was modeled in several ways for comparison, of which included OLS, Variance Component Modeling (VCM),

and Random Coefficient Modeling (RCM) (Du et al., 2016). They found that both the VCM and RCM were able to explain more of the variability due to the hierarchal structure of data. Models such as these can address when the effect size of predictors may vary regionally within a spatial dataset and have been shown to reduce spatial autocorrelation within residuals.

The spatiotemporal nature of UHI research can introduce distortion into typical OLS models. The 1st Law of Geography claiming "everything is related to everything else, but nearer things are more related than distant things" supports the potential for spatial autocorrelation within datasets (Tobler, 1970).Using data with spatial autocorrelation among temperature observations would create spatial clustering of residual values, therefore violating assumptions of independent and identically distributed residuals expected in OLS regression models. To address the spatial dependencies that violate OLS assumptions of residual independence, spatial regression models like the Spatial Error Model (SEM) and the Spatial Lag Model (SLM) are utilized across disciplines. SEM adjusts the error terms for spatial autocorrelation, while SLM incorporates a lag variable to mitigate the impact of spatial autocorrelation on the model's predictions (L. Zhang et al., 2009).

The spatial error model is commonly used in econometric topics (Anselin, 1988). It resembles a common OLS regression in form:

3) $\boldsymbol{Y = \alpha + \beta X + \lambda W \varepsilon + u}$

4) $\boldsymbol{Y = \alpha + \beta X + \varepsilon}$

Independent variable "X" serves as input multiplied by the linear rate of change determined by the term's regression coefficient "$\boldsymbol{\beta}$", all set by an initial output value $\boldsymbol{\alpha}$. This provides a linear fit line through the points defined by a dataset of values for "**X**" and the dependent variable "**Y**". Unless the model explains 100% of the variability (R^2=1.00), there will be vertical distance between each point and the model's fit line. These distances are stored in our error term "$\boldsymbol{\varepsilon}$".

The SEM modifies the error term to account for spatial autocorrelation, beginning with a parameter "**λ**" that quantifies autocorrelation in the errors "**ε**" from an OLS model, with values closer to 1 indicating higher autocorrelation. This parameter is combined with a spatial weights matrix "**W**", which assigns relationships between data points, based on methods such as inverse distance weighting or Gaussian Kernel weighting among other options. The resulting matrix adjusts the OLS residuals, aiming for them to satisfy the assumptions of independence and identical distribution, represented by "$\boldsymbol{u}$". Extended AIC and R^2 metrics have been developed to account for the spatial structure and provide valid model fit information, but the log-likelihood value is commonly included in addition to these metrics as it doesn't penalize for model complexity (Smith, 2014).

Methods

The following section details our study area, the data collection procedures, data processing, and modeling techniques used to quantify a relationship between temperature and exposure to pavement within microenvironments.

Study Area

Vermont's diverse topography, including green plains, river valleys, foothills, and mountains, experiences an average of 14 days annually with maximum temperatures reaching 86°F and a historical average summer temperature of 63.7°F. Its humid continental climate is influenced by Lake Champlain and proximity to the Atlantic Ocean. Our selection of mesoscales aimed to encompass the broadest possible spectrum of climatic conditions, elevation, urban patterns, and heat contributions, resulting in the choice of ten representative small cities and towns (**Table 1, Figure 5**).

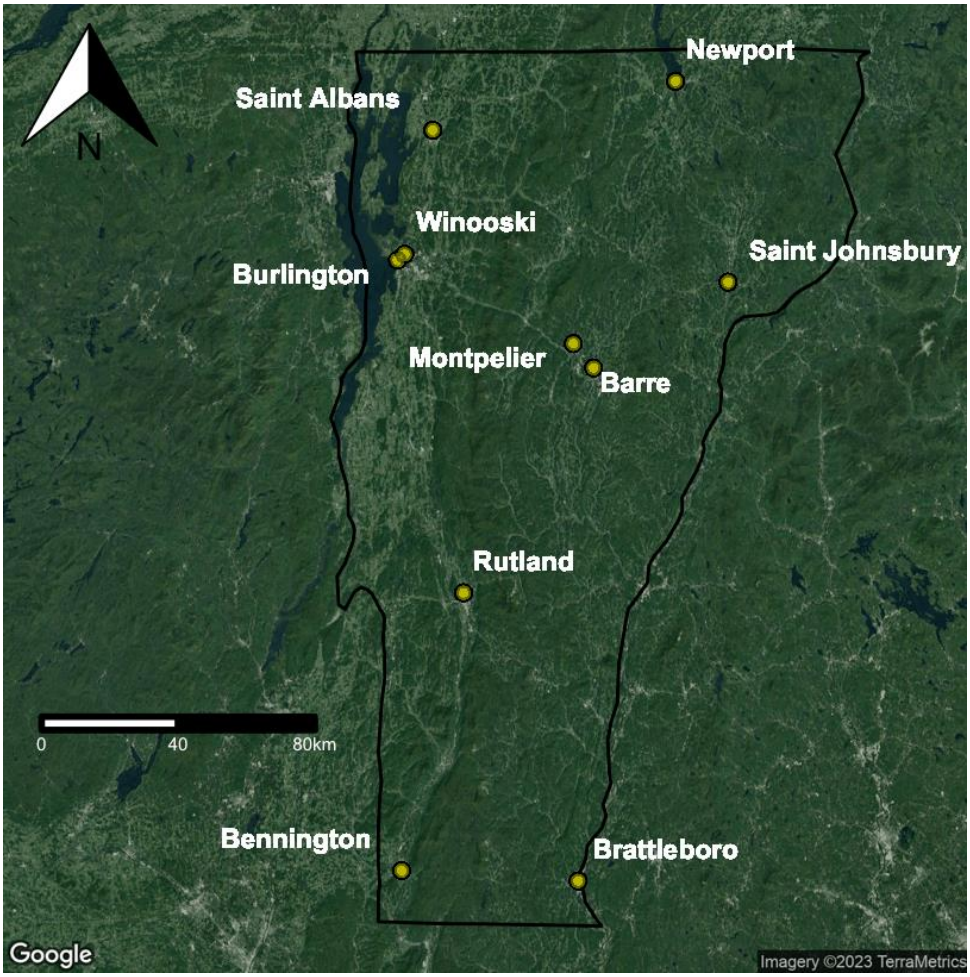

Figure 5: Study area. Ten cities within Vermont were used for a mobile sampling campaign during the summer of 2022.

Table 1: Details of mobile sampling conditions. Description of cities and towns visited, and weather conditions on days sampled.

City or Town	Date Sampled	Day Length[b]	Percent Land Cover as Pavement[c]	Number of Days 85F or Higher in 2022[a]	Elevation (Meters Above Sea Level)[b]
Barre	6/15/2022	15h, 31m	19.28	21	196
Bennington	6/29/2022	15h, 17m	5.25	37	212
Brattleboro	6/30/2022	15h, 17m			
	6/20/2022	15h, 25m	5.33	31	66*
Burlington	6/21/2022				
	6/28/2022	15h, 24m			
	7/4/2022	15h, 26m	13.26	29	68
Montpelier	7/19/2022	15h, 6m			
	8/1/2022	14h, 38m			
	7/20/2022	15h, 2m	7.54	21	163
Newport	7/22/2022	14h, 58m			
	7/10/2022	15h, 23m	7.92	7	212
Rutland	7/11/2022	15h, 22m			
	6/14/2022	15h, 25m	19.50	21	184
Saint Albans	8/3/2022	14h, 28m			
	6/25/2022	15h, 35m	2.37	17	135
Saint Johnsbury	7/7/2022	15h, 26m			
	7/26/2022	14h, 52m	4.38	21	184
Winooski	7/27/2022	14h, 49m			
	7/13/2022	15h, 16m	22.04	27	70

[a]Daily high temperature, maximum wind speed, and number of days reaching 85F or higher all obtained from Vermont ASOS network weather station data (Iowa State University, 2023). Maximum wind speed was the maximum reported during interval of mobile sampling from that day, while high temperature was maximum temperature reported from the entire day.
[b]Day length and elevation from data provided by suncalc.org. Elevation based on value at town's city hall location.
[c]Pavement land cover calculated using city data layer and Land Cover data from UVM Spatial Analysis Lab (2016)

*Brattleboro elevation ranges from 61-539m.

The design of our transects was guided by considerations of length, traffic safety, and the representation of diverse land uses, ensuring a balance between comprehensive coverage and minimizing time-related regional temperature variances. Transects varied from 11 to 32 kilometers and were strategically routed to include city centers, residential areas,

commercial zones, and the adjacent rural landscapes in order to maximize collection of the variability of the built environment and its influence on local heat dynamics.

Data Collection

Data collection targeted days when the forecast temperature was predicted to reach 85°F, with a likelihood of precipitation below 10 percent during sampling hours, wind speed below 10 mph, and minimal cloud coverage, all of which have been identified as optimal conditions for a UHI. Field researchers aimed for morning, mid-day, and evening samplings at approximately 07:00 AM, 2:00 PM, and 8:00 PM, respectively. Multiple visits to the same cities allowed for a broader understanding of varying conditions and heat exposure.

The e-bike was our chosen mode for mobile sampling, offering better access within urban spaces and more representative data of microenvironment-level heat exposure compared to vehicle-based methods. Sampling was conducted at speeds of 10 to 15 mph, ensuring temperature sampling every seven meters based on our 1 Hz sampling rate.

A custom-built sensor tower, attached to the e-bike's rear rack, housed all instruments. A type-T thermocouple was installed at the standard 2m height from the ground for air temperature readings and shielded within a PVC structure to enable passive airflow around the sensor, as illustrated in Callout 1 of **Figure 6**. Temperature data was logged with an Omega OM-74 logger fixed to the tower's base. Alongside, a QStarz Travel Recorder XT GPS unit logged positional data at the same frequency. Both temperature and GPS units were synchronized before starting each transect to ensure accurate time-stamped data.

Figure 6: Photograph of the E-Bike mobile sensor design: (1) Solar radiation shield and location of the thermocouple and humidity sensor. (2) Humidity sensor unit. (3) Frame bag storing Omega 2400 temperature logger, QStarz Travel Recorder XT GPS logging unit, and repair equipment. (4) Taillight. (5) Head light. (6) Phone mount for GPS route navigation.

Data Cleaning and Processing

The datasets from the temperature and GPS loggers were synchronized using their timestamp records to create a comprehensive dataset. Data from each transect underwent a cleaning process, which involved removing any measurements taken before and after the transect period, as well as discarding data points where the GPS indicated speeds slower than 0.5 mph to avoid overemphasizing areas where the researchers had to pause for safety. Despite the expectation of significant temperature variability during the morning's warm-up and the evening's cool-down, our analysis revealed notable temperature ranges during mid-day as well **(Figure 7)**.

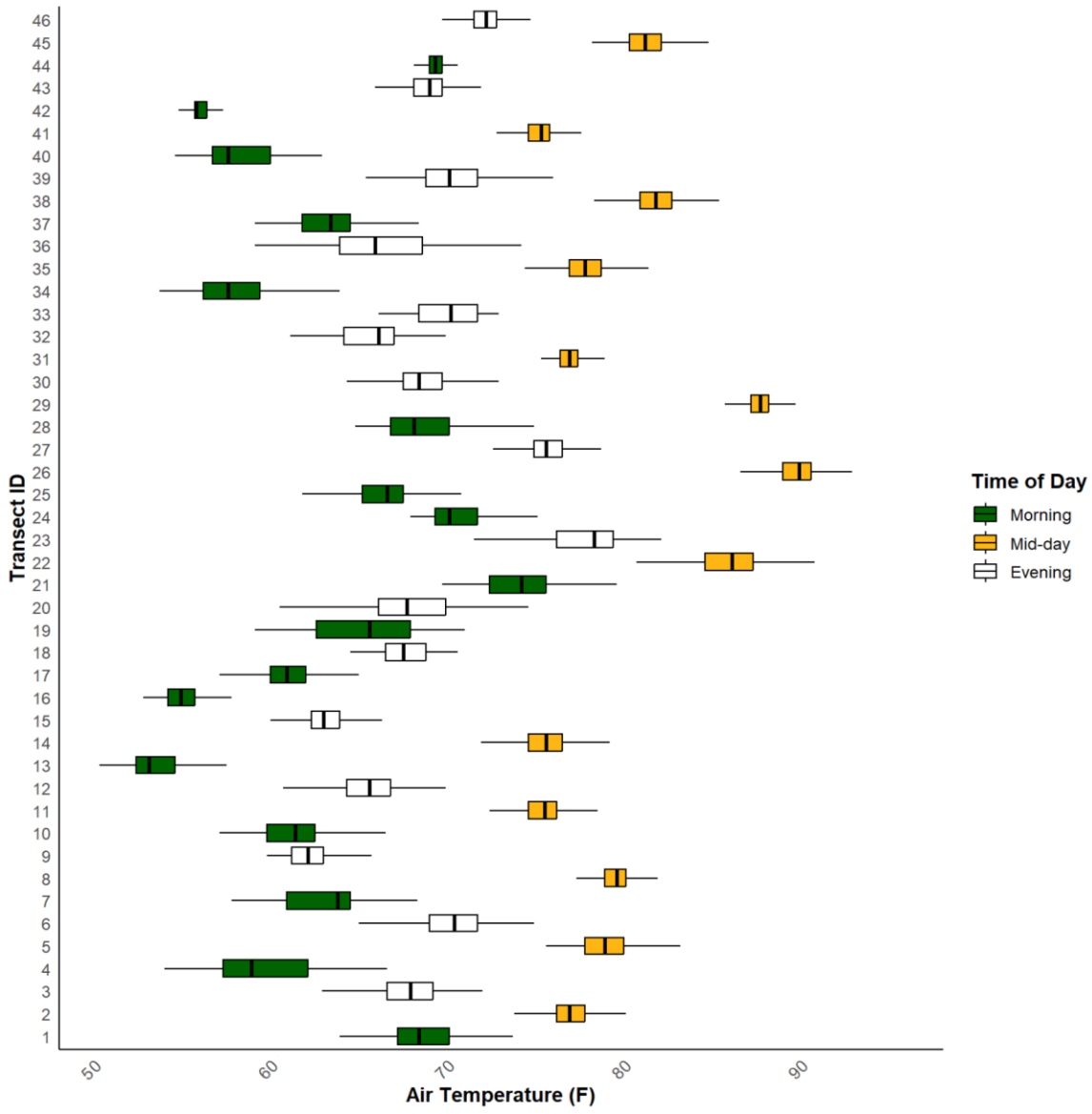

Figure 7: Distribution of air temperature measurements by transect.

Once the coordinates of each data point were mapped, three buffer zones with radii of 25m, 50m, and 100m were generated around each point using GIS to examine the impact of nearby environmental features at the microscale. These buffers were then intersected with high-resolution (0.5 meter) land cover data sourced from a combination of LiDAR

from 2013-2017 and 2016 orthoimagery (Vermont Open Geodata Portal, 2019) (**Figure 8C**). This detailed land cover classification included bare soil, railroad, buildings, roads, and other paved surfaces. For analytical purposes, “roads” and “other pavement” were aggregated into a single “pavement” class, while “buildings” were retained as a separate covariate.

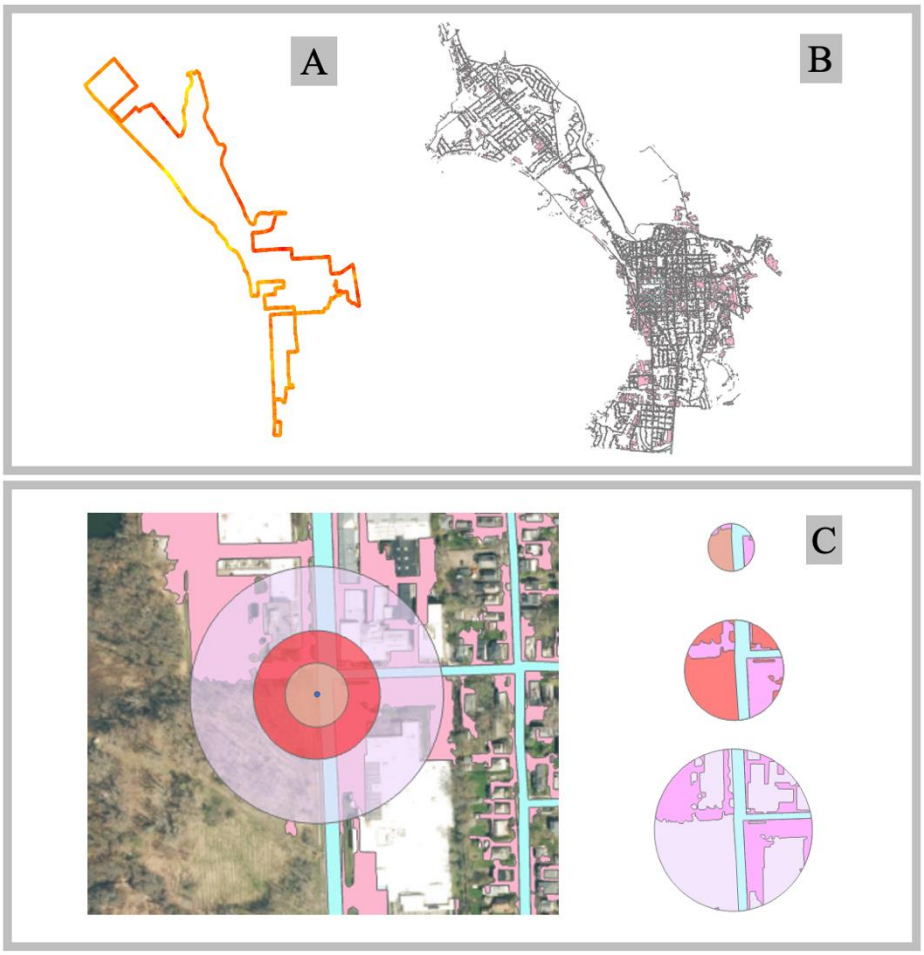

Figure 8: DATA PROCESSING. Each observation received a value for the percent pavement within 25m, 50m, and 100m of its location. (A) Data was first plotted, cleaned, and buffered at three different radii, (B) Land cover data for each town (C) was then intersected with each buffered observation. Percent pavement was then calculated based on the area of the intersected polygons and the area of their respective buffer.

The intersection of buffer zones and land cover data was then analyzed within R Studio, where the percentage of impervious surface area (ISA) coverage for each buffer size was calculated at every data point. The same intersection and calculation procedures were performed with tree cover data (0.5m resolution) from the same data source. This process was applied to each transect, culminating in a comprehensive dataset that combined all summer 2022 mobile sampling data, organized by transect ID and including percentages of each of the three land cover exposures within the three buffer sizes **(Appendix A).**

The elevation data accessed for this study were obtained using the USGS Elevation Point Query Service, leveraging the high-quality, high-resolution datasets from the 3D Elevation Program (3DEP). The 3DEP provides light detection and ranging (LiDAR) data with a 1-meter resolution for the conterminous United States, Hawaii, and territories, offering vertical accuracy within 10 centimeters. These data represent a reliable and detailed representation of the Earth's surface in Digital Elevation Model (DEM) format (USGS, 2023). Upon merging, each temperature observation had a corresponding elevation value in meters (**Appendix B).**

GPS coordinates were verified for precision, with an initial manual check eliminating points that deviated dramatically from the planned transect route. Additional analysis calculated the nearest distance of points to the route, flagging those beyond 20 meters for further manual review. Considering most roadway and pedestrian infrastructures lie within 20 meters of centerlines, flagged points appeared to be due to dense tree or building coverage, resulting in a final dismissal of 0.1% of the data and leaving 207,250 observations for analysis.

An exploratory comparison of air temperature (the dependent variable) against the nine permutations of buffer radii and diurnal sampling phases for percent pavement displayed a notable positive correlation, particularly with the 100-meter buffered variables during evening samplings (**Figure 9**). Additional plots for building and tree cover are provided in the supplementary materials (**Appendix C-Appendix** D).

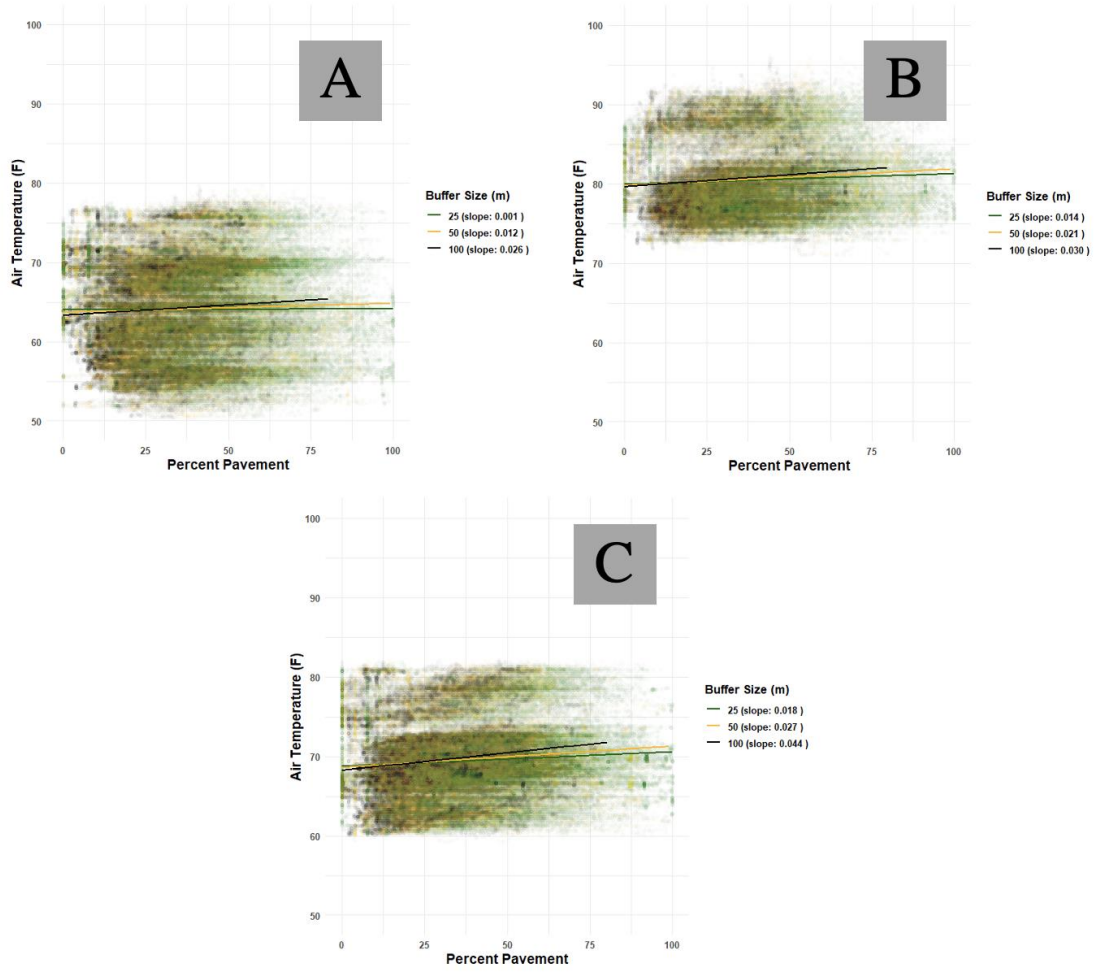

Figure 9: Scatter plot of Percent Pavement area within 25m, 50m, and 100m buffers versus air temperature for A) morning, B) mid-day, and C) evening. Fit lines denote their regression coefficients in the legends to indicate magnitude and direction of association.

Data from the Vermont and New Hampshire Automated Surface Observing Systems (ASOS) was sourced for key weather parameters such as air temperature, wind speed, and cloud cover at airport weather stations (Iowa State University, 2023). Daily high temperatures, max wind speed during sampling intervals, and max cloud cover during sampling intervals were collected and matched to each observation. Cloud coverage was categorized on a scale from 0 (clear sky) to 4 (overcast) based on airport station reports during the sampling period **(Appendix E).**

Each observation was also assigned a "time since sunrise" value in minutes, based on official sunrise times for the sampling date and location, to account for the diurnal temperature variation due to solar heating (**Figure 10**). This resulted in a comprehensive dataset of over 200,000 air temperature observations, enriched with daily weather conditions, diurnal phase as a categorical ID (morning, mid-day, evening), elevation data, and exposure metrics for both the built environment and tree cover during conditions conducive to UHI effects.

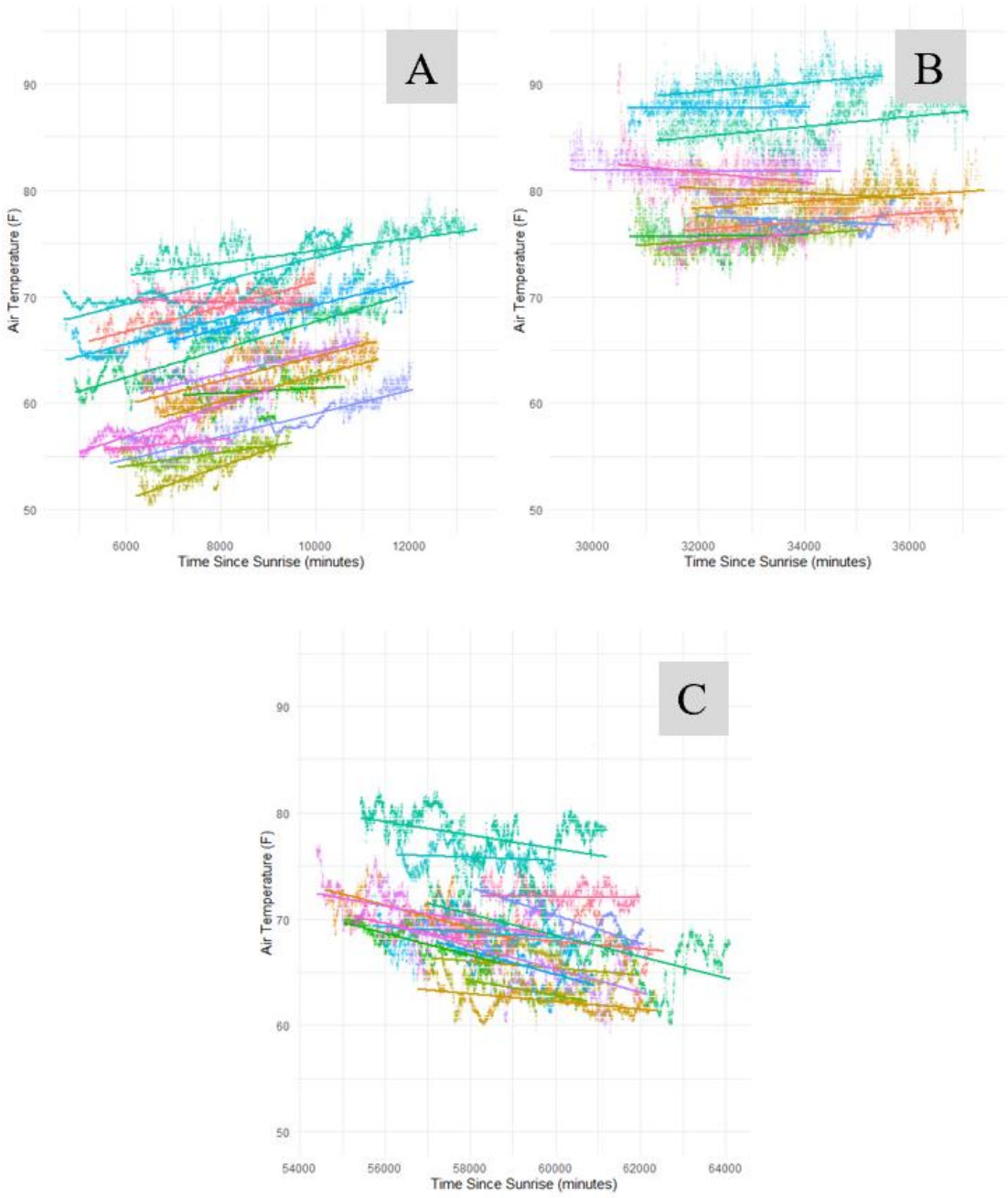

Figure 10: Spaghetti plots of time after sunrise (minutes) versus measured air temperature (F) for A) Morning, B) Mid-day, and C) Evening transects. Different colors represent separate transects.

Spatial Analysis

Statistical testing of the research question was conducted through hypothesis testing of the following null (***Eq 5)***:

$$\textbf{5) } \boldsymbol{H_o}: \boldsymbol{\beta_{Pavement,j,t}} \leq \mathbf{0}$$

The $\beta_{Pavement}$ coefficient pertains to a linear model of the recorded air temperature as a function of percent pavement within buffer size (j) for the categorical diurnal phase within the diurnal cycle (t). A negative value suggests an increase in the percent pavement within the specified radius is associated with a decrease in temperature: a cooling effect. Rejecting the null in this case confirms that an increase in pavement exposure is associated with a warming effect.

The testing of this hypothesis was conducted using a bootstrapping approach in conjunction with a spatial error model (SEM). This involved assessing the mean value of the $\beta_{Pavement}$ coefficient. A series of preliminary modeling was first necessary before being able to complete this bootstrapping process, all of which is outlined in this subsection.

Exploratory linear models were first generated in the process of building a model with the ideal terms to maximize model-fit through adjusted R^2 values. Forward stepwise model building took the initial form of simple linear regression **(*Eq 6)*:**

$$\textbf{6) } T_{i,j,t} = \alpha_{j,t} + \boldsymbol{\beta}_{\text{Pavement, j,t}} P_{i,j,t} + \varepsilon_{i,j,t}$$

The foundational model is depicted by the regression lines in **Figure 9**. In this model, the percentage of pavement exposure, denoted as 'P', serves as the independent variable, 'α'

represents the y-intercept, and the air temperature 'T' is the dependent variable, with each observation indexed by 'i'. To refine the model, additional covariates were sequentially introduced based on their correlation with air temperature. Each addition was scrutinized for its impact on model fit, potential collinearity assessed via the variance inflation factor (VIF) and the conditional index, and the direction and magnitude of the coefficient estimates. Upon reaching an optimal form, potential interaction variables were added in the same stepwise manner.

The final model took the form of:

$$7)\ T_{i,j,t} = \alpha_{,t} + \beta_{\text{Pavement, j,t}} P_{i,j,t} + \beta_{\text{Building, j,t}} B_{i,j,t} + \beta_{\text{TreeCover, j,t}} A_{i,j,t} + \beta_{\text{WaterCover, j,t}} G_{i,j,t} + \beta_{\text{Elevation,j,t}} E_{i,j,t} + \beta_{\text{Sunrise,j,t}} S_{i,j,t} + \beta_{\text{HighTemp,j,t}} H_{i,j,t} + \beta_{\text{CloudCover,j,t}} CC_{i,j,t} + \beta_{\text{MaxWind, j,t}} WS_{i,j,t} + \beta_{\text{Pavement, j,t}} P_{i,j,t} * \beta_{\text{Building, j,t}} B_{i,j,t} + \beta_{\text{Pavement, j,t}} P_{i,j,t} * \beta_{\text{CloudCover,j,t}} CC_{i,j,t} + \beta_{\text{Pavement, j,t}} P_{i,j,t} * \beta_{\text{MaxWind, j,t}} WS_{i,j,t} + \beta_{\text{Building, j,t}} B_{i,j,t} * \beta_{\text{CloudCover,j,t}} CC_{i,j,t} + \varepsilon_{i,j,t}$$

The model includes linear terms and interaction terms including percent pavement exposure, percent building cover exposure, percent tree cover exposure, elevation, time since sunrise, daily high temperature, cloud coverage during sampling, and max windspeed during sampling. This model was generated nine times for all combinations of buffer size and diurnal phase.

Various diagnostic procedures were employed to detect the existence, extent, and configurations of spatial autocorrelation within the linear models. Specifically, a Moran's I test for statistical significance, facilitated by Monte Carlo Simulation, was applied to the residuals of each model "$\varepsilon_{i,j,t}$". The null hypothesis was rejected in all nine linear models,

indicating the presence of spatial autocorrelation. This aligned with the expectations considering the spatiotemporal nature of the data collection process.

Additionally, the linear models' residuals were geographically plotted to examine for discernible spatial patterns. These visualizations, referenced locally from one transect in **Appendix F**, revealed evident spatial trends affecting the models' efficacy. This further confirmation of spatial autocorrelation skewed assumptions of independent and identically distributed residuals, which justified the transition from OLS regression to the use of spatial error regression (Anselin, 1988; Won Kim et al., 2003).

Prior to the development of an equivalent spatial error model, it was necessary to delineate the patterns of autocorrelation present in each transect. Initial linear regressions were performed on each transect individually, described as local models. The differences in the data between the global OLS models and these localized OLS models required a reduced number of terms compared to the more comprehensive prior models ***(Eq* 8*)***:

8) $T_{i,j} = \alpha_{i,j} + \boldsymbol{\beta}_{\text{Pavement, j}} P_{i,j} + \boldsymbol{\beta}_{\text{Building, j}} B_{i,j} + \boldsymbol{\beta}_{\text{TreeCover, j,}} A_{i,j,} + \boldsymbol{\beta}_{\text{WaterCover, j,}} G_{i,j,} + \boldsymbol{\beta}_{\text{Elevation,j,}} E_{i,j,} + \boldsymbol{\beta}_{\text{Sunrise,j,t}} S_{i,j} + \boldsymbol{\beta}_{\text{Pavement, j}} P_{i,j} * \boldsymbol{\beta}_{\text{Building, j}} B_{i,j} + \varepsilon_{i,j}$

In the process of individual transect analysis, variables for cloud cover, daily high temperature, windspeed, and their corresponding interaction terms were excluded due to their lack of variability across observations at the transect level. Each transect received three local models, differing by buffer size within land cover exposure terms. The resulting residuals from these models were utilized to construct semivariograms, which assisted in determining the 'range value'—the distance beyond which spatial correlation between data points ceases to be significant. Range values were systematically documented across all three models for each of the 46 transects.

Spatial Error Modeling

Informed by insights from Moran's I analysis, the clustering in residual maps, and semivariograms derived from the residuals of linear models for each transect, further spatial analytical techniques were required to generate the global SEMs. The SEM necessitates the incorporation of a spatial weights matrix, which introduces an error term specifically to counteract spatial dependencies observed in the original residuals. Among the various spatial weighting methodologies applied in different studies, a Gaussian Kernel Weighting (GKW) scheme was chosen for our spatial weights matrix. This scheme was preferred because it offers a moderate adjustment in weights relative to distance, along with fine-tuning capabilities via the bandwidth parameter, as shown in **Appendix G**. The GKW method assigns weights to neighboring observations using its kernel function:

$$9)\ w(d) = e^{\frac{-d^2}{2\sigma^2}}$$

The weighting assigned to each adjacent point is determined by their distance 'd', measured in meters, through a function that includes an exponentiated component with 'σ', representing the kernel's bandwidth. Each transect has a deduced range value from semivariograms, as well as an individually determined optimal bandwidth that facilitates effective spatial weighting. To estimate each transect's optimal bandwidths, local SEMs for each transect and buffer size. These models were simplified, but were augmented with new terms to account for the error introduced by spatial relationships **(*Eq 10*):**

$$10)\ T_{i,j} = \alpha_{i,j} + \boldsymbol{\beta}_{\text{Pavement},\,j} P_{i,j} + \boldsymbol{\beta}_{\text{Building},\,j} B_{i,j} + \boldsymbol{\beta}_{\text{TreeCover},\,j} A_{i,j,} + \boldsymbol{\beta}_{\text{WaterCover},\,j} G_{i,j,} + \boldsymbol{\beta}_{\text{Elevation},j} E_{i,j,} + \boldsymbol{\beta}_{\text{Sunrise},j,t} S_{i,j} + \boldsymbol{\beta}_{\text{Pavement},\,j} P_{i,j} * \boldsymbol{\beta}_{\text{Building},\,j} B_{i,j} + \lambda_j W_{i,j} \varepsilon_{i,j} + u_{i,j}$$

To develop the spatial weights matrix 'W' for a model, it was first necessary to create a neighbor matrix specific to the dataset. In this matrix, rows were indexed by observation 'i', and columns corresponded to the sequential nearest points from the same transect. With this structure, cells within the neighbor matrix denoted the index of these neighboring points. Only neighbors within the designated bandwidth distance for that local model were included in the neighbor matrix. Subsequently, Gaussian Kernel Weighting (GKW) was calculated for each neighbor. These calculated weights were then used to replace the corresponding index within the neighbor matrix to convert the matrix to a spatial weights matrix for that local SEM. Before generating the regression, each row of the spatial weights matrix was standardized to sum to one.

This process of generating local SEMs for each transect was conducted four times, employing bandwidth values that spanned from the nearest neighbor distance of the most isolated point within the transect to the transect's range value as indicated by its semivariogram generated from its residuals in the local OLS. This approach yielded a total of 552 SEMs across the 46 transects, three buffer sizes, and four potential bandwidth values. The model with a bandwidth that resulted in the minimum value of 'λ' was deemed the optimal bandwidth for that transect's data. Consequently, each observation was assigned an optimal bandwidth corresponding to its transect ID that allowed for more robust construction of the spatial weights matrix for the global SEMs.

Having established the necessary spatial granularity and patterns of autocorrelation, we proceeded to undertake comprehensive global spatial error modeling. Forming and utilizing a spatial weights matrix for the entirety of a dataset relevant to a global SEM proved to be computationally expensive. To address this, we employed a bootstrapping

method, generating 100 iterations of the $\beta_{Pavement}$ coefficient estimates from global SEMs conducted on samples of the entire dataset. This necessitated selecting a random sample of 5000 data points from the total available for each diurnal phase, corresponding to approximately 10-15% of all data from that diurnal phase subset. A neighbor matrix was then created for the sampled points, adhering to stricter criteria: neighbors had to belong to the same transect ID (meaning they were neighboring points collected from the same sampling session) and fall within the optimal bandwidth determined for that transect from the series of local SEMs from that transect. After computing the GKW values and transforming the neighbor matrix into a weights matrix, an SEM was generated. This model returned to similar form as the global OLS model:

$$\mathbf{11)}\ T_{i,j,t} = \alpha_{,t} + \boldsymbol{\beta}_{Pavement,\,j,t}P_{i,j,t} + \boldsymbol{\beta}_{Building,\,j,t}B_{i,j,t} + \boldsymbol{\beta}_{TreeCover,\,j,t}A_{i,j,t} + \boldsymbol{\beta}_{WaterCover,\,j,t}G_{i,j,t} + \boldsymbol{\beta}_{Elevation,j,t}E_{i,j,t} + \boldsymbol{\beta}_{Sunrise,j,t}S_{i,j,t} + \boldsymbol{\beta}_{HighTemp,j,t}H_{i,j,t} + \boldsymbol{\beta}_{CloudCover,j,t}CC_{i,j,t} + \boldsymbol{\beta}_{MaxWind,\,j,t}WS_{i,j,t} + \boldsymbol{\beta}_{Pavement,\,j,t}P_{i,j,t} * \boldsymbol{\beta}_{Building,\,j,t}B_{i,j,t} + \boldsymbol{\beta}_{Pavement,\,j,t}P_{i,j,t} * \boldsymbol{\beta}_{CloudCover,j,t}CC_{i,j,t} + \boldsymbol{\beta}_{Pavement,\,j,t}P_{i,j,t} * \boldsymbol{\beta}_{MaxWind,\,j,t}WS_{i,j,t} + \boldsymbol{\beta}_{Building,\,j,t}B_{i,j,t} * \boldsymbol{\beta}_{CloudCover,j,t}CC_{i,j,t} + \lambda_j W_{i,j}\varepsilon_{i,j} + u_{i,j}$$

From each SEM iteration, we extracted coefficients relevant to our research in pavement exposure, model fit indices, and autocorrelation parameters. After this extraction, the procedure was reiterated by randomly sampling another set of 5000 points from the data subset. This cycle was repeated for 100 iterations for each of the and diurnal phase combinations. The mean values of these coefficients were used to quantify the impact of land covers and other variables on air temperature, while their standard deviations provided a measure of variability to the bootstrapping process. The goodness-of-fit for the models was used by comparing the average log likelihood values from each iteration to those of corresponding OLS models. Upon completion for all nine buffer size and

diurnal phase combinations, inferences were made based on the averaged $\beta_{Pavement}$ coefficients in returning to the original null hypothesis.

Results

Linear Models Per Each Diurnal Phase and Buffer Size

Linear regression was used to quantify the effect of pavement on microenvironment air temperature. The 'Percent Pavement Exposure' coefficient in each of the nine models represents the effect size, as shown in **Table 2**, which was the primary focus of our analysis. This table is an abbreviated version, only showing coefficients relevant to land cover. The full regression tables can be found in **Appendix H**. The most substantial model is observed in the morning models, capturing over 91% of air temperature's variability. We observe a steady decline in model fit throughout the day, with the adjusted R^2 value dropping by over 10%. This has been found in similar work (Chun & Guhathakurta, 2017), and follow-up research should explore additional nonlinear effects present in evening cooling that isn't captured in the presented model. A consistent positive correlation is evident between pavement presence and air temperature across all nine scenarios. Specifically, the mid-day model with a 100m radius suggests that every 10% increase in pavement area is associated with a 0.71°F rise in temperature under optimal UHI conditions when other land cover terms and covariates are held constant. Within each diurnal phase, expanding the buffer size (therefore increasing the unit area size of pavement within an increasing boundary) demonstrates an increase in the warming effect of pavement on air temperature measurements.

Table 2. OLS Regression coefficients from models representing nine combinations of buffer sizes used to calculate land cover exposure and diurnal phase that data was collected. Bolded values for coefficient estimates denote statistical significance (α=0.05).

	Morning					
	25m Buffer		*50m Buffer*		*100m Buffer*	
	Coefficient	SE	Coefficient	SE	Coefficient	SE
Pavement Exposure (%)	**0.006**	0.001	**0.012**	0.001	**0.022**	0.001
Building Exposure (%)	0.001	0.002	**0.021**	0.002	**0.049**	0.003
Tree Cover Exposure (%)	**-0.010**	0.000	**-0.018**	0.000	**-0.025**	0.001
Pavement x Building	**0.000**	0.000	**-0.000**	0.000	**-0.001**	0.000
Adjusted R2	*0.913*		*0.916*		*0.918*	

	Mid-day					
	25m Buffer		*50m Buffer*		*100m Buffer*	
	Coefficient	SE	Coefficient	SE	Coefficient	SE
Pavement Exposure (%)	**0.046**	0.002	**0.053**	0.002	**0.071**	0.003
Building Exposure (%)	**0.037**	0.003	**0.044**	0.003	**0.079**	0.004
Tree Cover Exposure (%)	**-0.020**	0.001	**-0.026**	0.001	**-0.030**	0.001
Pavement x Building	**-0.000**	0.000	**-0.000**	0.000	**-0.001**	0.000
Adjusted R2	*0.855*		*0.856*		*0.859*	

	Evening					
	25m Buffer		*50m Buffer*		*100m Buffer*	
	Coefficient	SE	Coefficient	SE	Coefficient	SE
Pavement Exposure (%)	**0.030**	0.001	**0.036**	0.001	**0.046**	0.002
Building Exposure (%)	**0.030**	0.002	**0.038**	0.002	**0.090**	0.003
Tree Cover Exposure (%)	**0.003**	0.000	0.001	0.001	-0.001	0.001
Pavement x Building	0.000	0.000	**-0.000**	0.000	**-0.001**	0.000
Adjusted R2	*0.788*		*0.791*		*0.795*	

Spatial Error Model

Local SEMs were developed for each transect ID primarily to estimate the optimal bandwidth parameter for data from each transect, which was crucial for constructing the global SEMs that test our null hypothesis. Additionally, these smaller models yield preliminary and local insights into the interactions between air temperature and the built environment. We generated 138 local SEMs, each with an optimal bandwidth, spanning all sessions and the three buffer sizes. While these provided exploratory details around our primary research objective, they were primarily used to form the spatial weights matrices of the global SEMs **(Appendix I).**

The coefficient estimates of the global SEMs provide robust support for the hypotheses outlined in **Equation 5**, as reflected in **Table 3**. These results allow us to reject the null hypotheses for all nine models. The models suggest both a daytime and nocturnal UHI signal where each unit area of pavement is positively correlated with an increase in local microenvironment air temperature. The bootstrapping approach, executed across 100 iterations for each model, yields a normal distribution of coefficient values with minimal variability (**Appendix I**), suggesting that the central tendency of these distributions is likely to be precise and resemble results obtainable with full data utilization. This accounting for spatial autocorrelation brought forth an increase in the evening warming effect associated with pavement exposure from that found in the OLS models, as the pavement coefficients mirror each other from mid-day to evening models.

Table 3. Average land use coefficients and their interaction terms from SEM bootstrapping. Values in the table represent the mean of the coefficients generated from 100 iterations, the standard deviation of these coefficients, and the average log-likelihood values.

Morning

	25m Buffer		*50m Buffer*		*100m Buffer*	
	Coefficient	SD	Coefficient	SD	Coefficient	SD
Pavement Exposure (%)	0.014	0.004	0.024	0.006	0.042	0.007
Building Exposure (%)	-0.027	0.014	-0.009	0.014	-0.003	0.016
Tree Cover Exposure (%)	-0.012	0.002	-0.023	0.002	-0.032	0.002
Pavement x Building	0.000	0.000	-0.000	0.000	-0.001	0.000
Log Likelihood	*-10764*		*-10699*		*-10677*	

Mid-day

	25m Buffer		*50m Buffer*		*100m Buffer*	
	Coefficient	SD	Coefficient	SD	Coefficient	SD
Pavement Exposure (%)	0.040	0.004	0.048	0.007	0.067	0.008
Building Exposure (%)	0.052	0.010	0.100	0.013	0.159	0.016
Tree Cover Exposure (%)	-0.017	0.002	-0.021	0.002	-0.025	0.003
Pavement x Building	-0.000	0.000	0.000	0.000	-0.002	0.000
Log Likelihood	*-9311*		*-9272*		*-9215*	

Evening

	25m Buffer		*50m Buffer*		*100m Buffer*	
	Coefficient	SD	Coefficient	SD	Coefficient	SD
Pavement Exposure (%)	0.040	0.004	0.048	0.005	0.067	0.007
Percent Building (%)	0.045	0.009	0.054	0.012	0.095	0.014
Percent Tree (%)	0.009	0.002	0.009	0.002	0.010	0.003
Pavement x Building	-0.000	0.000	-0.000	0.000	-0.001	0.000
Log Likelihood	*-10681*		*-10644*		*-10581*	

Both mid-day and evening models find a 0.67°F temperature increase associated with a 10% increase in pavement coverage when considering a microenvironment boundary and corresponding unit area associated with the 100m buffer models. Model fit typically improves with larger buffer sizes along with the variability in coefficient estimate

(Appendix J). This suggests that while a larger buffer might capture more of the influential surface area, improving the model's fit, it also introduces greater complexity and a broader range of thermal interactions within the larger microenvironment. Incorporating additional built environment factors and daily weather conditions into our models reveals the strong likelihood of nocturnal UHI effects, even within Vermont, an area with less infrastructure and lower population density than regions traditionally associated with UHI studies.

All 900 iterations conducted across the nine combinations also included an equivalent linear model without spatial weighting. Log likelihood tests were calculated to compare the model fit between the paired linear models and spatial error models. For these statistical tests, we reject the null for 100% of cases, confirming that the spatial error model provides better model-fit for every bootstrapping iteration. This further supports our SEM bootstrapping techniques as an ideal method to reduce the influence of spatial autocorrelation within model residuals.

Conclusion

In returning to our primary research question, we reject the null hypothesis and quantify a positive association between pavement exposure and air temperature across nine models formed by combinations of diurnal phase and unit area size. Our data collection methodology provided an expansive range of built environment exposure, weather conditions, topography, and random effects specific to ten northern climate communities on some of their warmest days. This data served as inputs to form a spatially weighted regression model to quantify the effect of pavement on air temperature to reach as much

as an associated 0.67ºF increase per 10% increase in pavement within the microscale during mid-day warming and the nocturnal UHI.

It was not within the scope of our work to quantify effects of specific thermodynamic or evaporative properties of pavement, buildings, or tree cover as defined in thermal balance equations. Pavement has been defined as a contributor to microenvironment-level heat amplification due to its ability to hold heat, transfer heat through convection, reflect incoming radiation, and more (Menon et al., 2010; Qin, 2015a; Synnefa et al., 2008b). Buildings contribute in all of these ways in addition to the anthropogenic contributions from inside the buildings, such as HVAC systems that displace warm air to the outdoors (Tremeac et al., 2012). Existing models pertaining to UHI intensity are often either too coarse in resolution at the regional scale, or overly detailed, dissecting individual thermal components within microenvironments, which can be limiting for practical applications such as transportation planning. While it is important for continued efforts to divide the net effect of pavement into individual thermodynamic components based on previous thermal balance approaches (Oke, 1988), our work provides a tool for application in microenvironment-level planning of the built space.

Our data collection coincided with peak daily temperatures of at least 90°F on only two occasions, echoing findings that UHIs and related health impacts can occur even without extreme heat events (Hajat et al., 2006; Oke, 1982). Only a few of the cities and towns from our dataset possessed pavement land cover proportions comparable to US metropolitan areas known to range from 29-36% pavement coverage (Akbari & Rose, 2008), nonetheless our study area exhibited significant heat variability. While the growing majority of the global and US population live in urban areas, roughly 7% of the

US population lives among city populations greater than 1 million residents (Bureau, n.d.). Our findings build on the previously scarce research that the UHI phenomena transcends the urban core of major metropolises such as Phoenix, New York City, or London, and can even be found in small cities within northern climates (Buyantuyev & Wu, 2010; Gedzelman et al., 2003; Kolokotroni & Giridharan, 2008; S. Peng et al., 2012; D. Zhou et al., 2019).

Although our mobile sampling campaign is extensive in scope—covering a wide range of days, cities, and diurnal times—there is always potential for enhancing the models with additional data. The population density, roughness factor, northern climate, and proportion of built space varies dramatically in our dataset from common UHI research, and our findings may not be generalizable to larger metropolitan areas. In addition, future mapping and mitigation scenario analysis should expand to identify potential for mitigation of nocturnal heat exposure.

Our transects were designed to represent the heat exposure experienced by residents within these microenvironments. However, capturing air temperatures along bike lanes and roads with e-bikes may not fully represent the thermal experiences of pedestrians, as the heat generated by infrastructure and human activity could dissipate before reaching pedestrian areas. Future studies could refine the understanding of how anthropogenic heat varies and the rate at which it dissipates across different urban infrastructure and pedestrian pathways could be incorporated into similar models.

Future research in mobile sampling with an e-bike or other bicycle designs should explore the potential for convectional influences from the field researcher towards the

thermocouple. Others who have used bicycles have installed the thermocouple on the front of the bicycle or staggered to the side to avoid the flow of exerted heat from the human rider.

The unit area sizes selected in the spatial analysis of the mobile data (buffer sizes of 25m, 50m, 100m) were selected based on the definition of the microenvironment bounds and to arbitrarily define a unit area of pavement. Other buffer sizes should be explored, and potentially a decay rate for the effect of pavement on air temperature could be quantified through a similar analysis. Further, the land cover data was collected between 2013-2016. It is reasonable to consider that the land cover within our study area changed between the collection of the land cover data and the collection of our air temperature data in the summer of 2022. More recent land cover data would improve the internal validity of our analysis.

Regression modeling included variables to account for weather conditions during sampling, such as the daily high temperature, max windspeed during collection, and max cloud cover during collection. These were all reported by the nearest ASOS network weather station, which are typically located outside of the city at an airport. While they may not be subject to the influences of a built environment commonly found within the city, their ranging distance from the mobile sampling may not make them an ideal or consistent representation of the mesoscale air temperature, wind speed, and cloud cover. Further, these stations take measurements periodically, sometimes hourly. It is understood that temperature can vary a fair amount within this time, as well as wind speed and cloud cover. Lastly, cloud cover is identified at different altitudes for a single observation. We

chose to record whatever altitude possessed the maximum cloud cover for a single measurement, which may not fully or accurately contain the influence of the vertical dimension. This and windspeed could also be binned into high and low categorical values for similar modeling approaches.

Our regression models included a variable for time, anchored to the official sunrise, enhancing the fit by accounting for the warming and cooling patterns embedded in the diurnal cycle. While we accounted for the official sunrise specific to that city and date, the length of days changed throughout the sampling campaign. Use of UHI intensity as the dependent variable was considered to help control for the warming and cooling that occurred during sampling, but the previously described limitations of ASOS network station data injected noise into the model that reduced model fit when we interpolated the temperature values at these stations between the hourly measurements. In addition, lack of access to these stations didn't allow us to calibrate and synchronize our mobile instruments to them. This source of noise was prevalent in our models when we used time-adjusted temperature values based upon linearly interpolated corrections between the beginning and end of our loop-shaped transects, and therefore the raw temperature was kept as our dependent variable. Future work could consider use of their own controlled rural station to develop a UHI intensity metric as their dependent variable. Additionally, exploring humidity, heat indices, and other metrics focused on capturing physiological stress instead of air temperature is recommended.

When terms for greenspace were explored in our model, issues of multicollinearity arose as the model tended to perfectly predict the land cover within the buffered space around

an observation when we included pavement, buildings, and trees as well. Terms for percent blue space within a buffer and distance to nearest blue space were also explored. However, the interpretation of the effect of blue space on temperature contrasted the literature, frequently providing a warming effect, lacking statistical significance, reducing or not changing model fit, and introducing multicollinearity. We suspect that since many of the cities we collected data from possessed blue space regions near their city cores, our model terms for blue space were indirectly serving as a proxy term for proximity to downtown areas rather than capturing the known thermodynamic influence of blue space as a heat sink. Future work should perhaps limit their data and models to one mesoscale or the relationship with one body of water, as our model treated blue space such as Lake Champlain with the same regard as a small stream.

While the precision around our averaged coefficient estimate for pavement terms found from our spatial error models (**Table 3**) demonstrated strong precision through the small standard deviation values, coefficients such as percent building cover showed much wider distributions (**Appendix J**). This could be improved by a combination of larger sample draws during bootstrapping or more iterations, but our samples of 5000 observations and 100 iterations were deemed enough to meet our research goal pertaining to pavement.

Use of spatial analysis through parameters identified in semivariograms from local regression models treated datasets as if all measurements varied in space but were recorded at one instant. The relaxing of this assumption was supported by the basis that the autocorrelation demonstrated spatially, when addressed to reduce distortion to

regression coefficients, was closely coupled with the autocorrelation that could be identified temporally. Further accounting for this autocorrelation was addressed in the time since sunrise term as well, but future work should pursue modeling techniques that directly account for all sources of autocorrelation. Mixed effect modeling with structuring of the covariance matrix for these dependencies appears to be an ideal direction for the modeling.

Chapter 2—Statewide Potential for Heat Exposure Mitigation Through Scenarios of Pavement Reduction

Introduction

This chapter builds upon the models of the previous chapter to evaluate the effects of statewide reductions of pavement and replacement with tree cover at the household level. Three reduction scenarios are designed for different levels of modification to evaluate the spatial heterogeneity of heat exposure for optimal mid-day UHI conditions, as well as the difference in benefits across the urban-rural continuum. Lastly, the level of equity pertaining to heat reduction across these three land cover transformations is evaluated to identify the biggest winners across sociodemographic distinctions. This work was informed by previous research in environmental justice and environmental epidemiology pertaining to extreme heat as well as the literature that informed the first chapter of this dissertation.

Environmental Justice and Epidemiology in Heat Research

The prevalence of Urban Heat Island (UHI) effects in epidemiological research is well-established, focusing on heat-related illnesses and mortality within households, communities, and cities. Heat-related illnesses include conditions such as heat stroke, hyperthermia, heat rash, cramps, fainting, and heat exhaustion due to high temperatures. The National Association of Medical Examiners provides a definition of heat-related death as a death in which "exposure to high ambient temperature either caused the death or significantly contributed to it (Donoghue et al., 1997)." However, the attribution of death to heat exposure can be challenging, especially post-heatwave, when differential information bias may lead to an overestimation of heat-related mortality.

Early work in public health pertaining to heat was first presented in the form of an 86-city analysis of mortality due to heat events based on data from 1920-1934 (Gover, 1938). They identified a peak in 1934 at 2.64 deaths per 100,000 death certificates indicating heat as a cause. Methods and datasets have been refined to conduct finer scale research in this field since, as this became an interest of US military research after World War II (Schickele, 1947). Subsequent decades have seen a continued focus on mortality during heat waves and the physiological impacts of heat-related illnesses.

Heat stress is currently conceptualized similarly to air pollutant exposure metrics, being quantified as a time-weighted sum of temperature values across different locations over a given period. While this modeling approach provides a measure of heat exposure, introduction of noise in the data is possible. The variability of microenvironment conditions experienced by an individual can be difficult to track with accuracy and precision, and relying solely on local weather station data may not reflect the actual exposure of a population to varied microclimates within an area. Additionally, physiological research into heat stress has revealed significant variations in heat tolerance both within and between communities, nuances that are not fully captured by simple exposure metrics.

Time-series research in the context of heat exposure allows for the disaggregation of data and the creation of models that link heat exposure to physiological stress on specific bodily systems (Ballester et al., 1997; Kunst et al., 1993). Such models are particularly insightful for identifying and mitigating risks among vulnerable groups such as the elderly, who often have diminished thermoregulatory capabilities (Kenney & Hodgson,

1987). Physiologically focused studies measure the impact of heat exposure on both ambient temperatures and body temperatures. For instance, a study of the elderly in Baltimore found that median body temperature increased by 0.15°F for every 1°F rise in median ambient temperature (Basu & Samet, 2002a).

In epidemiological studies examining heat exposure and health outcomes, various temperature metrics are utilized, such as daily minimum, maximum, or average temperatures. The determination of appropriate lag times to correlate temperature with mortality rates is a critical aspect of this research. Studies often indicate that short-term exposure to extreme temperatures has a more substantial association with health outcomes. Time-series analysis across major eastern US cities over two decades has revealed that a lag time of 0-3 days between high temperatures and increased mortality rates yields the most significant correlations (Curriero et al., 2002).

In epidemiological studies, heat slope and heat threshold are two critical metrics used to quantify the impact of heat on populations. The heat threshold marks the temperature at which mortality increases, particularly among the most sensitive individuals. The heat slope measures the rate of increase in mortality with each unit of temperature increase beyond this threshold. A study of London, Budapest, and Milan revealed that Milan had the highest mean temperature threshold (74.7°F), yet London exhibited the highest average daily temperature and steepest heat slope, indicating a 7.2% rise in daily mortality per 1.8°F increase in mean temperature. This metric was derived from the daily minimum and maximum temperatures (Hajat et al., 2006). A meta-regression across 64 cities found that cities with higher average summertime temperatures had higher heat

thresholds, suggesting that populations in cooler climates are sensitive to heat at lower temperatures (Hajat & Kosatky, 2010). This was also seen when comparing proximity of these cities to the equator. Research from Japan showed a much higher threshold at 100.4°F, with an exponential effect of consecutive hot days on mortality (Nakai et al., 1999). These variations in thresholds and slopes underscore that community-specific factors like urbanization and demographics influence population-level heat risk.

In studying the heat risk to communities, particularly during heatwaves and the warmer seasons, research has highlighted significant disparities (Klinenberg, 2015; Mitchell & Chakraborty, 2014). Heat risk indices have been created to encapsulate various factors, including aspects of the built environment, health vulnerabilities, age, social isolation, and more. Studies across three U.S. metropolitan areas found that such heat risk indices positively correlate with lower economic status and minority communities (Mitchell & Chakraborty, 2014). Similarly, data simulations from Phoenix neighborhoods during the summer of 2003 indicated that lower socioeconomic and minority groups were more likely to live in hotter areas, with a noted positive correlation between the thermal heat index and factors like high settlement density, limited vegetation, and reduced open spaces (Harlan et al., 2006).

The investigation into the root causes of heat inequities has been notably conducted in areas affected by historical redlining, such as Baltimore, Kansas City, and Dallas. These redlined communities have been shown to have higher average LST measurements compared to neighboring communities, likely due to policies that enforced racial segregation and limited access to public amenities that counteract UHI effects such as

parks and greenspaces (Wilson, 2020). Nationwide analysis found that non-Hispanic black, non-Hispanic Asian, and Hispanic households are 52%, 32%, and 21% more likely, respectively, to live in areas with high heat risk-related land cover compared to non-Hispanic white households (Jesdale et al., 2013). Further, a study across 20 southwestern U.S. metropolitan areas incorporated the diurnal temperature cycle into their analysis and reported that the poorest 10% of neighborhoods were on average 4°F warmer than the wealthiest 10% during the day, a disparity that narrowed to 1°F at night (Dialesandro et al., 2021).

In the domain of environmental justice within the heat literature, there is a call for future research to incorporate geospatial datasets that include historical land use and policy data, emphasizing the need to address and prioritize current inequities (Wilson, 2020). A policy analysis of climate and sustainability plans from 28 medium to large U.S. cities has characterized the integration of equity goals as "secondary or tertiary" in relation to economic or environmental goals, failing to acknowledge the kinship that each of these sectors of policy goals possess (Schrock et al., 2015).

Using impervious surface area (ISA) as a proxy for heat, Michigan researchers identified correlation between ISA exposure and poverty rate, minority racial status, and prevalence of mobility-reducing disabilities at the census tract level (J. White-Newsome et al., 2009). Similar efforts have been developed in our study area of Vermont, as a statewide pavement exposure framework was formed to identify household-level pavement exposure within different buffer ranges. With this, characteristics such as race, income,

and other demographic characteristics were assessed for inequitable exposure levels to pavement (Antonczak et al., 2024).

Among the most vulnerable populations to heat exposure is the elderly. As of 2020, 16.8% of the US population's age was 65 and over, demonstrating a larger increase since 2010 than the previous 50 years before (Caplan, 2023). This demographic group faces challenges such as impaired thermoregulatory control, decreased thirst sensation, reduced sweating, and cardiovascular constraints, all of which are sometimes exacerbated by medications (Armstrong & Kenney, 1993; Dufour & Candas, 2007; Inbar et al., 2004; Kenney et al., 1997; Mack et al., 1994; Miescher & Fortney, 1989; Minson et al., 1998; Phillips et al., 1991). Laboratory studies suggest that thermal sensation in the elderly is predominantly influenced by air temperature, in contrast to younger individuals who are affected by both air and skin temperatures (Schellen et al., 2010). A post-heatwave study in France found that 35% of the elderly in Paris who died during a heat event succumbed to heat-related causes, with significantly higher risks associated with being bedridden or having a bed under the roof, highlighting the risks of isolation and the nocturnal UHI effect (Vandentorren et al., 2006). Similar effects from limited mobility and isolation were found among the elderly who died of heat-related death in the 1995 Chicago heat wave (Semenza et al., 1996). Further, the elderly is commonly on a fixed income which makes mitigation strategies such as purchasing of air conditioning units challenging for some (J. L. White-Newsome et al., 2012).

Heat-related morbidity and mortality in medical facilities, especially among the elderly, remain significant concerns in heat research (Basu & Samet, 2002b). A time-series study

in Germany from 2001 to 2005 involving over 95,000 nursing home residents found a rise in all-cause mortality at ambient temperatures above 78.8°F. This risk was especially pronounced in individuals aged 90 and above and in those requiring more intensive care (Klenk et al., 2010). However, comparisons with studies from other regions or earlier periods must consider the increased prevalence of air conditioning and changes in care standards, reducing the generalizability to current day in a climate and community such as those found in Vermont (Holstein et al., 2005; Mackenbach et al., 1997; Marmor, 1978).

Children are especially susceptible to heat exposure due to physiological and behavioral factors. Their higher surface-area-to-body-mass ratio compared to adults leads to greater heat absorption in the same environmental conditions (Falk & Dotan, 2008; Wenger, 1995). Thermoregulatory systems in children are less developed, often relying more on conductive rather than evaporative cooling mechanisms such as sweating (Falk, 1998, p. 199). Even before birth, heat exposure to pregnant mothers has been associated with lower birthweight (Deschênes et al., 2009). Children's reliance on adults for hydration and their limited ability to perceive heat risks necessitate adult vigilance in recognizing heat-related distress (Z. Xu et al., 2012). Vulnerable microenvironments for children include parks and schoolyards, where extended playtime occurs in areas often lacking in heat mitigation design features like shade, greenspaces, and hydration facilities (Dadvand et al., 2015). Infants under 1 year are particularly at risk during heatwaves, though studies generally focus on children aged 0-14 when assessing vulnerability to heat (Basagaña et al., 2011; Basu & Ostro, 2008; Hutter et al., 2007).

Additional morbidities beyond common heat-related illnesses have also shown to be correlated with ambient temperature. Research in Japan found a significant rise in hand, foot, and mouth disease incidence, with a 11.2% increase per 1.8°F rise in average temperature (Onozuka & Hashizume, 2011). Pediatric renal disease has been shown to increase during heat waves (Kovats et al., 2004; Nitschke et al., 2011). Studies in Peru, Bangladesh, and Taiwan observed positive associations between higher ambient temperatures and cases of diarrheal diseases in children (Checkley et al., 2000; Chou et al., 2010; Hashizume et al., 2007). Moreover, ambient temperature has been connected to a variety of child health issues, including asthma, malaria, gastrointestinal diseases, eczema, among others (Z. Xu et al., 2012).

Methods

This chapter's methodology is systematically divided into three distinct sections. I will first elaborate on the methods employed to develop the statewide pavement exposure framework, as completed by Antonczak et al (2024). The next subsection of the methodology incorporates the pavement exposure framework alongside the coefficient estimates obtained from the spatial error model presented in the first chapter to calculate household-level heat exposure reductions under three scenarios of pavement reduction and tree substitution. Lastly, I detail the process of spatial analysis and equity analysis across all Vermont households under these different scenarios.

Pavement Framework

Our study investigates residential heat exposure, particularly from heat exacerbated by transportation infrastructure such as paved surfaces, which significantly increase near-surface temperatures. We assessed household exposure to pavement throughout Vermont

using four key datasets: census socio-economic data, high-resolution land cover data, standardized statewide parcel data, and enhanced 911 address point data. The most current and detailed population and land cover datasets for our study area were utilized.

Initially, Antonczak et al (2024) identified residential buildings statewide using high-resolution (0.5m) impervious surface data from the Vermont Center for Geographic Information (2019), produced by the University of Vermont Spatial Analysis Laboratory, and standardized parcel data (2021) to delineate property boundaries. Residential buildings were classified into single-family (SF) or multi-family (MF) structures using the Enhanced 911 address points, which provides structure type data for emergency services. Residential classification was determined by the presence of an E911 residential site within a parcel. For parcels with multiple site locations, the structure was considered MF. Overall, 241,910 households were categorized, with 87.7% as SF and 12.3% as MF.

Next, Antonczak allocated population and demographic characteristics to households. Population distribution by race, ethnicity, income, age, and poverty status was derived from the 2020 Census and the 2016-2020 American Community Survey (U.S. Census Bureau, 2022). Researchers focused on specific demographic groups due to known vulnerability to heat-related health impacts, classifying individuals as White, Black, Asian, Other race alone, non-White, or Hispanic or Latino. Households were assigned median income and age data from their census block-group, and poverty status from their census tract.

Lastly, Antonczak quantified each household's exposure to pavement. From the land cover data layer, pavement was defined as roads and other paved surfaces, such as

driveways and parking lots as done in the first chapter of this dissertation. After distinguishing paved from non-paved roads, they buffered road centerlines based on their functional classification and formed a spatial union with the impervious surfaces land cover. Paved areas within multiple buffer distances from each household were quantified to determine household-level exposure to pavement. The resulting dataset represents the percentage of pavement within each household buffer across Vermont, along with the total population and demographic profile of each household. Upon completing these steps, researchers had formed a statewide pavement exposure framework, serving as a tool which allowed for the mitigation scenario analysis conducted in this dissertation.

Reduction Scenarios

Within the pavement exposure framework, the pavement exposure values for each Vermont household were integrated as the vector "P_i" within **Equation 12**. This equation also incorporated various coefficients from the first chapter's SEM, specifically those associated with the change in air temperature due to the percentage of pavement "$\beta_{Pavement,t}$":

$$\textbf{12)}\ \Delta T_{i,r} = Reduction_{Pavement} + Substitution_{Tree} + Reduction_{Interaction,}$$

$$= (1-r)\beta_{Pavement}\, P_i + r\beta_{Tree}\, P_i + (1-r)\, P_i\, B_i(\beta_{Int,Pavement*Building})$$

Here, $\Delta T_{i,r}$ represents the household-level change in air temperature indexed by household ID "i". The reductions, indexed by a value, r, correspond to 10%, 25%, and 50% reductions in pavement when set to 0.1, 0.25, and 0.5, respectively. Each reduction scenario anticipates that the paved area will be substituted with tree cover.

To map this change in heat exposure, Vermont was divided into a grid (500m x 500m cells) to create a mean heat exposure map (population-weighted) for each of the three reduction scenarios. Additionally, we analyzed household heat exposure by urban/rural status using the Economic Research Service Rural-Urban Commuting Areas (RUCA) classification scheme (Economic Research Service, Department of Agriculture, 2020). The RUCA codes, informed by population density, urbanization, and daily commuting patterns at the census tract level, were further simplified into four categories: metropolitan, micropolitan, small town, and rural. The RUCA code assigned to each household corresponds with the overlapping census tract, allowing a comparative analysis of heat exposure changes across urban and rural settings.

Lastly, we assessed exposure equity. Households were categorized into ten ordinal heat exposure deciles based on their potential reduction in temperature. Reduction deciles were then evaluated across racial and ethnic groups, poverty status, and income levels. We determined the proportions of these subpopulations within the various heat exposure deciles, offering insights into who benefits most from replacement of pavement with tree cover across different demographics during mid-day warming.

Results

Our initial findings offer a geographic perspective of household-level impacts across Vermont for each of the three mitigation scenarios. **Figure 11** shows the statewide potential for reduction from the most aggressively proposed mitigation scenario in which 50% of all household pavement exposure is replaced with tree cover. We can see in three of Vermont's major urban areas that the potential for reduction is heterogenous with adjacent local environments ranging in their cooling potential.

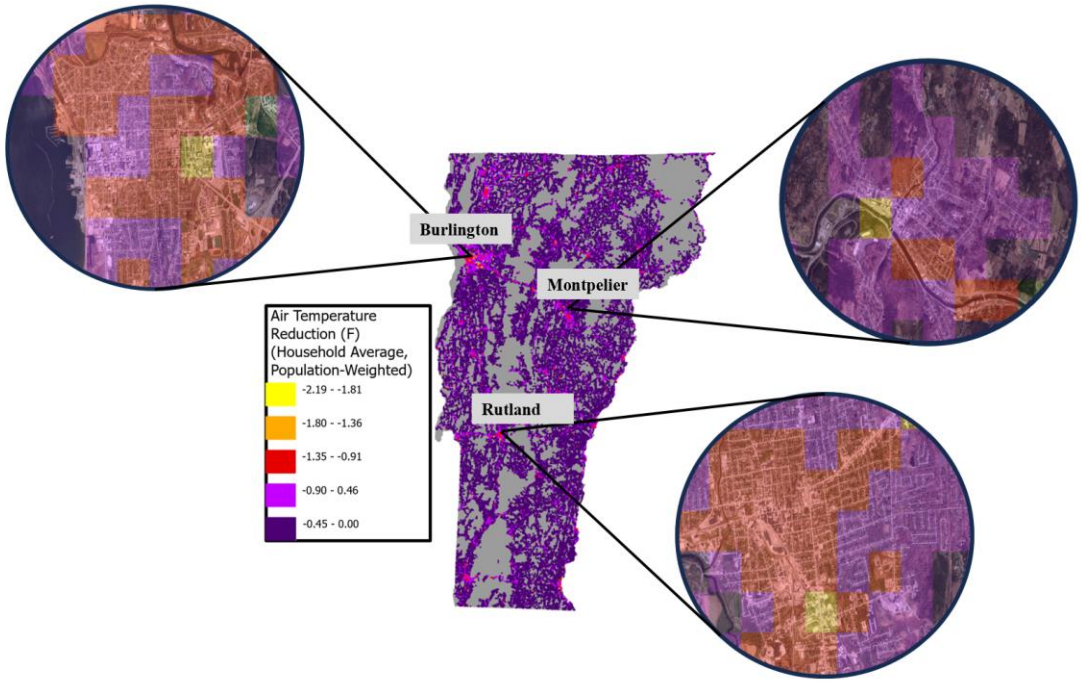

Figure 11: Gridded (500 m x 500 m) change in household average mid-day air temperature reduction (°F) based on a mitigation scenario involving a replacement of 50% of household pavement exposure with tree cover. Averages are population-weighted.

Our analysis of temperature reduction potential across the urban-rural continuum supports existing research suggesting that while extreme heat and UHIs are often associated with densely populated cities, it can be prevalent in less populated spaces (Ivajnšič et al., 2014; Pinho & Orgaz, 2000; Vardoulakis et al., 2013). In all three mitigation scenarios, the potential for cooling shows only a marginal increase with transitions in urban-rural status (**Figure 12**).

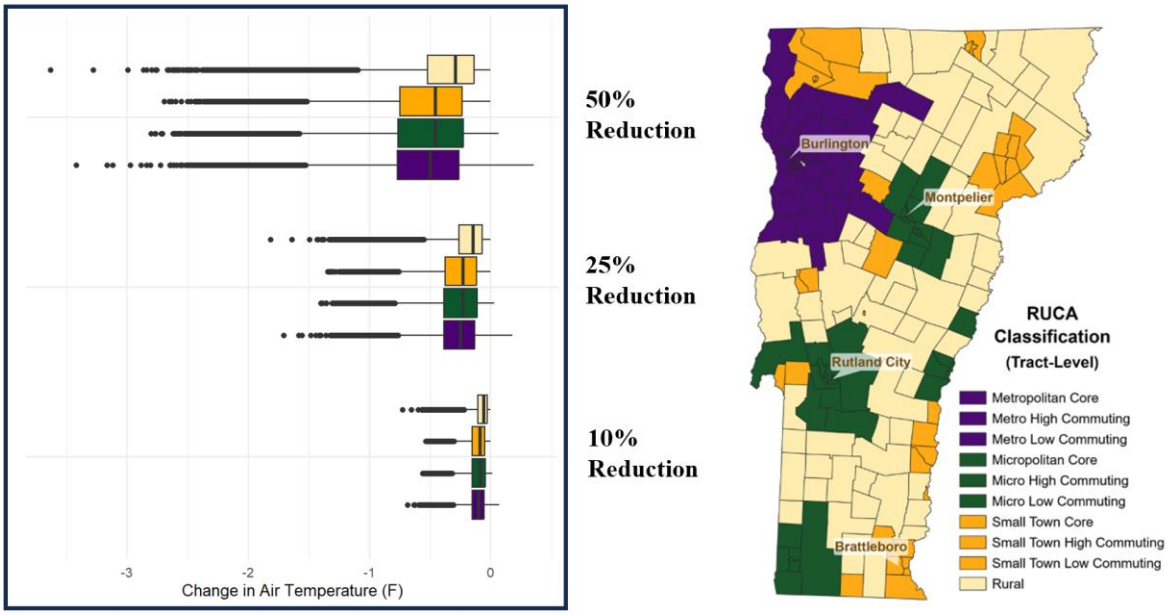

Figure 12: **Distribution of household temperature reductions by RUCA Classification for each mitigation scenario.**

The most notable differences emerge in the 50% pavement reduction scenario, yet even then, the median temperature reductions between metropolitan areas and smaller towns or micropolitan regions differ by less than 0.1°F. However, this scenario demonstrates a measurable drop-off at the rural distinction. Though the differences decrease in the more conservative scenarios, the pattern remains. This finding emphasizes the importance of addressing heat exposure in non-urban contexts.

Potential for mitigation was further analyzed across age, income, and race/ethnicity. When arranging household temperature reductions by decile, we see that much of the reductions are less than 1°F even at the top decile for the most aggressive scenario **(Figure 13C)**.

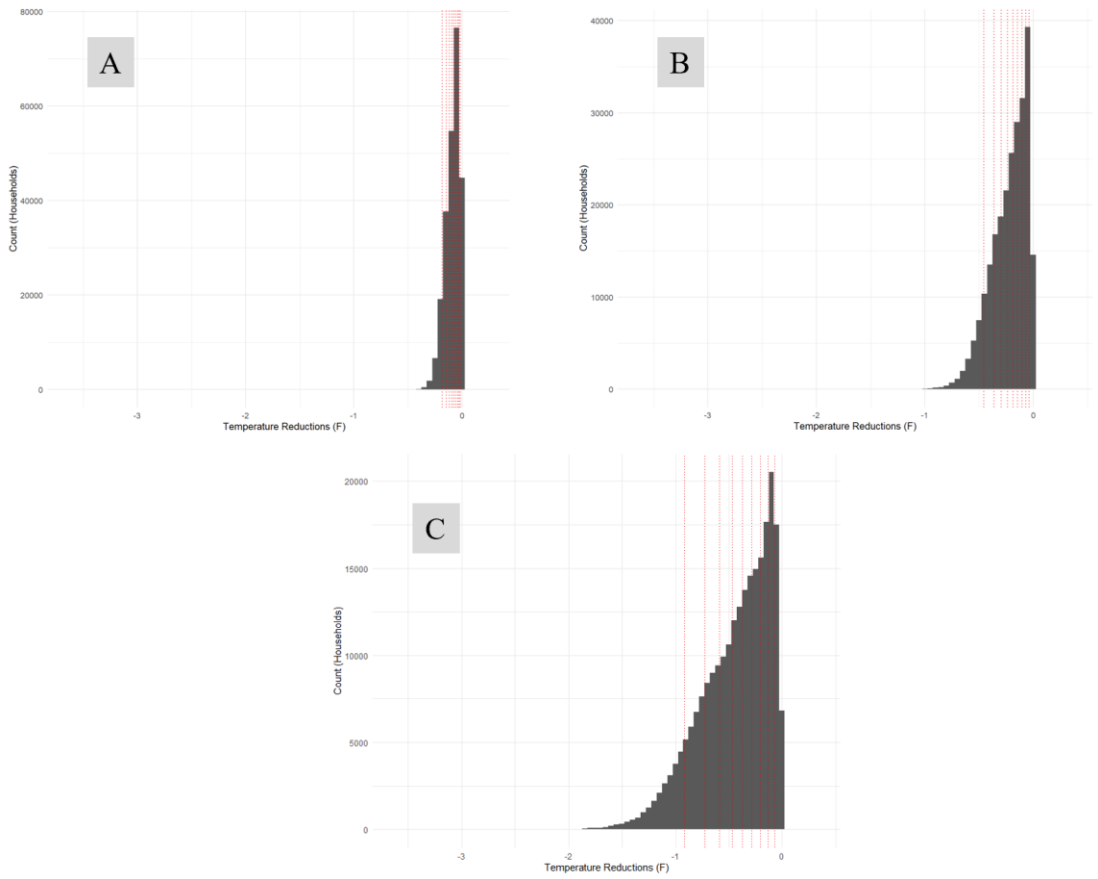

Figure 13. Distribution of temperature reductions per household in the A) 10% reduction scenario, B) 25% reduction scenario, and C) 50% reduction scenario. Red dotted lines signify the separation in deciles.

Figure 14 shows the declining relationship across the nonwhite population share with the temperature reduction. The share of the 10th decile exceeds the state's white alone population share by over 2% while the nonwhite population's share of the largest temperature reduction decile is nearly 3% less than the statewide proportion. This indicates a potential inequity, while the other two mitigation scenarios not only hover around their statewide proportions for both white and nonwhite populations, but they stay relatively constant across all reduction deciles.

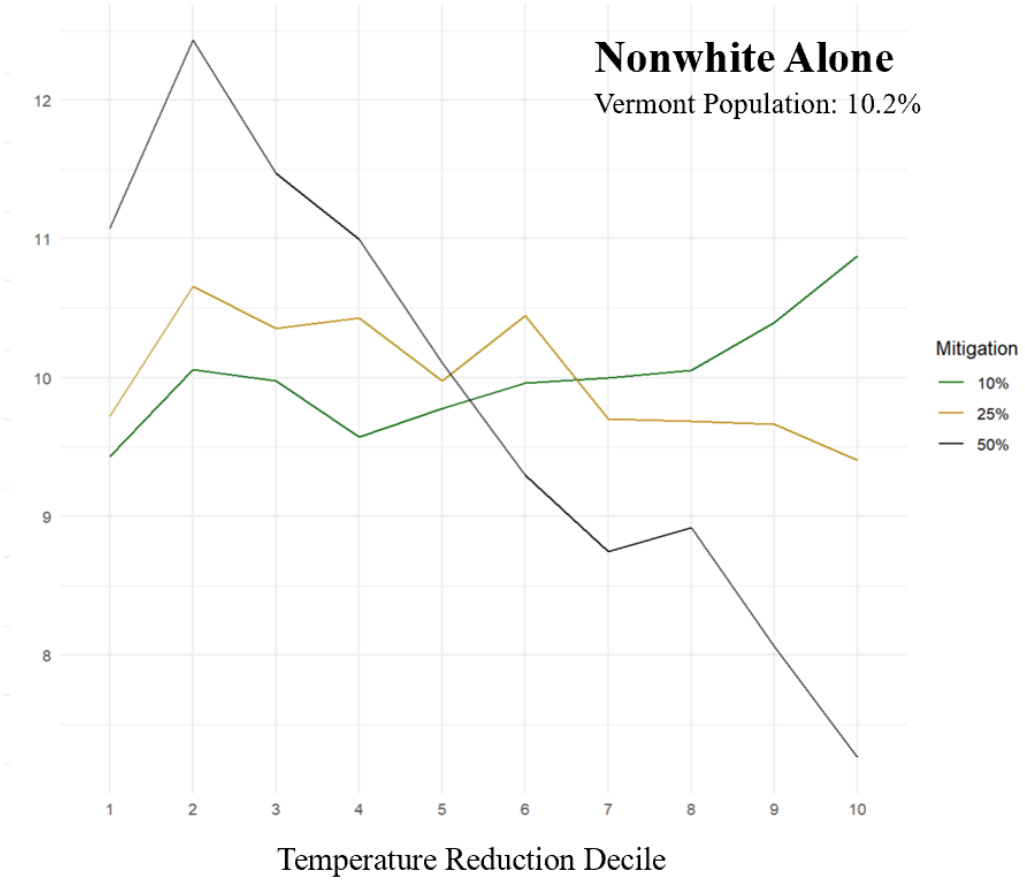

Figure 14. Population shares within temperature reduction deciles across all three mitigation scenarios for the nonwhite alone population. Data is at the block level.

Populations with documented vulnerability to extreme heat are children and the elderly. In our analysis, we see that all three scenarios demonstrate an increase in population share for the elderly demographic as cooling gains increase (**Figure 15)**. This is of note when considering 19.4% of Vermont's population falls in this age bracket, making the state the fourth oldest populations in the United States. However, we see a small decline in the higher deciles for population share of children five years old and younger. While the largest cooling gains correspond with minimum shares of this demographic, these

minimums are roughly 0.4-1% below the statewide population share for children 5 and younger.

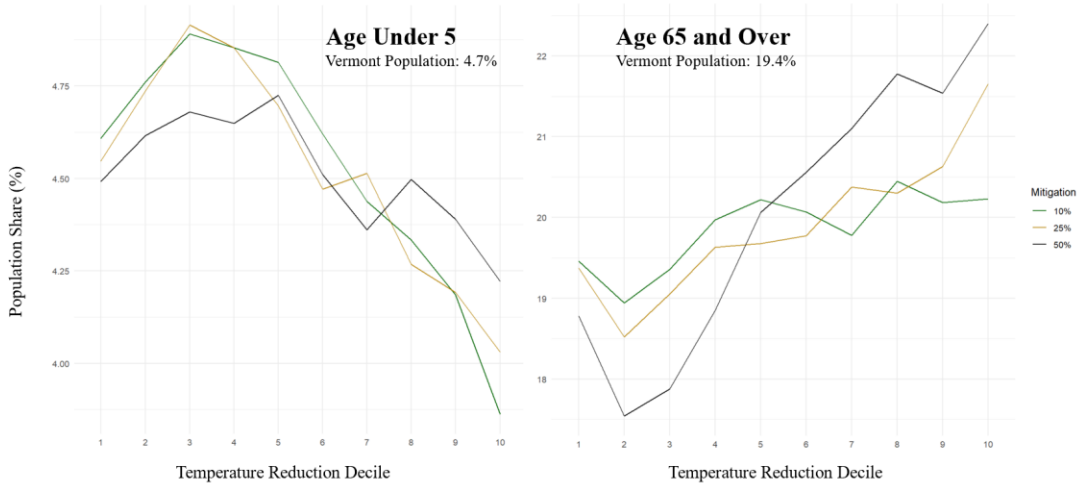

Figure 15. Population shares of vulnerable age groups within temperature reduction deciles across all three mitigation scenarios. Data for both are at the census block group level.

When evaluating these mitigation scenarios against household income, we see that the two conservative scenarios maintain above average population shares beyond the fifth temperature reduction decile and continue increasing **(Figure 16).** We interpret this to mean that larger proportions of those with financial barriers to mitigating their heat risk would see larger reductions in heat from these scenarios. However, this is a relatively small increase from the statewide proportion, showing that 14% of the top cooling decile includes households living below the poverty line for the 10% substitution scenario. Further, the greatest cooling gains from the most aggressive scenario show slightly less than the statewide share of this demographic in the top reduction decile. More decile plots across additional and more specific demographics are available in **Appendix K-Appendix M.**

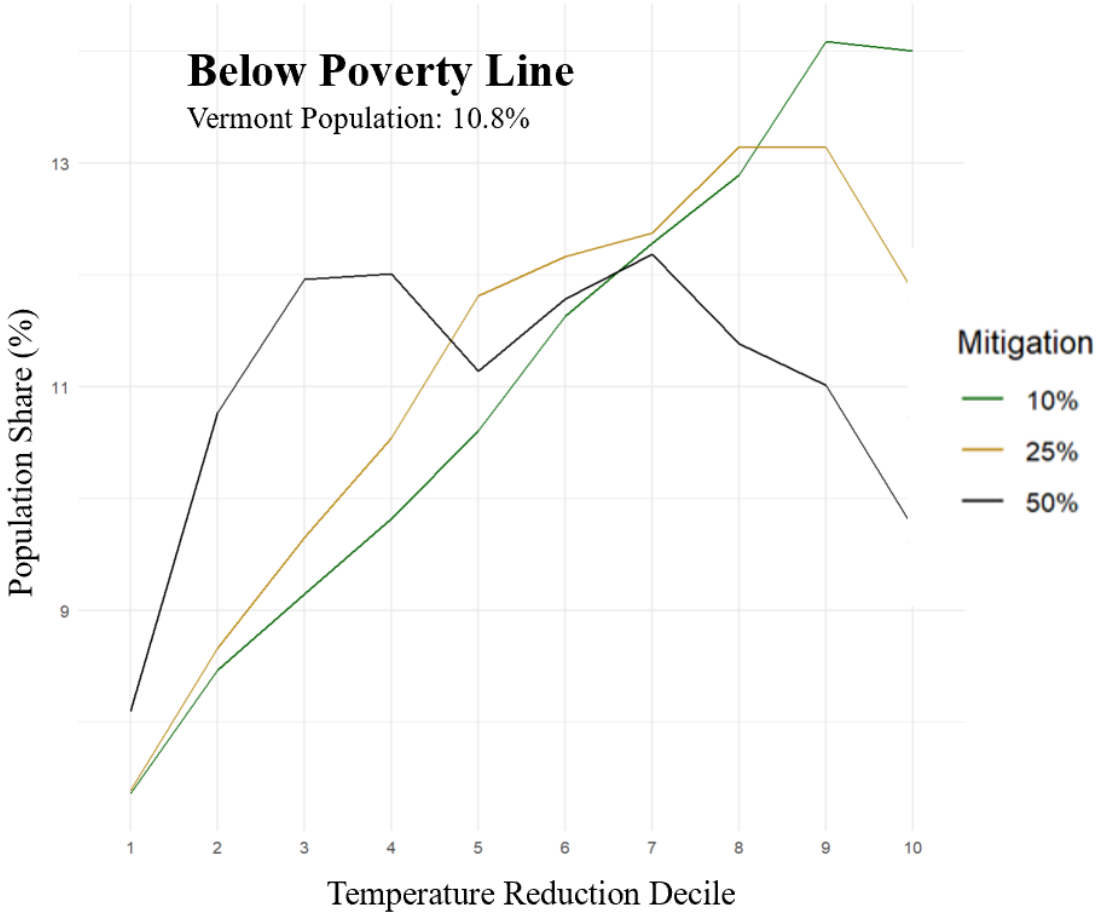

Figure 16. Population shares of households below the poverty line within temperature reduction deciles across all three mitigation scenarios. The data is at the census tract level.

Conclusion

We conclude this scenario analysis with the overarching finding that a general substitution of pavement for tree cover at the household level for all of Vermont doesn't result in distinguishable differences across the urban-rural spectrum, nor equitable differences across vulnerable sociodemographic populations. The statewide gridded average of reductions at the 500x500m resolution demonstrated heterogeneity in the potential for heat mitigation across local environments as observed from the heat exposure collected from our mobile transects. After grouping the expansive detail provided by RUCA codes into four larger distinctions across the urban-rural continuum, the mitigation scenarios presented minimal difference in heat reduction for all except those classified as rural households. As for the equity analysis, the potential for extensive reductions across vulnerable populations pertaining to race and income is not evident. Though there is potential for over 3^{o}F in mid-day air temperature reductions **(Figure 13)**, those come at the cost of a statewide 50% reduction in household pavement exposure, a strategy with consequences when it comes to current and future land use plans. Further, just 6.9% of households in this most aggressive scenario see cooling effects greater than 1^{o}F.

Limitations of this chapter are largely embedded in the limitations of the statewide pavement exposure framework (Antonczak et al., 2024) and the methodology of the previous chapter of which this analysis was built upon. We recommend more targeted mitigations of microenvironments with known heat amplification signals and local environments with known presence of vulnerable populations. Tools such as community-wide high resolution heat mapping can better identify high risk microenvironments

commonly occupied by vulnerable populations for more direct and effective interventions.

Chapter 3—Comparison of Decision-Tree Based Machine Learning Techniques in Predicting and Mapping Microenvironment Air Temperature

Introduction

The findings of the previous chapters further motivate the need for high-resolution heat exposure mapping. The primary research goal of this chapter is to compare two machine learning techniques in their ability to accurately and efficiently predict air temperature within the framework of data used in the previous chapters, and further, to map micro-scale air temperature beyond the bounds of the traveled sampling pathways to cover an entire city. Previous research informing this work includes application of the two decision tree algorithms both within heat mapping and in other predictive models, as well as the growing field of techniques to better interpret these models and the effects of their features.

Mapping Urban Heat Islands

The integration of satellite data with machine learning has advanced the identification of heat microenvironments and UHI effects, allowing for predictive modeling of heat distribution (Aniello et al., 1995; Sidiqui et al., 2016). Such techniques can pinpoint areas of heat intensity, aiding in recognizing and addressing UHI impacts on vulnerable populations (Shandas et al., 2019). This in turn can inform interventions and future planning for a region.

Gaussian models are instrumental in locating UHI centroids and assessing the diminishing effects of heat amplifiers with distance (Quan et al., 2014; Streutker, 2002). Others have suggested additional methods to supplement the Gaussian models to demonstrate non-elliptical spatial patterns (Flores R. et al., 2016). The process typically

involves using satellite imagery with the proper atmospheric corrections, then fitting the LST found in each pixel to a Gaussian surface (J. Zhou et al., 2011). Those that use a Gaussian volume model implement the methodology for Gaussian surfaces, with an added z-dimension that models the proportion of higher UHI effects within an area, forming a cylindrical volume around the centroid of the UHI (Quan et al., 2014).

A common machine learning technique with growing popularity in mapping UHI effects is the use of Random Forest (RF) predictive modeling, favored for its ability to detect non-linear patterns and its robustness to outliers and multicollinearity (Breiman, 2001; Lundberg et al., 2020). RF operates by creating an ensemble of decision trees, each generated from a subset of data. Nodes are split using criteria such as root mean squared error (RMSE), and the process repeats until a specified stopping criterion is reached. The model's predictive power is then assessed by averaging the output of all trees and validating against a reserved test dataset, with RMSE serving as a key performance metric.

Comparison between RF predictive models and regression models in southern Brazil showed that RF models demonstrated much higher model fit (R^2>0.96) for modeling both daytime and evening air temperature than regression (R^2=0.64, 0.34, respectively) (Oukawa et al., 2022). Further, the RF models concluded the validation process with a RMSE value of 1.15ºF. They leveraged predictors such as land cover proportion, topography, urban geomorphology, population density, weather conditions, and atmospheric vertical indices. Others compared the two predictive modeling approaches and found similar performance capabilities, though few identified and addressed the

spatial autocorrelation likely present in neighboring observations among their regression models beyond the use of coordinates as model features (Alonso & Renard, 2020; Voelkel & Shandas, 2017).

Another machine learning approach that is based on decision tree architecture is the gradient boosting machine (GBM) (Friedman, 2001). It is visualized and described as a network of decision trees, though typically shallower than those found in RF models. Learning is conducted through the sequential correcting of errors from previous trees that are added iteratively. Instead taking the average of models within the forest as done in RF models, “boosting” is the process of adding a new model sequentially as an iterative, weak base-learner model to be trained with respect to the error of all previous models in the ensemble. This encourages the base-learner model to be maximally correlated with the negative gradient of the loss function to that point in learning.

Advancements in Gradient Boosting Machines (GBMs) include tuning for accuracy, although overfitting can be a concern. Light gradient boosting machines (LightGBM) and extreme gradient boosting machines (XGBoost) are two such evolved frameworks. LightGBM uses histogram-based approaches for faster processing, while XGBoost includes regularization techniques to combat overfitting. XGBoost's efficiency, parallel processing, and handling of missing data have proven useful in urban heat studies, such as analyzing Shanghai's landscape on thermal conditions (S. Yu et al., 2020). In comparative studies, XGBoost has shown marginally better performance than LightGBM in predicting LST (Z. Liu et al., 2022). While GBMs are less commonly applied in heat

mapping, their potential for accuracy suggests they could be an effective alternative to RF models with careful consideration of overfitting risks.

A common concern among those who deploy machine learning techniques such as RF or GBM is the lack of output describing the effect of individual features. While they often are favored to traditional statistical methods for predictive accuracy and robustness to outliers and collinearity, this "black box" nature to the interpretation of such results continues to provide challenges in interpretation of results, communication of findings to stakeholders, and in this case, direct interventions to reduce heat exposure. A rising accommodation to this drawback is the use of a concept derived from game theory known as shapley values (Shapley, 1953; Sundararajan & Najmi, 2020; Winter, 2002). This need for interpretation has spanned across disciplines, and has even been used in recent heat literature to interpret the effect of features on heat-related mortality in a spatial domain within a RF model (Kim & Kim, 2022).

Shapley values quantify the marginal contribution of each feature towards a model's prediction while considering all possible feature subsets. This allows for distinction between the interdependencies between features, which transcends the capabilities of importance metrics provided by an RF model such as Gini Impurity or mean decrease in impurity that quantify the value of a feature to the accuracy or construction of the model. The shapley value can often be interpreted as a vector-based quantification of the unit-change in the dependent variable per change in each feature, similar in interpretation to a coefficient estimate in regression in some ways. While their calculation doesn't allow for an assigned statistical significance, additional bootstrapping techniques allow an

assigning of confidence intervals around the determined shapley value for a feature to provide a general level of certainty. Additionally, shapley values can be calculated for each input within the model, providing a distribution of such contributions to describe the variability of effect by a feature across a dataset.

Methods

The methodology of this chapter involves training of two separate machine learning techniques to predict air temperature at the microscale throughout our study area of Vermont. Primary goals included comparison and evaluation of the two techniques to more accurately predict UHI presence and intensity. Upon training the models using our mobile dataset, high resolution mapping of air temperature was completed throughout several Vermont cities.

Model Training

Pre-processing of the mobile dataset was completed in the earlier chapters. Both machine learning models would likely have more predictive capabilities with the addition of land cover features such as bare soil or greenspace and wouldn't be subject to the distortions of collinearity that limited these land cover variables as inputs in the spatial error model (SEM). However, feature selection was limited to those used in the previous chapters along with the Vermont UTM coordinates for more direct comparison and discussion of results as an extension of the findings from the SEM.

Table 4. List of features used in predictive machine learning models.

Features	Units
Pavement Exposure	Percentage, surface area within 100m buffer
Building Exposure	Percentage, surface area within 100m buffer
Tree Cover Exposure	Percentage, surface area within 100m buffer
Elevation	Meters
Time Since Sunrise	Minutes
Daily High Temperature	Fahrenheit
Maximum Windspeed (During Sampling)	Miles per hour
Maximum Cloud Cover (across all altitudes)	Ordinal from 0-4.
UTM Northing	Meters
UTM Easting	Meters

The architecture of both machine learning techniques deployed in this work required tuning of parameters to optimize predictive accuracy and prevent overfitting. Though the two techniques have different parameter options, they were evaluated on the same metric of RMSE and coefficient of determination (R^2). An 80:20 split of the mobile data was randomly selected for training and testing subsets, respectively.

The RF models were first evaluated on the number of trees (ntree) and the number of features sampled as candidates at each split (mtry). Additionally, tree depth (max_depth), minimum number of observations required to split a node (min_split), and minimum number of observations required for a terminal node (min_n) were explored to optimize training performance and maximize accuracy.

The XGBoost framework possessed several parameters to tune as well. They included the number of boosting rounds (nrounds), the learning rate (eta), the maximum depth of each tree (max_depth), the minimum sum of instance weights across child nodes (min_child_weight), the proportion of training instances used in each tree, the number of features sampled as candidates at each tree (colsample_bytree), and the minimum loss reduction required to make a further partition on a leaf node (gamma). We conducted hyperparameter tuning using a cross-validation approach with five folds to determine the optimal combination of parameters for the training of the final model.

For both the RF and XGBoost model, each combination of parameters trained on the training subset was then used to predict air temperature on the testing subset. RMSE and R^2 were calculated using the predictions and target values for comparison to the same metrics on the corresponding training dataset as a primary indication of overfitting. Geographic mapping of predictions was observed, as were the residuals. Plotting of predicted vs actual values were also observed for patterns and the potential for overfitting. A subset of values where error was greater than 0.5°F in either direction was formed for further review. Within this subset of poorly predicted instances, summary statistics, geographic mapping, and OLS regression of residuals as a function of the features was used to identify the features or characteristics of these observations that made them more challenging to accurately predict.

To bypass the black box reputation of these machine learning models, we generated metrics and values such as feature importance and accumulated local effects plots (ALE) using the predictive outputs from the testing subset. This allowed for identification of the most impactful features to the model performance, and quantification of the effect of

different features on microenvironment-level air temperature. Upon completion of this step, comparison of both machine learning methods was conducted based on accuracy, efficiency, and findings.

Mapping

An additional component of this chapter involved using the trained RF and XGBoost models to generate high resolution heat maps of Vermont cities. While maps of transects gave point data indication along our transects at a fine scale, interpolation throughout all microenvironments at high resolution within these cities could provide value for policymakers, residents, and relevant stakeholders for the Burlington and Montpelier communities in identifying spaces with amplified heat signals (Shandas et al., 2019).

Generating grid points within the identified mesoscales first began in ArcGIS Pro. The "Create a Fishnet" tool was used to form a grid of points within the viewing window that encapsulates the city of interest at distances of 25 meters. This grid was then intersected with the city boundaries to make a more refined grid of points within the precise city limits. Each point within the grid was then buffered at 100m radii, and the buffers were then intersected separately with the ISA and tree cover layers to form polygons of pavement and tree cover exposure within 100m of each point. In line with methods from previous chapters, polygons corresponding to individual grid points by their point ID were then summed for a total area of pavement exposure and tree cover exposure for each microenvironment. These total area values were converted to a percentage for a proportion of land cover within the 100m radii for each grid point.

After importing the grid dataset into R Studio, elevation was assigned to points as done in previous chapters, and the high temperature from the warmest day for that city in 2022 was assigned to each grid point as the daily high temperature input. Further, windspeed and cloud cover were both set to zero to assign ideal UHI conditions. The time was set to 3pm to map microenvironment heat during mid-day warming, and the corresponding time of sunrise from that day in 2022 for that city was used to calculate the time since sunrise term, which was uniformly assigned to all points so that maps depicted a cross-section in time of a hot day in these communities. These steps concluded the preprocessing required to predict air temperature with the previously trained RF and XGBoost models.

Grid points were then treated as inputs for the trained RF and XGBoost models without any sort of validation or target values to compare to their predicted temperatures. Semivariogram models were generated with the predicted temperatures and coordinates to obtain the optimal model type, partial sill, range value, and nugget value. Predicted temperature at each grid point coordinate was imported back into ArcGIS Pro, and the 'Geostatistical Wizard Tool' was used to conduct ordinary kriging with the identified parameters from the semivariogram to interpolate the air temperature in the space between grid points. Completion of this kriging allowed for the generation of a raster file of the region which was then adjusted to best visualize the high-resolution differences in air temperature from one microenvironment to the next.

Results

Model Performance

Random Forest

Modeling of air temperature through use of RF shows strong model fit when trained with our mobile sampling data. **Table 5** shows that through the training and validation of RF models, performance varied little across all combination of parameters and demonstrated high levels of accuracy and strong accounting of variability. Increasing the complexity of the decision tree structure increased training time measurably, and analysis of residuals from validation and comparison of metrics from training to validation didn't indicate potential for overfitting **(Table 5, Figure 17, Figure 18**). Therefore, additional parameters such as maximum tree depth and minimum observations at node for splitting were left as the defaults defined by the "randomForest" package for the optimal model and exploration of other parameter combinations.

Table 5. Performance of RF model across different parameters. Bolded values indicate parameters of the selected optimal model.

Parameters		Training		Validation	
Sampled Features	Number of Trees	RMSE	R^2	RMSE	R^2
5	100	0.359	99.42	0.354	99.43
	150	0.358	99.42	0.352	99.44
	200	**0.356**	**99.43**	**0.352**	**99.62**
	250	0.358	99.42	0.348	99.46
10	100	0.371	99.38	0.359	99.42
	150	0.369	99.38	0.358	99.43
	200	0.368	99.39	0.356	99.43
	250	0.367	99.39	0.356	99.43

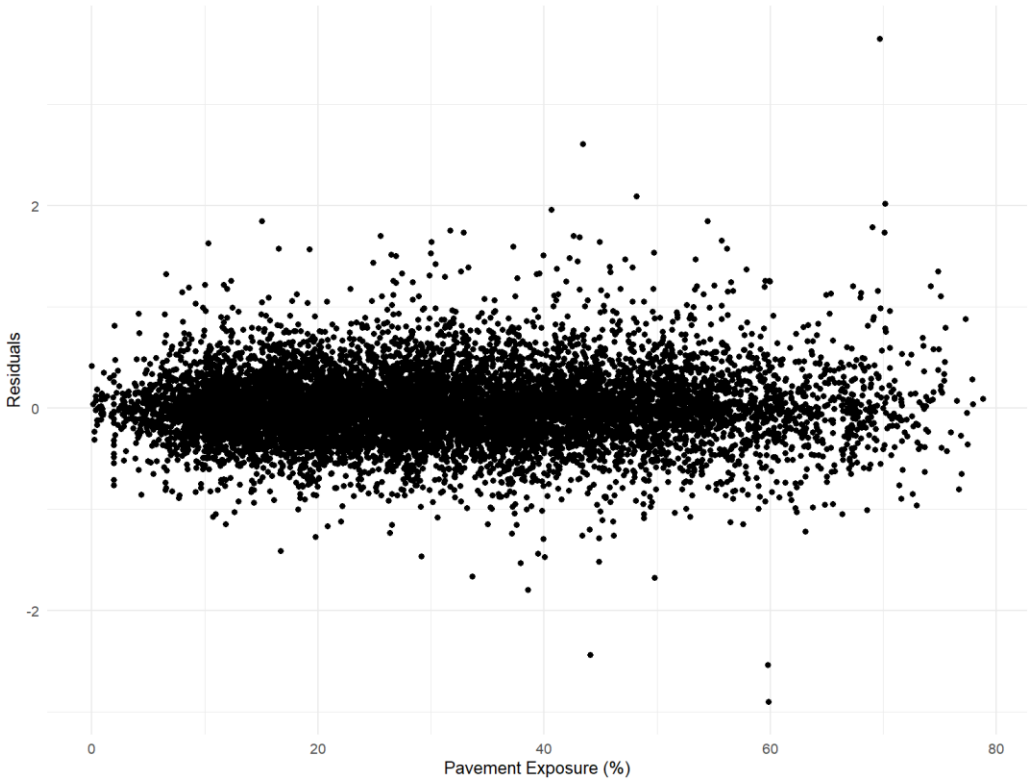

Figure 17. Predictor versus residuals of validation set.

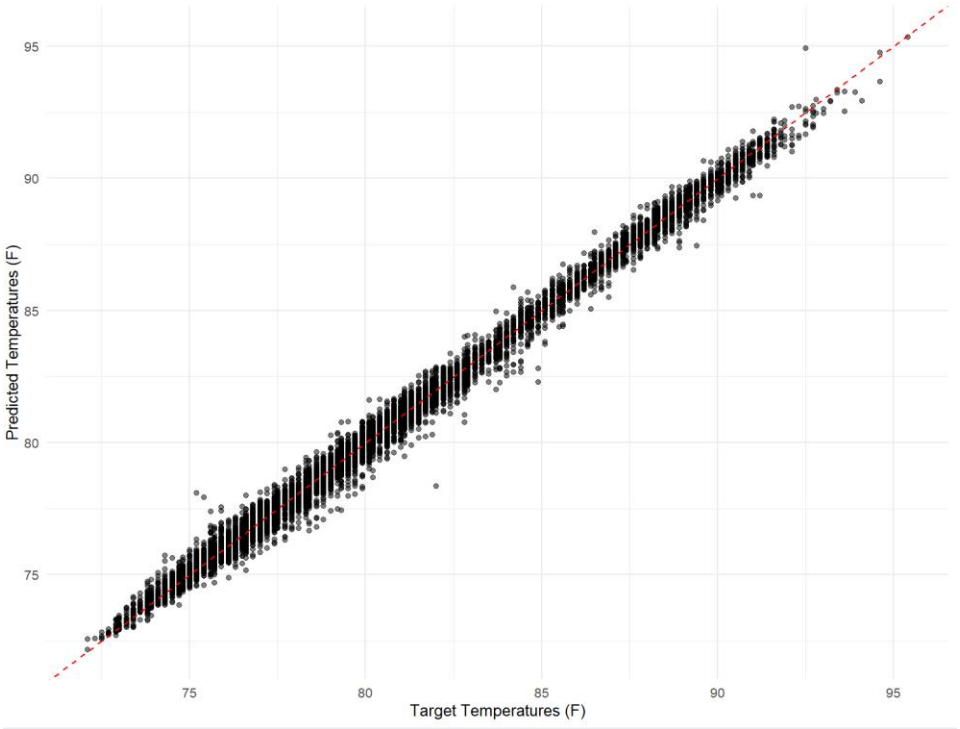

Figure 18. Target versus predicted air temperature values in validation set.

Feature importance was only explored in the optimal RF model (**Figure 19**). Traditional feature characteristics such as increase in node purity show different levels of importance in predicting air temperature with accuracy in comparison to a feature's role in increasing MSE. The daily high temperature is of more value to the model's predictive capability in terms of node purity change; it limits the possible predictive range to a smaller interval around that value in comparison to the global range of temperatures measured across the entire summer sampling campaign. With the assistance of the other weather terms such as maximum cloud cover and maximum wind speed, the model can identify the transect that an observation belongs to with confidence, and further reduce the temperature interval with higher confidence. We also leverage the spatiotemporal details of the dataset to predict temperature of values nearby in space in time through the features for time since sunrise and UTM coordinates. Elevation participates in this manner, but also informs predictions by detailing the empirical relationship that air temperature develops with changing elevation from a thermodynamic perspective across the dataset. These features all surpass our land cover exposure features by a measurable gap in node purity change, in which pavement leads tree cover and buildings.

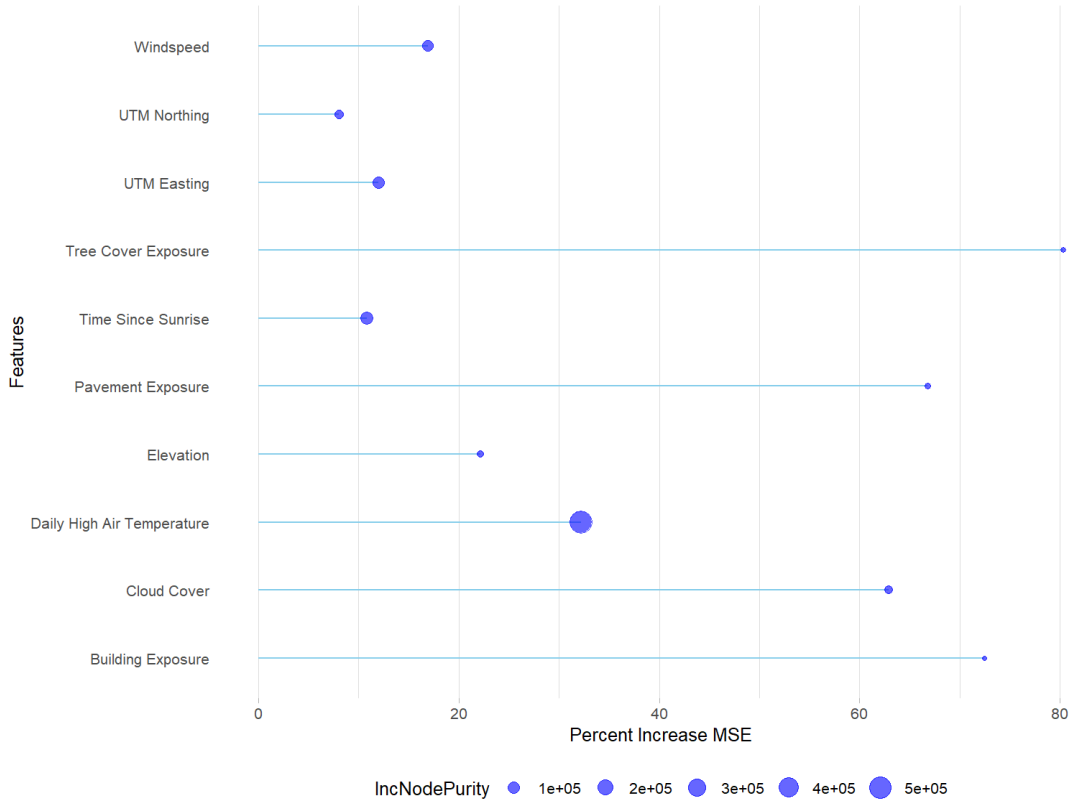

Figure 19. Feature importance among features from the optimal RF model.

The combination of continuous features and categorical features with more than two levels can bias the node purity metric by producing more unique splits in the model architecture, while the increase in MSE quantifies the impact of a feature's absence. Though both metrics are presented in **Figure 19**, the increase in MSE is the preferred metric in quantifying and comparison of feature influence. This is a standardized metric by way of its presentation as a percent change, and we see that feature importance is somewhat inverted when considering percent increase in MSE instead of increase in node purity. Tree cover is shown to be of highest importance, closely followed by pavement, building coverage, and maximum cloud cover. Elevation leads the spatiotemporal features, followed by windspeed and spatial coordinates.

The optimal RF model accounts for over 99% of the variability and average error values as described by RMSE stayed within 0.4°F in either direction of the target values **(Table 5)**. Distribution of residuals showed that more than 86% of predictions missed their target value within a range of 0.5°F in either direction **(Figure 20).** The Environmental Protection Agency indicates a range of temperature among daytime mesoscale UHI's spanning as much as 0.7°F (EPA, 2023a). This informs our arbitrary cutoff of +-0.5°F as a threshold in which larger error from our model is providing unacceptable predictions, and further exploration was conducted on a subset of the validation predictions with error greater than |0.5|.

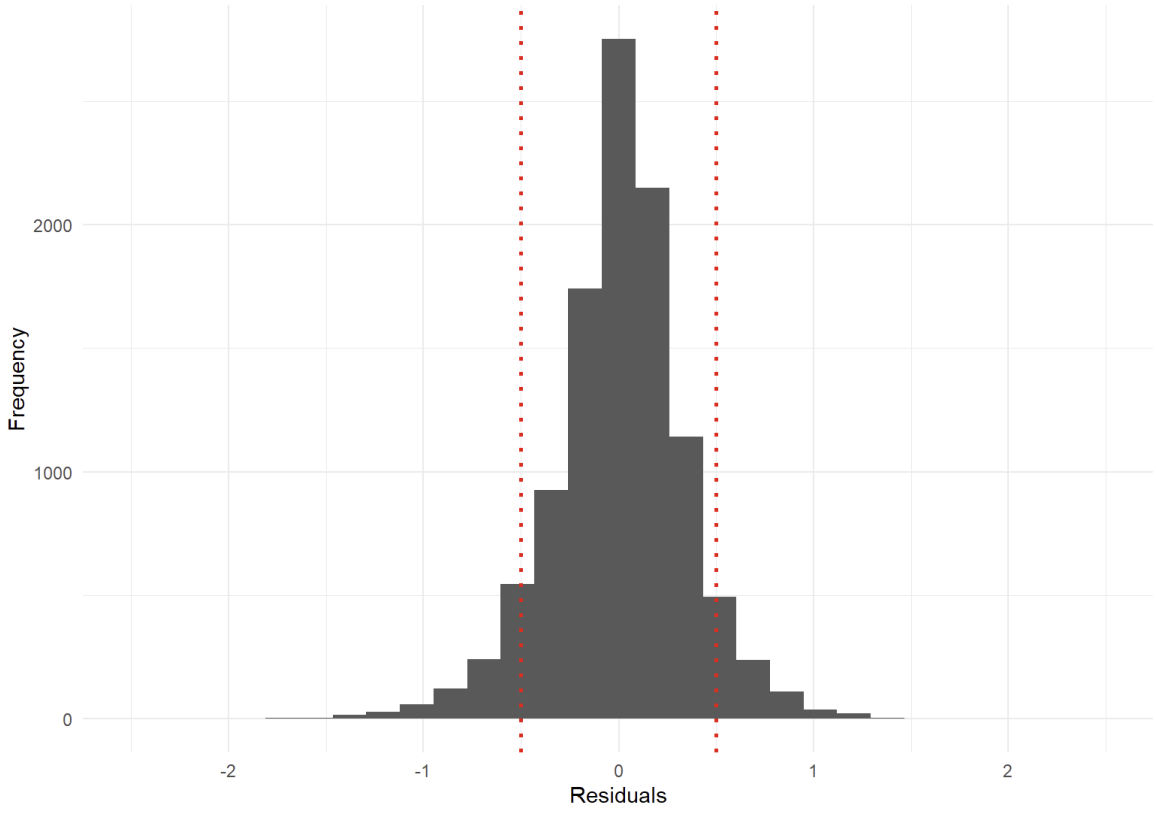

Figure 20. Residuals of validation set for optimal RF model.

When comparing validation data above and below our error threshold, summary statistics and distributions of the land cover and elevation features do not indicate a specific feature of the microenvironment or terrain that could be causal to the poor predictions **(Appendix N-Appendix Q).** Further, average residual values aren't greater than |0.022| for points from any single transect, nor does data from any single transect demonstrate an unbalanced proportion of predictions with error beyond our threshold.

An additional RF model was developed using the subset of poorly predicted temperatures from the validation data with the residuals serving as the output and all of the previous features continuing to serve as inputs. The model was generated with the same parameters as before and explains 11% of the variability with a RMSE of 0.54^{o}F, further supporting the conclusion that none of the features are particularly effective in explaining the excessive residuals from our predictive model. This suggests that improved or additional features would be needed to capture this variability.

XGBoost

Training and validation of the optimal XGBoost model demonstrated comparable accuracy and performance to the optimal RF model. Training speed was notably improved from the RF tuning process, which encouraged a more expansive hyperparameter tuning. A total of 3645 combinations were trained through a grid search combined with 5-fold cross-validation, of which the optimal model was selected by the ideal RMSE (**Figure 21**).

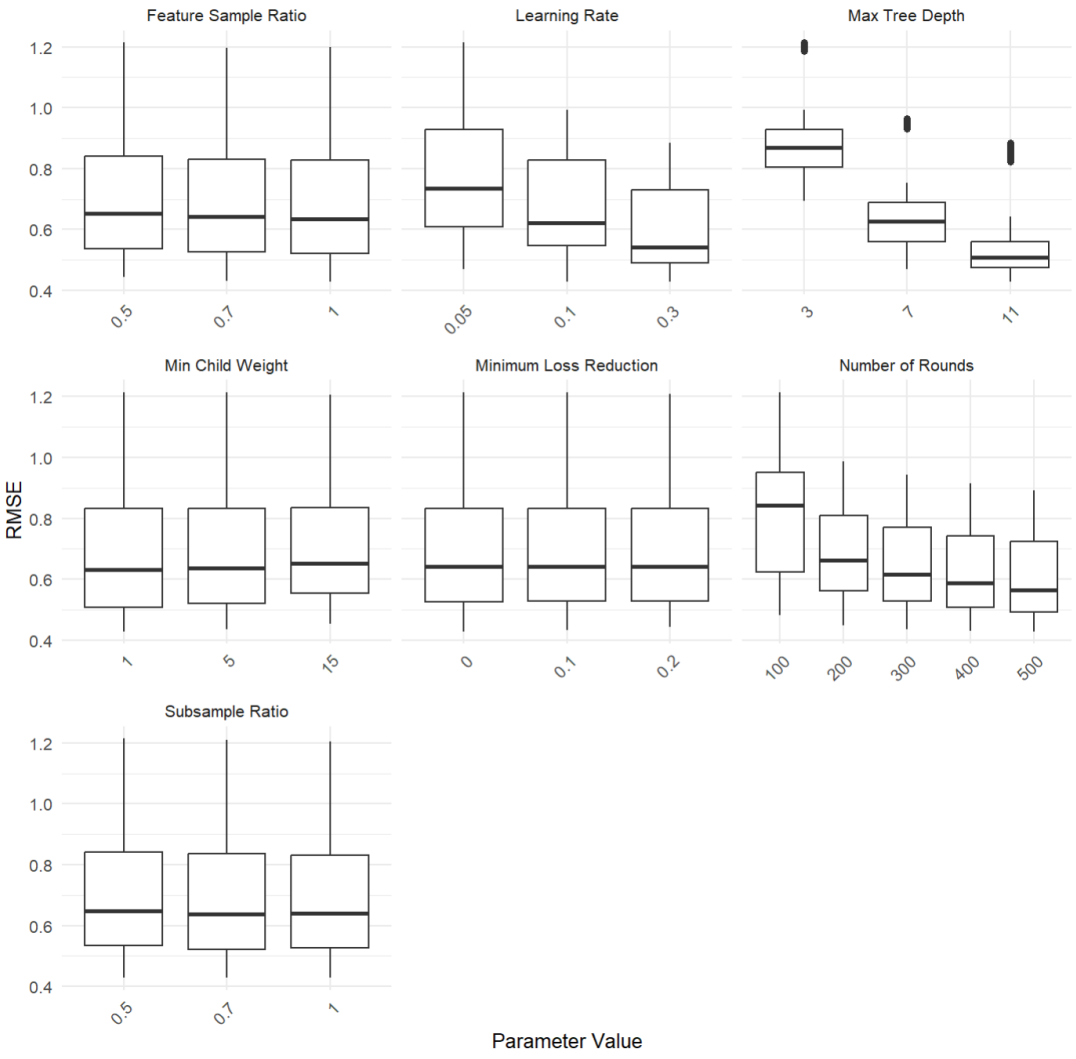

Figure 21. Distribution of RMSE across XGBoost hyperparameter tuning.

The optimal parameters involved a subsampling proportion of 0.7, 500 decision trees, a minimum loss reduction of zero, a minimum child weight of one, a maximum tree depth of 11, a learning rate of 0.3, and sampling the entirety of the available features. This resulted in a RMSE of 0.427 and a coefficient of determination (R^2) of 99.17%, demonstrating nearly 0.07 increase in error and 0.26 decrease in explanation of variability from the optimal RF model **(Table 5).** After predicting on the validation dataset with this model, RMSE decreases to 0.389 and R^2 increases to 99.32%, suggesting a robust and generalizing performance. Therefore, we maintained our selection of the previously listed parameters as the architecture of our optimal XGBoost model. Further, comparison of actual versus predicted values across both training and testing along with the RMSE and R^2 supported confirmation of this model (**Figure 22).**

Figure 22. Side by side comparison of actual versus predicted plots from training and testing of optimal XGBoost model.

Further examination of residuals in comparison to our predictor of interest demonstrates the random behavior preferred to trust the predictive capabilities of the model, however we do see slightly bulging of periphery residuals towards the center of the pavement exposure range and some predictions that were dramatically miscalculated towards observations within the 60-70% pavement exposure range **(Figure 23).** These patterns are reflected in the RF model as well **(Figure 17).**

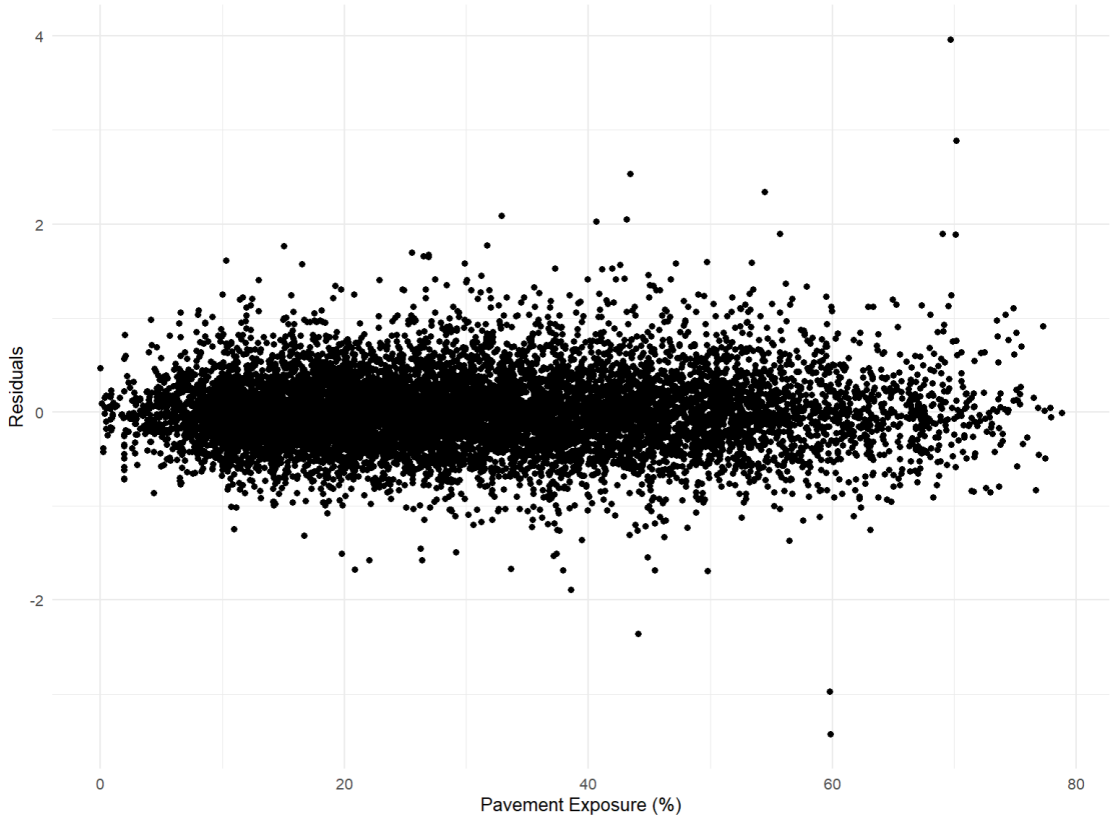

Figure 23. Pavement exposure feature values versus residuals from validation set of the optimal XGBoost model.

Due to the difference in model architecture to other tree-based models such as RF, feature importance for XGBoost models uses different metrics. This framework iteratively corrects errors from previous steps, and metrics such as “Gain” are crucial to the gradient boosting process and a value indication of a feature’s predictive capability. Before the model makes a split on a feature, it calculates how much that split will contribute to reducing the MSE and then averages these quantities across all splits. That is quantified in the Gain metric shown in **Figure 24**, therefore a higher gain indicates a more important feature to the model’s predictive capabilities. As before, the daily high temperature and spatiotemporal features such as the UTM coordinates and time since sunrise likely serve as proxies to a sort of transect ID in which the range of temperatures measured were

between a few degrees. The model's ability to identify this vastly reduces error. Due to the substantial difference in Gain between the daily high temperature feature and the nine remaining features, an enhanced image of the remaining features is provided in **Figure 24** without depiction of their Cover values to show a more detailed difference in gain at these lower magnitudes. Our mobile sampling data only captures a few different values for maximum windspeed because of our interest in capturing optimal UHI conditions. The empirical nature of our model and the somewhat qualitative contribution of our wind data likely utilizes windspeed as an additional indication of the transect that a prediction belongs to rather than leveraging the urban climate contribution of windspeed within our model. Beyond this, we see pavement exposure slightly leading our other land cover exposure features in Gain.

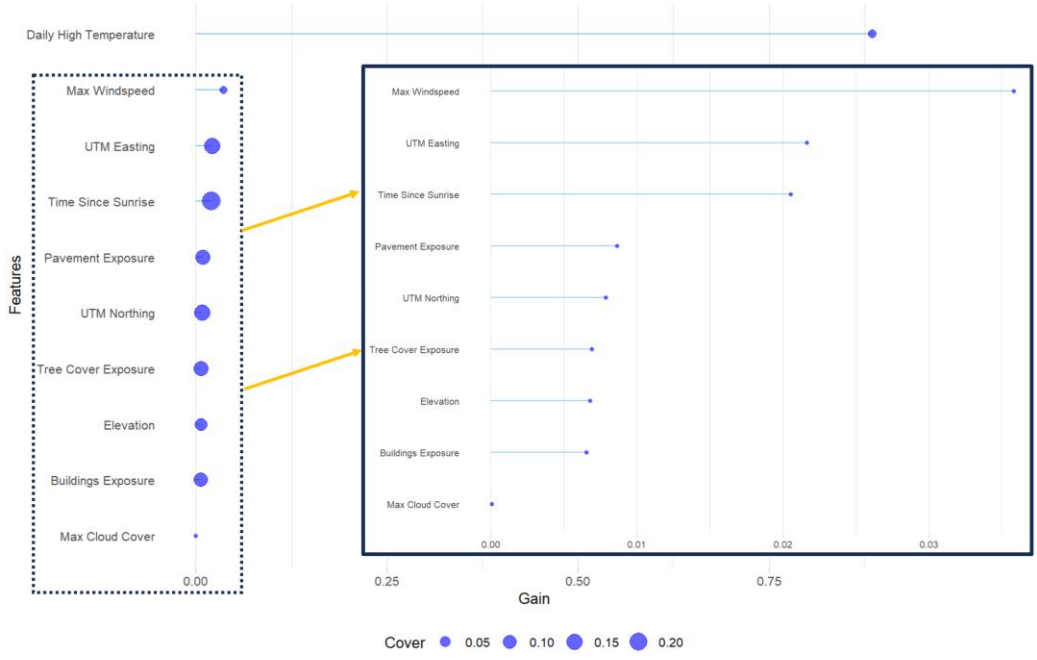

Figure 24. Feature importance plot for features from the optimal XGBoost model.

The Cover metric provides a different yet valuable insight in quantifying a feature's importance. When a feature is considered for a split in the tree-building process, the

model considers the sum of second-order gradients of subsampled training data that are sorted according to that feature's value. When summed across all trees, we refer to it as the "Cover". This Cover value is pertinent because it informs the model on whether to make a split by considering the variance of the loss reduction. Returning to feature importance, a high Cover value for a feature indicates that commonly, the feature has been influential in the partitioning of training data and therefore reducing variance. **Figure 24** shows that both land cover exposure and spatiotemporal features demonstrate high cover values, while the leader in Gain "Daily High Temperature" demonstrates minimal cover value. This means that while land cover might contribute much less to improvement in the model's predictive performance, it is essential within the decision-making process of the model training. Though these two metrics aren't directly comparable to those used for feature importance in the RF model, we see similarities in rankings of features between Gain and increase in node purity, and somewhat between increase in MSE and Cover (**Figure 19, Figure 24**).

Exploration of error within the predictions closely reflects that found from the RF model (**Appendix W-Appendix** Y). Just under 83% of the predictions' residuals fall within our threshold of 0.5°F in either direction of the target value (**Figure 25**). Summary statistics and distributions of the features showed little difference when grouped on either side of our acceptable error threshold, as found in the RF model (**Appendix N-Appendix** V). This supports the conclusion found in the RF model that additional and improved features would improve the extreme error found in predictions from both models.

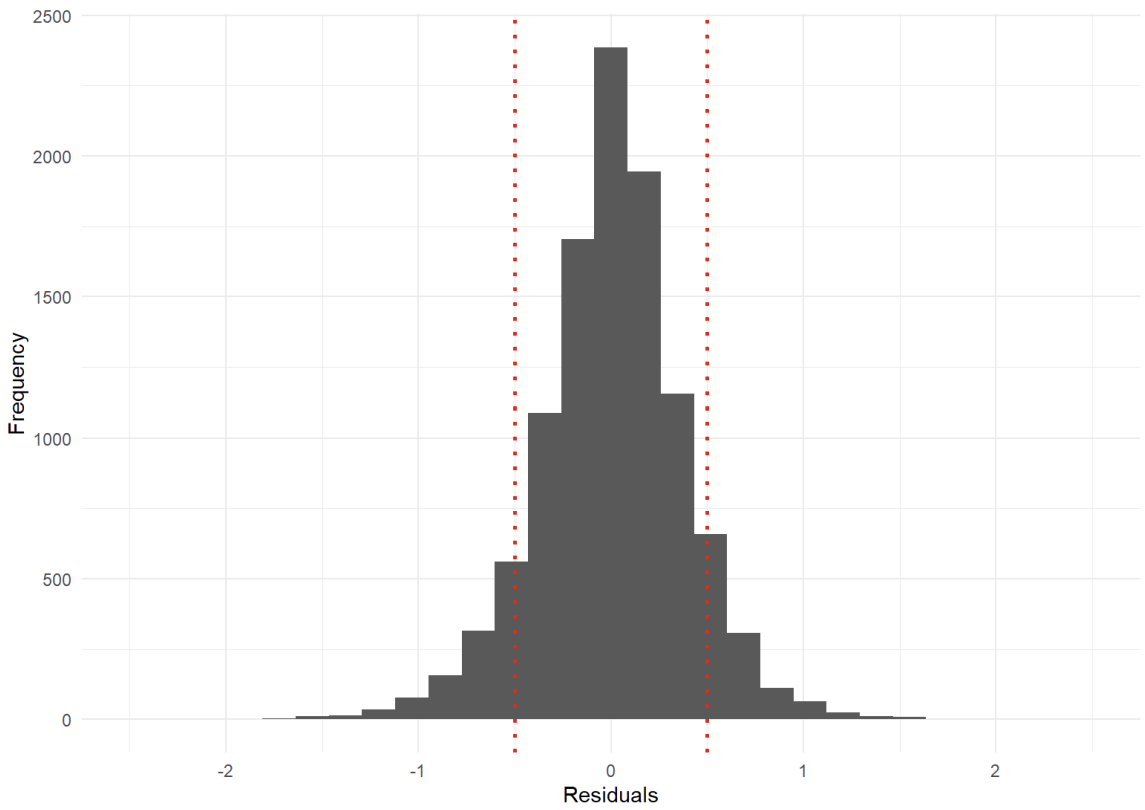

Figure 25. Distribution of residuals from predictions made on the validation data by the optimal XGBoost model.

Effect of Pavement Exposure

The accumulated local effect (ALE) plot is a technique among the growing number of approaches to reveal the contributions and effects behind features in such algorithms that were previously described as *black boxes* (Apley & Zhu, 2020). When generated for the pavement exposure feature across both the RF and XGBoost models, we identify trends that weren't captured in the previous chapter through the SEM. Across each model, the plots present a warming effect only after the pavement exposure approaches 25%. Further, the effect is not perfectly linear. The warming effect peaks and plateaus around 60% pavement exposure with a 0.25ºF increase in temperature, and interpretation around this point has less confidence with the reduced sample size. We interpret this point on the

plot to claim that an increase from the median pavement exposure of roughly 29% to 60% is associated with an average increase in the model's predicted air temperature by nearly 0.25ºF. The ALE plot from the XGBoost model confirms a similar pattern to that found in the RF model with a slightly higher maximum effect found in the XGBoost model (**Figure 26-Figure** 27). ALE plots for other land cover features are available in (**Appendix CC-Appendix** CC).

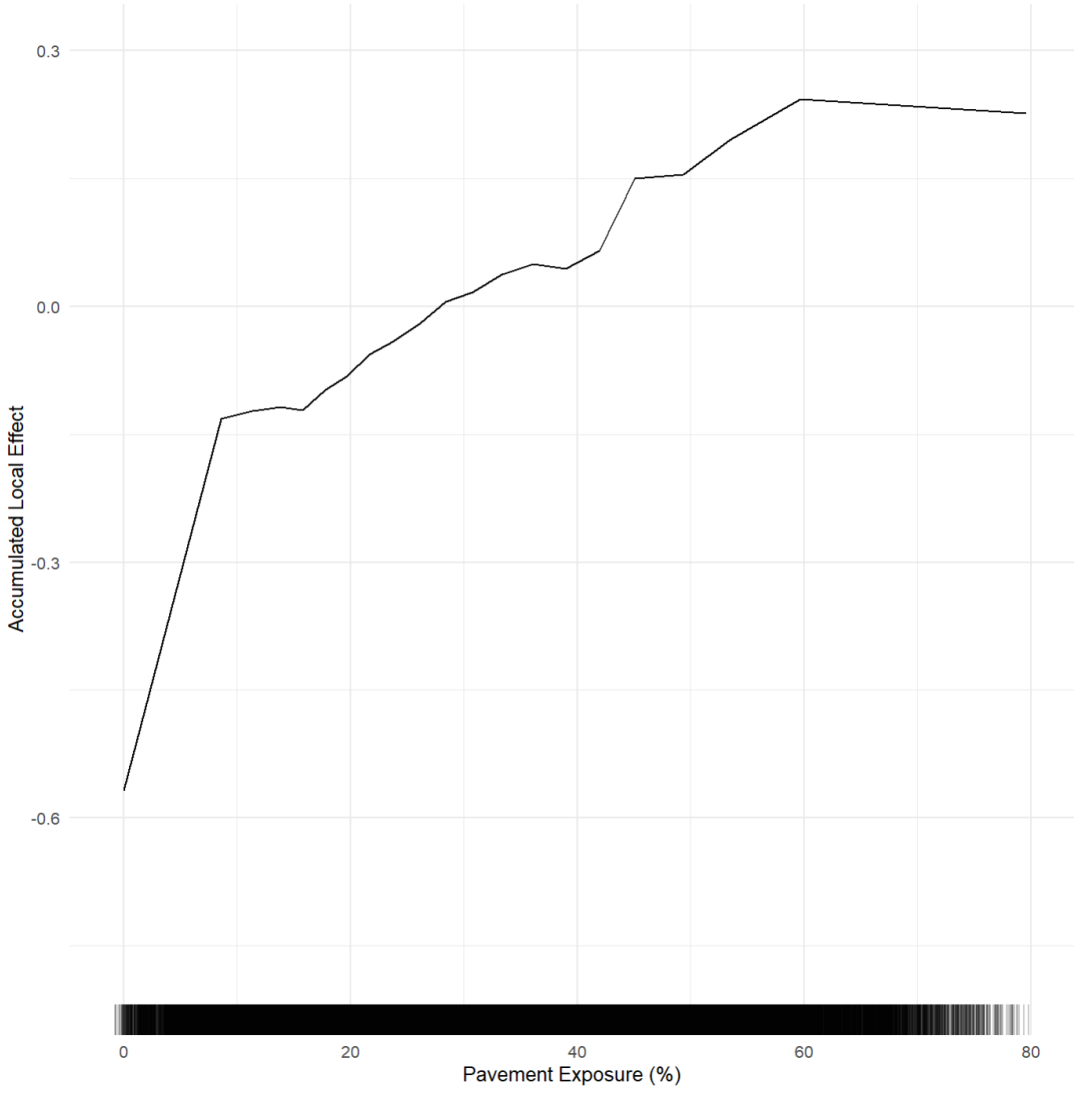

Figure 26. ALE plot of pavement exposure's effect on air temperature for optimal RF model.

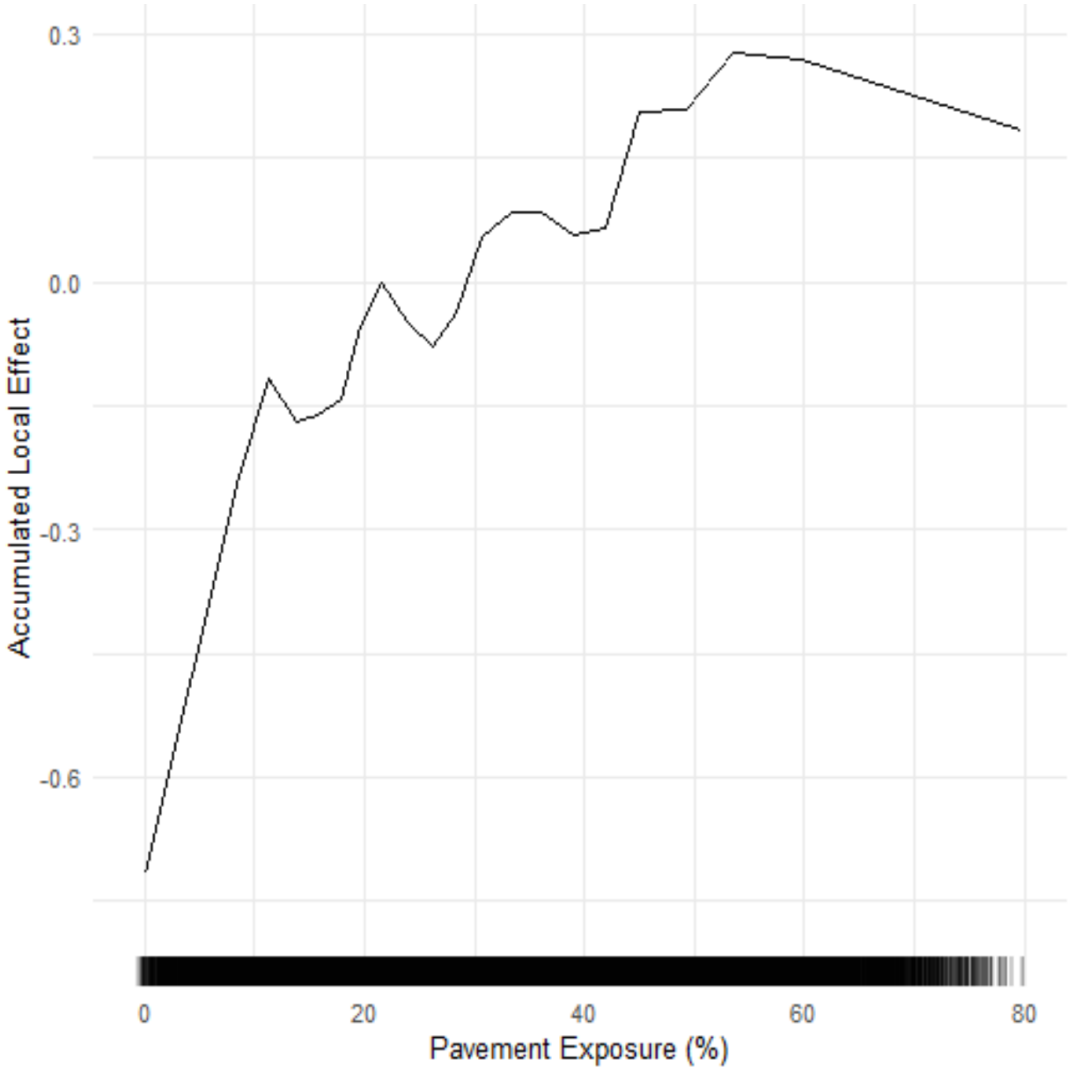

Figure 27. ALE plot of pavement exposure's effect on air temperature for the optimal XGBoost model.

Mapping

Further evaluation of the two machine learning approaches included generation of high-resolution maps at the city-wide scale of Burlington and Montpelier, both urban mesoscales within Vermont (**Figure 28-Figure** 31). Both models demonstrated similar patterns of warming throughout these cities and have potential to inform urban design and transportation infrastructure at the local level.

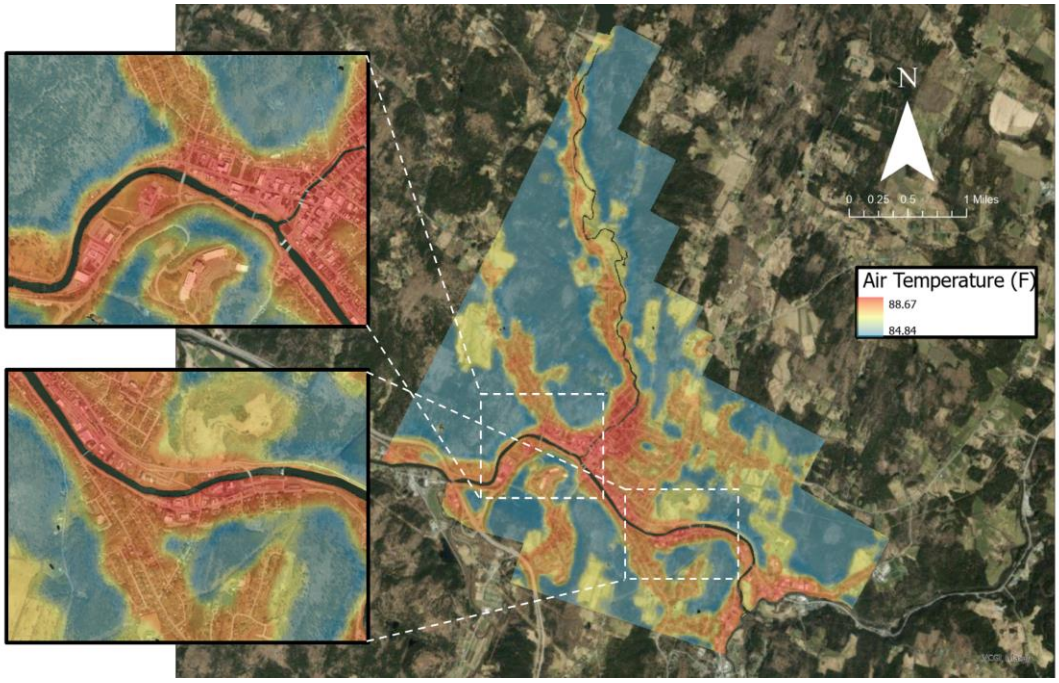

Figure 28. High resolution heat map of Montpelier, VT. Map was generated using RF regression model.

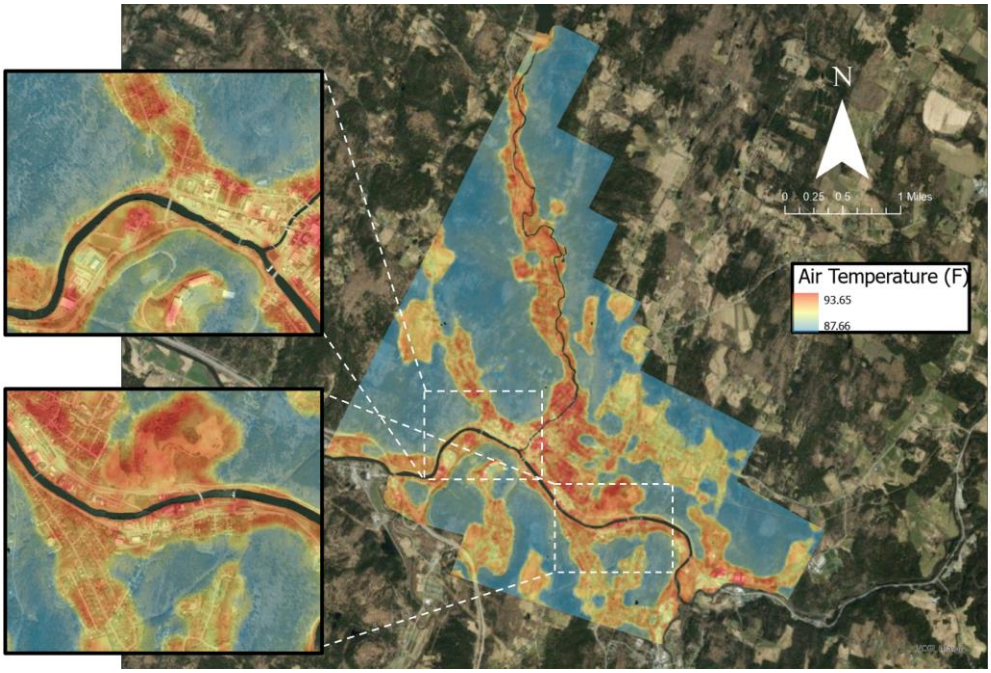

Figure 29. High resolution heat map of Montpelier, VT. Map was generated using XGBoost regression model.

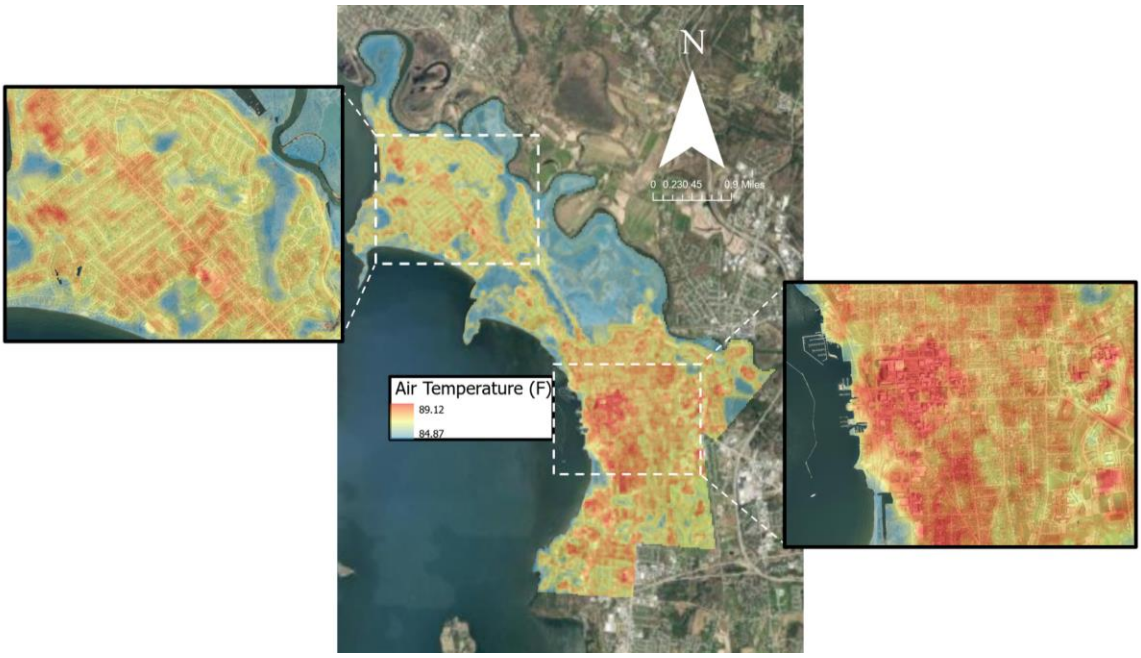

Figure 30. High resolution map of Burlington, VT. Map was generated using RF regression model.

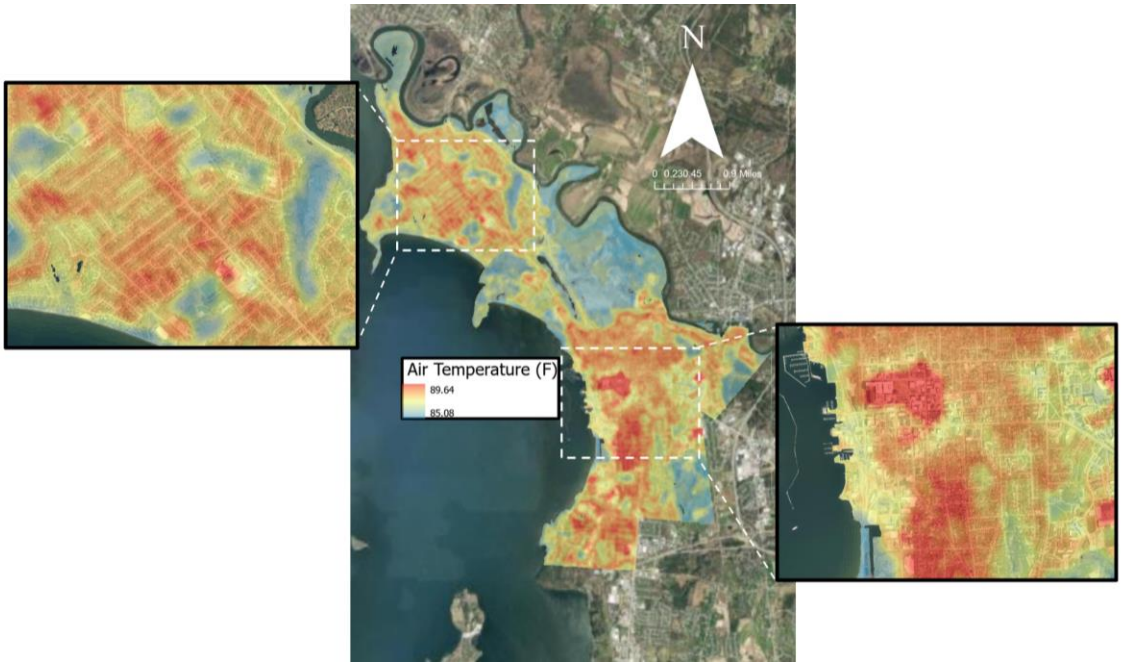

Figure 31. High resolution map of Burlington, VT. Map was generated using XGBoost regression model.

Both models were trained on the entire mobile sampling dataset with the optimal parameters previously identified for the respective model. Predicted air temperature values were generated from the trained models using the same feature inputs from training.

While there is no ground-truth verification procedure, indications of UHI signals in regions of lower vegetation and denser built space are present across all four maps. Both maps generated from RF possess a lower temperature range and tend to show larger island effects, while the XGBoost model demonstrates smaller and warmer microenvironments. This is either the manifestation of previously mentioned overfitting in the XGBoost model or perhaps higher precision. The XGBoost model also appears to predict warmer temperatures in areas that lack any of the three included land cover features.

Conclusion

This chapter effectively builds upon the frameworks and findings of the previous two chapters to create further enhanced tools for engineers, planners, and policymakers when balancing land use with heat exposure. The primary research goal involved evaluation of the two machine learning techniques in a predictive application, of which we found that the XGBoost model compromises a small amount of accuracy for a large gain in computational efficiency that could be valuable for larger datasets. Both models successfully map microenvironment heat signals throughout the entirety of two Vermont cities during optimal conditions for a mid-day UHI. Utilization of these non-parametric approaches also provided a quantification of the effect of a unit area of pavement on corresponding air temperature, as pursued in the first chapter through linear regression.

As the ALE plots demonstrated, this effect was nonlinear and therefore quantified in higher detail and accuracy through machine learning techniques.

Due to the sequential nature of the work in this dissertation, limitations of this chapter are predominantly described in previous chapters. Our models maintained the same predictors as used in the previous SEM models for features, but future work should include additional land cover features to better predict air temperature in local environments with bare soil, green space, or blue space. Further contributions to policymaking and planning could be made by generation of maps for evening UHI conditions and other cities within the study area, as well as sensitivity of this approach for when predictions within maps move further from the location of the ten original cities comprising the training data.

EV Incentive Policy Component

Chapter 4—The Efficacy and Efficiency of Electric Vehicle Purchase Incentive Policies

The primary research objectives of this chapter involve evaluating the efficacy and efficiency of the EV financial incentive policies available to Vermont consumers. We design and distribute a survey to vehicle purchasers to quantify the influence of the available incentives in their decision to purchase either an EV or an ICE vehicle and identify specifically who was most influenced by the available policies.

Introduction

EV Adoption Policy in the United States

The first federal incentive seen within the United States for EV purchases came in the form of the Energy Policy Act of 2005, which provided a framework for direct tax credits for hybrid electric vehicle (HEV) consumers. This initiative, totaling to $1.4 billion in expenses, proved to be effective as several American car manufacturers reached the sales threshold that triggered a phase-out of the credits by 2010 (Jenn et al., 2013). The Energy Improvement and Extension Act of 2008 then incentivized plug-in hybrid electric vehicles (PHEVs), with sales reportedly increasing by up to 32.5% due to the policy (Tal & Nicholas, 2016). The American Recovery and Reinvestment Act of 2009 introduced a federal credit of up to $7,500, which also included a phase-out mechanism once a manufacturer sold 200,000 vehicles. Tesla Motors reached this limit in 2018, followed by others such as General Motors. The Inflation Reduction Act of 2022 extended the $7,500 tax credit and introduced a $4,000 credit for used electric vehicles, along with a modification to the phase-out mechanism which allows some previously ineligible purchases to qualify for the tax credit.

At the time of this research, most U.S. states offer financial incentives for EV purchases or charging infrastructure. In Vermont, incentives include up to $4,000 for new EV purchases based on household income, with additional financial incentives from utility companies. These measures support Vermont's National Electric Vehicle Infrastructure (NEVI) Plan, aiming for 126,000 registered EVs by 2030 (State of Vermont National Electric Vehicle Infrastructure Plan, 2022).

Efficacy and Efficiency

Research assessing the impact of financial incentives on electric vehicle (EV) adoption has yielded varying conclusions. Diamond's early study used vehicle registration data against a backdrop of policy shifts to suggest that gasoline prices had a more substantial influence on EV adoption than incentives (2009). Subsequent findings, however, indicate incentives may play a more significant role. An agent-based model, utilizing survey and environmental data from San Francisco, indicated that withdrawing incentives could negatively impact sales, although the unique characteristics of the San Francisco area may inherently support EV uptake in comparison to regions such as Vermont (Adepetu et al., 2016).

Additionally, survey data from 14,000 California EV purchasers informed the finding that the influence of incentives has grown by 20% from 2010 to 2017 (Jenn et al., 2020). To further quantify a positive effect, an increase of $1000 in incentive value for a vehicle model has shown as much as an 11% increase in sales at the state level (Wee et al., 2018). Global findings of efficacy are also present in research conducted on markets in Canada,

China, and much of Europe (Azarafshar & Vermeulen, 2020; X. Huang & Ge, 2019; Lieven, 2015).

Concerns regarding the efficiency of EV incentive policies have emerged, particularly in terms of public awareness and the clarity of eligibility requirements (Krause et al., 2013). Research based on vehicle registration data showed that 62.1% of Atlanta households weren't eligible for the full tax credit, with larger families and those with lower incomes being less likely to qualify (H. Liu et al., 2022). Sheldon's (2022) review of the literature concluded the existence of a free-rider problem: PHEV incentives cost taxpayers $30,000 per vehicle sold, and that for each consumer who found the incentive to be influential in their purchase, five others who received the incentive would have made the purchase anyhow.

Methodologically, research in this area often relies on vehicle registration data to observe purchasing trends or on surveys of EV purchasers to inform simulations and other quantitative models (R. R. Kumar & Alok, 2020). These models typically include logit regression analyses considering household demographics, economic conditions at the time of surveying, vehicle preferences, and other variables (Jenn et al., 2020; Jia & Chen, 2021; Springel, 2021). Some studies have also employed psychological frameworks like the Theory of Planned Behavior (TPB) and the Transtheoretical Model (TTM) to explore the decision-making processes in vehicle purchasing (X. Huang & Ge, 2019; Langbroek et al., 2016).

Our research aims to enhance the body of knowledge on the effectiveness and efficiency of financial incentives for vehicle purchases, with a novel approach to survey methodology. We administer surveys at the point of sale in dealerships, which is a method not extensively used in prior studies (S. Wang et al., 2017). Further, we include all purchases of vehicles in Vermont and stratify by EV and ICE types to compare the level of purchasing induced by financial incentives and other influences between consumer groups, of which we have not seen in the literature. Our study area of Vermont allows us to investigate challenges such as range anxiety and the effects of cold weather on EV performance as confounders to the value of incentive policies to consumers. These elements allow us to examine barriers within a demographic profile and climatic conditions that are often underrepresented in research predominantly focused on warmer, more densely populated metropolitan areas.

Our survey tool was crafted to assess the effectiveness and efficiency of federal and state Electric Vehicle (EV) purchase incentives. 'Effectiveness' is gauged by the capacity of these incentives to stimulate purchases that would not have occurred otherwise, while 'efficiency' refers to the cost-effectiveness of these incentives in encouraging such purchases.

Methods

Survey Design

Our survey, distributed via an online questionnaire on the Qualtrics platform, targeted individuals who had recently purchased a vehicle from a Vermont dealership. The landing page provided a concise overview of what participation entailed, including an invitation to join a raffle for one of ten $100 cash cards in exchange for their participation.

Prospective participants could access more detailed information about the study and confidentiality details through an additional link available on the landing page. Consent was implied when they proceeded to the following page.

The initial part of the questionnaire focused on validating the participant as part of our target demographic by inquiring about the specifics of their recently purchased vehicle. We collected data on the vehicle's make, model, and year, as well as its type—battery electric vehicle (BEV), plug-in hybrid electric vehicle (PHEV), hybrid electric vehicle (HEV), or an internal combustion engine (ICE) vehicle. This distinction was critical to our analysis, acknowledging that incentives may vary in effectiveness across different vehicle types (Narassimhan & Johnson, 2018).

Next, the questionnaire identified factors beyond federal and state incentives that could influence vehicle purchasing decisions. These factors were grouped into three categories: Environmental, Performance, and Household factors, each potentially overlapping in general influence (**Figure 32**). Participants rated the extent of each factor's influence on their purchase decision on a Likert scale from No Influence to Strong Influence. Some were also framed in the context of ranking “How Important” a factor was in their purchase and given similar Likert scale response options.

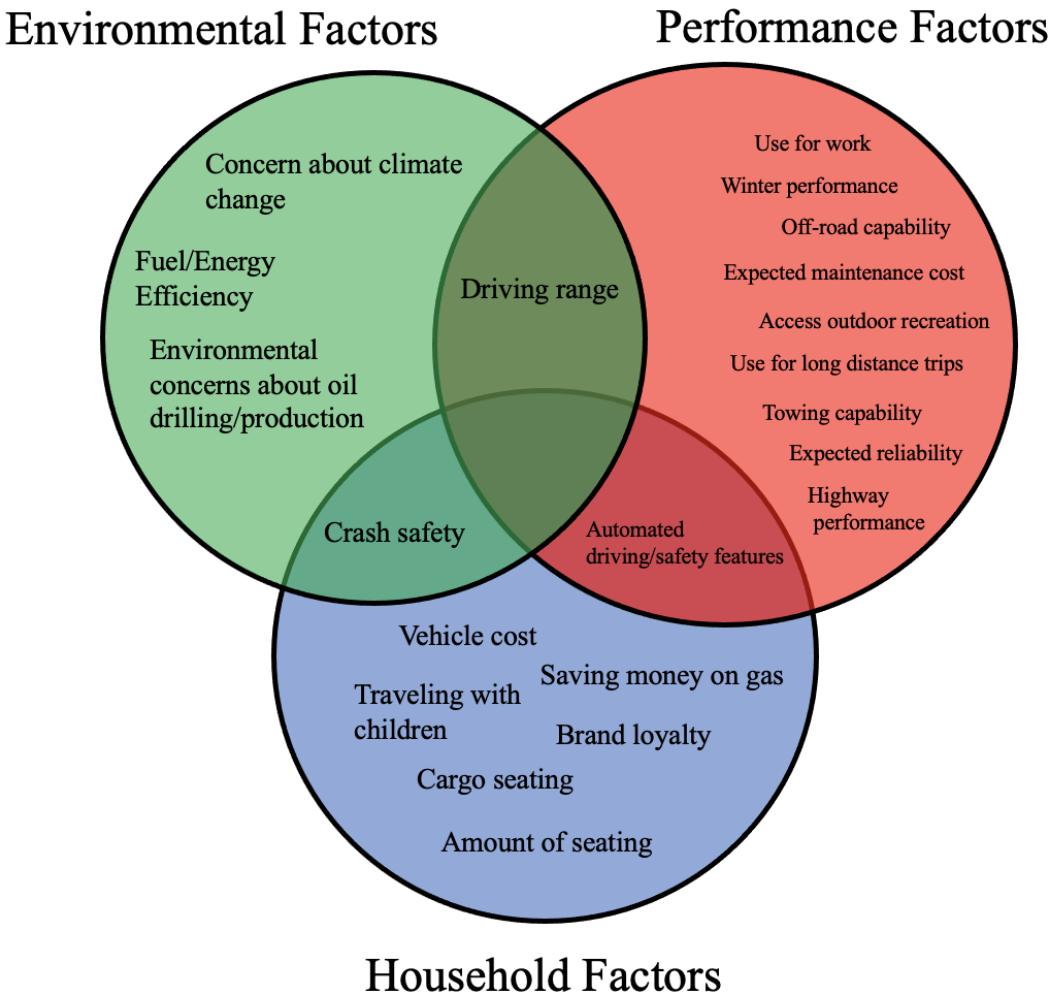

Figure 32: Categorization of purchase influences.

Participants were then branched to different pathways of questions depending on whether they purchased an electric vehicle (EV) or an internal combustion engine (ICE) vehicle. Initially, they responded to questions tailored to the specific influences related to either EV or ICE vehicle ownership. Next, they were asked about the cost of their vehicle and the perceived cost difference had they chosen the opposing fuel/energy type. For instance, BEV buyers were asked to estimate the cost difference with a comparable ICE

vehicle. This section concluded by assessing the participants' awareness and perceived impact of both federal and state EV purchase incentives on their decision-making process.

The final part of the survey collected comprehensive household and demographic information, with identical questions posed to all respondents. This allowed us to compile data on the number of EVs and ICE vehicles in each household, as well as the participant's age, gender, race, ethnicity, education level, zip code, and household income. We concluded by thanking them for their participation and offered an opportunity to enter the raffle via a separate link, ensuring the anonymity of their survey responses.

Recruitment

In addition to offering a raffle incentive, we attribute a significant portion of our substantive contribution to the existing body of knowledge to our direct recruitment strategy. We formed a partnership with the Vermont Vehicle and Automobile Distributors Association (VADA) to distribute our survey across a network of vehicle dealerships throughout Vermont **(Figure 33**).

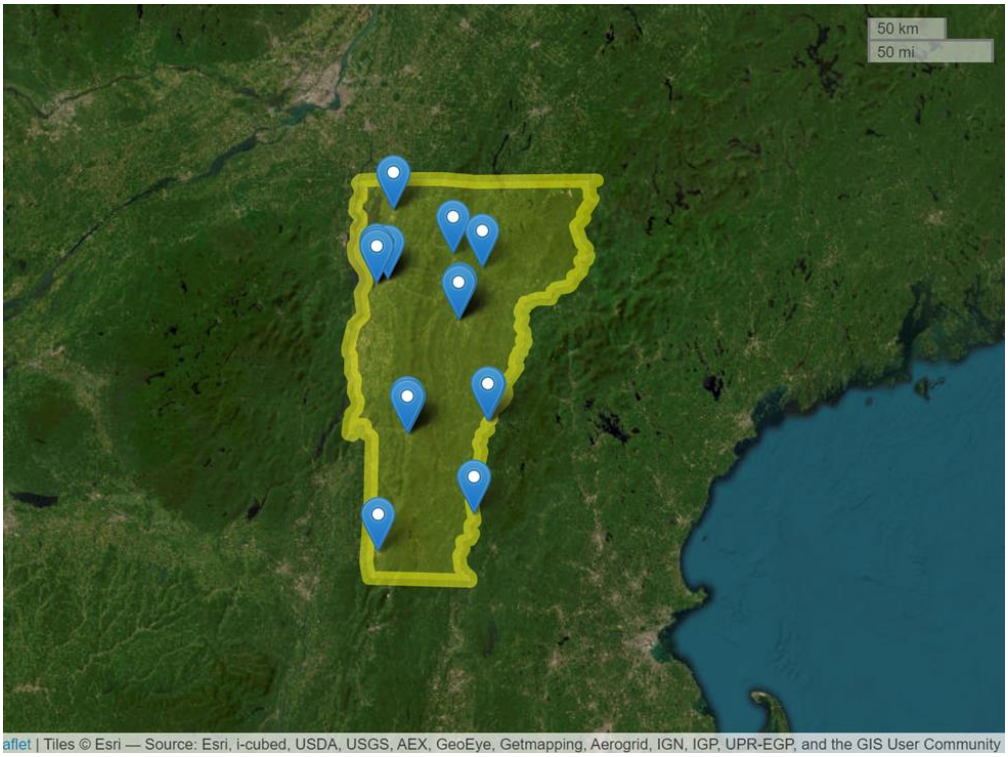

Figure 33. Network of participating Vermont automobile dealerships in survey recruitment.

At the point of sale, dealers provided customers with a flyer containing a QR code for immediate access to the survey, along with a website link for those who preferred to participate later. In addition, the survey link was included in follow-up emails from dealers to customers who had made purchases in the six months preceding the email campaign. A Vermont VADA representative contributed to the survey design, ensuring the language was appropriate—not hindering the dealers' sales processes while maintaining the survey's integrity for our research aims. We believe this targeted recruitment approach mitigates recall bias and other distortions commonly encountered in revealed preference methodologies.

Analysis

After gathering the survey data, the initial step involved an exploration of the dataset through summary statistics. Distribution of responses were visualized across the entire dataset and also compared between EV and ICE purchasers. The next step before model building was to handle the missing responses. Participants needed to complete at least 70% of the survey to be included in the dataset. The remaining missing values were imputed for all variables of interest using random forest imputation through the "missForest" package in R. Variables of interest were removed before the imputation process if they were greater than 30% missing (**Appendix DD**).

With the research objectives in mind, identifying the efficiency and efficacy of the purchase incentives was done through an XGBoost classifier model and analysis of the resulting Shapley values. The dependent variable was modeled as a binary response as to whether the purchase was an EV, and features included all variables of interest informed by the review of the literature. Several features detailed the participant's influence and awareness of the federal and state incentives, serving as the primary metric for our original research objective of identifying efficiency and efficacy of such policies.

Results

Recruitment of participants for the survey resulted in a final cleaned dataset including 87 participants. Of the final dataset, nine participants were recruited through the point-of-sale QR code. The remaining majority were contacted through the dealerships' email using IRB-approved language sent to all customers in the previous six months. While the email recruitment reduces the validity of the initial recruitment strategy by introducing further recall bias in comparison to recruitment closer in time to the point of sale through the flyer, it was much more effective in acquiring a necessary sample size. Zip code data from participants was highly missing, but available results are shown in **Figure 34**. The recruitment tool of access to a raffle for $100 cash cards received 56 participants from the dataset, indicating efficacy in incentivizing participation.

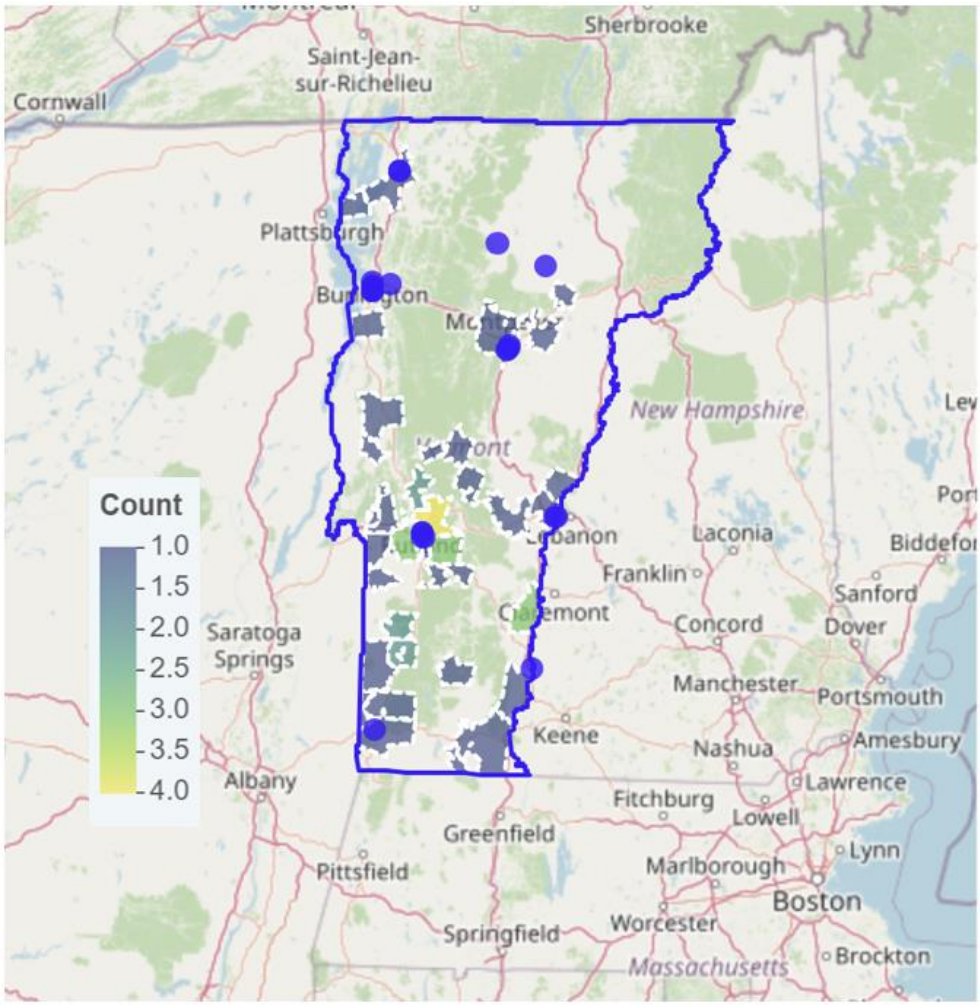

Figure 34. Spatial distribution of survey participants by zip code. Blue dots signify the location of participating dealerships.

An initial phase of data cleaning involved reducing the dataset to variables of interest pertaining to the primary research objective and potential features for modeling, in addition to make, model, and year of the vehicles purchased **(Appendix EE-Appendix GG).** Summary statistics and comparison across EV/ICE vehicle type provides preliminary indication of purchase influences and awareness of the EV purchase incentives across both groups.

Though we gathered data as to whether EV customers purchased a plug-in hybrid, a battery-EV, or a hybrid-EV, the limited sample size among all three encouraged an aggregated EV grouping of all three together versus the gas/diesel purchases (**Figure 35**). The proportion of EV purchasers in our sample was unusually high and suggests miscommunication between some of the dealerships in our request to recruit purchasers of all vehicle types. In addition, the number of missing values for an essential question to our research objectives is an acknowledged limitation of this work, and limited the effectiveness of the survey tool as participants proceed to answer questions specific to their vehicle type.

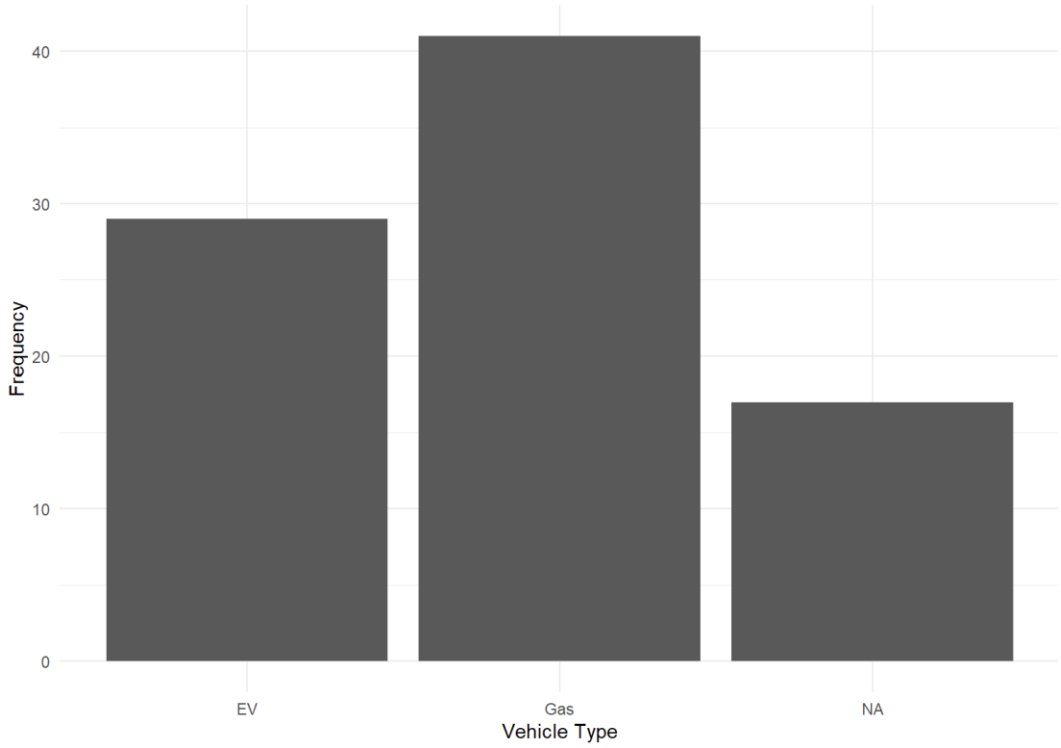

Figure 35. Distribution of survey participants by vehicle type.

From the second section of the survey tool, participants provided ordinal responses to questions about their influences, concerns, and preferences centered around a number of known influences in purchasing a vehicle (**Table 6-Table 7**). Some questions were on a 1-4 versus 1-5 scale and framed in the context of "influence" versus "importance", respectively. For this analysis, these scales were aggregated and re-coded to have a lesser influence (-1), moderate influence (0), and positive influence (1).

Table 6. Distribution of purchase factors and their importance across vehicle type.

	Lesser Importance				Moderate Importance				More Importance				NA (%)
	EV (%)	*CI*	Gas (%)	*CI*	EV (%)	*CI*	Gas (%)	*CI*	EV (%)	*CI*	Gas (%)	*CI*	
Vehicle Cost	3.4	*(0.0-10.0)*	9.8	*(0.0-18.9)*	20.7	*(6.0-35.4)*	24.4	*(11.3-37.5)*	69.0	*(52.2-85.8)*	63.4	*(48.7-78.1)*	*17.2*
Concerns About Climate Change	3.4	*(0.0-10.0)*	48.8	*(33.5-64.1)*	10.3	*(0.0-24.14)*	19.5	*(7.4-31.6)*	79.3	*(64.6-94.0)*	29.3	*(15.4-43.2)*	*17.2*
Saving Money on Gas	10.3	*(0.0-21.4)*	36.6	*(21.9-51.3)*	17.2	*(3.5-30.9)*	29.3	*(15.4-43.2)*	65.5	*(48.2-82.8)*	31.7	*(17.5-45.9)*	*17.2*
Brand Loyalty	55.2	*(37.1-73.3)*	12.2	*(2.2-22.2)*	17.2	*(3.5-30.9)*	9.8	*(0.0-18.9)*	20.7	*(6.0-35.4)*	75.6	*(62.5-88.7)*	*17.2*
Environmental Concerns About Drilling and Oiling	13.8	*(1.2-26.4)*	43.9	*(28.7-59.1)*	3.4	*(0.0-10.0)*	22.0	*(9.3-34.7)*	75.9	*(60.3-91.5)*	31.7	*(17.5-45.9)*	*17.2*
Use for Long Distance Road Trips	55.2	*(37.1-73.3)*	24.4	*(11.3-37.5)*	20.7	*(6.0-35.4)*	19.5	*(7.4-31.6)*	17.2	*(3.5-30.9)*	53.8	*(38.5-69.1)*	*17.2*

Table 7. Distribution of purchase factors and their influence across vehicle types.

	Lesser Influence				Moderate Influence				More Influence				NA (%)
	EV (%)	*CI*	Gas (%)	*CI*	EV (%)	*CI*	Gas (%)	*CI*	EV (%)	*CI*	Gas (%)	*CI*	
Fuel or energy efficiency	0.0	*(0.0-0.0)*	31.7	*(17.5-45.9)*	3.4	*(0.0-10.0)*	41.5	*(26.4-56.6)*	93.1	*(8.8-40.0)*	24.4	*(11.3-37.5)*	*16.1*
Winter Weather Performance	37.9	*(20.2-55.6)*	4.9	*(0.0-11.5)*	37.9	*(20.2-55.6)*	26.8	*(13.2-40.4)*	20.7	*(6.0-35.4)*	65.9	*(51.4-80.4*	*16.1*
Amount of Seating	51.7	*(33.5-69.9)*	26.8	*(13.2-40.4)*	37.9	*(20.2-55.6)*	39.0	*(24.1-53.9)*	3.4	*(0.0-10.0)*	29.3	*(15.4-43.2)*	*18.4*
Cargo Space	31.0	*(14.2-47.8)*	19.5	*(7.4-31.6)*	58.6	*(40.7-76.5)*	36.6	*(21.9-51.3)*	3.4	*(0.0-10.0)*	41.5	*(26.4-56.6)*	*17.2*
Expected Maintenance Costs	17.2	*(3.5-30.9)*	22.0	*(9.3-34.7)*	24.1	*(8.5-39.7)*	41.5	*(26.4-56.6)*	51.7	*(33.5-69.9)*	31.7	*(17.5-45.9)*	*18.4*
Expected Reliability	3.4	*(0.0-10.0)*	4.9	*(0.0-11.5)*	41.4	*(23.5-59.3)*	12.2	*(2.2-22.2)*	48.3	*(30.1-66.5)*	80.5	*(68.4-92.6)*	*17.2*
Crash Safety	31.0	*(14.2-47.8)*	12.2	*(2.2-22.2)*	34.5	*(17.2-51.8)*	26.8	*(13.2-40.4)*	27.6	*(11.3-43.9)*	56.1	*(40.9-71.3)*	*18.4*
Driving Range	10.3	*(0.0-21.4)*	36.6	*(21.9-51.3)*	44.8	*(26.7-62.9)*	36.6	*(21.9-51.3)*	37.9	*(20.2-55.6)*	24.4	*(11.3-37.5)*	*17.2*
Towing Capacity	89.7	*(78.6-100.0)*	41.5	*(26.4-56.6)*	3.4	*(0.0-10.0)*	29.3	*(15.4-43.2)*	0.0	*(0.0-0.0)*	24.4	*(11.3-37.5)*	*18.4*
Off-Road Capabilities	93.1	*(83.9-100.0)*	46.3	*(31.0-61.6)*	0.0	*(0.0-0.0)*	36.6	*(21.9-51.3)*	0.0	*(0.0-0.0)*	12.2	*(2.2-22.2)*	*18.4*
Automated Driving Features	55.2	*(37.1-73.3)*	31.7	*(17.5-45.9)*	24.1	*(8.5-39.7)*	34.1	*(19.6-48.6)*	13.8	*(1.2-26.4)*	29.3	*(15.4-43.2)*	*18.4*
Highway Performance	65.5	*(48.2-82.8)*	14.6	*(3.8-25.4)*	27.6	*(11.3-43.9)*	48.8	*(33.5-64.1)*	0.0	*(0.0-0.0)*	31.7	*(17.5-45.9)*	*18.4*

Comparison of responses in this section showed a stronger influence among EV customers across features including energy efficiency, concerns about climate change, saving on gas money, and environmental concerns about oil/drilling. Meanwhile, influential or important factors among those who purchased gas/diesel vehicles included winter weather performance, cargo space, crash safety, highway performance, brand loyalty, and use for long distance road trips. Both groups valued vehicle purchase cost strongly.

In the section of branching by vehicle type, all groups were asked about their awareness and potential utilization of the available EV purchase incentives at the state and federal level. The question was framed similarly for both EV and gas/diesel purchasers, though the sole affirmative option for gas/diesel was listed as “yes, I know about the incentives and how much I could save”, while EV purchasers saw “yes, I know about the incentives and I took advantage of the incentives with my recent purchase”, or planned to take advantage of incentives for the federal option through a tax credit. This was re-coded in a similar fashion with future modeling requirements in mind; selection of the affirmative option for either vehicle type was coded as “1”. Of the EV group, 75.9% of participants were aware of the federal incentives and planned on taking advantage of them. Meanwhile, 22.0% of gas/diesel purchasers showed full awareness of the federal incentives. For state incentives, utilization of the available incentives for EV users was at 72.4% while gas/diesel purchasers showed a slight increase to 26.8%.

The complexity of these policies has been a noted barrier (Z. Yang et al., 2016). We captured this barrier in our work, as 29.3% of gas/diesel purchasers claimed they were

unsure of their eligibility or how much they could save through the federal policy. This proportion of gas/diesel purchasers increased to 34.1% for state incentives. EV purchasers showed zero representation in this moderate awareness group among federal incentives and just one EV purchaser claimed this moderate level of awareness towards the state incentives. This lack of certainty was re-coded as "0" for both groups. Further, 39.0% of gas/diesel purchasers claimed complete lack of awareness towards the federal incentives and 34.1% at the state level. In comparison, EV purchasers claimed full unawareness of both federal and state policies at 13.8%. This indicates high levels of inefficiencies in both policies despite the range of influences previously identified as barriers to EV adoption.

The final section of the survey gathered household and sociodemographic data from participants. Of the 87 participants, only one answered race and ethnicity questions as nonwhite and one response to the gender question answered as nonbinary **(Figure 36).** This lack of representation is an additional limitation of the study in identifying the equity of the policies and forming results generalizable to Vermont and US vehicle purchasers.

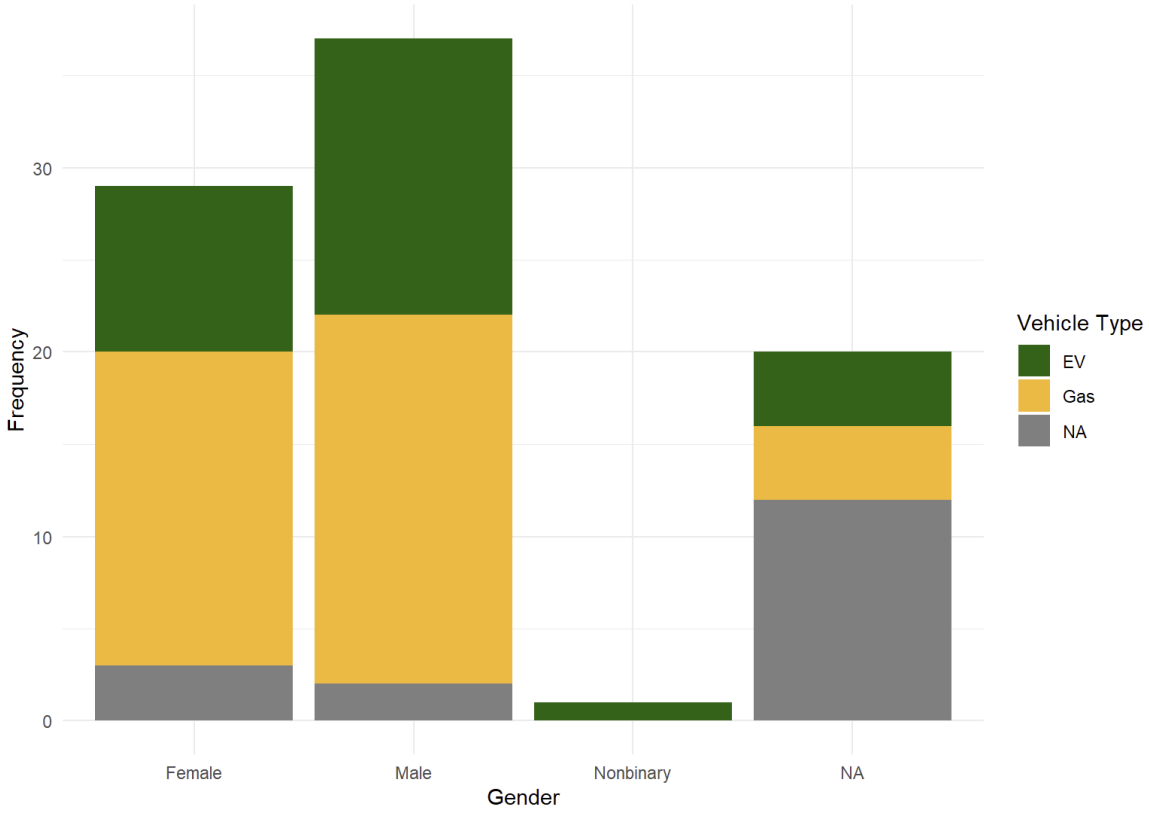

Figure 36. Distribution of gender among survey participants.

Participants commonly described their household as having two members and two vehicles **(Figure 37Figure 38).** Median age of survey participant was 62, skewing much older than the state's median age of 42.7, and was somewhat proportional across vehicle type **(Figure 39).** Household income was heavily represented below $100,000 with zero participants claiming below $25,000. This variable was binned as a binary for practicality at the $100,000 threshold **(Figure 40).** Both household size and age were scaled down to the same range as the other variables of interest for modeling purposes.

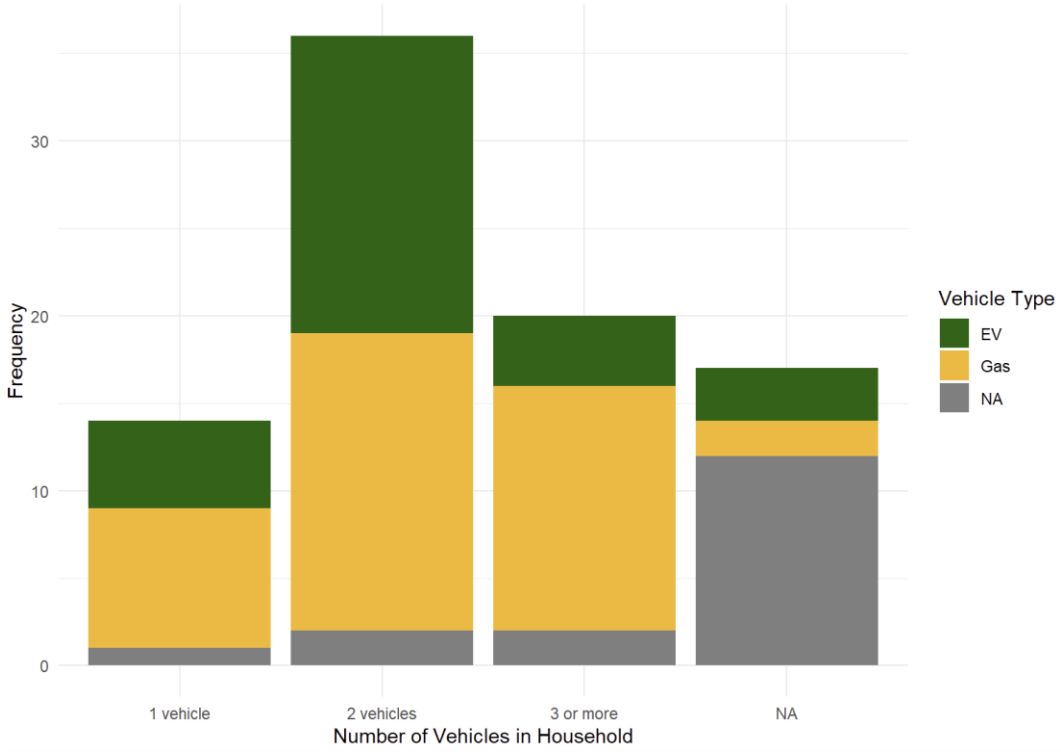

Figure 37. Distribution of the number of vehicles (including recent purchase) in household.

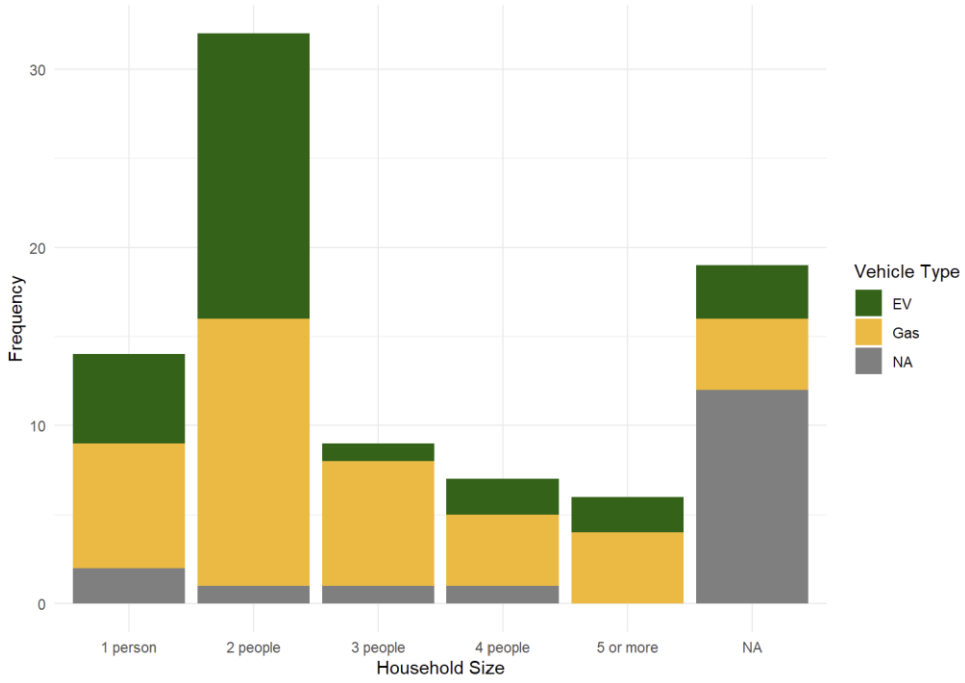

Figure 38. Distribution of household size among survey participants.

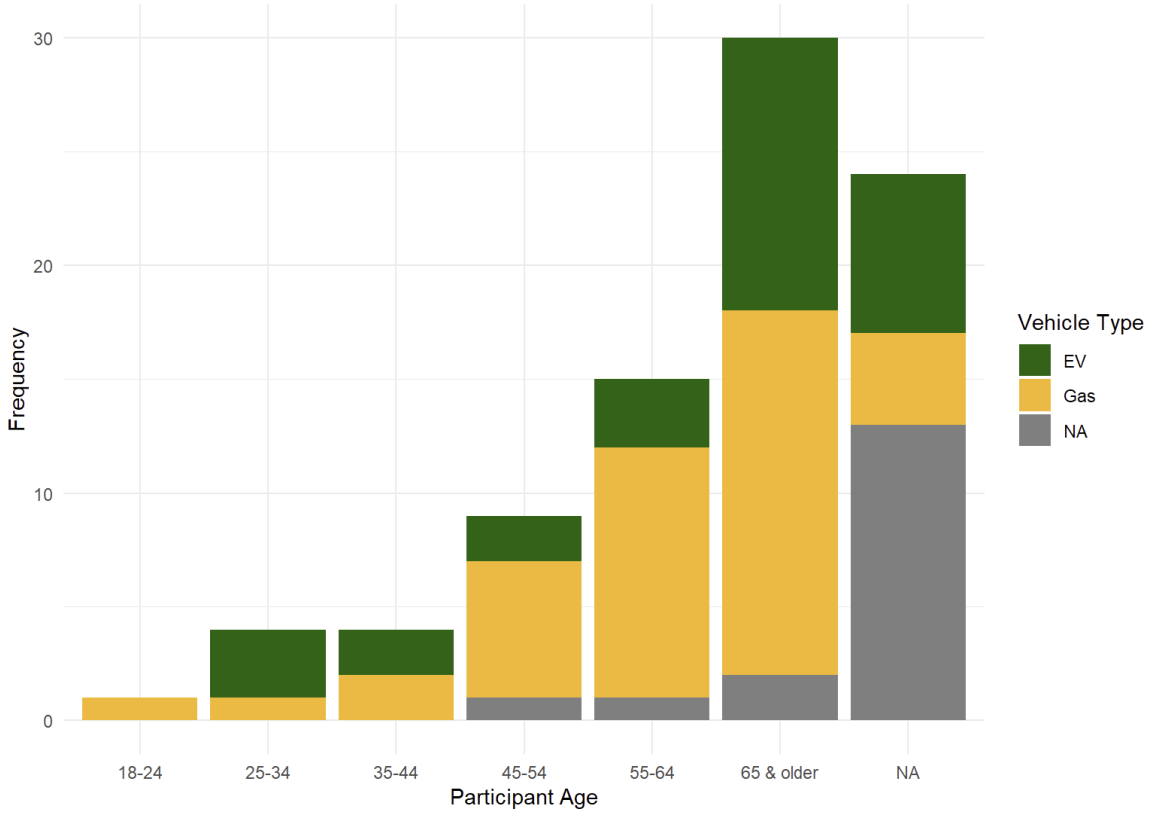

Figure 39. Distribution of age among survey participants.

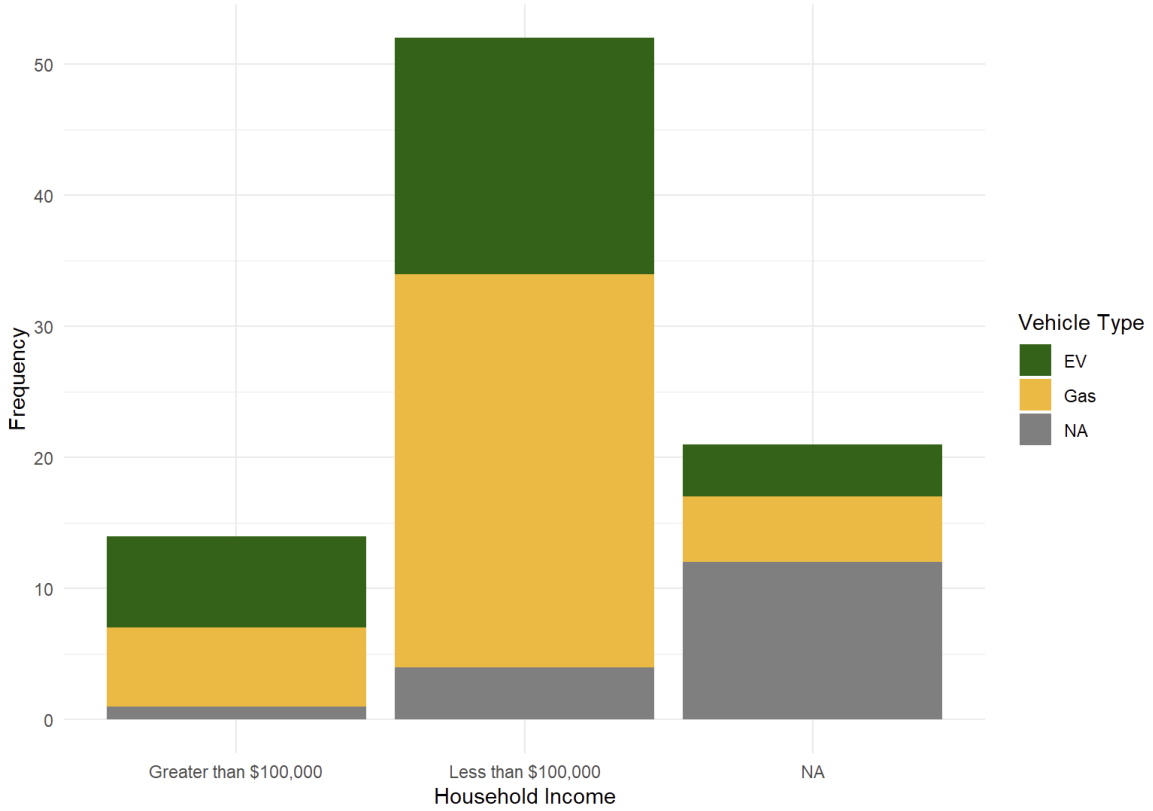

Figure 40. Distribution of household income among survey participants.

Missing values among variables of interest were then imputed for modeling purposes. The imputation of missing categorical data via the "missForest" package resulted in a Proportion of False Classifications (PFC) of approximately 34.3%, indicating that over one-third of the imputed values differed from their estimated true values based on the algorithm's internal validation. This level of imputation accuracy highlights the challenges inherent in predicting missing categorical data and underscores the importance of considering imputation-uncertainty in subsequent analyses.

The XGBoost construction included a 70/30 split of training and testing data to identify potential overfitting. Hyperparameter tuning through a grid search combined with 5-fold validation identified the optimal parameters. They included 100 total trees, a learning rate

of 0.3, a maximum tree depth of 3, a gamma value of 0, subsampling for each tree of 50% of the training data, 50% of features sampled at each tree, and a minimum child weight of 1. The grid search process examined 3645 combinations of parameters and identified the optimal model as the one with the highest ROC value (0.981).

Further diagnostics showed strong accuracy in the ability of this model to identify EV purchases based on the provided inputs. Predictions across all 15 observations in the validation set were nearly perfect, with one false positive and one false negative in predicting an EV purchase (**Table 8**). Predictions on the training data resulted in one falsely identified gas vehicle purchase, providing additional confidence that minimal noise was being captured in training and being presented in the form of overfitting in the validation set. A larger dataset would be able to provide further validation and confidence that overfitting isn't occurring, but the available metrics and the use of k-fold cross-validation in the training supports confirmation as the optimal parameters. Though the intention was not to create a predictive model, splitting and validation of the data through prediction was conducted as assessment of the optimal model's architecture. Training an inference-based model with these parameters on the entire dataset demonstrated an AOC value of 0.977.

Table 8. Confusion matrices of predictions on training and testing of optimal XGBoost classifier.

		Training			Testing	
		Target				
		Gas	*EV*		*Gas*	*EV*
Predicted	*Gas*	12	1	*Gas*	32	1
	EV	1	11	*EV*	0	29

Feature importance indicated similar trends across features using both the Gain and Cover metrics **(Figure 41).** Awareness of state incentives ranked 5th in Gain and 6th in Cover, indicating high importance in both accurate predictions and setting the architecture of the model by this feature. Awareness of federal incentives ranked 4th in Gain and 5th in Cover. Few sociodemographic features ranked highly in importance, as the leaders were primarily behavioral factors and performance preferences.

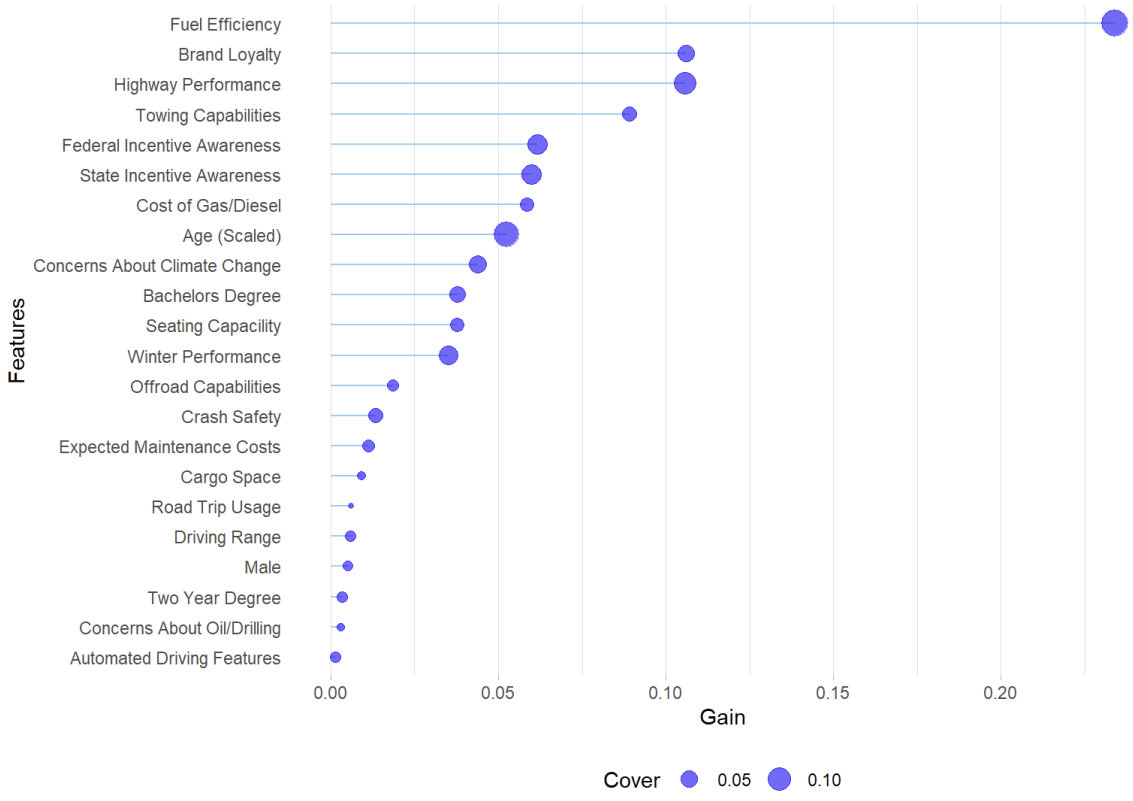

Figure 41. Feature importance of the XGBoost Classifier model.

Shapley values for this model showed a positive contribution by several features towards identifying an EV purchase **(Figure 42**). Calculating a mean shapley value across shapley scores from all observations for a single feature distorts the perceived contribution of that feature due to the polarity of factor levels in the features. The figure denotes the mean shap score of those identified to be gas vehicles, and then those identified as EVs, respectively, in parentheses next to the feature name. For example, a mean shapley score of -0.98 for those inferred to purchase gas/diesel vehicles indicates that a strong influence revealed in their survey response for fuel/energy efficiency in their purchase decision paradoxically decreases the likelihood of an EV purchase. This might indicate that other factors in their profile and background strongly favor a gas/diesel purchase. The

counterintuitive nature of this finding can be further explained by the distribution of scores; most gas/diesel purchasers with low shapley values for this feature also had a low feature value (-1), revealing low influence by this purchase factor. Meanwhile, a mean shapley score of 1.07 for predicted EV purchasers on this purchase factor is the largest in magnitude across any feature, indicating that revealing fuel efficiency as a strong influence is a powerful and positive contributor to identifying an EV purchase. A bias value for the model was calculated to be 0.12, which when used as an input in the logistic function gives us a baseline probability of the model identifying an EV purchase of 53.0%, akin to an intercept from a logistic regression model.

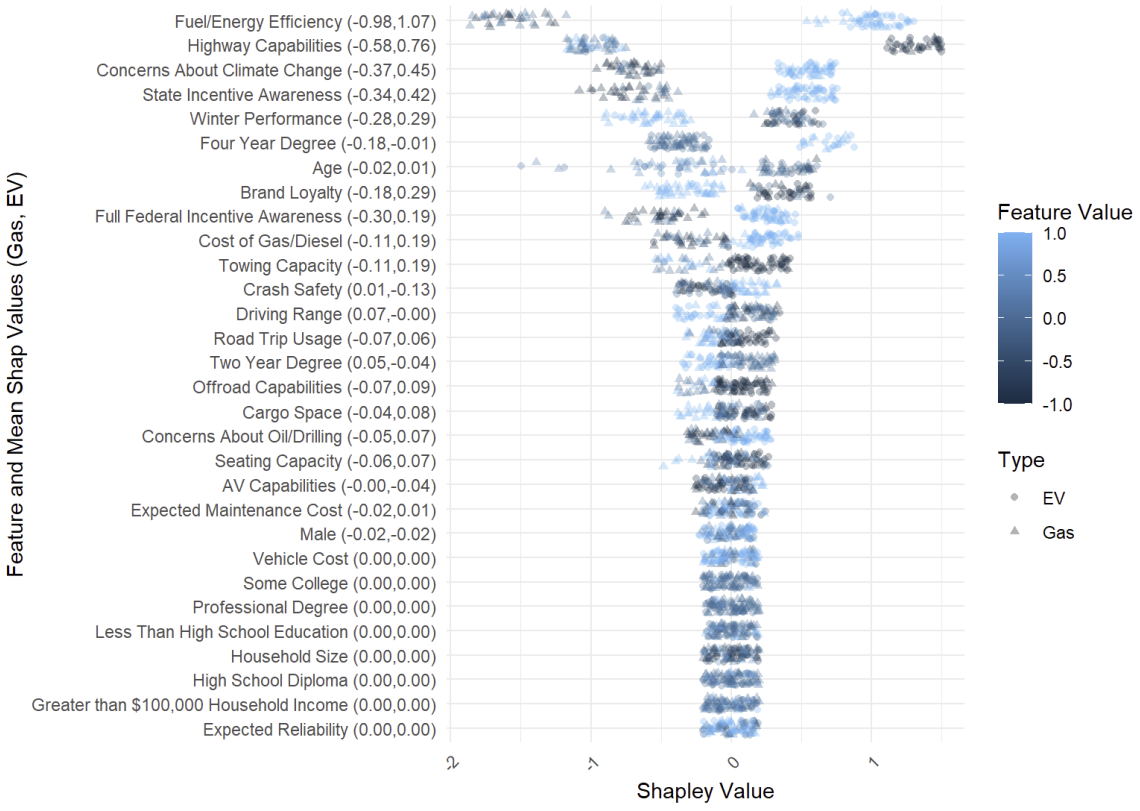

Figure 42. Distribution of Shapley values. Numbers in parentheses next to feature names represents average Shapley value for features across all observations.

To elaborate on features relevant to our primary research objective, full awareness of the federal incentives demonstrated an overall negative contribution to inferring an EV purchase. The mean shapley score for the feature across all observations was -0.06, meaning that the baseline probability of an EV purchase by the model drops from 53.0% to 51.5% when full awareness of the policy is revealed. Further, observing the two mean scores across the vehicle types separately shows a stronger yet negative contribution to inferring EV for predicted gas types (-0.30) versus the positive log odds value of 0.19 for those that were identified EV types.

The state incentive demonstrates different efficacy. It increases the baseline probability from the mean shapley score across all observations from 53.0% to 53.7%. In addition, the magnitude of the two mean shapley scores when separated by identified vehicle type is larger and positive for identified EV purchasers at 0.42 versus gas/diesel purchasers at (-0.34). This is indicative of varying levels of efficacy and complexity across the influence and awareness of the two policies.

When including all 35 features of interest in the model, 22 had a nonzero contribution to the model's inference demonstrated through their mean shapley score. While not providing contribution to the accuracy of the model, the lack of strong negative signal across those with mean shapley scores of zero indicates a lack of negative association with EV adoption among the participants and the particularly large proportion of gas/diesel purchasers who revealed they were unaware of the policies. Many of these features without measurable contribution to the model were from sociodemographic questions, which limits our ability to return to one of our primary research objectives of answer specifically who is benefitting from these policies. Future research should design

their recruitment strategies to gain accurate and representative samples of the vehicle consumer market.

While we can conclude a level of efficacy from these policy tools, we identify from the distributions of the different model features the complexity of the purchase decision for Vermont consumers. The decision to purchase an EV in a region such as Vermont is unique to the areas commonly studied for EV adoption, and the distribution of effect from features such as winter performance and concerns over climate change are indicative of how policymakers must consider more than a reduction in price-point to encourage electrification. Vehicle cost had zero contribution to EV purchase, supporting further is indication of the larger and more complex barriers at play in such efforts to direct Vermont consumer choices, particularly as the typical price of EVs continues the trajectory of decline.

Conclusion

This research seeks to provide perspective from a unique study area on the efficacy and efficiency of EV purchase incentives. Analysis of shapley scores from the XGBoost classifier indicates a small yet positive contribution to the association between awareness of the state incentives and purchasing an EV, while the federal incentives demonstrate a small yet negative association. Further, the vehicle cost was not a contributing feature for the model at large nor for either vehicle purchase type, indicating that effective policy should seek to understand the complexity of the barriers to incentivizing future purchases.

As for efficacy, summary statistics reveal that awareness of the policies is low among those who purchased gas/diesel vehicles. This is a direct identification of an inefficiency in the policy. Future research should identify the proper channels or tactics to simplify comprehension and access to policy details.

Previous research has identified inequities pertaining to these policies (H. Liu et al., 2022). We did not acquire a sufficiently representative sample to assess the equity of the policies. Further, questions of interest such as those about policy awareness had a high number of missing responses. The imputation algorithm indicated that the level of missingness across the variables of interest reduced the ability to impute values with confidence past 66%. Future work should seek to maintain the intention of our recruitment strategies to survey both EV and gas/diesel purchasers as closely in time to the point of sale as possible, while obtaining a more diverse and representative sample. In addition, questions seeking to gather the influence of charging infrastructure and some of the unique qualities of being an EV owner should be included in addition to the many factors included in our work.

Dissertation Closing Remarks

This dissertation comprises four chapters dedicated to exploring the effects of pavement on heat exposure at the microenvironment level, examining the mitigation potential through tree cover substitution in place of pavement, evaluating high-resolution heat mapping techniques, and analyzing the impact of EV purchase incentives. Each chapter contributes to the civil and environmental engineering fields under the pressing trends of climate change and urbanization.

The work is of public importance, contributing to a global dialogue as evidenced by willingness-to-pay studies for UHI mitigation where those surveyed in China and Singapore valued UHI mitigation at USD$29.64 and USD$563.80 per year, respectively (Borzino et al., 2020). Our work is increasingly relevant as less urbanized, cooler climate areas may become refuges in the face of climate migration (Lustgarten, 2020). In addition, assessing the effectiveness of current EV policies provides vital information that could steer collective action toward environmental sustainability, impacting individual consumers and informing large-scale policy decisions.

References

Adepetu, A., Keshav, S., & Arya, V. (2016). An agent-based electric vehicle ecosystem model: San Francisco case study. *Transport Policy*, *46*, 109–122.

Akbari, H., Menon, S., & Rosenfeld, A. (2009). Global cooling: Increasing world-wide urban albedos to offset CO2. *Climatic Change*, *94*(3), 275–286. https://doi.org/10.1007/s10584-008-9515-9

Akbari, H., & Rose, L. S. (2008). Urban surfaces and heat island mitigation potentials. *Journal of the Human-Environment System*, *11*(2), 85–101.

Alexander, P. J., & Mills, G. (2014). Local Climate Classification and Dublin's Urban Heat Island. *Atmosphere*, *5*(4), 755–774. https://doi.org/10.3390/atmos5040755

Alonso, L., & Renard, F. (2020). A New Approach for Understanding Urban Microclimate by Integrating Complementary Predictors at Different Scales in Regression and Machine Learning Models. *Remote Sensing*, *12*(15). https://doi.org/10.3390/rs12152434

Andersen, C. T., Foster, I. D., & Pratt, C. J. (1999). The role of urban surfaces (permeable pavements) in regulating drainage and evaporation: Development of a laboratory simulation experiment. *Hydrological Processes*, *13*(4), 597–609.

Aniello, C., Morgan, K., Busbey, A., & Newland, L. (1995). Mapping micro-urban heat islands using Landsat TM and a GIS. *Computers & Geosciences*, *21*(8), 965–969.

Anniballe, R., Bonafoni, S., & Pichierri, M. (2014). Spatial and temporal trends of the surface and air heat island over Milan using MODIS data. *Remote Sensing of Environment*, *150*, 163–171. https://doi.org/10.1016/j.rse.2014.05.005

Anselin, L. (1988). *Spatial econometrics: Methods and models* (Vol. 4). Springer Science & Business Media.

Antonczak, Doran, & Rowangould. (2024). *Household Proximity to Pavement: Heat Exposure and Equity Analysis in Small and Rural Communities*.

Apley, D. W., & Zhu, J. (2020). Visualizing the effects of predictor variables in black box supervised learning models. *Journal of the Royal Statistical Society Series B: Statistical Methodology*, *82*(4), 1059–1086.

Aram, F., Higueras García, E., Solgi, E., & Mansournia, S. (2019). Urban green space cooling effect in cities. *Heliyon*, *5*(4), e01339. https://doi.org/10.1016/j.heliyon.2019.e01339

Armson, D., Stringer, P., & Ennos, A. R. (2012). The effect of tree shade and grass on surface and globe temperatures in an urban area. *Urban Forestry & Urban Greening*, *11*(3), 245–255. https://doi.org/10.1016/j.ufug.2012.05.002

Armstrong, C. G., & Kenney, W. L. (1993). Effects of age and acclimation on responses to passive heat exposure. *Journal of Applied Physiology*, *75*(5), 2162–2167.

Asaeda, T., & Ca, V. T. (2000). Characteristics of permeable pavement during hot summer weather and impact on the thermal environment. *Building and Environment*, *35*(4), 363–375. https://doi.org/10.1016/S0360-1323(99)00020-7

Asaeda, T., Ca, V. T., & Wake, A. (1996). Heat storage of pavement and its effect on the lower atmosphere. *Atmospheric Environment*, *30*(3), 413–427. https://doi.org/10.1016/1352-2310(94)00140-5

Atkinson, B. W. (1969). A Further Examination of the Urban Maximum of Thunder Rainfall in London, 1951-60. *Transactions of the Institute of British Geographers*, *48*, 97–119. JSTOR. https://doi.org/10.2307/621493

Azarafshar, R., & Vermeulen, W. N. (2020). Electric vehicle incentive policies in Canadian provinces. *Energy Economics*, *91*, 104902. https://doi.org/10.1016/j.eneco.2020.104902

Balaresque, P. L., Ballereau, S. J., & Jobling, M. A. (2007). Challenges in human genetic diversity: Demographic history and adaptation. *Human Molecular Genetics*, *16*(R2), R134–R139. https://doi.org/10.1093/hmg/ddm242

Ballester, F., Corella, D., Pérez-Hoyos, S., Sáez, M., & Hervás, A. (1997). Mortality as a function of temperature. A study in Valencia, Spain, 1991-1993. *International Journal of Epidemiology*, *26*(3), 551–561.

Barber, E. S. (1957). Calculation of maximum pavement temperatures from weather reports. *Highway Research Board Bulletin*, *168*.

Basagaña, X., Sartini, C., Barrera-Gómez, J., Dadvand, P., Cunillera, J., Ostro, B., Sunyer, J., & Medina-Ramón, M. (2011). Heat waves and cause-specific mortality at all ages. *Epidemiology*, 765–772.

Basu, R., & Ostro, B. D. (2008). A multicounty analysis identifying the populations vulnerable to mortality associated with high ambient temperature in California. *American Journal of Epidemiology*, *168*(6), 632–637.

Basu, R., & Samet, J. M. (2002a). An exposure assessment study of ambient heat exposure in an elderly population in Baltimore, Maryland. *Environmental Health Perspectives*, *110*(12), 1219–1224.

Basu, R., & Samet, J. M. (2002b). Relation between Elevated Ambient Temperature and Mortality: A Review of the Epidemiologic Evidence. *Epidemiologic Reviews*, *24*(2), 190–202. https://doi.org/10.1093/epirev/mxf007

Berg, R. L. (1974). *Energy balance on a paved surface* (Issue 226). US Army Cold Regions Research and Engineering Laboratory.

Berry, R., Livesley, S. J., & Aye, L. (2013). Tree canopy shade impacts on solar irradiance received by building walls and their surface temperature. *Building and Environment*, *69*, 91–100. https://doi.org/10.1016/j.buildenv.2013.07.009

Borzino, N., Chng, S., Mughal, M. O., & Schubert, R. (2020). Willingness to pay for urban heat island mitigation: A case study of Singapore. *Climate*, *8*(7), 82.

Breiman, L. (2001). Random forests. *Machine Learning*, *45*, 5–32.

Briggs, N. (2022). Moving Forward by Looking Back: How Pre-Industrial Architectural Techniques Can Help Decrease Our Energy Consumption. *Available at SSRN 4108193*.

Bureau, U. C. (n.d.). *Data Profiles*. Census.Gov. Retrieved July 31, 2023, from https://www.census.gov/programs-surveys/acs/

Buyantuyev, A., & Wu, J. (2010). Urban heat islands and landscape heterogeneity: Linking spatiotemporal variations in surface temperatures to land-cover and socioeconomic patterns. *Landscape Ecology*, *25*, 17–33.

Cao, X., Onishi, A., Chen, J., & Imura, H. (2010). Quantifying the cool island intensity of urban parks using ASTER and IKONOS data. *Landscape and Urban Planning*, *96*(4), 224–231. https://doi.org/10.1016/j.landurbplan.2010.03.008

Caplan. (2023). *U.S. Older Population Grew From 2010 to 2020 at Fastest Rate Since 1880 to 1890*. US Census Bureau. https://www.census.gov/library/stories/2023/05/2020-census-united-states-older-population-grew.html#:~:text=The%20older%20population%20reached%2055.8,were%20age%2065%20and%20over.

Carnahan, W. H., & Larson, R. C. (1990). An analysis of an urban heat sink. *Remote Sensing of Environment*, *33*(1), 65–71.

Chakraborty, T., Hsu, A., Manya, D., & Sheriff, G. (2019). Disproportionately higher exposure to urban heat in lower-income neighborhoods: A multi-city perspective. *Environmental Research Letters*, *14*(10), 105003. https://doi.org/10.1088/1748-9326/ab3b99

Chapman, L., Bell, C., & Bell, S. (2017). Can the crowdsourcing data paradigm take atmospheric science to a new level? A case study of the urban heat island of London quantified using Netatmo weather stations. *International Journal of Climatology*, *37*(9), 3597–3605. https://doi.org/10.1002/joc.4940

Checkley, W., Epstein, L. D., Gilman, R. H., Figueroa, D., Cama, R. I., Patz, J. A., & Black, R. E. (2000). Effects of EI Niño and ambient temperature on hospital admissions for diarrhoeal diseases in Peruvian children. *The Lancet*, *355*(9202), 442–450.

Chester, M., Horvath, A., & Madanat, S. (2010). Parking infrastructure: Energy, emissions, and automobile life-cycle environmental accounting. *Environmental Research Letters*, *5*(3), 034001. https://doi.org/10.1088/1748-9326/5/3/034001

Cheung, P. K., Nice, K. A., & Livesley, S. J. (2022). Irrigating urban green space for cooling benefits: The mechanisms and management considerations. *Environmental Research: Climate*, *1*(1), 015001.

Chou, W.-C., Wu, J.-L., Wang, Y.-C., Huang, H., Sung, F.-C., & Chuang, C.-Y. (2010). Modeling the impact of climate variability on diarrhea-associated diseases in Taiwan (1996–2007). *Science of the Total Environment*, *409*(1), 43–51.

Choubane, B., & Tia, M. (1992). Nonlinear temperature gradient effect on maximum warping stresses in rigid pavements. *Transportation Research Record*, *1370*(1), 11.

Chun, B., & Guhathakurta, S. (2017). Daytime and nighttime urban heat islands statistical models for Atlanta. *Environment and Planning B: Urban Analytics and City Science*, *44*(2), 308–327. https://doi.org/10.1177/0265813515624685

Chung, M. H., & Park, J. C. (2016). Development of PCM cool roof system to control urban heat island considering temperate climatic conditions. *Energy and Buildings*, *116*, 341–348. https://doi.org/10.1016/j.enbuild.2015.12.056

Coseo, P., & Larsen, L. (2015). Cooling the Heat Island in Compact Urban Environments: The Effectiveness of Chicago's Green Alley Program. *Defining the Future of Sustainability and Resilience in Design, Engineering and Construction*, *118*, 691–710. https://doi.org/10.1016/j.proeng.2015.08.504

Cosgrove, A., & Berkelhammer, M. (2018). Downwind footprint of an urban heat island on air and lake temperatures. *Npj Climate and Atmospheric Science*, *1*(1), 46. https://doi.org/10.1038/s41612-018-0055-3

Curriero, F. C., Heiner, K. S., Samet, J. M., Zeger, S. L., Strug, L., & Patz, J. A. (2002). Temperature and Mortality in 11 Cities of the Eastern United States. *American Journal of Epidemiology*, *155*(1), 80–87. https://doi.org/10.1093/aje/155.1.80

Dadvand, P., Nieuwenhuijsen, M. J., Esnaola, M., Forns, J., Basagaña, X., Alvarez-Pedrerol, M., Rivas, I., López-Vicente, M., De Castro Pascual, M., & Su, J. (2015). Green spaces and cognitive development in primary schoolchildren. *Proceedings of the National Academy of Sciences*, *112*(26), 7937–7942.

Debbage, N., & Shepherd, J. M. (2015). The urban heat island effect and city contiguity. *Computers, Environment and Urban Systems*, *54*, 181–194. https://doi.org/10.1016/j.compenvurbsys.2015.08.002

Deschênes, O., Greenstone, M., & Guryan, J. (2009). Climate change and birth weight. *American Economic Review*, *99*(2), 211–217.

Dialesandro, J., Brazil, N., Wheeler, S., & Abunnasr, Y. (2021). Dimensions of thermal inequity: Neighborhood social demographics and urban heat in the Southwestern US. *International Journal of Environmental Research and Public Health*, *18*(3), 941.

Diamond, D. (2009). The impact of government incentives for hybrid-electric vehicles: Evidence from US states. *Energy Policy*, *37*(3), 972–983. https://doi.org/10.1016/j.enpol.2008.09.094

Donoghue, E. R., Graham, M. A., Jentzen, J. M., Lifschultz, B. D., Luke, J. L., & Mirchandani, H. G. (1997). Criteria for the diagnosis of heat-related deaths: National Association of Medical Examiners: Position paper. *The American Journal of Forensic Medicine and Pathology*, *18*(1), 11–14.

Doulos, L., Santamouris, M., & Livada, I. (2004). Passive cooling of outdoor urban spaces. The role of materials. *Solar Energy*, *77*(2), 231–249.

Du, S., Xiong, Z., Wang, Y.-C., & Guo, L. (2016). Quantifying the multilevel effects of landscape composition and configuration on land surface temperature. *Remote Sensing of Environment*, *178*, 84–92. https://doi.org/10.1016/j.rse.2016.02.063

Dudorova, N. V., & Belan, B. D. (2022). The Energy Model of Urban Heat Island. *Atmosphere*, *13*(3). https://doi.org/10.3390/atmos13030457

Dufour, A., & Candas, V. (2007). Ageing and thermal responses during passive heat exposure: Sweating and sensory aspects. *European Journal of Applied Physiology*, *100*(1), 19–26.

Economic Research Service, Department of Agriculture. (2020). *Rural-Urban Commuting Area (RUCA) Codes, 2010*. https://www.ers.usda.gov/data-products/rural-urban-commuting-area-codes.aspx

Ellis, F. P., Prince, H. P., Lovatt, G., & Whittington, R. M. (1980). Mortality and morbidity in Birmingham during the 1976 heatwave. *QJM: An International Journal of Medicine*, *49*(1), 1–8.

Emmanuel, R., & Krüger, E. (2012). Urban heat island and its impact on climate change resilience in a shrinking city: The case of Glasgow, UK. *Building and Environment*, *53*, 137–149. https://doi.org/10.1016/j.buildenv.2012.01.020

EPA. (2023a). *Learn About Heat Islands*. EPA. https://www.epa.gov/heatislands/learn-about-heat-islands

EPA. (2023b). *Sources of Greenhouse Gas Emissions*. EPA. https://www.epa.gov/ghgemissions/sources-greenhouse-gas-emissions

Estoque, R. C., & Murayama, Y. (2017). Monitoring surface urban heat island formation in a tropical mountain city using Landsat data (1987–2015). *ISPRS Journal of Photogrammetry and Remote Sensing*, *133*, 18–29. https://doi.org/10.1016/j.isprsjprs.2017.09.008

Fabrizi, R., Bonafoni, S., & Biondi, R. (2010). Satellite and Ground-Based Sensors for the Urban Heat Island Analysis in the City of Rome. *Remote Sensing*, *2*(5), 1400–1415. https://doi.org/10.3390/rs2051400

Falk, B. (1998). Effects of thermal stress during rest and exercise in the paediatric population. *Sports Medicine*, *25*, 221–240.

Falk, B., & Dotan, R. (2008). Children's thermoregulation during exercise in the heat—A revisit. *Applied Physiology, Nutrition, and Metabolism*, *33*(2), 420–427.

Fallmann, J., Forkel, R., & Emeis, S. (2016). Secondary effects of urban heat island mitigation measures on air quality. *Atmospheric Environment*, *125*, 199–211. https://doi.org/10.1016/j.atmosenv.2015.10.094

Ferreira, M. J., de Oliveira, A. P., & Soares, J. (2011). Anthropogenic heat in the city of São Paulo, Brazil. *Theoretical and Applied Climatology*, *104*(1), 43–56. https://doi.org/10.1007/s00704-010-0322-7

Flores R., J. L., Pereira Filho, A. J., & Karam, H. A. (2016). Estimation of long term low resolution surface urban heat island intensities for tropical cities using MODIS remote sensing data. *Urban Climate*, *17*, 32–66. https://doi.org/10.1016/j.uclim.2016.04.002

Friedman, J. H. (2001). Greedy Function Approximation: A Gradient Boosting Machine. *The Annals of Statistics*, *29*(5), 1189–1232. JSTOR.

Gedzelman, S. D., Austin, S., Cermak, R., Stefano, N., Partridge, S., Quesenberry, S., & Robinson, D. A. (2003). Mesoscale aspects of the urban heat island around New York City. *Theoretical and Applied Climatology*, *75*, 29–42.

Golden, J. S., & Kaloush, K. E. (2006). Mesoscale and microscale evaluation of surface pavement impacts on the urban heat island effects. *The International Journal of Pavement Engineering*, *7*(1), 37–52.

Gover, M. (1938). Mortality during Periods of Excessive Temperature. *Public Health Reports (1896-1970)*, *53*(27), 1122–1143. JSTOR. https://doi.org/10.2307/4582590

Gunawardena, K. R., Wells, M. J., & Kershaw, T. (2017). Utilising green and bluespace to mitigate urban heat island intensity. *Science of The Total Environment*, *584–585*, 1040–1055. https://doi.org/10.1016/j.scitotenv.2017.01.158

Hajat, S., Armstrong, B., Baccini, M., Biggeri, A., Bisanti, L., Russo, A., Paldy, A., Menne, B., & Kosatsky, T. (2006). Impact of High Temperatures on Mortality: Is There an Added Heat Wave Effect? *Epidemiology*, *17*(6). https://journals.lww.com/epidem/Fulltext/2006/11000/Impact_of_High_Temperatures_on_Mortality__Is_There.7.aspx

Hajat, S., & Kosatky, T. (2010). Heat-related mortality: A review and exploration of heterogeneity. *Journal of Epidemiology and Community Health*, *64*(9), 753. https://doi.org/10.1136/jech.2009.087999

Harlan, S. L., Brazel, A. J., Prashad, L., Stefanov, W. L., & Larsen, L. (2006). Neighborhood microclimates and vulnerability to heat stress. *Social Science & Medicine*, *63*(11), 2847–2863. https://doi.org/10.1016/j.socscimed.2006.07.030

Hashizume, M., Armstrong, B., Hajat, S., Wagatsuma, Y., Faruque, A. S., Hayashi, T., & Sack, D. A. (2007). Association between climate variability and hospital visits for non-cholera diarrhoea in Bangladesh: Effects and vulnerable groups. *International Journal of Epidemiology*, *36*(5), 1030–1037.

Hayashida, K., Shimizu, K., & Yokota, H. (2019). Severe heatwave in Japan. *Acute Medicine & Surgery*, *6*(2), 206–207.

Heaviside, C., Vardoulakis, S., & Cai, X.-M. (2016). Attribution of mortality to the urban heat island during heatwaves in the West Midlands, UK. *Environmental Health*, *15*, 49–59.

Hester, E. T., & Bauman, K. S. (2013). Stream and Retention Pond Thermal Response to Heated Summer Runoff From Urban Impervious Surfaces1. *JAWRA Journal of the American Water Resources Association*, *49*(2), 328–342. https://doi.org/10.1111/jawr.12019

Heusinkveld, B. G., Steeneveld, G. J., van Hove, L. W. A., Jacobs, C. M. J., & Holtslag, A. A. M. (2014). Spatial variability of the Rotterdam urban heat island as

influenced by urban land use. *Journal of Geophysical Research: Atmospheres*, *119*(2), 677–692. https://doi.org/10.1002/2012JD019399

Heusinkveld, B. G., Van Hove, L. W. A., Jacobs, C. M. J., Steeneveld, G. J., Elbers, J. A., Moors, E. J., & Holtslag, A. A. M. (2010). Use of a mobile platform for assessing urban heat stress in Rotterdam. *Proceedings of the 7th Conference on Biometeorology*, 433–438.

Hinkel, K. M., Nelson, F. E., Klene, A. E., & Bell, J. H. (2003). The urban heat island in winter at Barrow, Alaska. *International Journal of Climatology: A Journal of the Royal Meteorological Society*, *23*(15), 1889–1905.

Holstein, J., Canouï-Poitrine, F., Neumann, A., Lepage, E., & Spira, A. (2005). Were less disabled patients the most affected by 2003 heat wave in nursing homes in Paris, France? *Journal of Public Health*, *27*(4), 359–365.

Howard, L. (1833). *The climate of London: Deduced from meteorological observations made in the metropolis and at various places around it* (Vol. 3). Harvey and Darton, J. and A. Arch, Longman, Hatchard, S. Highley [and] R. Hunter.

Hsieh, C.-M., & Huang, H.-C. (2016). Mitigating urban heat islands: A method to identify potential wind corridor for cooling and ventilation. *Computers, Environment and Urban Systems*, *57*, 130–143. https://doi.org/10.1016/j.compenvurbsys.2016.02.005

Hsu, A., Sheriff, G., Chakraborty, T., & Manya, D. (2021). Disproportionate exposure to urban heat island intensity across major US cities. *Nature Communications*, *12*(1), 2721. https://doi.org/10.1038/s41467-021-22799-5

Huang, K., Li, X., Liu, X., & Seto, K. C. (2019). Projecting global urban land expansion and heat island intensification through 2050. *Environmental Research Letters*, *14*(11), 114037. https://doi.org/10.1088/1748-9326/ab4b71

Huang, X., & Ge, J. (2019). Electric vehicle development in Beijing: An analysis of consumer purchase intention. *Journal of Cleaner Production*, *216*, 361–372. https://doi.org/10.1016/j.jclepro.2019.01.231

Hutchison, P. J. (2008). Journalism and the perfect heat wave: Assessing the reportage of North America's worst heat wave, July-August 1936. *American Journalism*, *25*(1), 31–54.

Hutter, H.-P., Moshammer, H., Wallner, P., Leitner, B., & Kundi, M. (2007). Heatwaves in Vienna: Effects on mortality. *Wiener Klinische Wochenschrift*, *119*.

Inbar, O., Morris, N., Epstein, Y., & Gass, G. (2004). Comparison of thermoregulatory responses to exercise in dry heat among prepubertal boys, young adults and older males. *Experimental Physiology*, *89*(6), 691–700.

Iowa State University. (2023). *Iowa Environmental Mesonet* [dataset]. https://mesonet.agron.iastate.edu/request/download.phtml

Ivajnšič, D., Kaligarič, M., & Žiberna, I. (2014). Geographically weighted regression of the urban heat island of a small city. *Applied Geography*, *53*, 341–353. https://doi.org/10.1016/j.apgeog.2014.07.001

J. Zhou, Y. Chen, J. Wang, & W. Zhan. (2011). Maximum Nighttime Urban Heat Island (UHI) Intensity Simulation by Integrating Remotely Sensed Data and Meteorological Observations. *IEEE Journal of Selected Topics in Applied Earth Observations and Remote Sensing*, *4*(1), 138–146. https://doi.org/10.1109/JSTARS.2010.2070871

Jacobson, M. Z., & Ten Hoeve, J. E. (2012). Effects of Urban Surfaces and White Roofs on Global and Regional Climate. *Journal of Climate*, *25*(3), 1028–1044. https://doi.org/10.1175/JCLI-D-11-00032.1

Jenn, A., Azevedo, I. L., & Ferreira, P. (2013). The impact of federal incentives on the adoption of hybrid electric vehicles in the United States. *Energy Economics*, *40*, 936–942. https://doi.org/10.1016/j.eneco.2013.07.025

Jenn, A., Lee, J. H., Hardman, S., & Tal, G. (2020). An in-depth examination of electric vehicle incentives: Consumer heterogeneity and changing response over time. *TRANSPORTATION RESEARCH PART A-POLICY AND PRACTICE*, *132*, 97–109. https://doi.org/10.1016/j.tra.2019.11.004

Jesdale, B. M., Morello-Frosch, R., & Cushing, L. (2013). The racial/ethnic distribution of heat risk–related land cover in relation to residential segregation. *Environmental Health Perspectives*, *121*(7), 811–817.

Jia, W., & Chen, T. D. (2021). Are Individuals' stated preferences for electric vehicles (EVs) consistent with real-world EV ownership patterns? *Transportation Research Part D: Transport and Environment*, *93*, 102728. https://doi.org/10.1016/j.trd.2021.102728

Jiang, J., Liu, Y., Mao, J., & Wu, G. (2023). Extreme heatwave over Eastern China in summer 2022: The role of three oceans and local soil moisture feedback. *Environmental Research Letters*, *18*(4), 044025.

Ju, J., & Roy, D. P. (2008). The availability of cloud-free Landsat ETM+ data over the conterminous United States and globally. *Remote Sensing of Environment*, *112*(3), 1196–1211. https://doi.org/10.1016/j.rse.2007.08.011

Karlessi, T., Santamouris, M., Synnefa, A., Assimakopoulos, D., Didaskalopoulos, P., & Apostolakis, K. (2011). Development and testing of PCM doped cool colored coatings to mitigate urban heat island and cool buildings. *Building and Environment*, *46*(3), 570–576. https://doi.org/10.1016/j.buildenv.2010.09.003

Kenney, W. L., & Hodgson, J. L. (1987). Heat tolerance, thermoregulation and ageing. *Sports Medicine*, *4*, 446–456.

Kenney, W. L., Morgan, A. L., Farquhar, W. B., Brooks, E. M., Pierzga, J. M., & Derr, J. A. (1997). Decreased active vasodilator sensitivity in aged skin. *American Journal of Physiology-Heart and Circulatory Physiology*, *272*(4), H1609–H1614.

Ketterer, C., & Matzarakis, A. (2015). Comparison of different methods for the assessment of the urban heat island in Stuttgart, Germany. *International Journal of Biometeorology*, *59*(9), 1299–1309. https://doi.org/10.1007/s00484-014-0940-3

Kim, Y., & Kim, Y. (2022). Explainable heat-related mortality with random forest and SHapley Additive exPlanations (SHAP) models. *Sustainable Cities and Society*, *79*, 103677. https://doi.org/10.1016/j.scs.2022.103677

Klenk, J., Becker, C., & Rapp, K. (2010). Heat-related mortality in residents of nursing homes. *Age and Ageing*, *39*(2), 245–252. https://doi.org/10.1093/ageing/afp248

Klinenberg, E. (2015). *Heat wave: A social autopsy of disaster in Chicago*. University of Chicago press.

Kolokotroni, M., & Giridharan, R. (2008). Urban heat island intensity in London: An investigation of the impact of physical characteristics on changes in outdoor air temperature during summer. *Solar Energy*, *82*(11), 986–998.

Kong, F., Yin, H., James, P., Hutyra, L. R., & He, H. S. (2014). Effects of spatial pattern of greenspace on urban cooling in a large metropolitan area of eastern China. *Landscape and Urban Planning*, *128*, 35–47. https://doi.org/10.1016/j.landurbplan.2014.04.018

Kong, J., Zhao, Y., Carmeliet, J., & Lei, C. (2021). Urban Heat Island and Its Interaction with Heatwaves: A Review of Studies on Mesoscale. *Sustainability*, *13*(19). https://doi.org/10.3390/su131910923

Kousis, I., Pigliautile, I., & Pisello, A. L. (2021). Intra-urban microclimate investigation in urban heat island through a novel mobile monitoring system. *Scientific Reports*, *11*(1), 9732.

Kovats, R. S., Hajat, S., & Wilkinson, P. (2004). Contrasting patterns of mortality and hospital admissions during hot weather and heat waves in Greater London, UK. *Occupational and Environmental Medicine*, *61*(11), 893–898.

Krause, R. M., Carley, S. R., Lane, B. W., & Graham, J. D. (2013). Perception and reality: Public knowledge of plug-in electric vehicles in 21 US cities. *Energy Policy*, *63*, 433–440.

Krishna, R. (1972). *Remote sensing of urban heat islands from an environmental satellite*.

Kumar, R., & Mishra, V. (2019). Decline in surface urban heat island intensity in India during heatwaves. *Environmental Research Communications*, *1*(3), 031001.

Kumar, R. R., & Alok, K. (2020). Adoption of electric vehicle: A literature review and prospects for sustainability. *Journal of Cleaner Production*, *253*, 119911. https://doi.org/10.1016/j.jclepro.2019.119911

Kunst, A. E., Looman, C. W., & Mackenbach, J. P. (1993). Outdoor air temperature and mortality in the Netherlands: A time-series analysis. *American Journal of Epidemiology*, *137*(3), 331–341.

Lai, L.-W., & Cheng, W.-L. (2009). Air quality influenced by urban heat island coupled with synoptic weather patterns. *Science of The Total Environment*, *407*(8), 2724–2733. https://doi.org/10.1016/j.scitotenv.2008.12.002

Langbroek, J. H. M., Franklin, J. P., & Susilo, Y. O. (2016). The effect of policy incentives on electric vehicle adoption. *Energy Policy*, *94*, 94–103. https://doi.org/10.1016/j.enpol.2016.03.050

Li, H., Zhou, Y., Li, X., Meng, L., Wang, X., Wu, S., & Sodoudi, S. (2018). A new method to quantify surface urban heat island intensity. *Science of The Total Environment*, *624*, 262–272. https://doi.org/10.1016/j.scitotenv.2017.11.360

Li, S., Zhao, Z., Miaomiao, X., & Wang, Y. (2010). Investigating spatial non-stationary and scale-dependent relationships between urban surface temperature and environmental factors using geographically weighted regression. *Environmental Modelling & Software*, *25*(12), 1789–1800. https://doi.org/10.1016/j.envsoft.2010.06.011

Li, X., Li, W., Middel, A., Harlan, S. L., Brazel, A. J., & Turner, B. L. (2016). Remote sensing of the surface urban heat island and land architecture in Phoenix, Arizona: Combined effects of land composition and configuration and cadastral–demographic–economic factors. *Remote Sensing of Environment*, *174*, 233–243. https://doi.org/10.1016/j.rse.2015.12.022

Li, X., Zhou, Y., Asrar, G. R., & Zhu, Z. (2018). Creating a seamless 1km resolution daily land surface temperature dataset for urban and surrounding areas in the conterminous United States. *Remote Sensing of Environment*, *206*, 84–97. https://doi.org/10.1016/j.rse.2017.12.010

Lieven, T. (2015). Policy measures to promote electric mobility – A global perspective. *Transportation Research Part A: Policy and Practice*, *82*, 78–93. https://doi.org/10.1016/j.tra.2015.09.008

Lindsey, & Dahlman. (2023). *Climate Change:Global Temperature* (Understanding Climate) [NOAA Article]. NOAA. https://www.climate.gov/news-features/understanding-climate/climate-change-global-temperature

Liu, H., Dai, Z., Rodgers, M. O., & Guensler, R. (2022). Equity issues associated with U.S. plug-in electric vehicle income tax credits. *Transportation Research Part D: Transport and Environment*, *102*, 103159. https://doi.org/10.1016/j.trd.2021.103159

Liu, Z., Ma, X., Hu, L., Liu, Y., Lu, S., Chen, H., & Tan, Z. (2022). Nonlinear Cooling Effect of Street Green Space Morphology: Evidence from a Gradient Boosting Decision Tree and Explainable Machine Learning Approach. *Land*, *11*(12), 2220.

Lundberg, S. M., Erion, G., Chen, H., DeGrave, A., Prutkin, J. M., Nair, B., Katz, R., Himmelfarb, J., Bansal, N., & Lee, S.-I. (2020). From local explanations to global understanding with explainable AI for trees. *Nature Machine Intelligence*, *2*(1), 56–67. https://doi.org/10.1038/s42256-019-0138-9

Lustgarten, A. (2020). How climate migration will reshape America. *New York Times Magazine*, *15*.

Mack, G. W., Weseman, C. A., Langhans, G. W., Scherzer, H., Gillen, C. M., & Nadel, E. R. (1994). Body fluid balance in dehydrated healthy older men: Thirst and renal osmoregulation. *Journal of Applied Physiology*, *76*(4), 1615–1623.

Mackenbach, J. P., Borst, V., & Schols, J. M. (1997). Heat-related mortality among nursing-home patients. *The Lancet*, *349*(9061), 1297–1298.

Makido, Y., Shandas, V., Ferwati, S., & Sailor, D. (2016). Daytime Variation of Urban Heat Islands: The Case Study of Doha, Qatar. *Climate*, *4*(2). https://doi.org/10.3390/cli4020032

Mallick, R. B., Chen, B.-L., & Bhowmick, S. (2009). Harvesting energy from asphalt pavements and reducing the heat island effect. *International Journal of Sustainable Engineering*, *2*(3), 214–228. https://doi.org/10.1080/19397030903121950

Marmor, M. (1978). Heat wave mortality in nursing homes. *Environmental Research*, *17*(1), 102–115.

Memon, R. A., Leung, D. Y. C., & Liu, C.-H. (2010). Effects of building aspect ratio and wind speed on air temperatures in urban-like street canyons. *International Symposium on the Interaction between Human and Building Environment Special Issue Section*, *45*(1), 176–188. https://doi.org/10.1016/j.buildenv.2009.05.015

Meng, Q., Zhang, L., Sun, Z., Meng, F., Wang, L., & Sun, Y. (2018). Characterizing spatial and temporal trends of surface urban heat island effect in an urban main built-up area: A 12-year case study in Beijing, China. *Remote Sensing of Environment*, *204*, 826–837.

Menon, Akbari, Mahanama, Sednev, & Levinson. (2010). Radiative forcing and temperature response to changes in urban albedos and associated CO2 offsets. *ENVIRONMENTAL RESEARCH LETTERS*, *5*(1). https://doi.org/10.1088/1748-9326/5/1/014005

Miescher, E., & Fortney, S. M. (1989). Responses to dehydration and rehydration during heat exposure in young and older men. *American Journal of Physiology-Regulatory, Integrative and Comparative Physiology*, *257*(5), R1050–R1056.

Minson, C. T., Wladkowski, S. L., Cardell, A. F., Pawelczyk, J. A., & Kenney, W. L. (1998). Age alters the cardiovascular response to direct passive heating. *Journal of Applied Physiology*, *84*(4), 1323–1332.

Mitchell, B. C., & Chakraborty, J. (2014). URBAN HEAT AND CLIMATE JUSTICE: A LANDSCAPE OF THERMAL INEQUITY IN PINELLAS COUNTY, FLORIDA. *GEOGRAPHICAL REVIEW*, *104*(4), 459–480. https://doi.org/10.1111/j.1931-0846.2014.12039.x

Morris, C. J. G., Simmonds, I., & Plummer, N. (2001). Quantification of the Influences of Wind and Cloud on the Nocturnal Urban Heat Island of a Large City. *Journal of Applied Meteorology*, *40*(2), 169–182. https://doi.org/10.1175/1520-0450(2001)040<0169:QOTIOW>2.0.CO;2

Moss, J. L., Doick, K. J., Smith, S., & Shahrestani, M. (2019). Influence of evaporative cooling by urban forests on cooling demand in cities. *Green Infrastructures: Nature Based Solutions for Sustainable and Resilient Cities*, *37*, 65–73. https://doi.org/10.1016/j.ufug.2018.07.023

Mussetti, G., Davin, E. L., Schwaab, J., Acero, J. A., Ivanchev, J., Singh, V. K., Jin, L., & Seneviratne, S. I. (2022). Do Electric Vehicles Mitigate Urban Heat? The Case of a Tropical City. *Frontiers in Environmental Science*, *10*. https://www.frontiersin.org/articles/10.3389/fenvs.2022.810342

Nakai, S., Itoh, T., & Morimoto, T. (1999). Deaths from heat-stroke in Japan: 1968–1994. *International Journal of Biometeorology*, *43*, 124–127.

Narassimhan, E., & Johnson, C. (2018). The role of demand-side incentives and charging infrastructure on plug-in electric vehicle adoption: Analysis of US States. *Environmental Research Letters*, *13*(7), 074032.

Nemirovsky, E. M., Welker, A. L., & Lee, R. (2013). Quantifying evaporation from pervious concrete systems: Methodology and hydrologic perspective. *Journal of Irrigation and Drainage Engineering*, *139*(4), 271–277.

Nitschke, M., Tucker, G. R., Hansen, A. L., Williams, S., Zhang, Y., & Bi, P. (2011). Impact of two recent extreme heat episodes on morbidity and mortality in Adelaide, South Australia: A case-series analysis. *Environmental Health*, *10*(1), 1–9.

Oke, T. R. (1973). City size and the urban heat island. *Atmospheric Environment (1967)*, *7*(8), 769–779. https://doi.org/10.1016/0004-6981(73)90140-6

Oke, T. R. (1982). The energetic basis of the urban heat island. *Quarterly Journal of the Royal Meteorological Society*, *108*(455), 1–24.

Oke, T. R. (1988). The urban energy balance. *Progress in Physical Geography*, *12*(4), 471–508.

Oke, T. R. (1997). Urban environments. *The Surface Climates of Canada*, 303–327.

Oke, T. R. (2004). *Initial Guidance to Obtain Representative Meteorological Observations at Urban Sites*. World Meteorological Organization. https://books.google.com/books?id=uJkznQEACAAJ

Oke, T. R. (2011). Urban heat islands. *The Handbook of Urban Ecology*, 120–131.

Onozuka, D., & Hashizume, M. (2011). The influence of temperature and humidity on the incidence of hand, foot, and mouth disease in Japan. *Science of the Total Environment*, *410*, 119–125.

Oukawa, G. Y., Krecl, P., & Targino, A. C. (2022). Fine-scale modeling of the urban heat island: A comparison of multiple linear regression and random forest approaches. *Science of The Total Environment*, *815*, 152836. https://doi.org/10.1016/j.scitotenv.2021.152836

Paul, M. J., & Meyer, J. L. (2001). Streams in the Urban Landscape. *Annual Review of Ecology and Systematics*, *32*(1), 333–365. https://doi.org/10.1146/annurev.ecolsys.32.081501.114040

Peng, J., Xie, P., Liu, Y., & Ma, J. (2016). Urban thermal environment dynamics and associated landscape pattern factors: A case study in the Beijing metropolitan

region. *Remote Sensing of Environment*, *173*, 145–155. https://doi.org/10.1016/j.rse.2015.11.027

Peng, S., Piao, S., Ciais, P., Friedlingstein, P., Ottle, C., Bréon, F.-M., Nan, H., Zhou, L., & Myneni, R. B. (2012). Surface Urban Heat Island Across 419 Global Big Cities. *Environmental Science & Technology*, *46*(2), 696–703. https://doi.org/10.1021/es2030438

Philip, S. Y., Kew, S. F., van Oldenborgh, G. J., Anslow, F. S., Seneviratne, S. I., Vautard, R., Coumou, D., Ebi, K. L., Arrighi, J., Singh, R., van Aalst, M., Pereira Marghidan, C., Wehner, M., Yang, W., Li, S., Schumacher, D. L., Hauser, M., Bonnet, R., Luu, L. N., … Otto, F. E. L. (2022). Rapid attribution analysis of the extraordinary heat wave on the Pacific coast of the US and Canada in June 2021. *Earth System Dynamics*, *13*(4), 1689–1713. https://doi.org/10.5194/esd-13-1689-2022

Phillips, P. A., Bretherton, M., Johnston, C. I., & Gray, L. (1991). Reduced osmotic thirst in healthy elderly men. *American Journal of Physiology-Regulatory, Integrative and Comparative Physiology*, *261*(1), R166–R171.

Pichierri, M., Bonafoni, S., & Biondi, R. (2012). Satellite air temperature estimation for monitoring the canopy layer heat island of Milan. *Remote Sensing of Environment*, *127*, 130–138.

Pigliautile, I., & Pisello, A. L. (2018). A new wearable monitoring system for investigating pedestrians' environmental conditions: Development of the experimental tool and start-up findings. *Science of The Total Environment*, *630*, 690–706. https://doi.org/10.1016/j.scitotenv.2018.02.208

Pinho, O. S., & Orgaz, M. D. M. (2000). The urban heat island in a small city in coastal Portugal. *International Journal of Biometeorology*, *44*(4), 198–203. https://doi.org/10.1007/s004840000063

Qin, Y. (2015a). A review on the development of cool pavements to mitigate urban heat island effect. *Renewable and Sustainable Energy Reviews*, *52*, 445–459. https://doi.org/10.1016/j.rser.2015.07.177

Qin, Y. (2015b). Urban canyon albedo and its implication on the use of reflective cool pavements. *Energy and Buildings*, *96*, 86–94. https://doi.org/10.1016/j.enbuild.2015.03.005

Quan, J., Chen, Y., Zhan, W., Wang, J., Voogt, J., & Wang, M. (2014). Multi-temporal trajectory of the urban heat island centroid in Beijing, China based on a Gaussian volume model. *Remote Sensing of Environment*, *149*, 33–46. https://doi.org/10.1016/j.rse.2014.03.037

Rahman, M. A., Armson, D., & Ennos, A. R. (2015). A comparison of the growth and cooling effectiveness of five commonly planted urban tree species. *Urban Ecosystems*, *18*(2), 371–389. https://doi.org/10.1007/s11252-014-0407-7

Rahman, M. A., Smith, J. G., Stringer, P., & Ennos, A. R. (2011). Effect of rooting conditions on the growth and cooling ability of Pyrus calleryana. *Urban Forestry & Urban Greening*, *10*(3), 185–192. https://doi.org/10.1016/j.ufug.2011.05.003

Rahman, M. A., Stratopoulos, L. M. F., Moser-Reischl, A., Zölch, T., Häberle, K.-H., Rötzer, T., Pretzsch, H., & Pauleit, S. (2020). Traits of trees for cooling urban heat islands: A meta-analysis. *Building and Environment*, *170*, 106606. https://doi.org/10.1016/j.buildenv.2019.106606

Rajagopalan, P., Lim, K. C., & Jamei, E. (2014). Urban heat island and wind flow characteristics of a tropical city. *Solar Energy*, *107*, 159–170. https://doi.org/10.1016/j.solener.2014.05.042

Ramamurthy, P., González, J., Ortiz, L., Arend, M., & Moshary, F. (2017). Impact of heatwave on a megacity: An observational analysis of New York City during July 2016. *Environmental Research Letters*, *12*(5), 054011.

Rigo, G., Parlow, E., & Oesch, D. (2006). Validation of satellite observed thermal emission with in-situ measurements over an urban surface. *Thermal Remote Sensing of Urban Areas*, *104*(2), 201–210. https://doi.org/10.1016/j.rse.2006.04.018

Romero Rodríguez, L., Sánchez Ramos, J., & Álvarez Domínguez, S. (2023). Simplifying the process to perform air temperature and UHI measurements at large scales: Design of a new APP and low-cost Arduino device. *Sustainable Cities and Society*, *95*, 104614. https://doi.org/10.1016/j.scs.2023.104614

Romero Rodríguez, L., Sánchez Ramos, J., Sánchez de la Flor, F. J., & Álvarez Domínguez, S. (2020). Analyzing the urban heat Island: Comprehensive methodology for data gathering and optimal design of mobile transects. *Sustainable Cities and Society*, *55*, 102027. https://doi.org/10.1016/j.scs.2020.102027

Roof, S., & Callagan, C. (2003). The climate of Death Valley, California. *Bulletin of the American Meteorological Society*, *84*(12), 1725–1740.

Rose, L. S., Akbari, H., & Taha, H. (2003). *Characterizing the fabric of the urban environment: A case study of Greater Houston, Texas*. Lawrence Berkeley National Lab.(LBNL), Berkeley, CA (United States).

Rötzer, T., Rahman, M. A., Moser-Reischl, A., Pauleit, S., & Pretzsch, H. (2019). Process based simulation of tree growth and ecosystem services of urban trees under present and future climate conditions. *Science of The Total Environment*, *676*, 651–664. https://doi.org/10.1016/j.scitotenv.2019.04.235

Saaroni, H., Ben-Dor, E., Bitan, A., & Potchter, O. (2000). Spatial distribution and microscale characteristics of the urban heat island in Tel-Aviv, Israel. *Landscape and Urban Planning*, *48*(1), 1–18. https://doi.org/10.1016/S0169-2046(99)00075-4

Salamanca, F., Georgescu, M., Mahalov, A., Moustaoui, M., Wang, M., & Svoma, B. M. (2013). Assessing summertime urban air conditioning consumption in a semiarid environment. *Environmental Research Letters*, *8*(3), 034022.

Santamouris, M. (2013). Using cool pavements as a mitigation strategy to fight urban heat island—A review of the actual developments. *Renewable and Sustainable Energy Reviews*, *26*, 224–240. https://doi.org/10.1016/j.rser.2013.05.047

Santamouris, M., Gaitani, N., Spanou, A., Saliari, M., Giannopoulou, K., Vasilakopoulou, K., & Kardomateas, T. (2012). Using cool paving materials to improve microclimate of urban areas – Design realization and results of the flisvos project. *Building and Environment*, *53*, 128–136. https://doi.org/10.1016/j.buildenv.2012.01.022

Santamouris, M., Paraponiaris, K., & Mihalakakou, G. (2007). Estimating the ecological footprint of the heat island effect over Athens, Greece. *Climatic Change*, *80*(3–4), 265–276.

Schellen, L., van Marken Lichtenbelt, W. D., Loomans, M. G., Toftum, J., & De Wit, M. H. (2010). Differences between young adults and elderly in thermal comfort, productivity, and thermal physiology in response to a moderate temperature drift and a steady-state condition. *Indoor Air*, *20*(4), 273–283.

Schickele, E. (1947). Environment and fatal heat stroke: An analysis of 157 cases occurring in the army in the US during World War II. *The Military Surgeon (United States)*, *100*(3), 235–256.

Scholz, M., & Grabowiecki, P. (2007). Review of permeable pavement systems. *Building and Environment*, *42*(11), 3830–3836.

Schrock, G., Bassett, E. M., & Green, J. (2015). Pursuing equity and justice in a changing climate: Assessing equity in local climate and sustainability plans in US cities. *Journal of Planning Education and Research*, *35*(3), 282–295.

Schwarz, N., Schlink, U., Franck, U., & Großmann, K. (2012). Relationship of land surface and air temperatures and its implications for quantifying urban heat island indicators—An application for the city of Leipzig (Germany). *Ecological Indicators*, *18*, 693–704. https://doi.org/10.1016/j.ecolind.2012.01.001

Semenza, J. C., Rubin, C. H., Falter, K. H., Selanikio, J. D., Flanders, W. D., Howe, H. L., & Wilhelm, J. L. (1996). Heat-related deaths during the July 1995 heat wave in Chicago. *New England Journal of Medicine*, *335*(2), 84–90.

Shandas, V., Makido, Y., & Upraity, A. N. (2023). Evaluating Differences between Ground-Based and Satellite-Derived Measurements of Urban Heat: The Role of Land Cover Classes in Portland, Oregon and Washington, D.C. *Land*, *12*(3). https://doi.org/10.3390/land12030562

Shandas, V., Voelkel, Williams, & Hoffman. (2019). Integrating Satellite and Ground Measurements for Predicting Locations of Extreme Urban Heat. *Climate*, *7*(1). https://doi.org/10.3390/cli7010005

Shapley, L. S. (1953). *A value for n-person games*.

Shashua-Bar, L., Pearlmutter, D., & Erell, E. (2009). The cooling efficiency of urban landscape strategies in a hot dry climate. *Landscape and Urban Planning*, *92*(3), 179–186. https://doi.org/10.1016/j.landurbplan.2009.04.005

Sheldon, T. L. (2022). Evaluating Electric Vehicle Policy Effectiveness and Equity. *Annual Review of Resource Economics*, *14*(1), null. https://doi.org/10.1146/annurev-resource-111820-022834

Shen, H., Li, X., Cheng, Q., Zeng, C., Yang, G., Li, H., & Zhang, L. (2015). Missing information reconstruction of remote sensing data: A technical review. *IEEE Geoscience and Remote Sensing Magazine*, *3*(3), 61–85.

Sherman, P., Lin, H., & McElroy, M. (2022). Projected global demand for air conditioning associated with extreme heat and implications for electricity grids in poorer countries. *Energy and Buildings*, *268*, 112198. https://doi.org/10.1016/j.enbuild.2022.112198

Sidiqui, P., Huete, A., & Devadas, R. (2016). Spatio-temporal mapping and monitoring of Urban Heat Island patterns over Sydney, Australia using MODIS and Landsat-8. *2016 4th International Workshop on Earth Observation and Remote Sensing Applications (EORSA)*, 217–221. https://doi.org/10.1109/EORSA.2016.7552800

Silva, H. R., Bhardwaj, R., Phelan, P. E., Golden, J. S., & Grossman-Clarke, S. (2009). Development of a Zero-Dimensional Mesoscale Thermal Model for Urban Climate. *Journal of Applied Meteorology and Climatology*, *48*(3), 657–668. https://doi.org/10.1175/2008JAMC1962.1

Smith. (2014). *Notebook on Spatial Data Analysis*. https://www.seas.upenn.edu/~tesmith/NOTEBOOK/index.html

Springel, K. (2021). Network Externality and Subsidy Structure in Two-Sided Markets: Evidence from Electric Vehicle Incentives. *AMERICAN ECONOMIC JOURNAL-ECONOMIC POLICY*, *13*(4), 393–432. https://doi.org/10.1257/pol.20190131

Spronken-Smith, R. A., & Oke, T. R. (1998). The thermal regime of urban parks in two cities with different summer climates. *International Journal of Remote Sensing*, *19*(11), 2085–2104. https://doi.org/10.1080/014311698214884

Starke, P., Göbel, P., & Coldewey, W. G. (2011). Effects on evaporation rates from different water-permeable pavement designs. *Water Science and Technology*, *63*(11), 2619–2627.

State of Vermont National Electric Vehicle Infrastructure Plan. (2022). Vermont Agency of Transportation. https://www.fhwa.dot.gov/environment/nevi/ev_deployment_plans/vt_nevi_plan.pdf

Stathopoulou, M., & Cartalis, C. (2009). Downscaling AVHRR land surface temperatures for improved surface urban heat island intensity estimation. *Remote Sensing of Environment*, *113*(12), 2592–2605. https://doi.org/10.1016/j.rse.2009.07.017

Stewart, I. D. (2011). A systematic review and scientific critique of methodology in modern urban heat island literature. *International Journal of Climatology*, *31*(2), 200–217. https://doi.org/10.1002/joc.2141

Stewart, I. D., & Oke, T. R. (2012). Local Climate Zones for Urban Temperature Studies. *Bulletin of the American Meteorological Society*, *93*(12), 1879–1900. https://doi.org/10.1175/BAMS-D-11-00019.1

Stone Brian, Hess Jeremy J., & Frumkin Howard. (2010). Urban Form and Extreme Heat Events: Are Sprawling Cities More Vulnerable to Climate Change Than Compact

Cities? *Environmental Health Perspectives*, *118*(10), 1425–1428. https://doi.org/10.1289/ehp.0901879

Streutker, D. R. (2002). A remote sensing study of the urban heat island of Houston, Texas. *International Journal of Remote Sensing*, *23*(13), 2595–2608. https://doi.org/10.1080/01431160110115023

Sun, Y.-J., Wang, J.-F., Zhang, R.-H., Gillies, R. R., Xue, Y., & Bo, Y.-C. (2005). Air temperature retrieval from remote sensing data based on thermodynamics. *Theoretical and Applied Climatology*, *80*, 37–48.

Sundararajan, M., & Najmi, A. (2020). The many Shapley values for model explanation. *International Conference on Machine Learning*, 9269–9278.

Synnefa, A., Dandou, A., Santamouris, M., Tombrou, M., & Soulakellis, N. (2008a). On the Use of Cool Materials as a Heat Island Mitigation Strategy. *Journal of Applied Meteorology and Climatology*, *47*(11), 2846–2856. https://doi.org/10.1175/2008JAMC1830.1

Synnefa, A., Dandou, A., Santamouris, M., Tombrou, M., & Soulakellis, N. (2008b). On the Use of Cool Materials as a Heat Island Mitigation Strategy. *Journal of Applied Meteorology and Climatology*, *47*(11), 2846–2856. https://doi.org/10.1175/2008JAMC1830.1

Syrrakou, C., & Pinder, G. F. (2014). Experimentally determined evaporation rates in pervious concrete systems. *Journal of Irrigation and Drainage Engineering*, *140*(1), 04013003.

Taha, H., Akbari, H., Rosenfeld, A., & Huang, J. (1988). Residential cooling loads and the urban heat island—The effects of albedo. *Building and Environment*, *23*(4), 271–283. https://doi.org/10.1016/0360-1323(88)90033-9

Takebayashi, H., & Moriyama, M. (2012). Study on surface heat budget of various pavements for urban heat island mitigation. *Advances in Materials Science and Engineering*, *2012*.

Tal, G., & Nicholas, M. (2016). Exploring the impact of the federal tax credit on the plug-in vehicle market. *Transportation Research Record*, *2572*(1), 95–102.

Tan, J., Zheng, Y., Tang, X., Guo, C., Li, L., Song, G., Zhen, X., Yuan, D., Kalkstein, A. J., & Li, F. (2010). The urban heat island and its impact on heat waves and human health in Shanghai. *International Journal of Biometeorology*, *54*, 75–84.

Tan, Z., Lau, K. K.-L., & Ng, E. (2016). Urban tree design approaches for mitigating daytime urban heat island effects in a high-density urban environment. *SI: Countermeasures to Urban Heat Island*, *114*, 265–274. https://doi.org/10.1016/j.enbuild.2015.06.031

Theeuwes, N. E., Solcerová, A., & Steeneveld, G. J. (2013). Modeling the influence of open water surfaces on the summertime temperature and thermal comfort in the city. *Journal of Geophysical Research: Atmospheres*, *118*(16), 8881–8896. https://doi.org/10.1002/jgrd.50704

Tobler, W. R. (1970). A computer movie simulating urban growth in the Detroit region. *Economic Geography*, *46*(sup1), 234–240.

Tominaga, Y., Sato, Y., & Sadohara, S. (2015). CFD simulations of the effect of evaporative cooling from water bodies in a micro-scale urban environment: Validation and application studies. *Sustainable Cities and Society*, *19*, 259–270. https://doi.org/10.1016/j.scs.2015.03.011

Tran, H., Uchihama, D., Ochi, S., & Yasuoka, Y. (2006). Assessment with satellite data of the urban heat island effects in Asian mega cities. *International Journal of Applied Earth Observation and Geoinformation*, *8*(1), 34–48. https://doi.org/10.1016/j.jag.2005.05.003

Tremeac, B., Bousquet, P., de Munck, C., Pigeon, G., Masson, V., Marchadier, C., Merchat, M., Poeuf, P., & Meunier, F. (2012). Influence of air conditioning management on heat island in Paris air street temperatures. *Applied Energy*, *95*, 102–110. https://doi.org/10.1016/j.apenergy.2012.02.015

Tsin, P. K., Knudby, A., Krayenhoff, E. S., Ho, H. C., Brauer, M., & Henderson, S. B. (2016). Microscale mobile monitoring of urban air temperature. *Urban Climate*, *18*, 58–72. https://doi.org/10.1016/j.uclim.2016.10.001

United Nations. (2019). *World Urbanization Prospects, the 2018 Revision*. Department of Economic and Social Affairs. https://population.un.org/wup/Publications/Files/WUP2018-Report.pdf

U.S. Census Bureau. (2022). *American Community Survey, 2020 5-year Estimates, Tables B01001, B19013, and B25033*. U.S. Census Bureau. https://www.census.gov/programs-surveys/decennial-census/about/census-acs.html

U.S. National Center for Environmental Health. (2013). *Climate Change and Extreme Heat Events*. https://www.cdc.gov/climateandhealth/pubs/ClimateChangeandExtremeHeatEvents.pdf

USGS. (2023). *USGS Elevation Point Query Service* [dataset]. https://data.usgs.gov/datacatalog/data/USGS:77ae0551-c61e-4979-aedd-d797abdcde0e

Vahmani, P., & Ban-Weiss, G. (2016). Climatic consequences of adopting drought-tolerant vegetation over Los Angeles as a response to California drought. *Geophysical Research Letters*, *43*(15), 8240–8249.

Vandentorren, S., Bretin, P., Zeghnoun, A., Mandereau-Bruno, L., Croisier, A., Cochet, C., Ribéron, J., Siberan, I., Declercq, B., & Ledrans, M. (2006). August 2003 Heat Wave in France: Risk Factors for Death of Elderly People Living at Home. *European Journal of Public Health*, *16*(6), 583–591. https://doi.org/10.1093/eurpub/ckl063

Vardoulakis, E., Karamanis, D., Fotiadi, A., & Mihalakakou, G. (2013). The urban heat island effect in a small Mediterranean city of high summer temperatures and

cooling energy demands. *Solar Energy*, *94*, 128–144. https://doi.org/10.1016/j.solener.2013.04.016

Vermont Center for Geographic Information. (2019). *Vermont Impervious Surfaces Land Cover, 2016*. https://geodata.vermont.gov/pages/land-cover

Vermont Center for Geographic Information. (2021). *Parcels Datasets*. Vermont Open Geodata Portal. https://geodata.vermont.gov/pages/parcels

Vermont Open Geodata Portal. (2019). *Vermont Land Cover* [Map]. https://geodata.vermont.gov/pages/land-cover

Voelkel, J., & Shandas, V. (2017). Towards Systematic Prediction of Urban Heat Islands: Grounding Measurements, Assessing Modeling Techniques. *Climate*, *5*(2). https://doi.org/10.3390/cli5020041

Völker, S., Baumeister, H., Claßen, T., Hornberg, C., & Kistemann, T. (2013). Evidence for the temperature-mitigating capacity of urban blue space—A health geographic perspective. *Erdkunde*, 355–371.

Voogt, J. A., & Oke, T. R. (2003). Thermal remote sensing of urban climates. *Urban Remote Sensing*, *86*(3), 370–384. https://doi.org/10.1016/S0034-4257(03)00079-8

Wang, H., Wu, S., Chen, M., & Zhang, Y. (2010). Numerical simulation on the thermal response of heat-conducting asphalt pavements. *Physica Scripta*, *2010*(T139), 014041.

Wang, S., Li, J., & Zhao, D. (2017). The impact of policy measures on consumer intention to adopt electric vehicles: Evidence from China. *Transportation Research Part A: Policy and Practice*, *105*, 14–26.

Wang, S., Ma, Q., Ding, H., & Liang, H. (2018). Detection of urban expansion and land surface temperature change using multi-temporal landsat images. *Resources, Conservation and Recycling*, *128*, 526–534. https://doi.org/10.1016/j.resconrec.2016.05.011

Weather Related Fatality and Injury Statistics. (2021). National Weather Service. https://www.weather.gov/hazstat/

Wee, S., Coffman, M., & La Croix, S. (2018). Do electric vehicle incentives matter? Evidence from the 50 U.S. states. *Research Policy*, *47*. https://doi.org/10.1016/j.respol.2018.05.003

Wenger, C. B. (1995). The regulation of body temperature. *Medical Physiology. New York: Little, Brown*, 587–613.

White-Newsome, J. L., Sánchez, B. N., Jolliet, O., Zhang, Z., Parker, E. A., Dvonch, J. T., & O'neill, M. S. (2012). Climate change and health: Indoor heat exposure in vulnerable populations. *Environmental Research*, *112*, 20–27.

White-Newsome, J., O'Neill, M. S., Gronlund, C., Sunbury, T. M., Brines, S. J., Parker, E., Brown, D. G., Rood, R. B., & Rivera, Z. (2009). Climate change, heat waves, and environmental justice: Advancing knowledge and action. *Environmental Justice*, *2*(4), 197–205.

Williamson, R. H. (1972). Effects of environment on pavement temperatures. *Intl Conf Structural Design Proc*, *1*(Proc).

Wilson, B. (2020). Urban Heat Management and the Legacy of Redlining. *Journal of the American Planning Association*, *86*(4), 443–457. https://doi.org/10.1080/01944363.2020.1759127

Winter, E. (2002). Chapter 53 The shapley value. In *Handbook of Game Theory with Economic Applications* (Vol. 3, pp. 2025–2054). Elsevier. https://doi.org/10.1016/S1574-0005(02)03016-3

Won Kim, C., Phipps, T. T., & Anselin, L. (2003). Measuring the benefits of air quality improvement: A spatial hedonic approach. *Journal of Environmental Economics and Management*, *45*(1), 24–39. https://doi.org/10.1016/S0095-0696(02)00013-X

Xu, L.-Y., Yin, H., & Xie, X.-D. (2014). Health Risk Assessment of Inhalable Particulate Matter in Beijing Based on the Thermal Environment. *International Journal of Environmental Research and Public Health*, *11*(12), 12368–12388. https://doi.org/10.3390/ijerph111212368

Xu, Z., Etzel, R. A., Su, H., Huang, C., Guo, Y., & Tong, S. (2012). Impact of ambient temperature on children's health: A systematic review. *Environmental Research*, *117*, 120–131. https://doi.org/10.1016/j.envres.2012.07.002

Yaghoobian, N., & Kleissl, J. (2012). Effect of reflective pavements on building energy use. *Urban Climate*, *2*, 25–42. https://doi.org/10.1016/j.uclim.2012.09.002

Yang, L., Qian, F., Song, D.-X., & Zheng, K.-J. (2016). Research on Urban Heat-Island Effect. *Fourth International Conference on Countermeasures to Urban Heat Island, 30-31 May and 1 June 2016*, *169*, 11–18. https://doi.org/10.1016/j.proeng.2016.10.002

Yang, X., Peng, L. L., Jiang, Z., Chen, Y., Yao, L., He, Y., & Xu, T. (2020). Impact of urban heat island on energy demand in buildings: Local climate zones in Nanjing. *Applied Energy*, *260*, 114279.

Yang, Z., Slowik, P., Lutsey, N., & Searle, S. (2016). Principles for effective electric vehicle incentive design. *International Council Clean Transportation June*.

Yin, C., Yuan, M., Lu, Y., Huang, Y., & Liu, Y. (2018). Effects of urban form on the urban heat island effect based on spatial regression model. *Science of the Total Environment*, *634*, 696–704.

Yin, Z., Zhou, B., Duan, M., Chen, H., & Wang, H. (2023). Climate extremes become increasingly fierce in China. *The Innovation*, *4*(2), 100406.

Yu, S., Chen, Z., Yu, B., Wang, L., Wu, B., Wu, J., & Zhao, F. (2020). Exploring the relationship between 2D/3D landscape pattern and land surface temperature based on explainable eXtreme Gradient Boosting tree: A case study of Shanghai, China. *Science of The Total Environment*, *725*, 138229. https://doi.org/10.1016/j.scitotenv.2020.138229

Yu, Z., Guo, X., Jørgensen, G., & Vejre, H. (2017). How can urban green spaces be planned for climate adaptation in subtropical cities? *Ecological Indicators*, *82*, 152–162. https://doi.org/10.1016/j.ecolind.2017.07.002

Zhang, D., & Gaston, D. (2004). Northern China maximum temperature in the summer of 1743: A historical event of burning summer in a relatively warm climate background. *Chinese Science Bulletin*, *49*(23), 2508–2514. https://doi.org/10.1007/BF03183723

Zhang, L., Ma, Z., & Guo, L. (2009). An Evaluation of Spatial Autocorrelation and Heterogeneity in the Residuals of Six Regression Models. *Forest Science*, *55*(6), 533–548. https://doi.org/10.1093/forestscience/55.6.533

Zhang, L., Meng, Q., Sun, Z., & Sun, Y. (2017). Spatial and Temporal Analysis of the Mitigating Effects of Industrial Relocation on the Surface Urban Heat Island over China. *ISPRS International Journal of Geo-Information*, *6*(4). https://doi.org/10.3390/ijgi6040121

Zhang, X., Friedl, M. A., Schaaf, C. B., Strahler, A. H., & Schneider, A. (2004). The footprint of urban climates on vegetation phenology. *Geophysical Research Letters*, *31*(12).

Zhang, Y., Miao, S., Dai, Y., & Bornstein, R. (2017). Numerical simulation of urban land surface effects on summer convective rainfall under different UHI intensity in Beijing. *Journal of Geophysical Research: Atmospheres*, *122*(15), 7851–7868. https://doi.org/10.1002/2017JD026614

Zhang, Y., Murray, A. T., & Turner, B. L. (2017). Optimizing green space locations to reduce daytime and nighttime urban heat island effects in Phoenix, Arizona. *Landscape and Urban Planning*, *165*, 162–171. https://doi.org/10.1016/j.landurbplan.2017.04.009

Zhou, D., Xiao, J., Bonafoni, S., Berger, C., Deilami, K., Zhou, Y., Frolking, S., Yao, R., Qiao, Z., & Sobrino, J. A. (2019). Satellite Remote Sensing of Surface Urban Heat Islands: Progress, Challenges, and Perspectives. *Remote Sensing*, *11*(1). https://doi.org/10.3390/rs11010048

Zhou, W., Wang, J., & Cadenasso, M. L. (2017). Effects of the spatial configuration of trees on urban heat mitigation: A comparative study. *Remote Sensing of Environment*, *195*, 1–12. https://doi.org/10.1016/j.rse.2017.03.043

Zhou, X., Yamamoto, M., Yan, S., Ishida, Y., Cai, M., Ji, Q., Makvandi, M., & Li, C. (2022). Exploring the impacts of heat release of vehicles on urban heat mitigation in Sendai, Japan using WRF model integrated with urban LCZ. *Sustainable Cities and Society*, *82*, 103922. https://doi.org/10.1016/j.scs.2022.103922

Zhou, Y., Wang, M., Hao, H., Johnson, L., Wang, H., & Hao, H. (2015). Plug-in electric vehicle market penetration and incentives: A global review. *Mitigation and Adaptation Strategies for Global Change*, *20*(5), 777–795. https://doi.org/10.1007/s11027-014-9611-2

Zhu, D., Zhou, X., & Cheng, W. (2022). Water effects on urban heat islands in summer using WRF-UCM with gridded urban canopy parameters—A case study of

Wuhan. *Building and Environment*, *225*, 109528. https://doi.org/10.1016/j.buildenv.2022.109528

Appendix

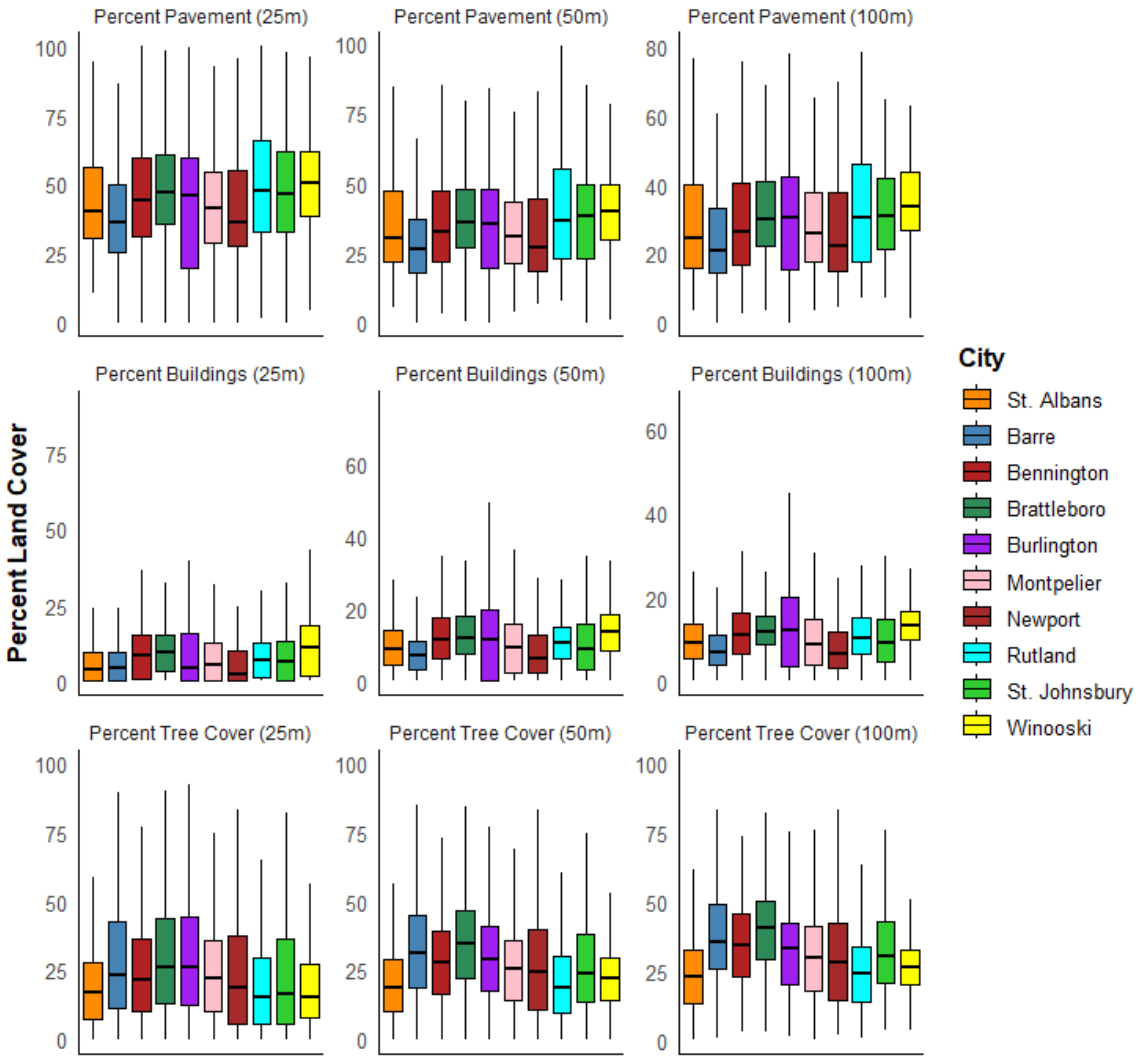

Appendix A. Percent Land Cover Exposure within three different radii. Land cover types include Pavement (the sum of the land cover classes "roads" and "other pavement" as provided by geodata), Buildings, and Tree Cover. Individual boxplots represent the city that measurements were recorded in.

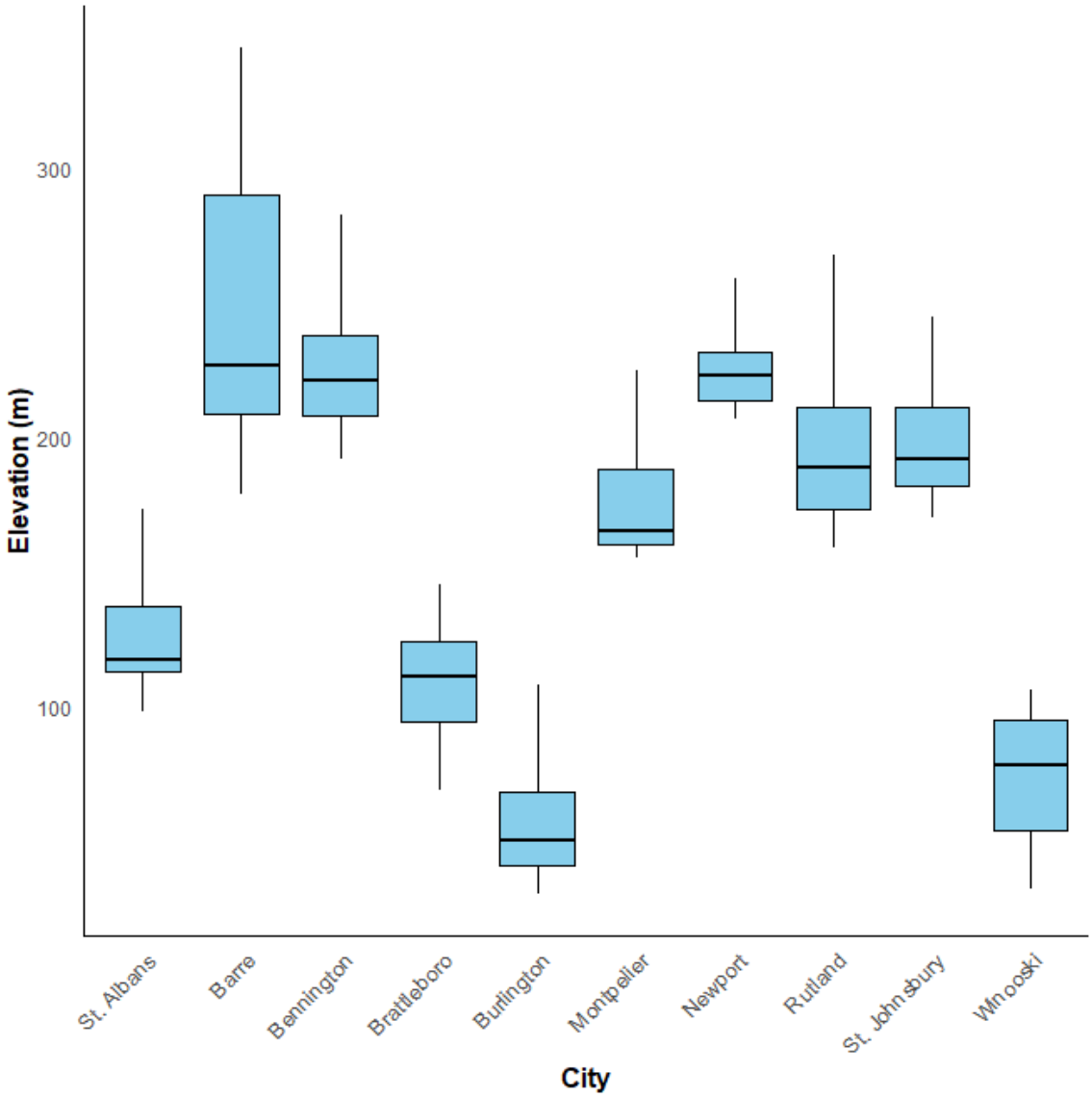

Appendix B. Distribution of elevation (m) for each air temperature measurement by city.

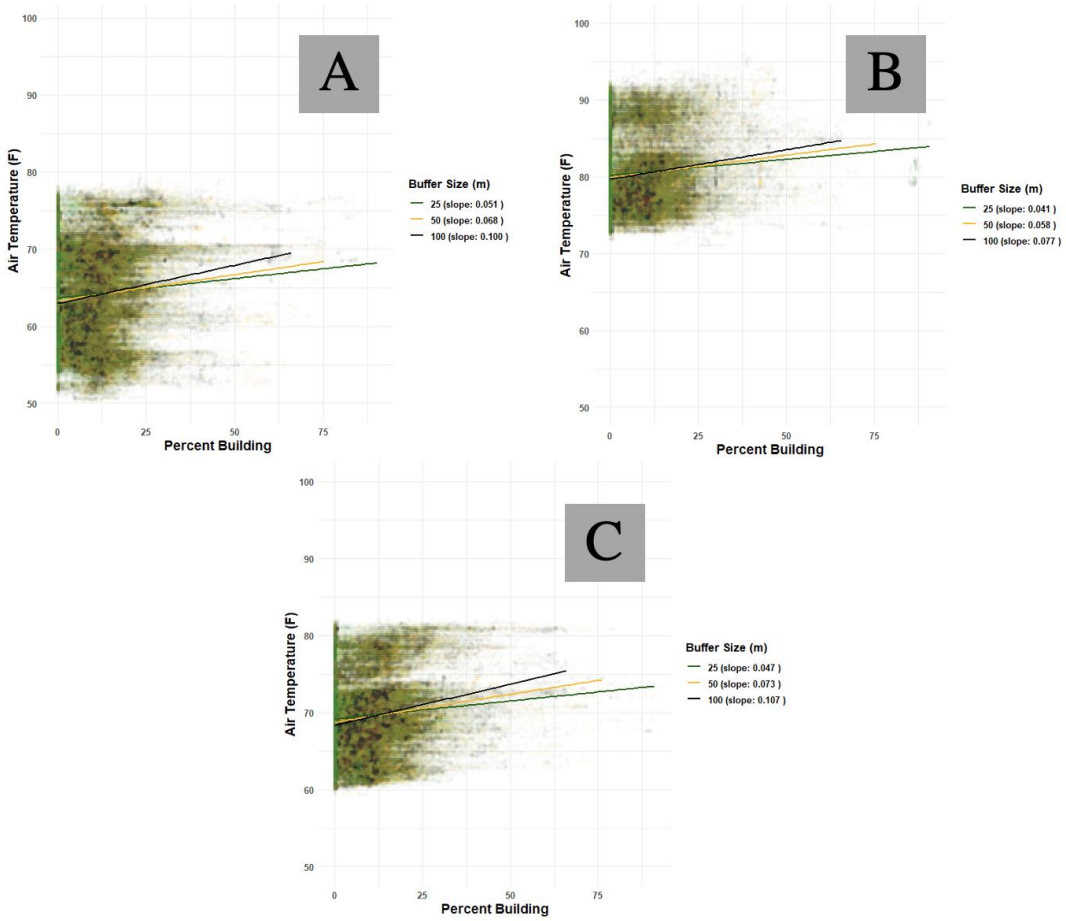

Appendix C. Scatter plots of Percent Building Exposure within three buffer ranges versus air temperature fror A) morning, B) mid-day, and C) evening.

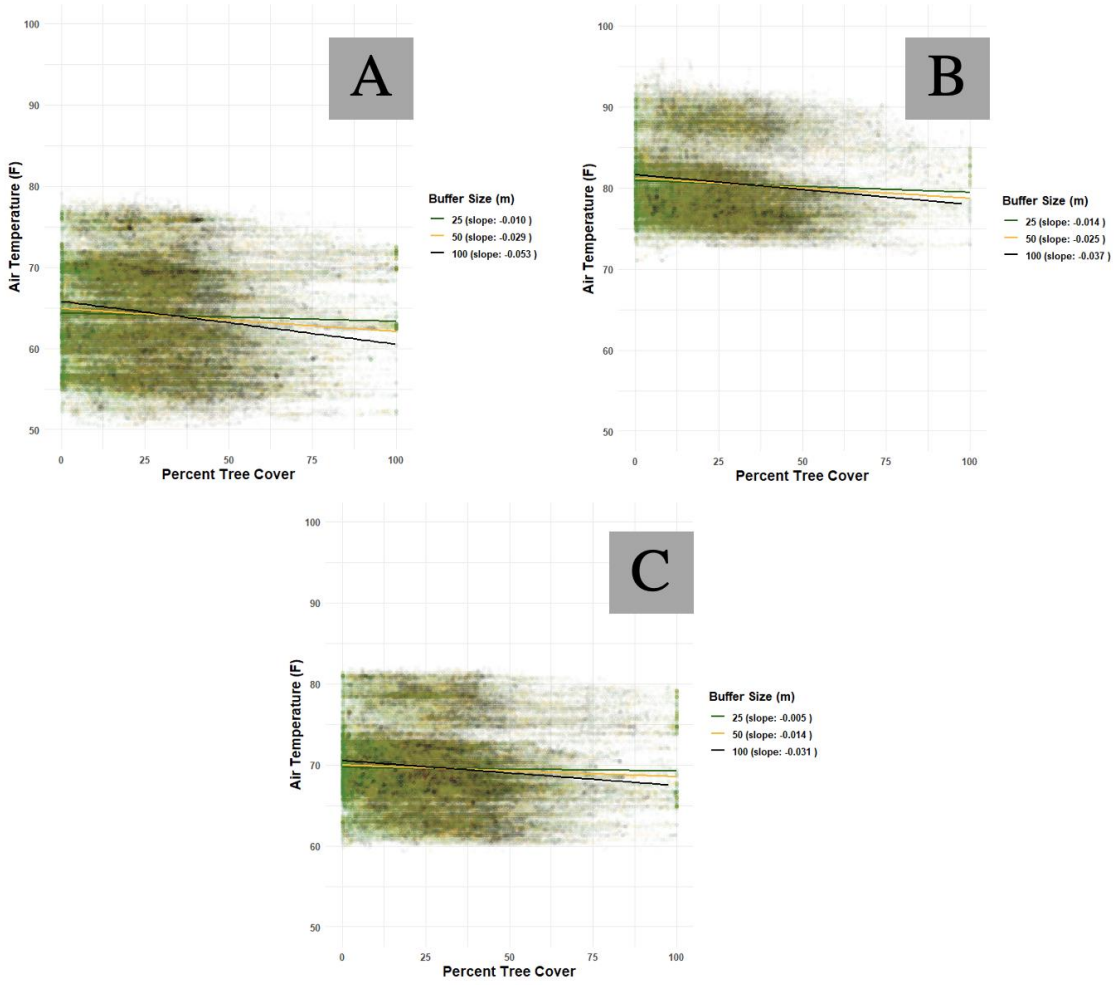

Appendix D. Scatter plot of Percent Tree Cover Exposure within three buffer ranges versus air temperature for A) morning, B) mid-day, and C) evening.

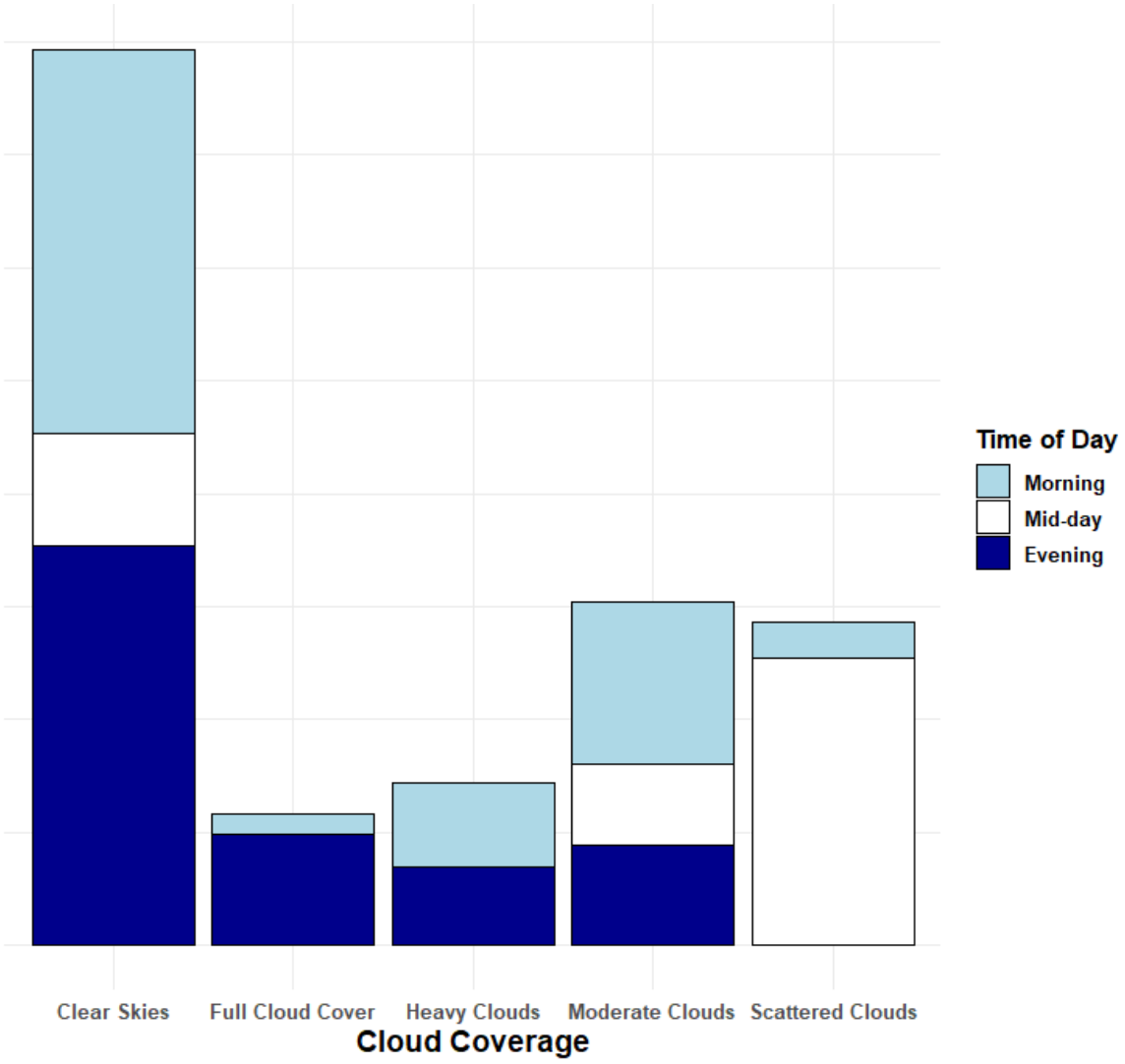

Appendix E. Distribution of cloud coverage as reported by local airport stations during sampling intervals.

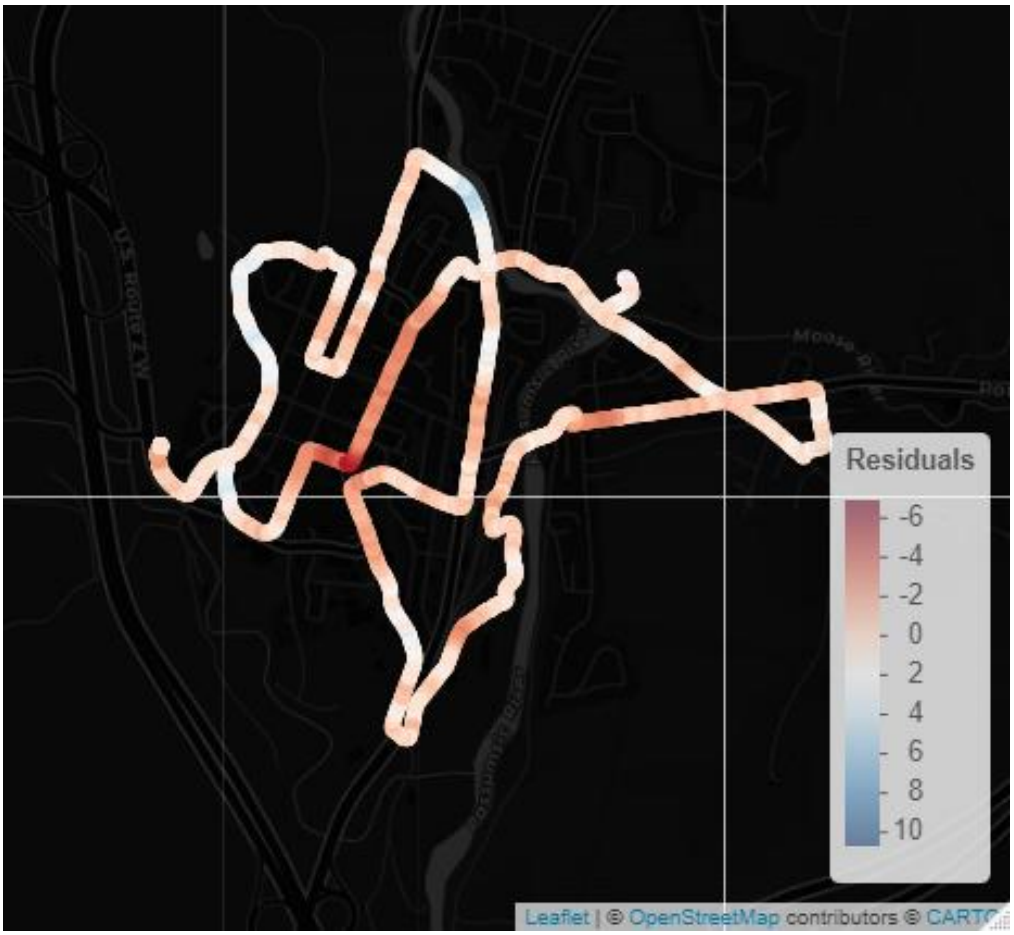

Appendix F. Example of spatial clustering the residuals of a global OLS model. Map shows a subset of residuals from a single transect in St. Johnsbury, VT.

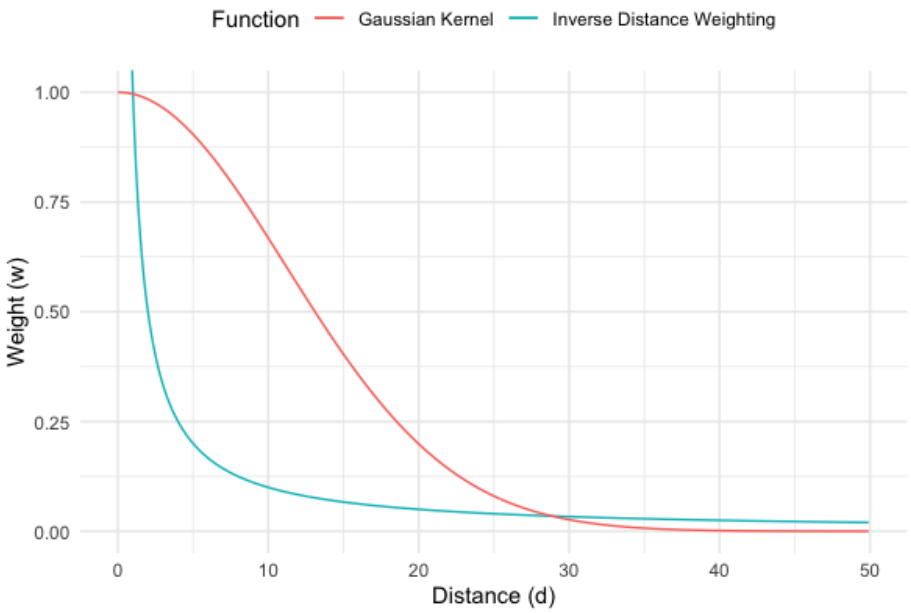

Appendix G. Comparison of spatial weighting through inverse distance vs GKW.

Appendix H. Full OLS regression tables from global models for all nine combinations of buffer size and diurnal phase. Coefficients are bolded if statistically significant (α=0.05).

	Morning					
	25m Buffer		*50m Buffer*		*100m Buffer*	
	Coefficient	SE	Coefficient	SE	Coefficient	SE
Intercept	**-6.059**	0.134	**-5.757**	0.134	**-5.698**	0.133
Percent Pavement (%)	**0.006**	0.001	**0.012**	0.001	**0.022**	0.001
Percent Building (%)	0.001	0.002	**0.021**	0.002	**0.049**	0.003
Percent Tree (%)	**-0.010**	0.000	**-0.018**	0.000	**-0.025**	0.001
Elevation (m)	**0.002**	0.000	**0.002**	0.000	**0.003**	0.000
Time Since Sunrise (s)	**0.001**	0.000	**0.001**	0.000	**0.001**	0.000
High Temperature (F)	**0.718**	0.001	**0.715**	0.001	**0.715**	0.001
Cloud Cover						
Few	**3.442**	0.083	**3.491**	0.074	**3.519**	0.072
Scattered	**3.715**	0.046	**3.804**	0.044	**3.972**	0.043
Broken	**6.508**	0.072	**6.517**	0.069	**6.546**	0.069
Overcast	**0.893**	0.119	**0.905**	0.111	**0.875**	0.117
Windspeed (mph)	**-0.324**	0.009	**-0.314**	0.008	**-0.305**	0.008
Pavement x Cloud Cover						
Few	**-0.005**	0.002	**-0.010**	0.002	**-0.019**	0.003
Scattered	**0.012**	0.001	**0.005**	0.001	**-0.007**	0.001
Broken	**-0.010**	0.001	**-0.011**	0.001	**-0.009**	0.002
Overcast	**-0.048**	0.002	**-0.056**	0.003	**-0.065**	0.004
Building x Cloud Cover						
Few	**-0.010**	0.004	-0.002	0.004	**0.013**	0.005
Scattered	**0.025**	0.002	**0.035**	0.002	**0.050**	0.002
Broken	**0.018**	0.002	**0.017**	0.002	**0.007**	0.003
Overcast	**-0.026**	0.004	**-0.023**	0.004	**-0.020**	0.006
Pavement x Windspeed	**0.005**	0.000	**0.005**	0.000	**0.005**	0.000
Pavement x Building	**0.000**	0.000	**-0.000**	0.000	**-0.001**	0.000
Adjusted R2	*0.913*		*0.916*		*0.918*	

	Mid-day					
	25m Buffer		*50m Buffer*		*100m Buffer*	
	Coefficient	SE	Coefficient	SE	Coefficient	SE
Intercept	**-6.546**	0.282	**-6.296**	0.280	**-6.523**	0.276
Percent Pavement (%)	**0.046**	0.002	**0.053**	0.002	**0.071**	0.003
Percent Building (%)	**0.037**	0.003	**0.044**	0.003	**0.079**	0.004
Percent Tree (%)	**-0.020**	0.001	**-0.026**	0.001	**-0.030**	0.001
Elevation (m)	**0.013**	0.000	**0.013**	0.000	**0.014**	0.000
Time Since Sunrise (s)	**0.000**	0.000	**0.000**	0.000	**0.000**	0.000
High Temperature (F)	**0.906**	0.002	**0.907**	0.002	**0.910**	0.002
Cloud Cover						
Few	**0.236**	0.062	**0.229**	0.057	**0.159**	0.054
Scattered	**-0.403**	0.066	**-0.360**	0.063	**-0.159**	0.061
Broken	X	X	X	X	X	X
Overcast	X	X	X	X	X	X
Windspeed (mph)	**0.313**	0.008	**0.339**	0.007	**0.344**	0.007
Pavement x Cloud Cover						
Few	**-0.022**	0.001	**-0.022**	0.000	**-0.024**	0.002
Scattered	**-0.013**	0.001	**-0.007**	0.001	**-0.006**	0.002
Broken	X	X	X	X	X	X
Overcast	X	X	X	X	X	X
Building x Cloud Cover						
Few	**-0.010**	0.002	**-0.015**	0.002	**-0.014**	0.003
Scattered	**-0.033**	0.003	**-0.054**	0.003	**-0.077**	0.003
Broken	X	X	X	X	X	X
Overcast	X	X	X	X	X	X
Pavement x Windspeed	**-0.001**	0.000	**-0.002**	0.000	**-0.002**	0.000
Pavement x Building	**-0.000**	0.000	**-0.000**	0.000	**-0.001**	0.000
Adjusted R2	*0.855*		*0.856*		*0.859*	

	Evening					
	25m Buffer		*50m Buffer*		*100m Buffer*	
	Coefficient	SE	Coefficient	SE	Coefficient	SE
Intercept	**54.612**	0.347	**53.718**	0.348	**52.856**	0.345
Percent Pavement (%)	**0.030**	0.001	**0.036**	0.001	**0.046**	0.001
Percent Building (%)	**0.030**	0.002	**0.048**	0.002	**0.090**	0.003
Percent Tree (%)	**0.003**	0.000	0.001	0.001	-0.001	0.001
Elevation (m)	**-0.010**	0.000	**-0.010**	0.000	**-0.009**	0.000
Time Since Sunrise (s)	**-0.001**	0.000	**-0.001**	0.000	**-0.001**	0.000
High Temperature (F)	**0.612**	0.002	**0.614**	0.002	**0.615**	0.002
Cloud Cover						
Few	X	X	X	X	X	X
Scattered	**1.307**	0.069	**1.328**	0.069	**1.451**	0.069
Broken	**-0.828**	0.067	**-0.804**	0.067	**-0.834**	0.067
Overcast	**-1.491**	0.057	**-1.502**	0.051	**-1.551**	0.048
Windspeed (mph)	**0.465**	0.008	**0.467**	0.007	**0.476**	0.007
Pavement x Cloud Cover						
Few	X	X	X	X	X	X
Scattered	**0.007**	0.001	**0.012**	0.001	**0.019**	0.002
Broken	**0.029**	0.001	**0.035**	0.001	**0.051**	0.002
Overcast	**-0.006**	0.001	**-0.003**	0.001	**0.007**	0.002
Building x Cloud Cover						
Few	X	X	X	X	X	X
Scattered	**0.004**	0.002	**-0.006**	0.002	**-0.030**	0.003
Broken	**0.040**	0.002	**0.034**	0.002	0.005	0.003
Overcast	**-0.040**	0.003	**-0.043**	0.002	**-0.068**	0.004
Pavement x Windspeed	**-0.001**	0.000	**-0.002**	0.000	**-0.002**	0.000
Pavement x Building	0.000	0.000	**-0.000**	0.000	**-0.001**	0.000
Adjusted R2	*0.806*		*0.809*		*0.813*	

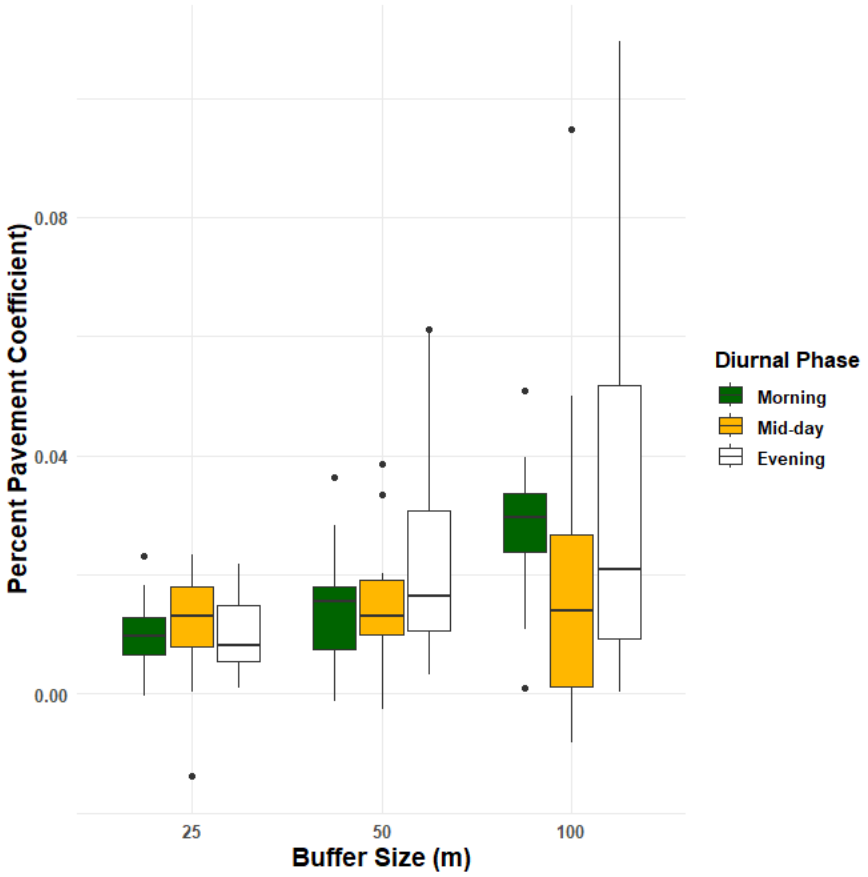

Appendix I. Distribution of pavement exposure coefficients from local SEMs generated with optimal bandwidth parameter.

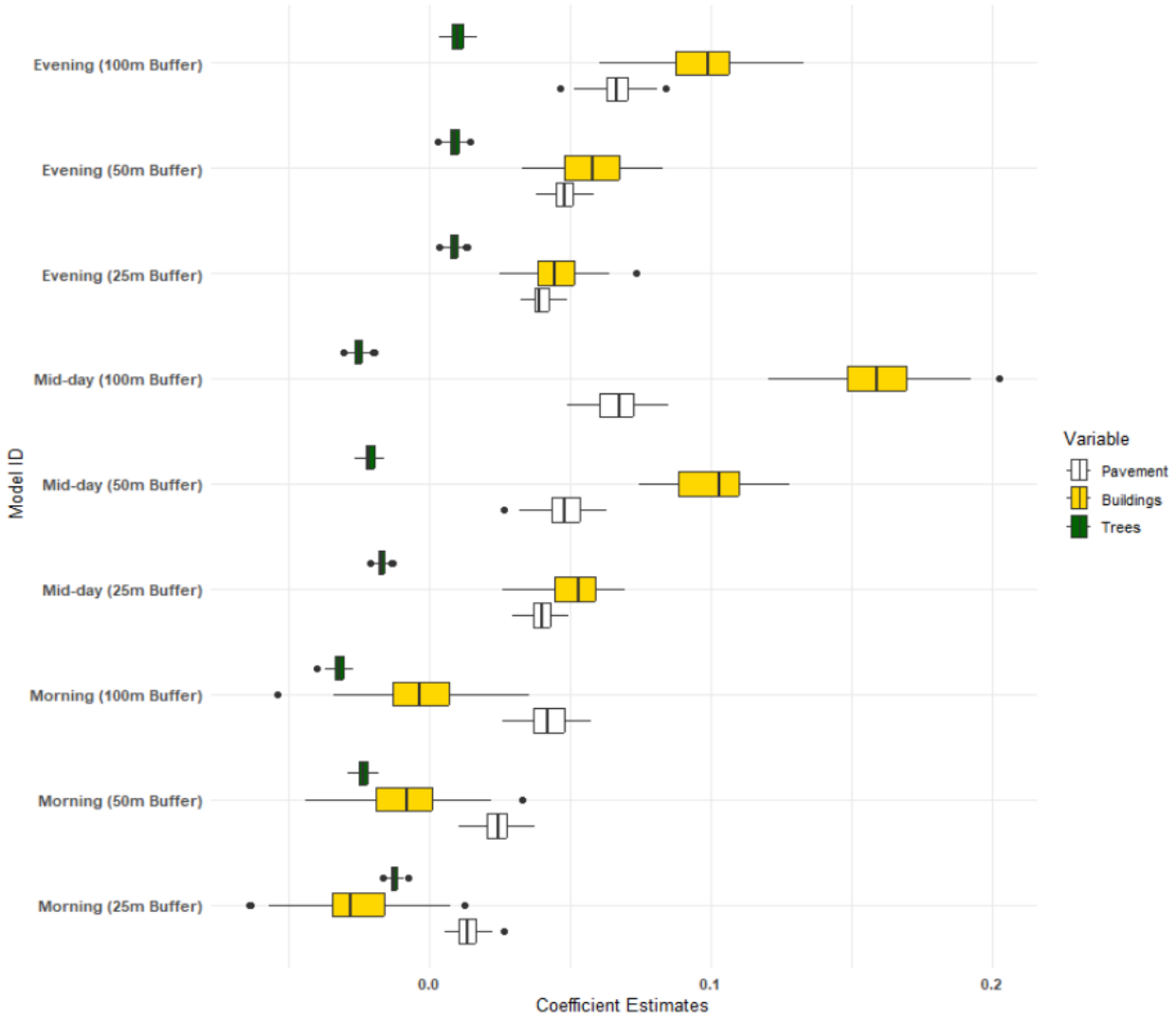

Appendix J. Distributions of the coefficient estimates from each of the nine SEMs. Each boxplot represents the coefficient pertaining to the exposure to a specific land cover within the selected buffer size and diurnal phase for that model.

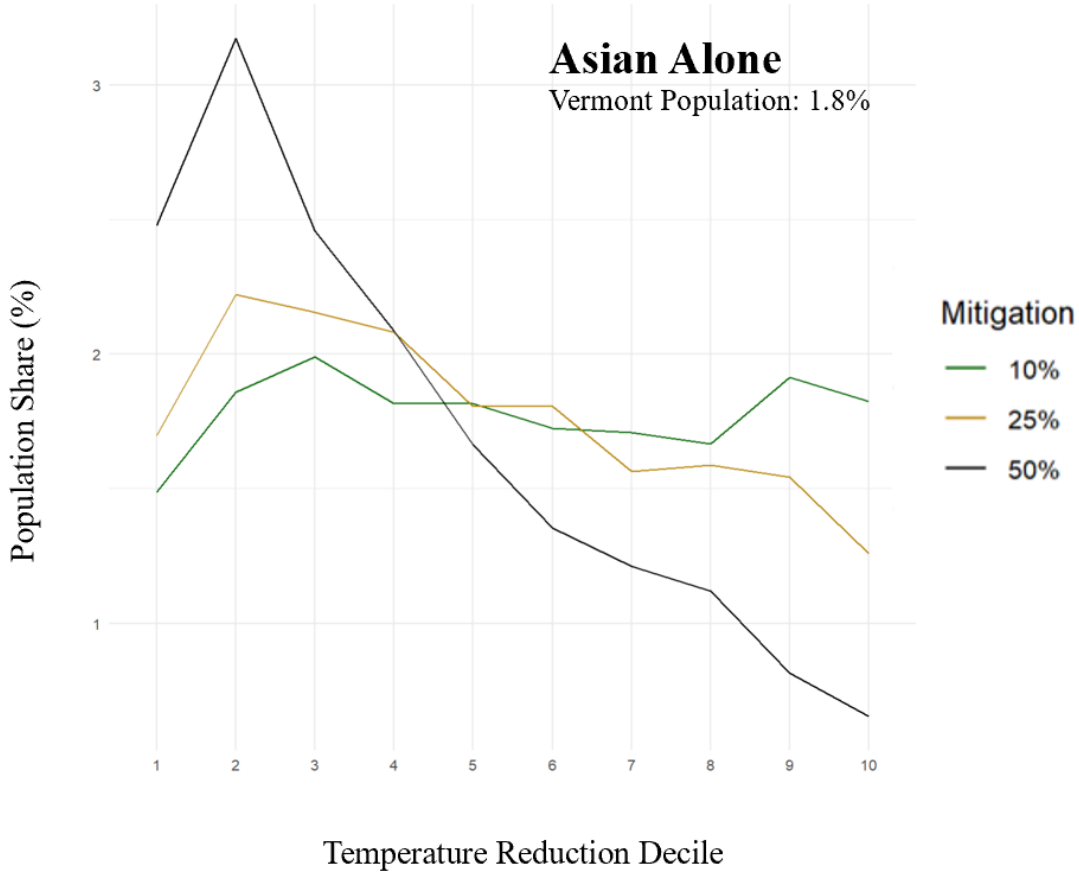

Appendix K. Asian Alone population shares among temperature reduction deciles across all three mitigations scenarios.

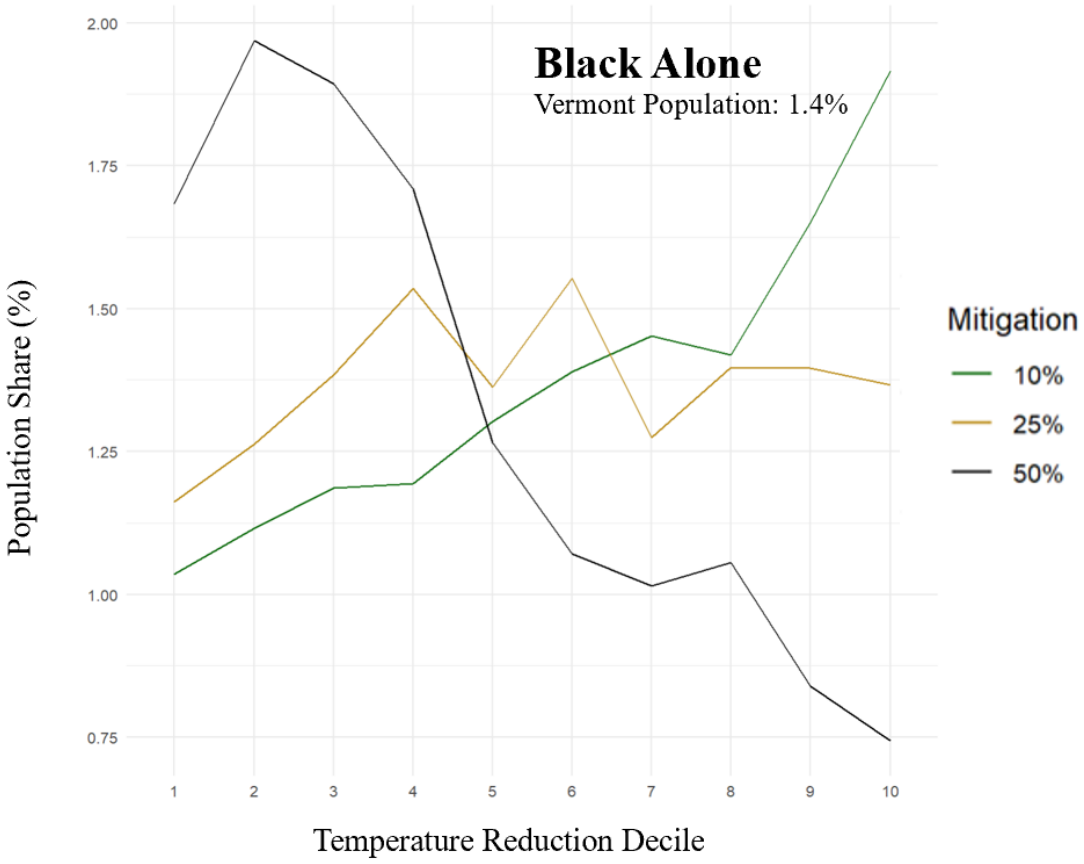

Appendix L. Black Alone population shares among temperature reduction deciles across all three mitigation scenarios.

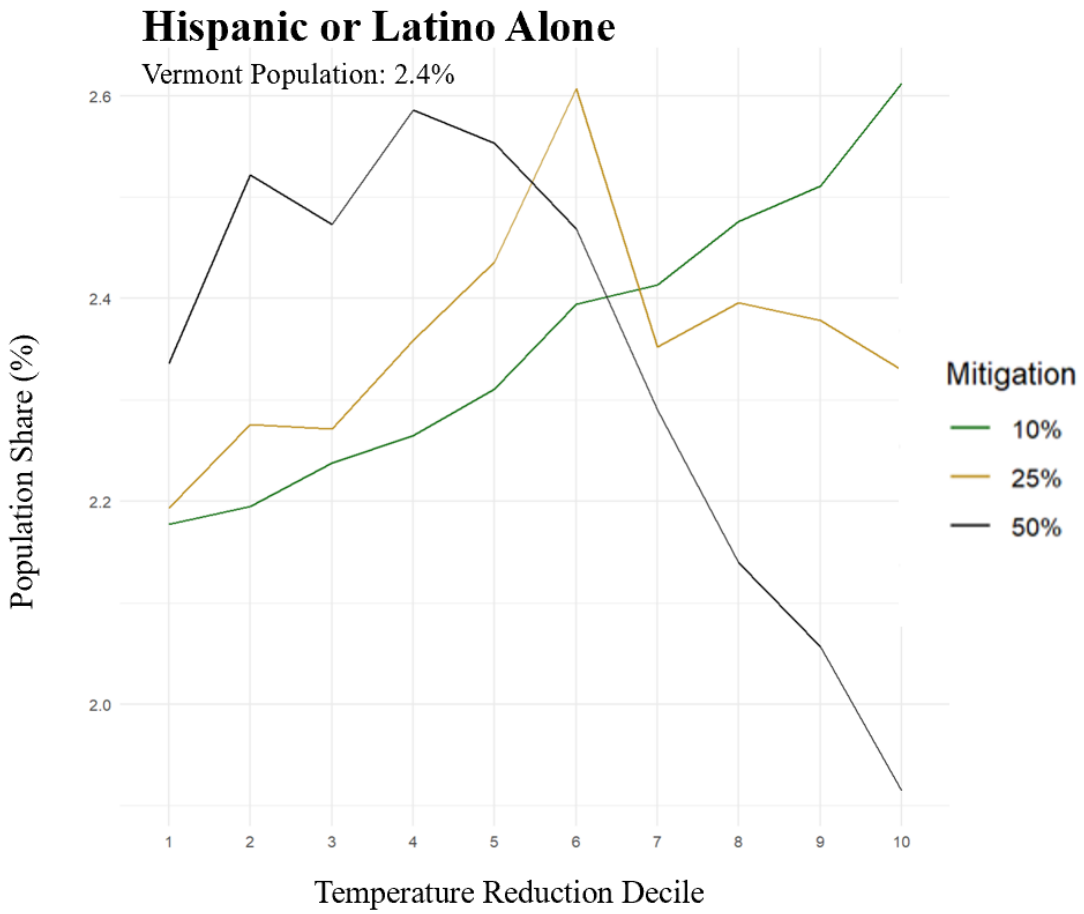

Appendix M. Hispanic or Latino Alone population shares among temperature reduction deciles across all three mitigation scenarios.

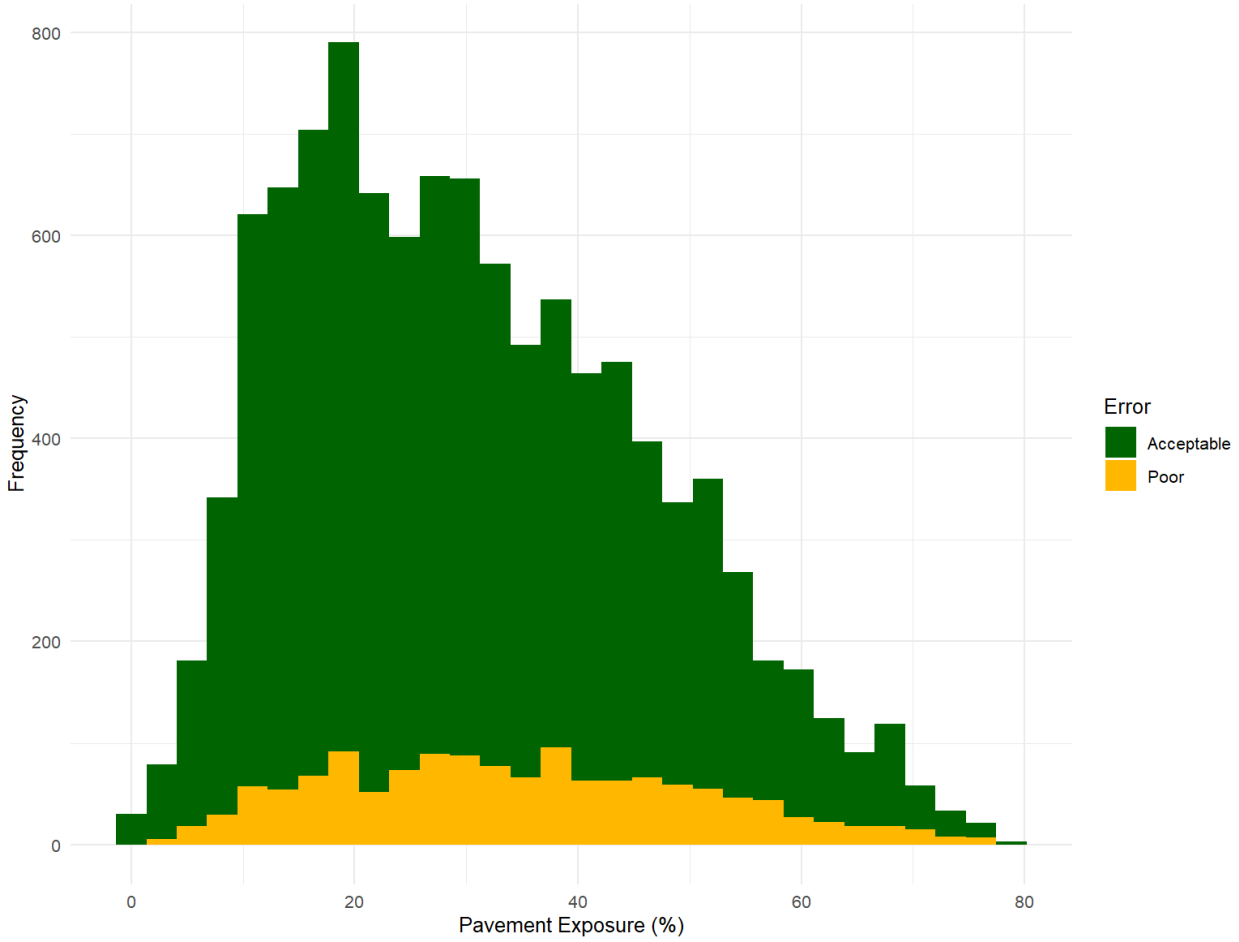

Appendix N. Distribution of pavement exposure values between observations that were predicted within the thresholds of +/- 0.5ºF versus outside of them for the optimal RF model.

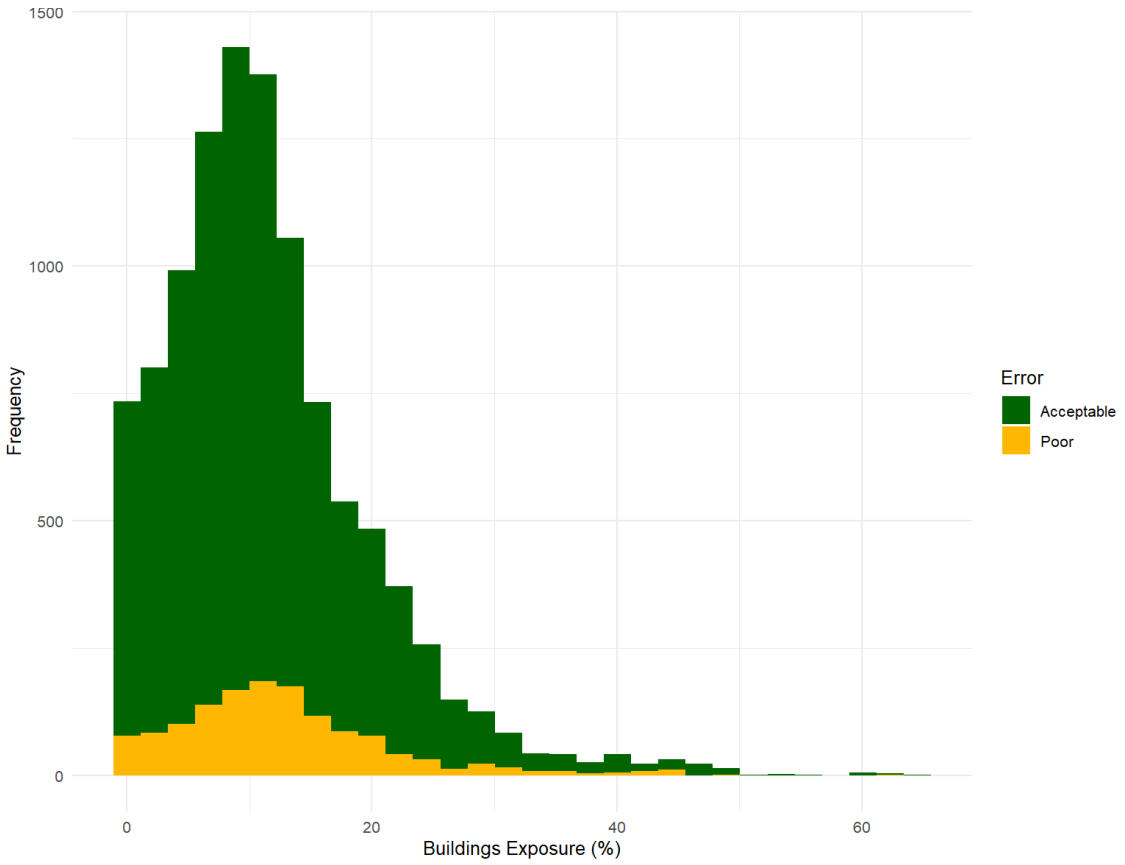

Appendix O. Distribution of building exposure values between observations that were predicted within the thresholds of +/- 0.5ºF versus outside of them for the optimal RF model.

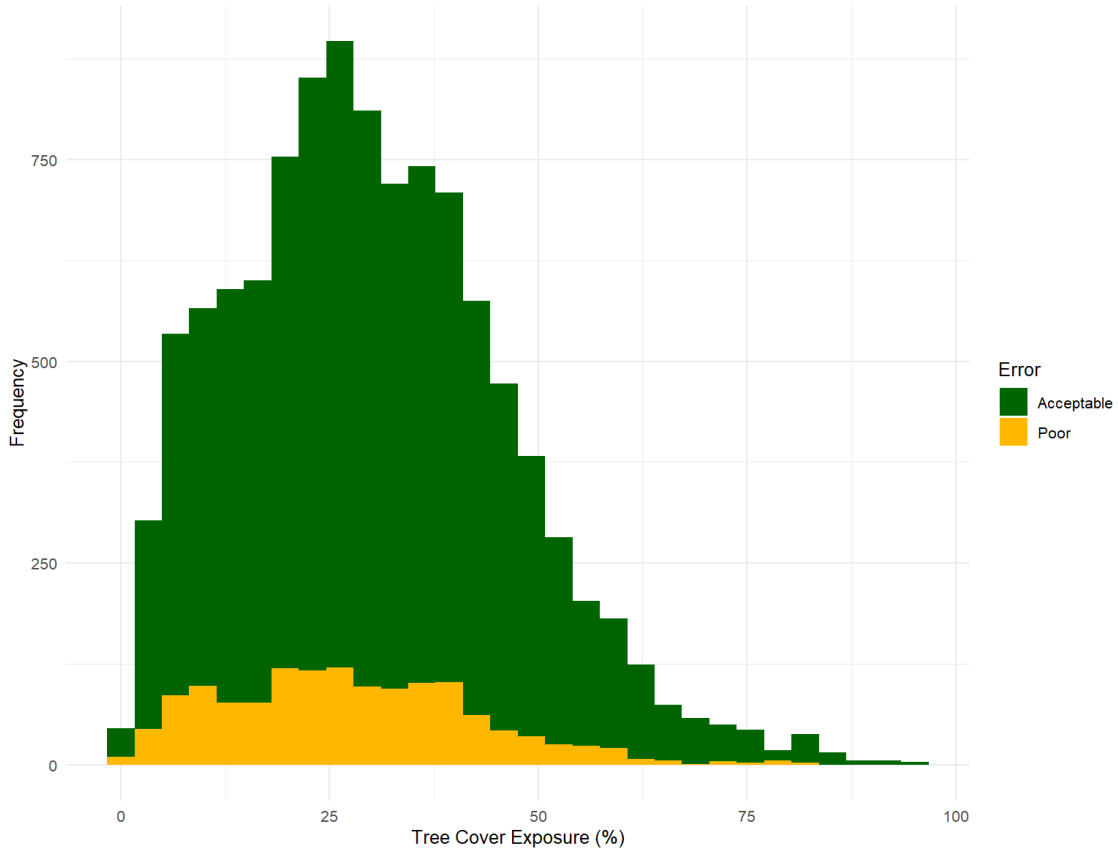

Appendix P. Distribution of tree cover exposure values between observations that were predicted within the thresholds of +/- 0.5ºF versus outside of them for the optimal RF model.

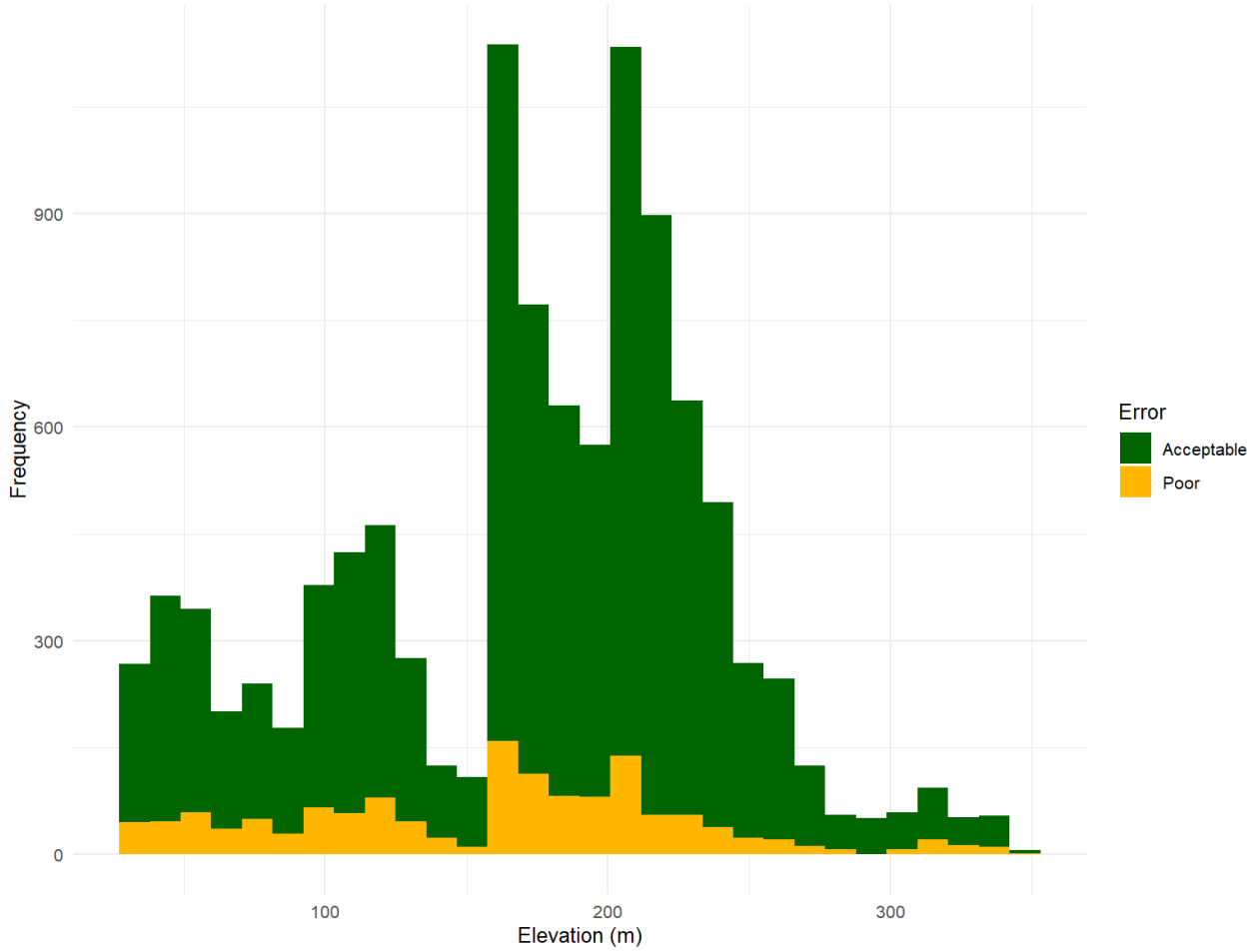

Appendix Q. Distribution of elevation values between observations that were predicted within the thresholds of +/- 0.5ºF versus outside of them for the optimal RF model.

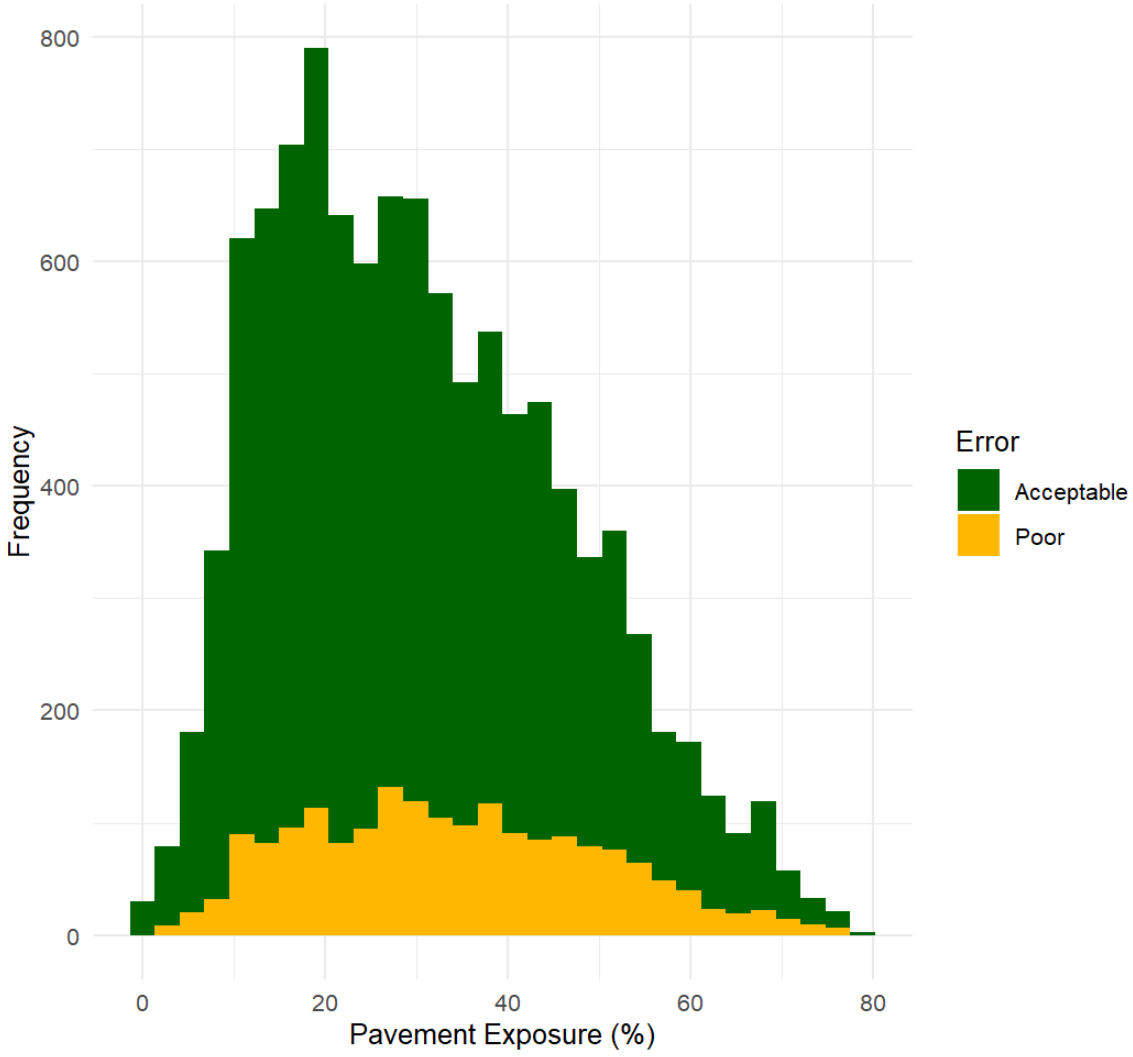

Appendix R. Distribution of pavement exposure values between observations that were predicted within the thresholds of +/- 0.5ºF versus outside of them for the optimal XGBoost model.

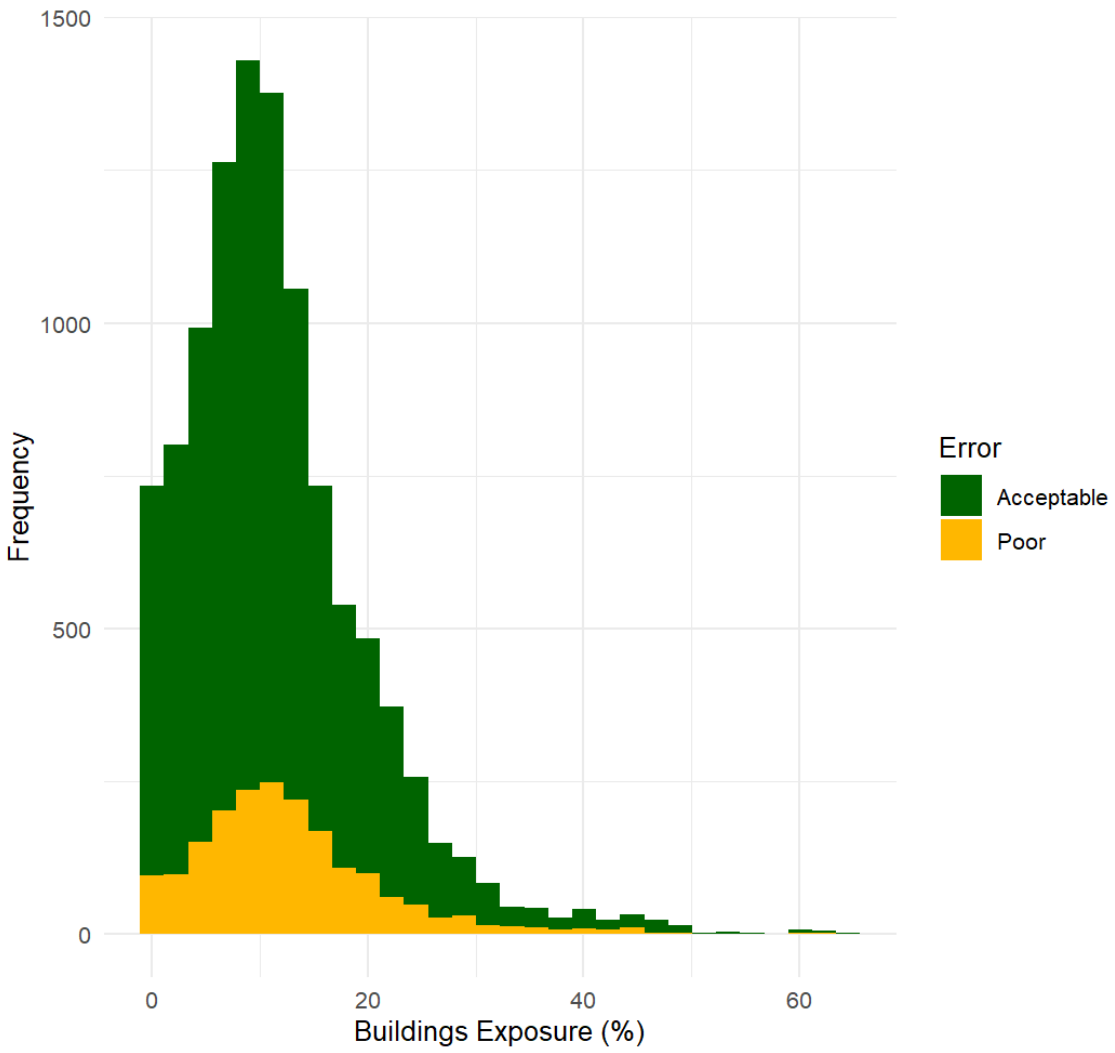

Appendix S. Distribution of building exposure values between observations that were predicted within the thresholds of +/- 0.5ºF versus outside of them for the optimal XGBoost model.

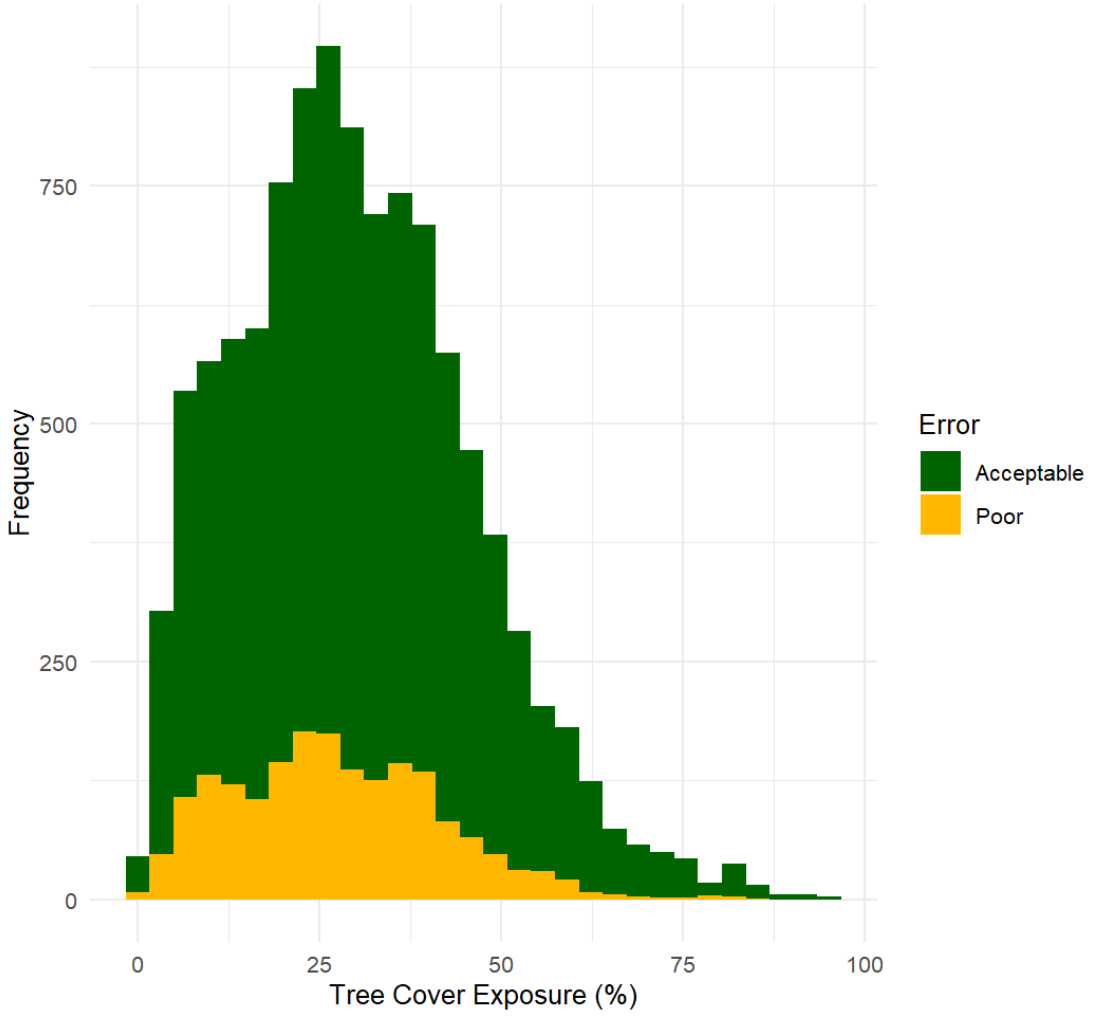

Appendix T. Distribution of tree cover exposure values between observations that were predicted within the thresholds of +/- 0.5ºF versus outside of them for the optimal XGBoost model.

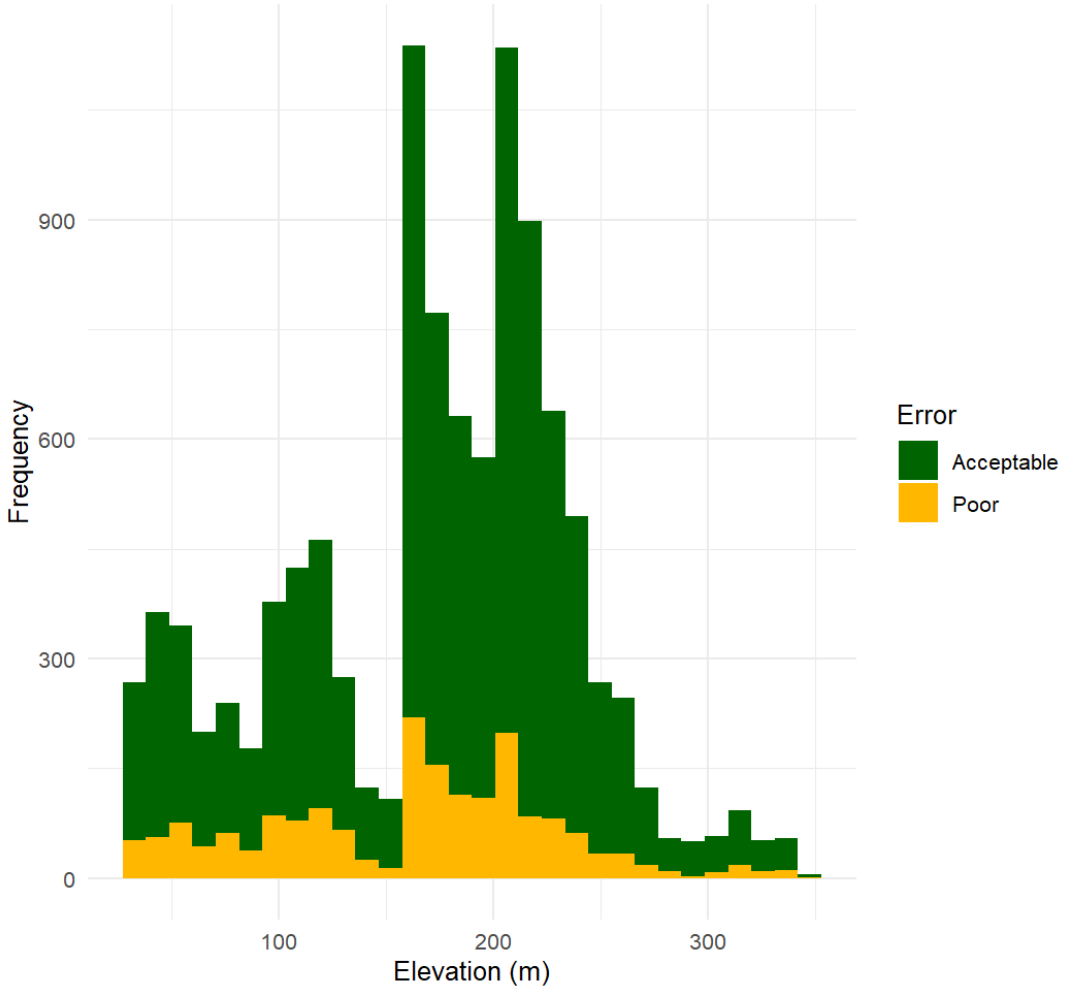

Appendix U. Distribution of elevation values between observations that were predicted within the thresholds of +/- 0.5ºF versus outside of them for the optimal XGBoost model.

Appendix V. Comparison of summary statistics for select features across predictions with errors within and beyond +/-0.5ºF, shown for both optimal machine learning models.

Features	Random Forest				XGBoost			
	Acceptable		Poor		Acceptable		Poor	
	Median	SD	Median	SD	Median	SD	Median	SD
Pavement Exposure	28.03	15.77	33.10	16.29	27.86	15.83	32.56	15.89
Building Exposure	9.99	8.34	11.40	8.60	9.93	8.34	11.27	8.51
Tree Cover Exposure	28.96	16.33	26.10	14.99	29.18	16.49	26.13	14.43
Elevation	183.0	66.19	168.0	68.74	183.00	66.57	170.00	66.39

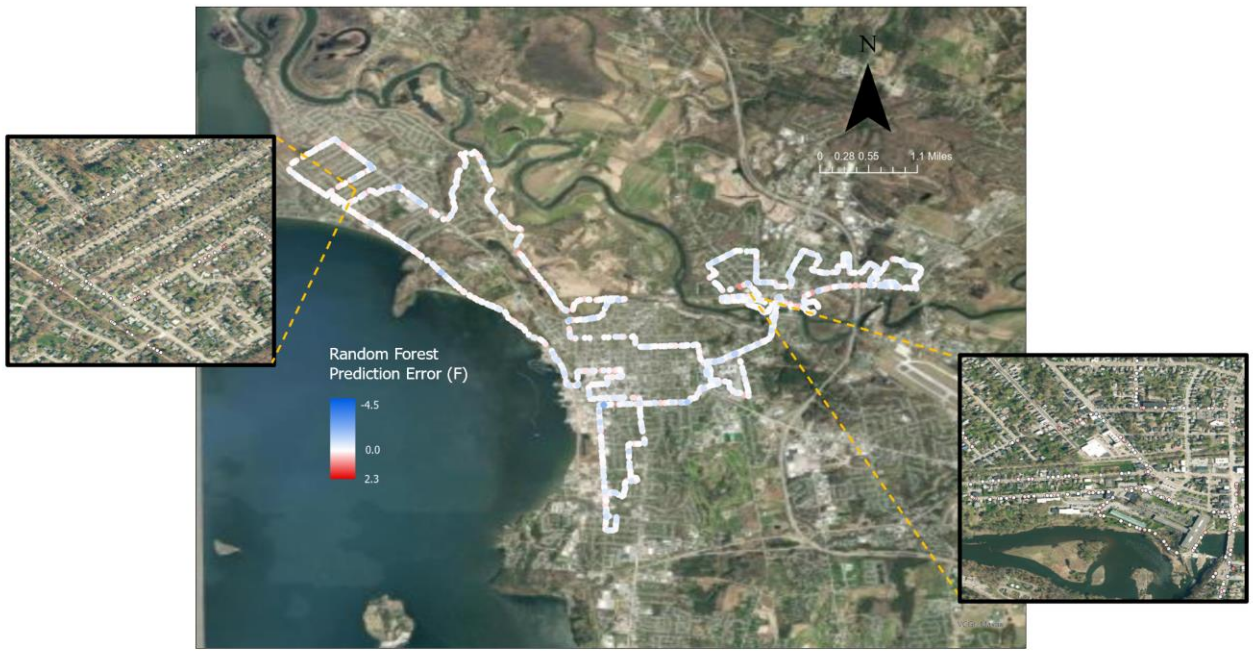

Appendix W. Spatial distribution of error in predictions made on observations in Burlington or Winooski belonging to the validation subset by the optimal RF model.

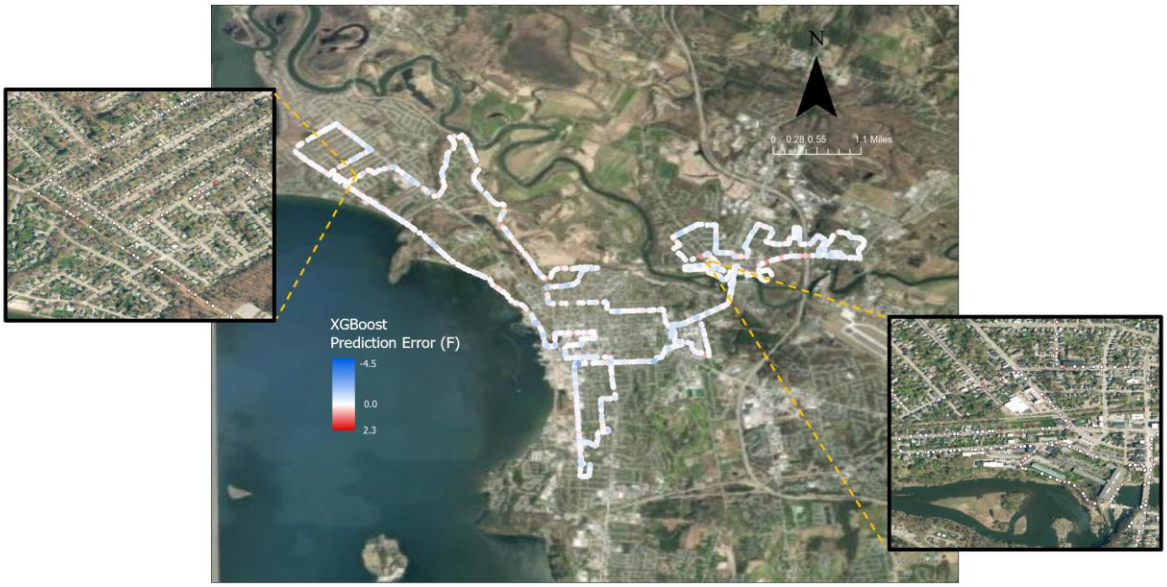

Appendix X. Spatial distribution of error in predictions made on observations in Burlington or Winooski belonging to the validation subset by the optimal XGBoost model.

Appendix Y. Spatial distribution of the difference in error between the optimal RF and optimal XGBoost model in Burlington or Winooski belonging to the validation subset.

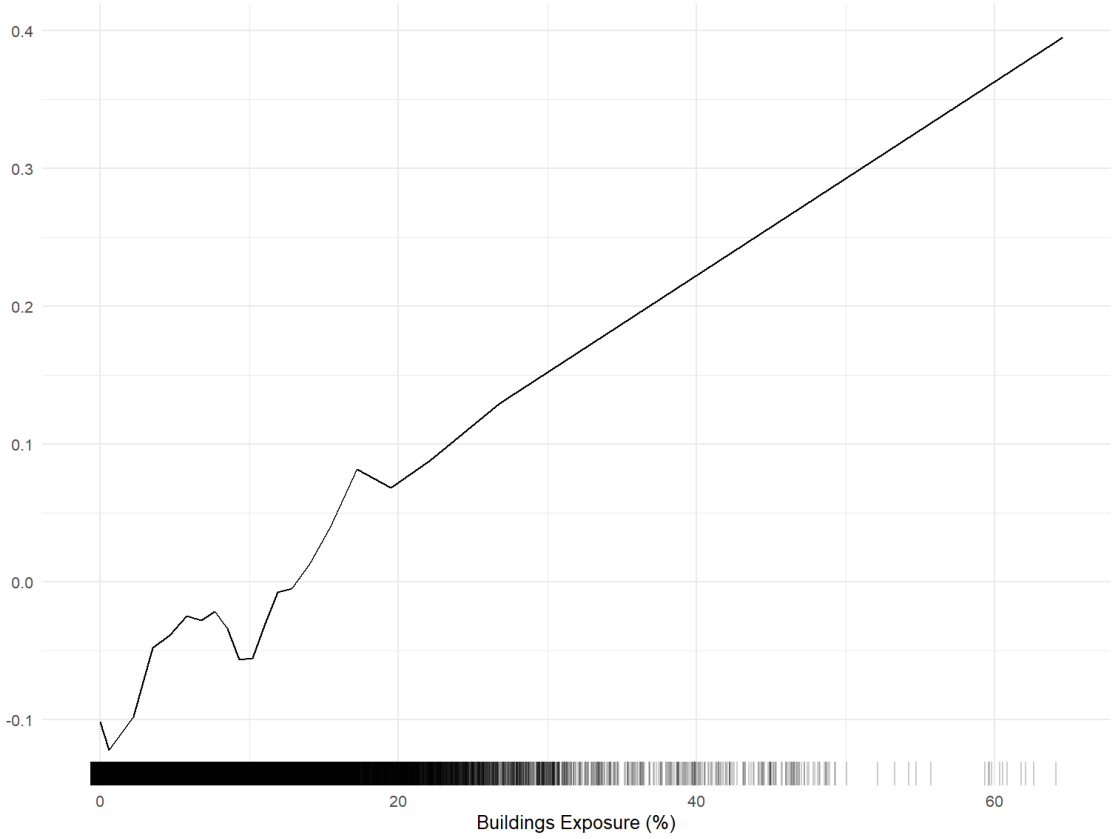

Appendix Z. ALE plot of building exposure's effect on air temperature from optimal RF model.

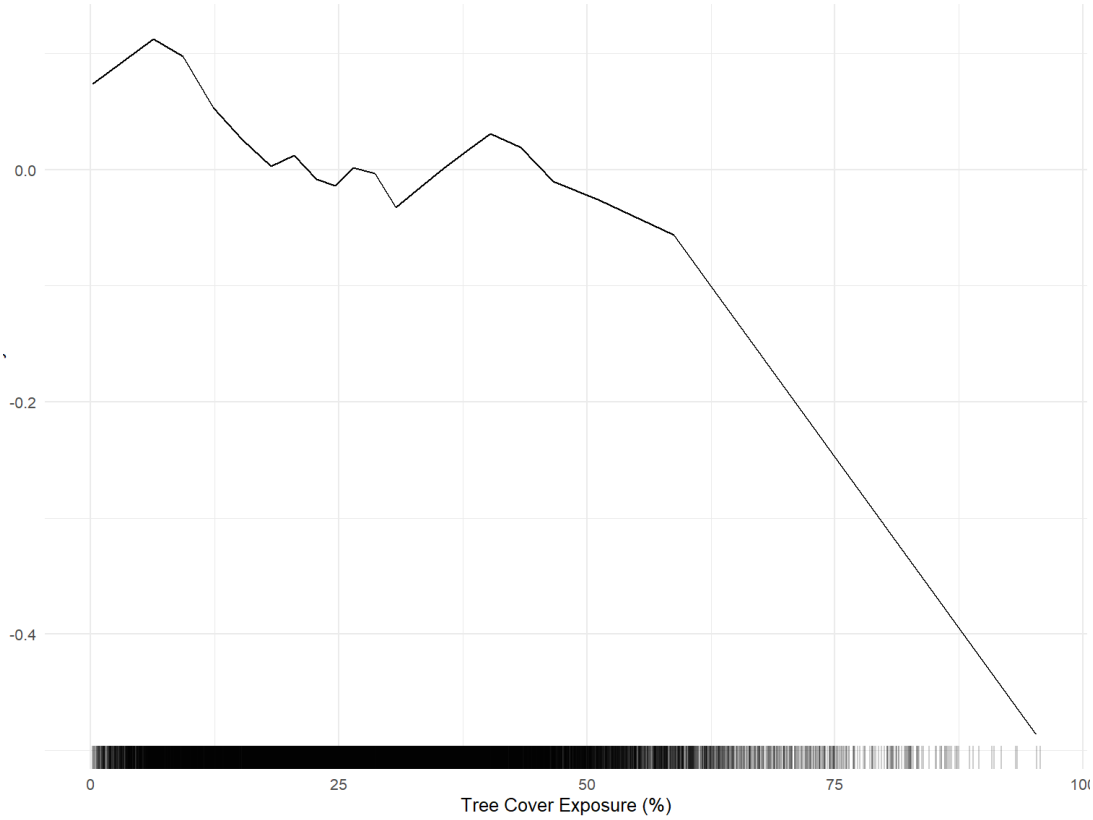

Appendix AA. ALE plot of tree cover exposure's effect on air temperature from optimal RF model.

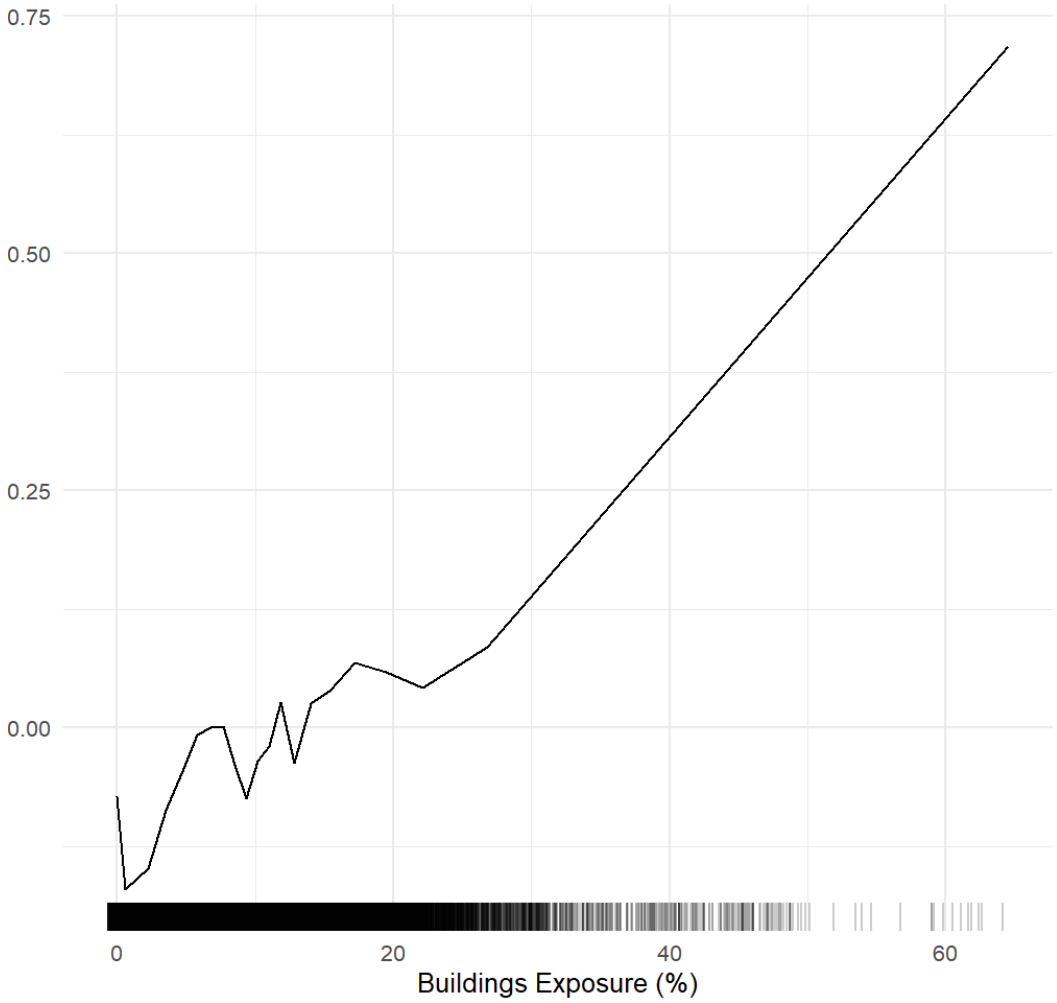

Appendix BB. ALE plot of building exposure's effect on air temperature from optimal XGBoost model.

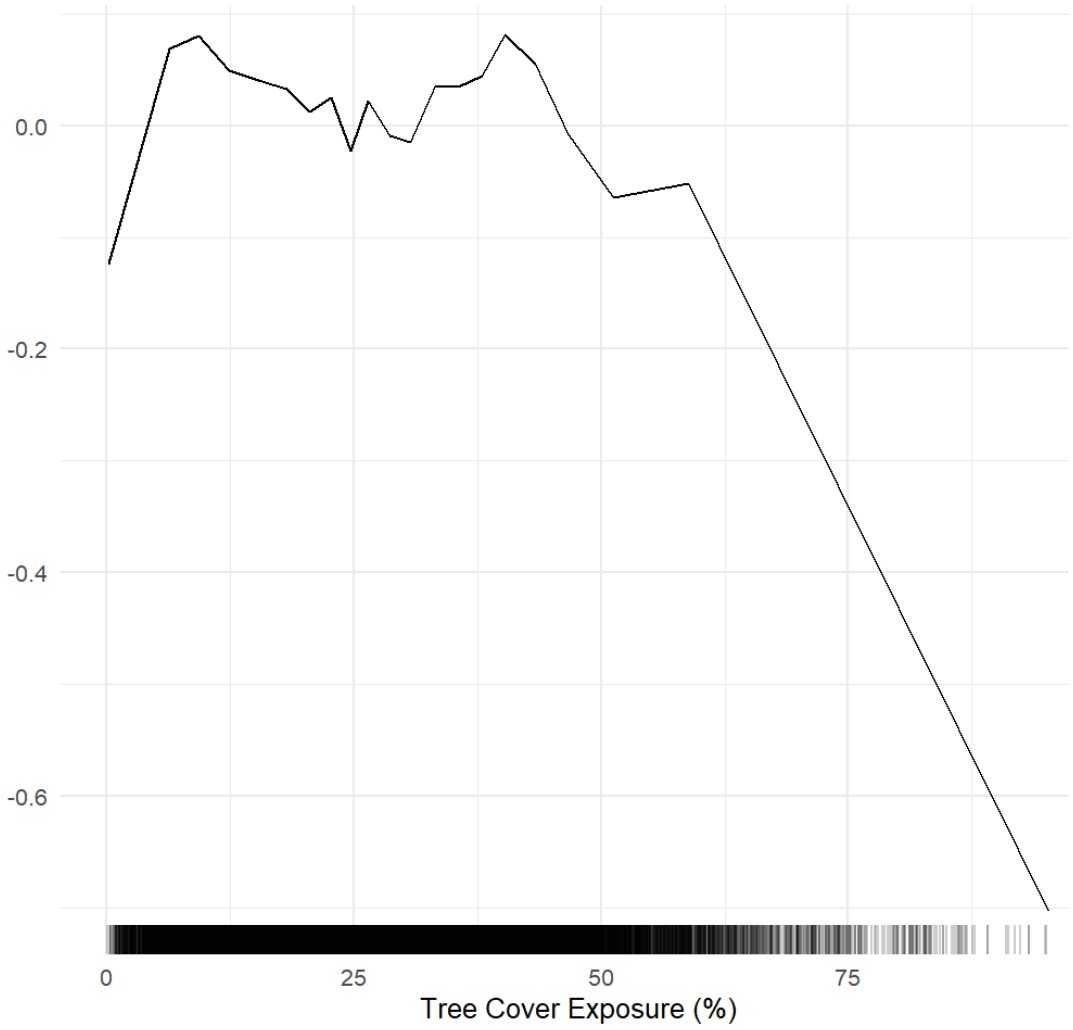

Appendix CC. ALE plot of tree cover exposure's effect on air temperature from optimal XGBoost model.

Appendix DD. Variables of interest with details as to their missingness and central values.

Feature	Missing Values	Central Value
Make	11	Toyota
Model	11	Bolt
Year	11	2023
Vehicle Type	17	Gas/Diesel
Fuel Efficiency Influence	14	Strong Influence
Winter Performance Influence	14	Strong Influence
Seating Amount Influence	16	Slight Influence
Cargo Space Influence	15	Moderate Influence
Maintenance Cost Influence	16	Strong Influence
Reliability Influence	15	Strong Influence
Crash Safety Influence	16	Strong Influence
Driving Range Influence	15	Strong Influence
Towing Capacity Influence	16	No Influence
Off Road Capability Influence	16	No Influence
Highway Capability Influence	16	Slight-Moderate Influence
Automated Features Influence	16	Slight Influence
Vehicle Cost Importance	15	Extremely Important
Concerns of Climate Change	15	Extremely Important
Gas Money Importance	15	Extremely Important
Brand Loyalty	15	Extremely Important
Impacts of Oil and Drilling	15	Extremely Important
Road Trip Capability	15	Moderately Important
Federal Incentive Awareness	22	Full Awareness
State Incentive Awareness	24	Full Awareness
Household Vehicle Count	17	2 vehicles
Participant Age	24	Median=65.78
Number of People in Household	19	2
Gender	20	Male
Household Income	21	Less than $100,000
Household Highest Education	19	Four Year Degree
Zip Code	28	05156

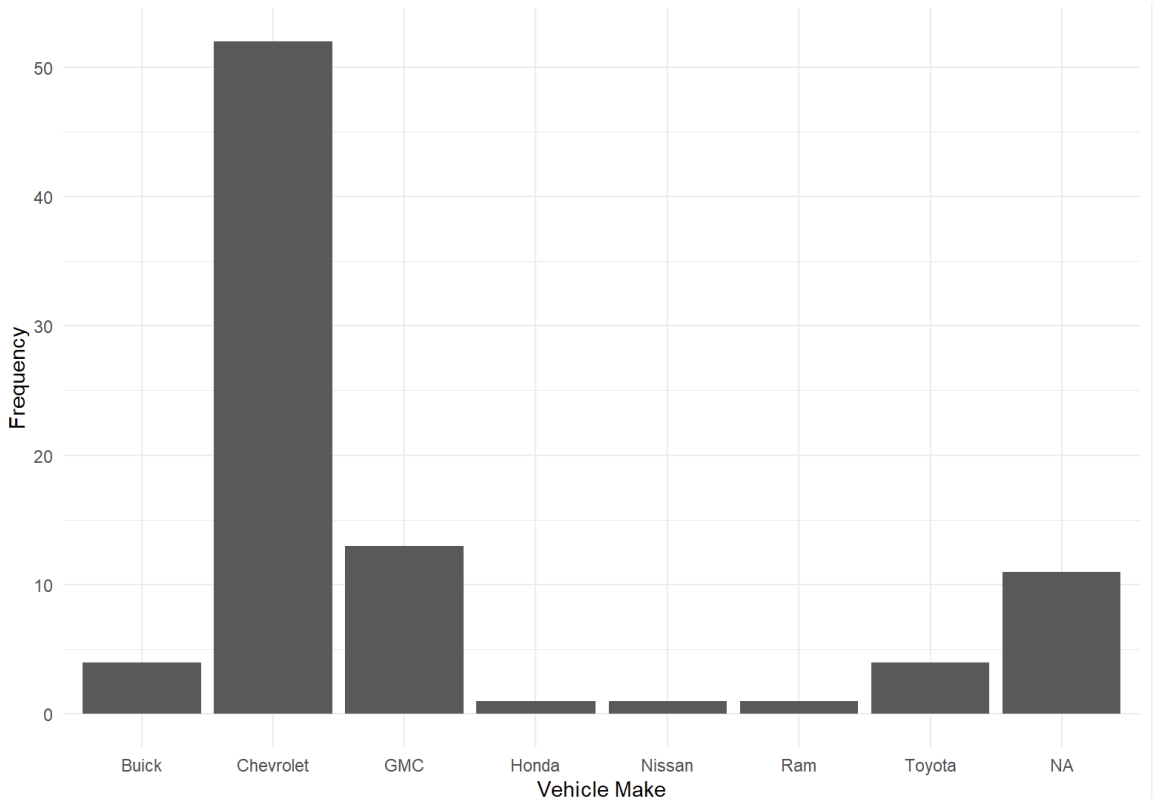

Appendix EE. Distribution of survey participants by vehicle make.

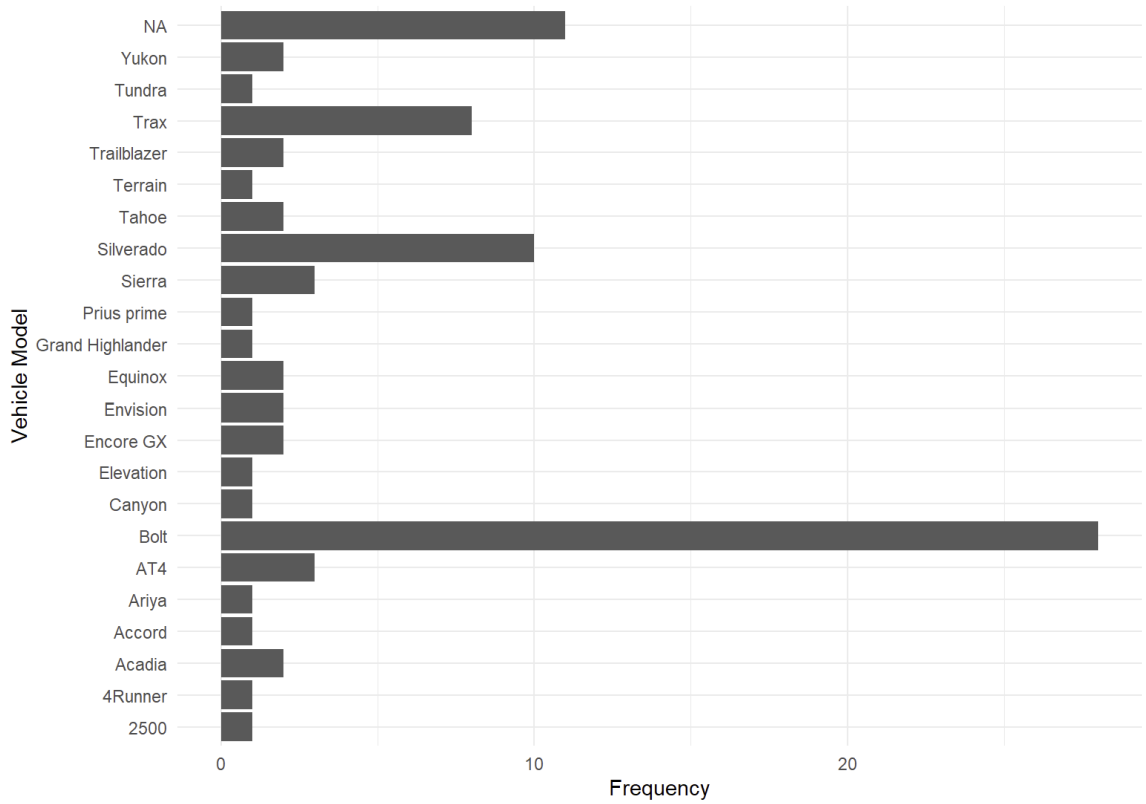

Appendix FF. Distribution of survey participants by vehicle model.

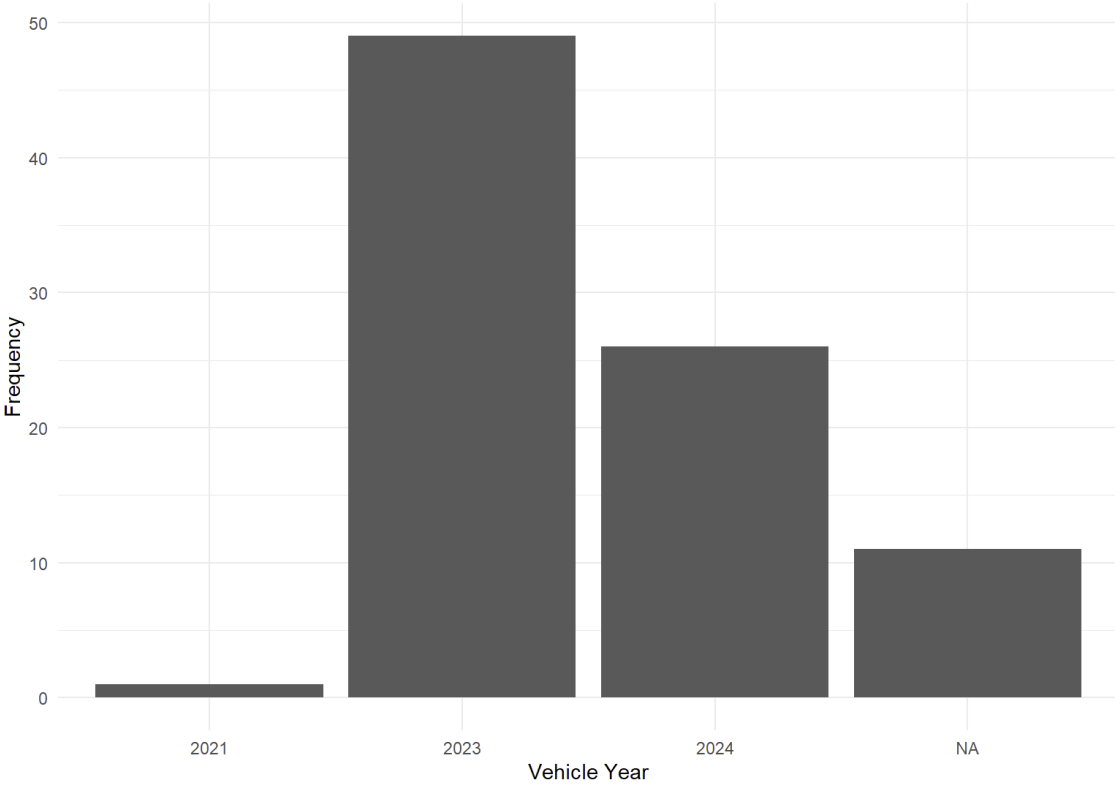

Appendix GG. Distribution of survey participants by vehicle year.